Discovery potential of neutral MSSM Higgs bosons decaying to tau-lepton pairs in the ATLAS experiment

William Edwin Davey

Submitted in total fulfilment of the requirements of the degree of

Doctor of Philosophy

under a Cotutelle arrangement with

The University of Melbourne and *Università degli Studi di Milano*

Produced on archival quality paper

July, 2011

School of Physics

The University of Melbourne

Abstract

The Large Hadron Collider (LHC) is the highest energy particle collider ever built. It recently began operation at CERN and will probe physics at unprecedented scales. ATLAS is a particle detector located at one of the collision points on the LHC ring and is designed to be sensitive to the wide range of physics that could be produced. The primary objective of the LHC experiments is to determine the mechanism of electroweak symmetry breaking, of which many theoretical models exist. In the Minimal Supersymmetric Standard Model (MSSM), electroweak symmetry breaking is achieved through the Higgs mechanism, however, the Higgs sector must be extended with respect to the Standard Model and contains five physical Higgs bosons. The discovery potential of the MSSM Higgs bosons in ATLAS has been evaluated in previous studies, demonstrating adequate sensitivity for discovery or exclusion over a large region of the parameter space. However, these studies were performed using now outdated software, without an estimation of the expected systematic uncertainties or the inclusion of data-driven background estimation procedures.

In this thesis, the discovery potential of the neutral MSSM Higgs bosons when decaying to tau-lepton pairs in the ATLAS experiment is evaluated. One tau is required to decay leptonically while the other is required to decay hadronically. Higgs boson mass hypotheses in the range 150 GeV - 800 GeV are considered. The study assumes a proton-proton collision energy of 14 TeV and an integrated luminosity of $30\,\mathrm{fb}^{-1}$. The expected systematic uncertainty on the background measurement is evaluated and included in the calculation of the discovery potential. Data-driven estimation techniques are developed for the W+jets and QCD di-jet backgrounds.

The contributions of all signal and background processes are estimated using Monte Carlo simulated event samples. The discovery potential is interpreted in the $m_h^{\max}$ benchmark scenario, and is presented in the $m_A\text{-}\tan\beta$ plane. A small degradation in performance with respect to the previous studies is found for Higgs boson masses below 450 GeV due to the inclusion of systematic uncertainties. It is confirmed that a large fraction of the parameter space will be accessible to the ATLAS experiment, which will be able to probe far beyond the regions already excluded by the LEP and Tevatron experiments.

Two separate studies are also included, describing contributions to the modelling of hadronic tau reconstruction in the ATLAS fast simulation packages ATLFAST-I and ATLFAST-II. Firstly, a complete parameterisation of the calorimeter-based hadronic tau reconstruction for use in ATLFAST-I is presented. Secondly, the validation of the track-based hadronic tau reconstruction in ATLFAST-II is presented, including the extraction of correction terms to match the performance in ATLFAST-II to the standard ATLAS simulation.

Declaration

This is to certify that

i. the thesis comprises only my original work towards the PhD except where indicated in the Preface,

ii. due acknowledgement has been made in the text to all other material used,

iii. the thesis is less than 100,000 words in length, exclusive of tables, bibliographies and appendices.

William Edwin Davey

Preface

The ATLAS collaboration consists of more than 3000 scientists. In such a collaboration it is rare that an individual would perform any substantial body of work in isolation. The standard procedure is to work within groups that are assigned specific roles in the collaboration, and to contribute a body of work to the group.

The work in Section 5.3 and Section 5.4 was carried out in collaboration with the ATLFAST task-force, however, is the complete work of the author.

The work in Chapter 6 was carried out in a small group dedicated to the task of evaluating the discovery potential for neutral MSSM Higgs bosons in the di-tau channel at ATLAS. The result of the group has been written up as a public ATLAS note [1]. The vast majority of the work was performed by the author, with the exception of the data-driven $t\bar{t}$ and $Z \rightarrow \tau\tau$ estimation procedures, which were developed by other members of the group. The results from these studies are incorporated into the final result of the thesis, however, the studies themselves are not included. At the conclusion of the study, a few of the members were involved in a projection of the analysis to evaluate what could be expected in the first full year of running at the Large Hadron Collider. The results of this projection are briefly discussed in Section 6.7.7, however, the work was mainly carried out by other members of the group. Other than this only a few small distinct pieces of work were performed by other members of the group, and are detailed explicitly. All the work shown in Chapter 6 is the complete work of the author, except: the parameterisation of the trigger in Section 6.2.9 and the optimisation of the b-tagged analysis in Section 6.3.4.2.

To my parents, for their encouragement and inspiration. . .

Acknowledgements

While standing near the end of the road, looking back upon all the events that have in one way or another shaped my experience as a PhD student, it seems impossible to acknowledge all those individuals whose contributions have meant so much.

To Geoff 'G-Force' Taylor, I sincerely thank you, not only for providing the opportunity to work on the ATLAS experiment, but for your guidance as a supervisor and mentor. Donatella, you took me in as one of your own students, found a place for me to live, discussed with great thought any result or idea no matter how big or small, and of course bought me countless cappucci e briochi at the bar di fisica. To you, I am forever grateful. Elisabetta, without whom I would never have ended up in Milano, your advice regarding research has been invaluable. Andy Greentree, our conversations though occasional, provided a perspective from outside the field that has been extremely valuable. I only hope that at least one of the lines within this thesis might measure up to the style and clarity of the 'Little Book'.

To the IT gurus, Tim and Tom in Melbourne and Massimo in Milano, you always took the time to make things work, you guys rock! To all the dominators who have offered their wisdom and advice, Bruce Yabsley, Antonio Limosani, Uli Felzmann, Aldo Saavedra, Markus Bischofberger, Tony Gherghetta, Silvia Resconi, Michael Dührssen, Stan Lai, Karl Jakobs and many more, thank you. Dave Peake, your all-round coding genius is unbelievable. The number of times you have advised me on how to approach a problem, how to improve my code or have actually just straight out fixed a segfault, are too many to count. Thanks for taking time out to help the novices around you. To the friends I have made along the way, Viv, Dave, Rob 'n' Bryn, Anna, T'Mir, Nads, Uli, Mas, Tim 'n' Tom, Lydia, Machi, Chiara, Ilaria, Simone and the rest of the Post Grad physics students who like discussing life's perversities over a pint at the Cylde, I have had an unforgettable few years. Thank you all for making it so. To Cate, my big sister in Italy, thanks for watching over me.

Finally, to the soon to be Dr. Dre, thank you for putting up with me over the years, for sharing your intellect, wisdom and humility, for reading this thesis numerous times and for your love of culture, food and fine beverages. You truly are awesome!

Contents

List of Figures

List of Tables

1

Introduction

The Large Hadron Collider (LHC) is the highest energy particle collider ever built. It recently began operation at CERN and will probe physics at unprecedented scales, with the hope that new discoveries will lead to a more complete understanding of fundamental physics. ATLAS is a particle detector located at one of the collision points on the LHC ring and is designed to be sensitive to the wide range of physics that could be produced. The primary objective of the LHC experiments is to discover the mechanism of electroweak symmetry breaking (EWSB), which is required to generate the masses of the fundamental particles. In the Standard Model (SM), EWSB is achieved via the Higgs mechanism, which requires the existence of an additional scalar particle called the Higgs boson. To date, no significant evidence of the Higgs boson has been found. Experiments conducted thus far have had insufficient collision energy to scan for the Higgs boson over the complete range of theoretically allowed masses up to approximately 1 TeV (although the Tevatron is close to sensitivity for a SM Higgs over the preferred SM Higgs range up to 200 GeV). The LHC, with a design collision energy of 14 TeV, will cover the entire range up to 1 TeV. The ATLAS collaboration has directed a significant portion of its research towards the development of SM Higgs boson searches, and a definitive answer regarding the existence of a SM-like Higgs boson will be reached. At the same time, a number of theoretical difficulties with the SM Higgs boson exist. Alternative theories have been proposed to eliminate these problems, while still providing a mechanism for EWSB. Of these theories, some contain SM-like Higgs sectors, some contain very different Higgs sectors, and some contain no Higgs sector

at all. Differentiating between these theories will be an extremely important task for the LHC experiments. One of the more popular theories is Supersymmetry, where each Standard Model particle is paired with a superpartner. The Higgs mechanism is still employed to achieve EWSB, however a more complex sector containing at least five Higgs bosons is required. In general, the couplings of the Supersymmetric and Standard Model Higgs bosons to other particles are very different, and the favoured production and decay channels for SM Higgs boson searches no longer provide adequate sensitivity. In Supersymmetric models it is quite common for the Higgs boson coupling to down-type fermions to be significantly enhanced, and Higgs boson production and decay through b-quarks and tau-leptons becomes dominant. The bulk of this thesis is dedicated to analysing the discovery potential of neutral Higgs bosons in the Minimal Supersymmetric Standard Model (MSSM) decaying to tau-lepton pairs at the ATLAS experiment. A chapter is also dedicated to Monte Carlo simulation of the ATLAS detector, where the author's contributions to the modelling of tau-leptons in the two fast simulation packages: ATLFAST-I and ATLFAST-II, is described.

A motivation for Higgs boson searches is given in Chapter 2. A basic description of the LHC and the ATLAS detector is given in Chapter 3. The ATLAS hadronic tau reconstruction algorithms are described in Chapter 4. Chapter 5 begins with a brief introduction to the ATLAS simulation software followed by motivation for the use of fast simulation, and then proceeds with a detailed account of the author's contribution towards the development of the ATLFAST-I and ATLFAST-II simulation packages. The complete analysis of the discovery potential for neutral MSSM Higgs bosons decaying to tau-lepton pairs at ATLAS is given in Chapter 6.

2

Theoretical motivation

Ever since its inception at the turn of the 20$^{\text{th}}$ century, particle physics has sought a description of nature at its most fundamental level. For centuries it was believed that the atom was the fundamental building block of nature. However, in 1897, the discovery of the electron [2] disproved this belief and a move toward the study of sub-atomic physics began. Over the course of the 20$^{\text{th}}$ century hundreds of particles were discovered, from the very earliest discoveries of the proton and neutron [3, 4], to the most recent discoveries of the top-quark [5, 6] and tau-neutrino [7]. Today, the vast complexity of matter states can be described by combinations of just 12 fundamental spin-$\frac{1}{2}$ particles, called fermions. Of the fermions, there exist six quarks and six leptons, each grouped into three families. Each fermion has an anti-fermion partner with identical properties but opposite charge.

The interactions between the particles are mediated by four fundamental forces: electromagnetism, the weak and strong nuclear forces, and gravity. Of these forces, all but gravity have been successfully modelled in a quantum mechanical framework, which is required for a description of particles and their interactions at sub-atomic scales. A self consistent model of quantum gravity remains one of the main focuses of theoretical physics. Fortunately, for most purposes gravity can be omitted in the description of the interactions since it is so much weaker than the other forces at energy scales accessible by experiment. The description of the fermions and their interactions (excluding gravity) is contained within one model: the Standard Model (SM), which has been extensively tested and has shown remarkable agreement with experimental data. The final piece of

the SM is the Higgs mechanism, which was proposed as a means to spontaneously break electroweak symmetry (EWSB), allowing mass generation for the mediating particles of the weak force and the fermions. The Higgs mechanism requires the existence of a new scalar particle, the Higgs boson. To date, no experimental evidence for the Higgs boson has been found. Yet, the inclusion of a mechanism for EWSB is paramount to a successful description of nature, so the Higgs boson was tentatively included as a member of the SM, and remains its only unobserved particle.

2.1 Quantum Field Theory

The dynamics of particles can be described by Quantum Field Theory (QFT), which combines Quantum Mechanics and Special Relativity in a Lagrangian formalism. The dynamics are completely contained in a single Lagrangian density ($\mathcal{L}$), where the Euler-Lagrange equations can be solved to obtain the equations of motion. In this description, the fields are operators that create and annihilate particles. The simple scenario of a massless fermion field $\psi(x)$ in the absence of interactions can be written down as:

$$\mathcal{L}_{\text{fermion}} = i\bar{\psi}\gamma^{\mu}\partial_{\mu}\psi. \tag{2.1}$$

Interactions between the fermion fields can be introduced by requiring $\mathcal{L}$ to be invariant under local transformations of the fermion fields of the form:

$$\psi(x) \rightarrow U(x)\psi(x), \tag{2.2}$$

where $U(x)$ is an $n \times n$ matrix belonging to the $O(n)$ symmetry group. The transformation alone alters $\mathcal{L}_{\text{fermion}}$. However, if the usual space-time derivative ∂_{μ} is simultaneously transformed as such:

$$\partial_{\mu} \rightarrow D_{\mu}(x) = \partial_{\mu} - igA_{\mu}^{a}t^{a} \tag{2.3}$$

where t^{a} are the independent generators of the local symmetry, then invariance is returned. The new fields $A_{\mu}^{a}(x)$ are known as a gauge fields, and comprise N spin-1 vector fields, where N is equal to the number of independent generators of the $O(n)$ group. By defining the gauge field strength tensor:

$$F_{\mu\nu}^{a} \equiv \partial_{\mu}A_{\nu}^{a} - \partial_{\nu}A_{\mu}^{a} + gf^{abc}A_{\mu}^{b}A_{\nu}^{c} \tag{2.4}$$

where f^{abc} are a set of numbers called *structure constants*, the full gauge invariant Lagrangian can then be written as:

$$
\begin{aligned}
\mathcal{L} &= i\bar{\psi}\gamma^\mu\partial_\mu\psi + g\bar{\psi}\gamma^\mu A_\mu^a t^a\psi - \frac{1}{4}F^{a\mu\nu}F_{\mu\nu}^a \qquad (2.5)\\
&= \mathcal{L}_{\text{fermion}} + \mathcal{L}_{\text{interaction}} + \mathcal{L}_{\text{gauge}}
\end{aligned}
$$

where $\mathcal{L}_{\text{fermion}}$ and $\mathcal{L}_{\text{gauge}}$ are the kinetic terms of the fermions and gauge fields, and $\mathcal{L}_{\text{interaction}}$ describes interactions between fermions mediated by the gauge field. The strength of the interaction is determined by the dimensionless gauge coupling constant, g. If $N = 1$, Quantum Electrodynamics is obtained, which is known as an abelian gauge theory. For larger values of N the gauge interactions become more complicated, and self interaction of the gauge fields are allowed. The weak and strong nuclear force are described by gauge theories of this type, called non-abelian gauge theories.

2.2 Standard Model

The Standard Model (SM) is the current description of the fundamental particles and their interactions. The 12 fermions are combined with an $SU(3) \times SU(2) \times U(1)$ gauge symmetry which defines the interactions. Each symmetry gives rise to gauge fields that are associated with physical spin-1 gauge bosons. The symmetries are classified into interactions as follows:

- $SU(3)$ - strong interaction, mediated by the gluon field, G^i ($i \in [1,8]$)

- $SU(2) \times U(1)_{\text{Y}}$ - electroweak interaction, mediated by the W^i ($i \in 1,2,3$) and B fields. In reality the symmetry is broken down to $SU(2) \times U(1)_{\text{EM}}$. The $SU(2)$ symmetry defines the weak interaction, mediated by the physical $W^\pm$ and Z fields. The $U(1)_{\text{EM}}$ symmetry defines the electromagnetic interaction, mediated by the photon field, A.

The weak interaction contains a chiral asymmetry, and does not interact with right-handed fermions. To accommodate this, the fermions are split into chiral groups, where the left-handed fermions are placed in $SU(2)$ doublets, and the right-handed fermions in $SU(2)$ singlets. No right-handed neutrinos have been observed in nature, and they
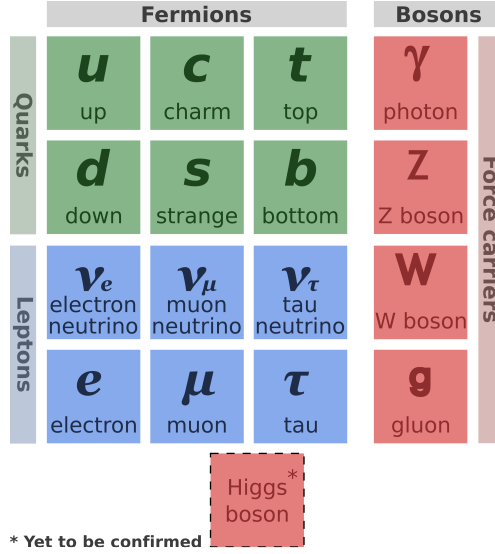
Figure 2.1: Particles of the Standard Model.

are omitted from the SM. Furthermore, the neutrinos are assumed to be massless in the SM. The particles are summarised in Figure 2.1.

Following the discoveries of the top-quark[1] and tau-neutrino[2], the existence of all the fermions and gauge bosons of the SM had been experimentally verified. Many precision measurements have been made with agreement up to one part per million. In fact, the only experimental evidence that deviates significantly from the SM is the recent discovery of non-zero neutrino masses, through flavour oscillations [8] (although, natural mechanisms for neutrino mass generation are easily added to the SM). Furthermore, despite its incredible accuracy in describing the fundamental particles and their interactions, the SM has only 19 free parameters, each of which is determined experimentally. As a consequence, the model holds large predictive power. This has been realised in the prediction of many of the SM particles before their experimental discovery, including: the W and Z gauge bosons (by the Glashow-Weinberg-Salam electroweak theory [9, 10, 11]), the gluon (by quantum chromodynamics), and the top and charm quarks.

Despite its success, the SM still contains one experimentally unobserved particle, the Higgs boson. The Higgs boson is a manifestation of the Higgs mechanism [12], pro-

---

[1]The top-quark was discovered in 1995 by the CDF and D0 experiments at the Tevatron [5, 6].

[2]The tau-neutrino was discovered in 2000 by the DONUT experiment at Fermilab [7]

posed as the method of electroweak symmetry breaking (EWSB) that spontaneously breaks the electroweak $SU(2) \times U(1)_Y$ symmetry down to $SU(2) \times U(1)_{EM}$ in the SM. Some form of EWSB is required to generate non-zero masses for the Z and W gauge bosons while retaining gauge invariance. Despite the theoretically motivated inclusion of the Higgs mechanism in the SM, the real method for EWSB remains unknown. Furthermore, the SM does not include gravity, and no self-consistent quantum theory of gravity has yet been proposed. There is good reason to believe that gravity becomes strongly interacting at some large energy scale, and quantum gravitational effects become important. Therefore, the SM, although being exceptionally successful, is a low energy effective theory. In addition, there are a number of theoretical problems with the SM, in particular the hierarchy problem, the inability to explain the number of generations and the absence of a suitable dark matter candidate. Many theories beyond the standard model (BSM) have been proposed to answer some of the shortcomings of the SM. It is likely that the SM will be replaced by a more complete theory, however, the specific theory will only be determined by experimental verification.

2.3 Higgs

It has long been known that the EW gauge bosons, W and Z are heavy, with approximate masses 80 GeV and 91 GeV respectively. However, gauge theories predict massless gauge bosons. The inclusion of such fields into a gauge theory is nontrivial, as gauge boson mass terms of the form $M^2 V_\mu V^\mu$ (introduced by hand) break the local gauge invariance. To solve this problem, the gauge theory must be spontaneously broken, which is achieved in the SM through the Higgs mechanism, where a new complex scalar field (ϕ) is introduced. The Lagrangian for the simple case of a single massless gauge field A_μ is given here for example:

$$\mathcal{L} = -\frac{1}{4} F^{\mu\nu} F_{\mu\nu} + |D_\mu \phi|^2 - V(\phi), \tag{2.6}$$

where $V(\phi)$ is the scalar potential defined as,

$$V(\phi) = -\mu^2 |\phi|^2 + \frac{\lambda}{2} |\phi|^4. \tag{2.7}$$

The scalar field is designed in such a way that the minimum of the scalar potential, $V(\phi)$, occurs at a non-zero field value ($|\phi| = \frac{v}{\sqrt{2}} = \sqrt{\frac{\mu^2}{2\lambda}}$). If a change of state occurs,

causing a transition from high energy density to low energy density (such as in the early universe), the field will spontaneously fall into a minimum of the potential. As the field at the minima has non-zero expectation values ($\langle \phi \rangle = \pm v$), the original symmetry is broken. At its minimum, the field can be written as:

$$\phi = v + \frac{1}{\sqrt{2}}(\phi_1 + i\phi_2). \tag{2.8}$$

Upon substitution of eqn. (2.8) into eqn. (2.6), one finds a mass term for the gauge boson of the form $g^2 v^2 A_\mu A^\mu$, and a single physical scalar field ϕ_1 with mass $m_{\phi_1} = \sqrt{\lambda v^2}$. The mass term for the gauge boson completely defines v, however due to the remaining unknown parameter λ, the mass of ϕ_1 is unpredicted. Self-coupling terms of the scalar also arise, but depend on λ, so are unpredictable. On the other hand, gauge coupling terms of the form $vg^2 \phi_i A_\mu A^\mu$ and $g^2 \phi_i^2 A_\mu A^\mu$ appear, and since they depend only on g and v, their strengths are completely predicted. The prediction of the coupling strength of the scalar to a pair of gauge bosons is extremely important, as it allows strong statements regarding the existence of such a particle to be made, from experimental observation of the particle in production and decay via pairs of gauge bosons. Finally, the field ϕ_2 remains massless, and as it can be removed by a gauge transformation is considered unphysical. The field ϕ_2 is referred to as a Goldstone boson, and its original degree of freedom manifests as the longitudinal polarisation state of the gauge boson.

In the SM, ϕ is required to be an $SU(2)$ doublet $\left(\begin{smallmatrix}\phi^+\\\phi^0\end{smallmatrix}\right)$, containing four real fields. Spontaneous symmetry breaking (SSB) results in one physical Higgs boson and three massive gauge bosons ($W^\pm$ and Z). Despite the added complexity, the basic mechanics of the Higgs mechanism remains unchanged. The vacuum expectation value, v, in the SM is then given by,

$$v = 2m_W/g_W = \left(\frac{1}{\sqrt{2}G_F}\right)^{\frac{1}{2}} = 246 \text{ GeV}, \tag{2.9}$$

where g_W is the dimensionless weak coupling constant, and G_F is the Fermi coupling constant.

The inclusion of mass terms for the chiral fermion fields in the SM is also problematic because left-handed fermions (f_L) are in $SU(2)$ doublets, while right-handed fermions (f_R) are in $SU(2)$ singlets. Terms of the form $m\bar{f}f = m(\bar{f}_L f_R + \bar{f}_R f_L)$ include products

of doublets and singlets, and therefore break $SU(2)$ invariance. However, inclusion of the SM Higgs into the fermion sector results in terms of the form:

$$g_f[(\bar{f}_L\phi)f_R + h.c.]$$ (2.10)

where the product $\bar{f}_L\phi$ is an $SU(2)$ singlet. After acquiring a vacuum expectation value the fermions obtain mass terms of the form:

$$\sqrt{\frac{1}{2}}g_f v(\bar{f}_L f_R + \bar{f}_R f_L)$$ (2.11)

where g_f is a Yukawa coupling constant that is proportional to the fermion mass. The Yukawa couplings are determined by the measured masses of the fermions, therefore the production and decay rates of the Higgs boson through fermion pairs are predicted in the SM. Thus, the Higgs mechanism that was originally introduced as a method for EWSB is also able to generate gauge invariant mass terms for chiral fermions. With the inclusion of fermion mass terms, couplings of the Higgs boson to both fermions and gauge bosons is completely defined, which maps out a large fraction of phase space that can be experimentally probed.

Although the Higgs mechanism was introduced into the SM primarily to allow mass terms for the weak gauge bosons and was also able to generate chiral fermion masses, the prediction of a scalar boson has another more theoretical implication. The contribution from scalar boson loop corrections in the scattering amplitude of longitudinally polarised WW and ZZ bosons is actually required for unitarity [13]. Without such corrections, the amplitude grows linearly with the interaction energy, and the weak interaction eventually becomes strongly interacting.

The theoretical motivations for the Higgs mechanism outlined in this section have been the driving forces behind Higgs boson searches over the past five decades. However, without a direct discovery, the real method for EWSB will remain unknown.

2.4 Theoretical limits on the mass of the Standard Model Higgs boson

As the parameter, λ is unknown, there is no direct prediction of the Higgs boson mass, m_H, in the SM. In general, this makes the search for such a particle very difficult. However, with some assumptions, usually regarding the energy scale, Λ, up to which

the SM is valid, some theoretical limits can be derived. The three traditional limits come from analysis of Unitarity [13], Triviality [14], and Vacuum Stability [15, 16, 17]. The interpretation of such limits requires some comment. In general, the theoretical limits on the mass of the SM Higgs boson do not definitively rule out the existence of the Higgs boson in certain mass regions, but indicate that a discovery in such a region would point to the existence of new physics occurring at a mass scale $\Lambda_{NP} < \Lambda$.

Unitarity requires that the tree level contribution to the first partial wave a_0, in the expansion of various scattering amplitudes does not exceed the unitarity bound,

$$|\Re a_0| \leq \frac{1}{2}, \tag{2.12}$$

before the scale Λ. As already mentioned, without a scalar boson the unitarity bound is automatically violated in weak boson scattering. The bound is broken at $\sqrt{s} \sim 1.2$ TeV, thus without the Higgs boson, new physics is required below this scale to keep the theory from becoming strongly coupled. The inclusion of a scalar boson results in a partial cancellation, dependent on the mass of the scalar. By requiring that the most divergent process (longitudinal $2W_L^+W_L^- + Z_L Z_L$) satisfies the unitarity bound up to the Planck scale, a limit on m_H can be derived,

$$m_H \lesssim 780 \text{ GeV}. \tag{2.13}$$

The Triviality bound arises from requiring self-interactions of the Higgs field to remain perturbative from the EW scale, Λ_{EW} to some arbitrarily high energy scale, Λ. The evolution of the Higgs quartic self-coupling, λ from Λ_{EW} to Λ, is governed (at one-loop) by the renormalisation group equation [17],

$$32\pi^2 \frac{\partial \lambda}{\partial \ln(q^2/\Lambda_{EW}^2)} = 12(\lambda^2 - y_t^4 + \lambda y_t^2) - (3g'^2 + 9g^2)\lambda + \frac{9}{4}\left[\frac{1}{3}g'^4 + \frac{2}{3}g'^2 g^2 + g^4\right] \tag{2.14}$$

where g and g' are the $SU(2)$ and $U(1)$ coupling constants, and y_t is the top-quark Yukawa coupling. By requiring that λ remain finite for $q^2 < \Lambda^2$, an upper-limit on m_H can be calculated as a function of Λ. This gives the upper limit in Figure 2.2.

Conversely, due to the large top-quark mass, eqn. (2.14) can become negative for small Higgs boson masses. In this case λ will be driven to negative values with increasing q^2, which can lead to a vacuum instability of the Higgs field. This results in a lower bound on m_H, again as a function of Λ. It has been suggested that this complete

stability bound may be too stringent, and that a metastable vacuum with lifetime longer than the age of the universe would also agree with experiment [15]. The authors consider two scenarios: decay from thermal fluctuations at high temperatures in the early universe, and decay from zero-temperature quantum tunnelling. Figure 2.2 shows all three lower bounds on m_H.
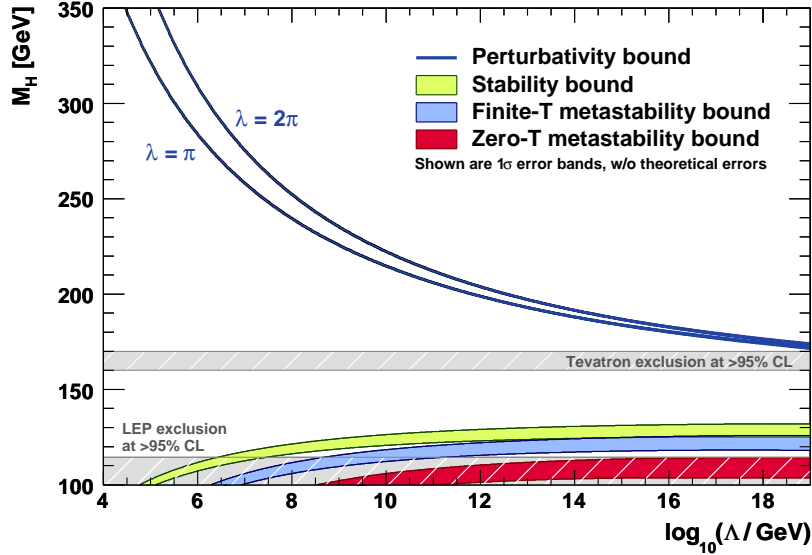
Figure 2.2: Limits on the SM Higgs boson mass as a function of the cutoff scale, Λ to which the Standard Model is valid [18]. The upper limit comes from the triviality (perturbativity) bound, and the lower limit comes from vacuum stability. The experimentally excluded regions from LEP and the Tevatron are also included.

2.5 Problems with the SM Higgs boson

Thus far, the generation of fermion and gauge boson mass has been introduced by considering tree level couplings to the Higgs field. The tree level coupling generates a bare mass term m_{bare}, however, any field that couples to the Higgs field at tree level will also receive corrections to its mass via higher order interactions. The physical mass is the result of the summation of all such terms. Furthermore, the higher order terms involve particle loops in which the momenta of particles are not fixed, and an integration must be performed over all possible momenta. These loops are usually integrated up to a high-energy cutoff (ultraviolet cutoff), Λ_{UV}, which is indicative of the scale at

which new physics beyond the SM appears. As a consequence, the correction terms are dependent on Λ_{UV}. The mass corrections of the fermions and gauge bosons of the SM are only logarithmically dependent on Λ_{UV}, and are said to be UV insensitive. The reasons for this lie in the symmetries (chiral and gauge) that prevented the fields from acquiring mass in the absence of SSB. The Higgs field on the other hand, is a scalar field, and possesses no such symmetry that would prevent mass terms of the form $\Lambda_{UV}^2 \phi^\dagger \phi$ in the Lagrangian. As a consequence, the corrections to the Higgs mass-squared parameter are proportional to Λ_{UV}^2, and the Higgs boson mass is said to be UV sensitive. In a natural theory, m_H would be of the order of the cutoff scale Λ_{UV}. Through measurement of the Fermi coupling, m_H has been determined to be roughly of the order 100 GeV. Therefore in a natural theory, Λ_{UV} could be no larger than $\mathcal{O}(1 \text{ TeV})$. Such small values of Λ_{UV} lead to weak suppression of dimension 5 and 6 operators (suppressed by factors of $1/\Lambda_{UV}$ and $1/\Lambda_{UV}^2$ respectively), and lower limits on Λ_{UV} of around 5 TeV have already been set by their absence in electroweak precision measurements [19]. At the same time, it is possible that the SM could be valid all the way to the reduced Planck scale, $M_P \sim 10^{18}$ GeV, where quantum gravity effects are assumed to become important. If this is the case, and there is no new physics, then an incredible fine-tuning is required between the bare-mass and the corrections terms:

$$m_{\text{phys}}^2 = m_{\text{bare}}^2 + \frac{\Lambda_{UV}^2}{8\pi^2} [\sum_{\text{fermions}} -|\lambda_f|^2 + \sum_{\text{scalars}} \frac{\lambda_S}{2} + ...], \qquad (2.15)$$

to the order of 10^{-32}, to obtain a physical Higgs boson mass around 100 GeV. Such a fine-tuning is generally considered unphysical, since there is no known physical mechanism to produce it. The problem arises since there are 16 orders of magnitude between the EW scale and the reduced Planck scale. This is known as the SM hierarchy problem, and a number of possible solutions have been suggested. It is hoped that searches made at the LHC experiments will help to determine the true nature of the conflicting scales.

A very brief summary of the common theoretical solutions given in the literature is presented here. Firstly, it is acknowledged that if the UV cutoff scale were only a few TeV above the current experimental limit then the Higgs sensitivity to the cutoff scale wouldn't be problematic. However, independent of the UV cutoff, m_H^2 receives corrections from each particle it couples to (either directly or indirectly), proportional

to its mass-squared [20]. Therefore, simply proposing the existence of a new theory at moderate energy without some regulatory behaviour, is unlikely to provide a satisfactory answer as it would require no new particles to exist above the EW scale. The existence of extra hidden dimensions could significantly reduce the Planck scale to just a few TeV [21]. This would resolve the hierarchy problem, but would require a quantum theory of gravity. Little Higgs models have been proposed where the Higgs is the pseudo-Goldstone boson of a much higher energy theory [22]. This would allow the scale of new physics to be pushed up to 10 TeV while still keeping the SM natural, however comes at the expense of expanding the SM to include new TeV mass particles. There are also numerous theories where there is no fundamental Higgs boson (e.g. technicolour [23, 24], top-quark condensate [25] and composite Higgs [26]).

2.6 Supersymmetry

One of the more popular BSM theories is Supersymmetry (SUSY), where a new symmetry between fermions and bosons is imposed on top of the SM. The Supersymmetry operator Q is designed to transform fermionic and bosonic states as such:

$$Q\,|\,\text{fermion}\,\rangle = |\,\text{boson}\,\rangle, \qquad\qquad Q\,|\,\text{boson}\,\rangle = |\,\text{fermion}\,\rangle. \qquad (2.16)$$

Each SM particle is put in a *supermultiplet* paired with its own *superpartner*. The superpartner must have the same gauge group representation, and the supermultiplet must have equal fermionic and bosonic degrees of freedom. The SM fermions are paired with two complex scalar superpartners called *sfermions*, and the SM gauge bosons are paired with a two component spin-$\frac{1}{2}$ Weyl fermion superpartner, called a *gaugino*.

The introduction of Supersymmetry into the SM Lagrangian has a direct effect on the mass corrections for scalar particles. As seen in eqn. (2.15) the corrections from scalar and fermion loops have opposite signs. As long as the SUSY scale is around 1 TeV, the correction terms from the superpartners will largely cancel the corrections from the SM particles. This allows the bare mass of the Higgs to remain at the electroweak scale without fine-tuning. SUSY also contains other theoretically attractive features (such as a suitable dark-matter candidate), which have led to its popularity. However, despite its popularity, a number of concessions have to be made to obtain a phenomenologically sound SUSY model.

Unbroken SUSY predicts superpartners with identical mass to their SM counterparts. Therefore, SUSY must be a spontaneously broken symmetry, but the method of symmetry breaking is unknown. Although SUSY results in the regulation of the Higgs boson mass, it creates another problem, namely that it is difficult to explain why the SUSY scale should be so much smaller than the Planck scale. Furthermore, the Higgs sector from the SM is no longer sufficient to give mass to both the up and down type fermions, and a more complicated sector is required. The sector must contain at least one light Higgs boson, which can only exist in a small region of parameter space that has not yet been excluded by experiment. Nevertheless, SUSY has a number of well motivated theoretical features, and is strongly predictive, allowing verification or exclusion over a large range of parameter space at the LHC.

2.7 Minimal Supersymmetric Standard Model

Supersymmetry requires at least two Higgs doublets to generate the masses of the up and down type fermions. Here, the minimal extension of the SM Higgs sector required for SUSY is discussed, which is the sector assumed in the Minimal Supersymmetric Standard Model (MSSM). The sector contains two complex Higgs doublets: H_1, which couples to up-type fermions and H_2, which couples to down-type fermions. The doublets acquire vacuum expectation values v_1 and v_2, whose ratio is defined as $\tan \beta \equiv \frac{v_1}{v_2}$. After SSB, five physical Higgs bosons remain: two charged scalars $H^{\pm}$, two CP-even scalars h^0 and H^0, and one CP-odd scalar A^0. By definition $m_{h^0} < m_{H^0}$. In general there are six free parameters describing the Higgs sector: four Higgs boson masses, $\tan \beta$ and the mixing angle α between the CP-even states. In the MSSM, relationships between the parameters can be determined from the structure of the superpotential, leaving only two free parameters at tree-level, generally taken to be m_{A^0} and $\tan \beta$. The masses and coupling strengths to fermions and gauge bosons of all the Higgs bosons are completely defined at tree-level by the choice of these two parameters. The relationships also result

in a number of important limits on the masses of the scalars:

$$
\begin{aligned}
m_{H^\pm} &\geq m_W \\
m_{H^0} &\geq m_Z \\
m_{A^0} &\geq m_{h^0} \\
m_{h^0} &\leq m_Z.
\end{aligned}
$$

The last limit gives a large constraint on the model, requiring at least one light Higgs boson below the Z boson mass. In fact, the LEP 95% exclusion limit covers the complete allowed range for m_{h^0} at tree level. However, loop corrections to m_{h^0} can be significant. Depending on couplings to the top quark, heavy scalars and mixing in the stop sector, m_{h^0} can be pushed up to ~ 135 GeV. This is known as the m_h-max scenario [27], and is often chosen when representing experimentally excluded regions of the MSSM as it is the most conservative.

Not only does the MSSM Higgs sector contain a completely different mass spectrum to the SM Higgs sector, but it can also result in very different couplings to the SM particles. Table 2.1 gives the ratio of the couplings of the neutral MSSM Higgs bosons to up-type fermions (f_u), down-type fermions (f_d) and the weak gauge bosons, with respect to the SM Higgs boson couplings. Of particular importance are the couplings to gauge bosons (which are heavily relied upon in SM Higgs boson searches), which are suppressed or even absent, and the couplings to down-type fermions, which are enhanced by $\tan\beta$ (which can be much larger than unity). In general, searches for h^0, H^0 and A^0 require different experimental techniques than searches for the SM Higgs boson, and often rely on production and decay through pairs of b-quarks or tau-leptons. Ultimately, searches for Higgs bosons need to be as extensive as possible to cover the range of theoretical possibilities.

While the discussion of the MSSM Higgs sector was motivated by the theoretically appealing features of Supersymmetry, the MSSM Higgs sector is actually a constrained case of the more general class of two-Higgs-doublet models (2HDM). In fact, there is no reason why a 2HDM could not exist within the Standard Model or other BSM theories. The general 2HDM has a number of theoretically appealing features [28], and differentiation between a SM Higgs boson and a SM-like Higgs boson from a 2HDM will be necessary independent of establishing the existence of SUSY. Fortunately, the

Neutral MSSM Higgs boson coupling strengths

Higgs Boson	f_u	f_d	W/Z
h	$\cos\alpha/\sin\beta$	$-\sin\alpha/\cos\beta$	$\sin(\alpha-\beta)$
H	$\sin\alpha/\sin\beta$	$\cos\alpha/\cos\beta$	$\cos(\alpha-\beta)$
A	$1/\tan\beta$	$\tan\beta$	-

Table 2.1: Coupling strengths of the neutral MSSM Higgs bosons compared to the SM Higgs boson, to up-type fermions (f_u), down-type fermions (f_d) and the weak gauge bosons.

search techniques developed for the MSSM Higgs bosons are often directly transferable to a 2HDM, especially for the group of Type-II 2HDMs in which the two doublets have the same coupling structure to the fermions as in the MSSM.

2.8 Experimental limits

Despite the various theoretical limits placed on the Higgs bosons of the SM and BSM theories, a full scan of the Higgs mass parameter space up to 1 TeV is necessary. If the true method of EWSB is to be determined, a large amount of experimental information will be needed to discriminate between the various possible models. To date, no experiment has reported any significant excess of Higgs boson events over the SM background. However, large regions of parameter space have been excluded by LEP and the Tevatron.

LEP (the Large Electron-Positron Collider) finished operation in 2000, reaching a final collision energy of 209 GeV. Higgs searches were made in the production mode $e^+e^- \to ZH$, where a Higgs boson is radiated off a Z. After the combination of the results from the four LEP experiments, a lower limit of 114.4 GeV on the SM Higgs boson was reported at the 95% confidence level [29]. Large regions of the MSSM parameter space were also excluded at the 95% confidence level [30]. The exclusion contours for m_{h^0} and m_{A^0} vs. $\tan\beta$ in the m_h-max scenario are given in Figure 2.3. The regions $m_{h^0} < 92.9$ GeV and $m_{A^0} < 93.4$ GeV, and $0.9 < \tan\beta < 1.5$ are completely excluded.

The Tevatron is a $p\bar{p}$ collider with collision energy of 1.96 TeV. Searches for a SM Higgs boson have been conducted in a variety of channels, including three production
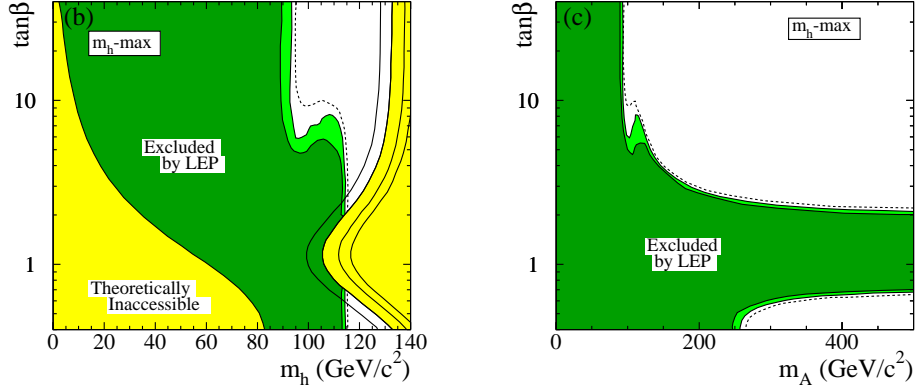
Figure 2.3: LEP exclusions, at 95% CL (medium-grey or light-green) and the 99.7% CL (dark-grey or dark-green), of the h^0 (left) and A^0 (right) MSSM Higgs bosons in the m_h-max scenario, for $m_t = 174.3$ GeV [30]. The theoretical upper-limit on m_h is given for four values of the top quark mass; from left to right: $m_t = 169.3, 174.3, 179.3$ and 183.0 GeV.

modes: production in association with vector bosons ($q\bar{q} \to HW/Z$), gluon-gluon fusion ($gg \to H$) and vector boson fusion ($q\bar{q} \to q'\bar{q}'$), and four decay modes: $H \to b\bar{b}$, $H \to W^+W^-$, $H \to \tau^+\tau^-$, $H \to \gamma\gamma$. The latest combined results from the Tevatron's two experiments CDF and D0 (as of July 2010) report an exclusion at the 95% confidence level of a SM Higgs boson in the mass range 158 GeV $< m_H <$ 175 GeV [31]. The main contribution to the exclusion around $m_H \sim 170$ GeV comes from the $gg \to H \to W^+W^-$ channel.

The 95% CL limit on the SM Higgs production cross section as a ratio to the theoretical prediction is shown in Figure 2.4. The excluded region is expected to continue expanding as more data is collected and the search techniques are refined. However, the Tevatron will not be able to cover the whole region up to 1 TeV, and while it is possible that a 95% CL exclusion could be achieved over the preferred SM Higgs mass range (in the absence of signal excess), it is unlikely that 3-sigma evidence could be found if an excess were observed. Searches for neutral MSSM Higgs bosons have been conducted in the $H \to \tau\tau$, $bH \to b\tau\tau$ and $bH \to bbb$ channels [32, 33, 34]. The 95% CL exclusion limits in the m_h-max scenario are given in Figure 2.5. Again, it is expected that the exclusion limits will continue to push into the $\tan\beta$-m_A plane, however a full coverage of the parameter space up to 1 TeV is not possible.
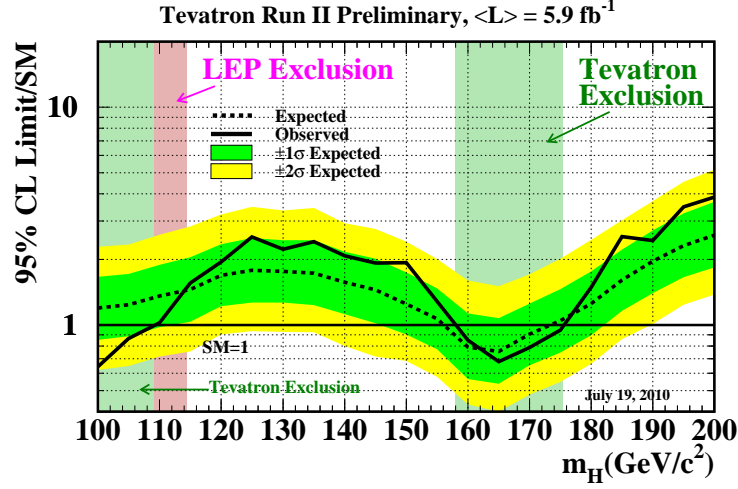
Figure 2.4: Tevatron 95% CL limit on the SM Higgs production cross section as a ratio to the theoretical prediction vs. Higgs boson mass [31].

Independent of the direct searches for the Higgs boson, electroweak precision data from both LEP and the Tevatron has been used to predict the mass of the Higgs boson through its inclusion in loop corrections. A global fit to the data assuming validity of the SM with a given Higgs sector is performed. A fit assuming the minimal SM Higgs sector including the most recent data from the Tevatron is performed in [35], and is shown in Figure 2.6 (left). A preferred value for the mass of the SM Higgs boson of $m_H < 158$ GeV is found at the 95% confidence level. A fit is also performed assuming a general Type-II 2HDM and the preferred regions of parameter space can be seen in Figure 2.6 (right).

2.9 Future searches at the Large Hadron Collider

For years the Tevatron was the highest energy particle collider, and was at the forefront of Higgs boson searches. However, it was recently surpassed when the Large Hadron Collider (LHC) began operation. Given that the Tevatron will not be able to sufficiently probe the Higgs parameter space, it will be very important for the experiments running at the Large Hadron Collider (LHC): ATLAS and CMS, to cover as much of this
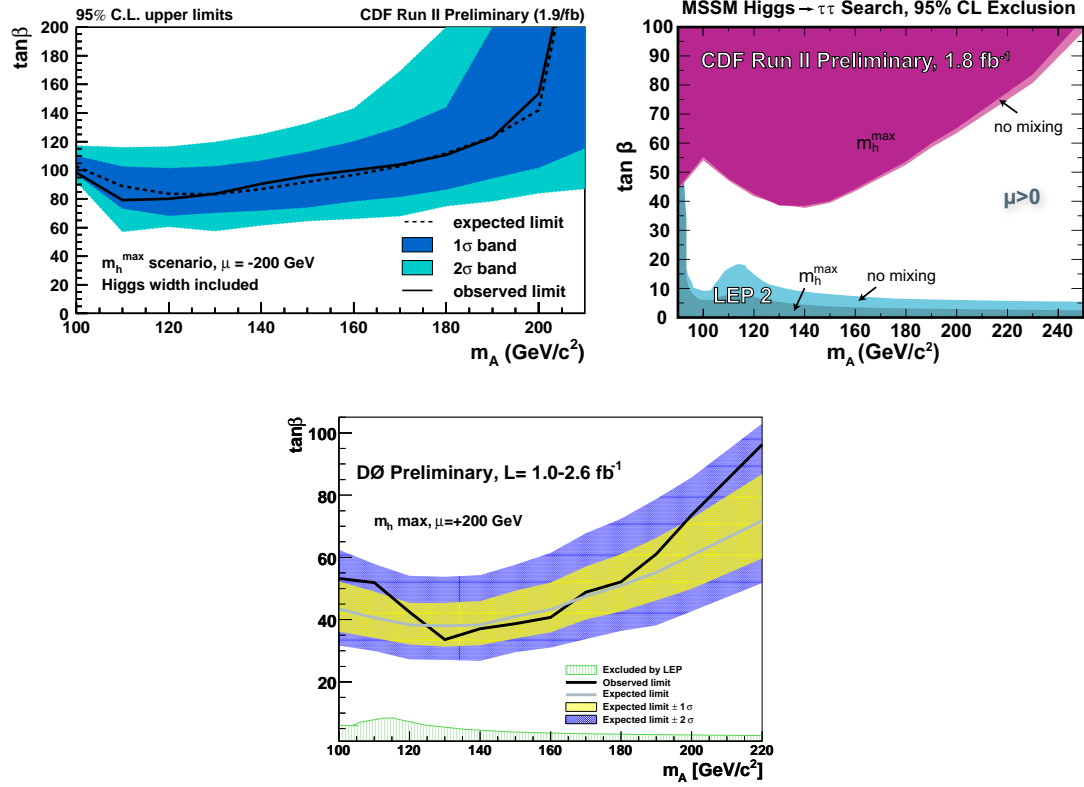
Figure 2.5: 95% CL exclusion on the MSSM parameter space from the Tevatron experiments for the m_h-max scenario. The result from the CDF $b\phi \rightarrow bbb$ analysis (top left) [32], the CDF $\phi \rightarrow \tau\tau$ analysis (top right) [33] and the D0 result for the combination of the $b\phi \rightarrow bbb$, $\phi \rightarrow \tau\tau$ and $b\phi \rightarrow b\tau\tau$ analyses (bottom) [34] are given.
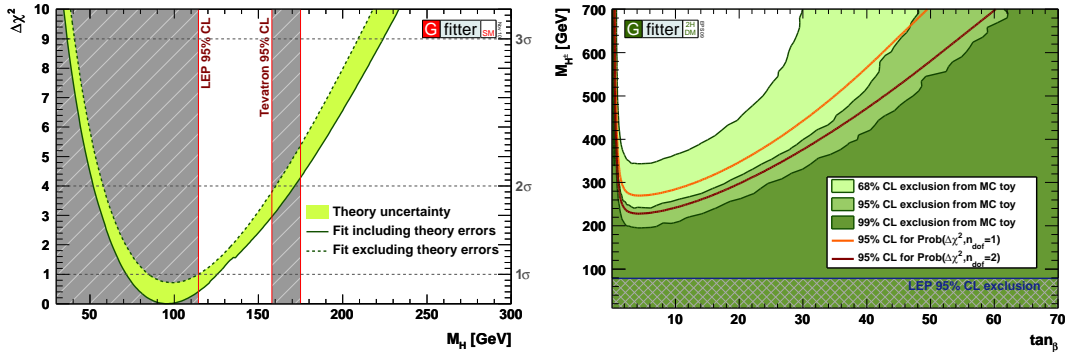
Figure 2.6: Fits to the most recent electroweak precision data from LEP and the Tevatron assuming the validity of the SM with the minimal Higgs sector (left) and a general Type-II 2HDM (right), where the exclusion curves are given in the $m_{H^\pm}$-$\tan\beta$ plane [35].

parameter space as possible. The most recent evaluation of the discovery potential for a SM Higgs boson performed by both experiments concluded that a discovery over the complete mass range would be possible after a few years running at design collision energy and luminosity [36, 37]. The discovery potential for MSSM Higgs bosons has also been evaluated by both collaborations. In this thesis, the full evaluation of the discovery potential for neutral MSSM Higgs bosons decaying into tau-lepton pairs in the ATLAS experiment is given. Over the next few years the LHC will operate at 7 TeV (half the design collision energy) and is expected to deliver somewhere between $1 - 5\mathrm{fb}^{-1}$. While this may not be sufficient for a 5-sigma discovery over the entire mass range, it should allow significant extensions of the current exclusion limits.

3

LHC and the ATLAS experiment

The study of physics relies on the observation of physical phenomena. The ability to observe, however, is often limited by one's access to a phenomenon. Throughout the history of High Energy Physics (HEP) the favoured approach has been to directly produce new phenomena in the laboratory where they can be observed. More recently, as the study of HEP expands into ever higher energy regimes, the use of particle colliders has not only grown, but has become the only route to explore the majority of physics at the most fundamental level. In general, the new physics that may occur at these energy regimes is associated with new massive particles. Most massive particles are not found naturally in the low energy density of our current universe since they spontaneously decay into combinations of lighter particles. The principle behind particle colliders is to create these new massive particles by converting the kinematic energy of lighter particles into mass energy through interactions. Inevitably, if a new massive particle is created in such a process, it will decay immediately, and one must infer its existence by observing its decay products and reconstructing a possible decay chain. The observation of the decay products is performed by highly specialised particle detectors.

The Large Hadron Collider (LHC), which recently began operation at CERN, is the highest energy collider ever built. At design specifications, the LHC will provide almost an order of magnitude increase in the maximum attainable collision energy, previously reached by the Tevatron. As discussed in the previous chapter, significant theoretical motivation suggests that new physics must emerge around the TeV scale, which will be accessible to the experiments at the LHC. It is extremely important for the success

of the LHC, that these experiments are optimised to be sensitive to the largest range of possible new physics. ATLAS is one of the particle detectors located at a collision point on the LHC ring designed to search for the signatures of new physics in the LHC collisions. A brief description of both the LHC and ATLAS are given in this chapter, however, much more detailed accounts can be found in [38] and [39].

3.1 The Large Hadron Collider

The process of producing new particles via collisions, and inferring their existence from the reconstruction of decay products has an inherent difficulty. The real nature of a single event can never be determined categorically. Rather, one seeks to observe a statistically significant sample of events in which a new particle was reconstructed, before claiming its existence or measuring its properties. To do this, it is advantageous to produce as many events containing the new particle as possible. Fortunately, the physics of particle colliders is well known, and the rate of production of a given event is:

$$R_{\text{event}} = L \cdot \sigma_{\text{event}}, \tag{3.1}$$

where σ_{event} is the production cross section for the event and L the collider luminosity. The production cross section is dependent on the centre of mass energy $\sqrt{s}$ of the two collider beams, and falls rapidly as the total mass-energy produced in an event approaches $\sqrt{s}$. Thus, the rate is controlled by the two machine properties: $\sqrt{s}$ and L.

The Large Hadron Collider is at the forefront of accelerator technology, and at design specifications will collide two 7 TeV, counter-rotating proton beams at a luminosity of $10^{34}\,\text{cm}^{-2}\text{s}^{-1}$. Both the centre of mass energy and luminosity are unprecedented in collider experiments, allowing searches for physics in completely new regions of phase space. The production cross sections of a number of processes at proton-(anti)proton colliders are given in Figure 3.1. Of particular interest is the cross section for Higgs boson production at the LHC, which in the case of large Higgs mass can increase by many orders of magnitude with respect to the Tevatron. In general, the increase in collision energy from the Tevatron to the LHC results in a huge increase in the production cross section for any new particles in the mass range 500 GeV $\lesssim m \lesssim$ 5 TeV. This provides sensitivity to a large range of phase space (including many BSM theories) that was inaccessible to the Tevatron.

One particularly important aspect of hadronic colliders compared to leptonic colliders is that hadrons are not fundamental. They are made up partons, each of which carry a fraction of the total momentum of the hadron. While the average fraction of longitudinal momentum carried by the partons is governed by the parton distribution function of the hadron, the fraction on an event-by-event basis is unknown. Furthermore, it is very difficult to measure the longitudinal momentum components of the colliding partons since a large amount of the total momentum is directed down the beam-pipe where it is impossible to detect. This has two very important consequences: 1. the energy available for particle creation in the collision of two partons is significantly lower than the total centre-of-mass energy of the two hadrons, 2. transverse quantities (p_T and E_T) rather than 3D quantities (p and E) are the focus of kinematic measurements. In addition to the second consequence, the inability to determine the total longitudinal momentum means that while missing transverse energy can be determined by momentum conservation in the plane transverse to the colliding beams, the total missing energy cannot be measured. In turn, the focus on transverse quantities plays a large role in the design of the detectors at hadronic colliders.

The LHC is installed at CERN, in the existing 26.7 km long tunnel built for the Large Electron-Positron (LEP) collider. The existing tunnel and injector system were used to save costs. The injector system is comprised of a number of rings that accelerate the beams to 450 GeV. The injection beams are transferred into the LHC ring via two 2.5 km tunnels, where they are further accelerated to a maximum of 7 TeV by radio-frequency oscillating electric fields. The beams are directed around the ring by 1232 superconducting dipole magnets, made from NbTi Rutherford cables. The magnets are housed in cryostats of superfluid helium cooled to 1.9 K. The maximum energy of the beams is limited by the integrated magnetic field around the ring, and each magnet can deliver field strengths up to 8.33 T.

It is advantageous for accelerators to use beams of opposite charge, as a common magnet system can be used to counter-rotate the beams. However, the use of an anti-proton beam was not feasible for the LHC, as it is impossible to obtain a beam intensity high enough to achieve the desired luminosity. Instead, the LHC must have two rings with opposite magnetic fields to create counter rotating proton-proton beams. Along with the beam intensity, a number of other beam parameters define the final luminosity
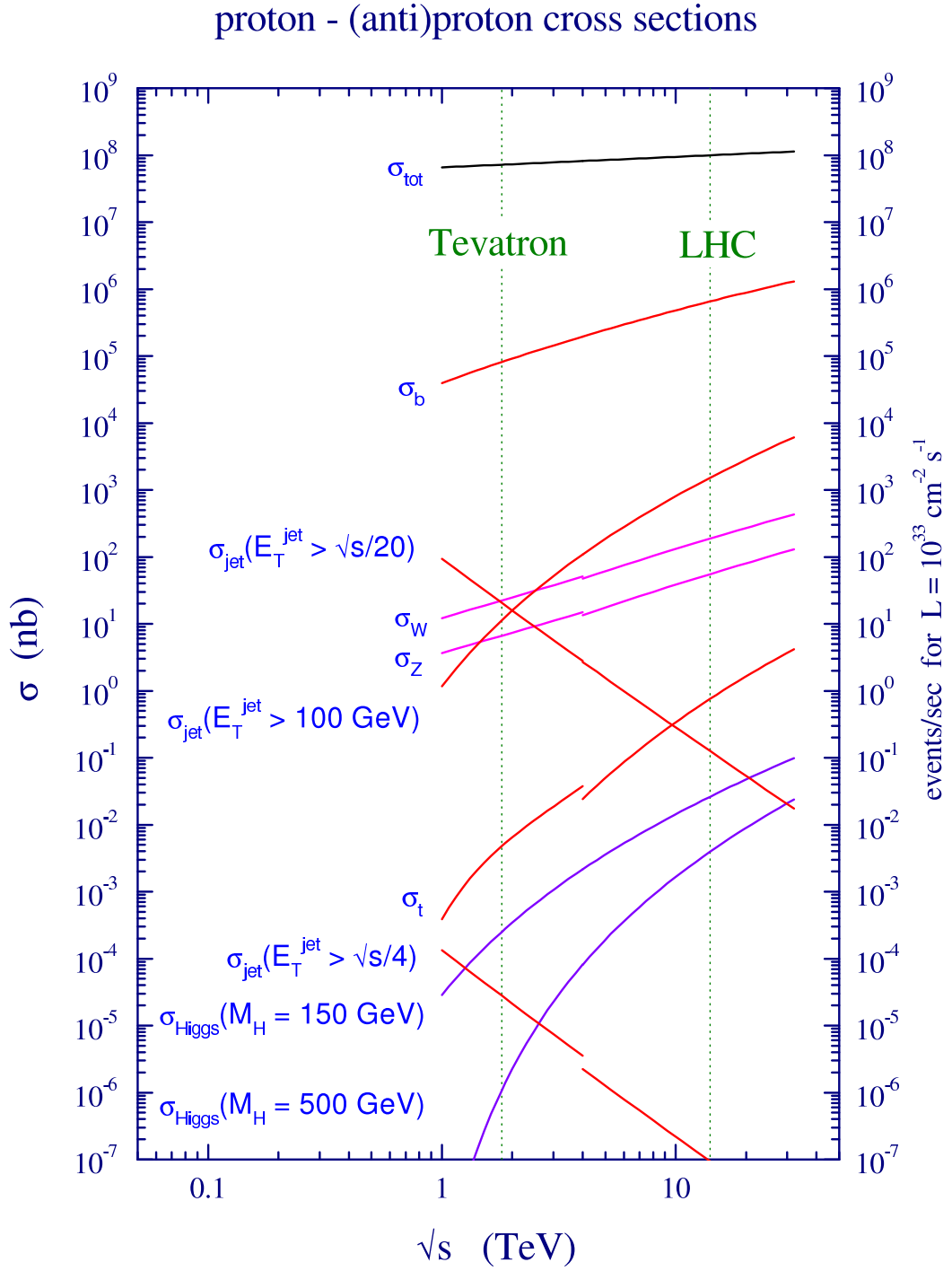
Figure 3.1: Cross sections vs. collision energy ($\sqrt{s}$) for physics processes at proton-(anti)proton colliders [40]. Note the large increase in the rate of Higgs boson production from the Tevatron to the LHC.

achievable by the LHC. The luminosity can be calculated by approximating the LHC as two identical circular gaussian proton beams, for which:

$$L = N_b f \frac{n_p^2}{4\pi\sigma_{\mathrm{T}}} F \qquad (3.2)$$

where N_b is the number of proton bunches per beam, f the revolution frequency, n_p the number of protons per bunch, σ_T the beam radius at the interaction point (IP), and F a geometric luminosity reduction factor of order unity[1]. Details of the LHC beam parameters are given in Table 3.1.

LHC beam parameters

Maximum beam energy	7 TeV
Maximum luminosity	$10^{34}\,\mathrm{cm}^{-2}\mathrm{s}^{-1}$
Number of bunches (N_b)	2808
Number of protons per bunch (n_p)	1.15×10^{11}
Revolution Frequency (f)	14.27 kHz
Time between collisions	24.95 ns
Beam radius at IP (σ_{T})	16.6 μm
Beam length (σ_z)	7.55 cm
Full crossing angle (θ_c)	$\approx 300\ \mu$ rad

Table 3.1: LHC beam parameters

The total integrated luminosity per year expected at the interaction points of the LHC is not only dependent on the maximum instantaneous luminosity, but also on the decay time of the beam, τ_L, and the total turnaround time taken to fill, accelerate and finally dump the beams. The average turnaround time expected at the LHC is estimated to be approximately seven hours [38]. The integrated luminosity from a single run is given by

$$L_{\mathrm{int}} = L\tau_L \left[1 - e^{-T_{\mathrm{run}}/\tau_L}\right] \qquad (3.3)$$

where T_{run} is total length of the run. Assuming the LHC can be run for 200 days per year with a beam lifetime of 15 hours, the optimum length for a single run is estimated to be 12 hours [38]. This corresponds to a maximum expected integrated luminosity of 80 fb^{-1} per year. The total quantity of data collected by the LHC experiments will be

---

[1]F is the reduction factor due to the crossing angle required to collide the two spatially separate beams at the impact point, with an approximate value of 0.8 at the LHC.

orders of magnitude larger than previous experiments, allowing searches for extremely rare processes.

The LEP tunnel has eight possible interaction points, of which four are active at the LHC. Two general purpose experiments: ATLAS and CMS are positioned at Point 1 and Point 5, with focus on the discovery of new physics. LHCb is located at Point 8 and is designed to study B-physics. As well as providing high-energy proton-proton collisions, the LHC will also collide lead-ion beams at 2.76 TeV per nucleon at a peak luminosity of $L = 10^{27}\,\mathrm{cm^{-2}s^{-1}}$. ALICE (located at Point 2), is a dedicated experiment for the study of quark-gluon plasma, which is expected to be produced in the Pb collisions. There are also two specific purpose experiments that share interaction points with the other experiments: TOTEM[1] and LHCf[2].

3.2 ATLAS

As the technology of particle colliders advances, so too must the technology of the detectors. The luminosity and centre-of-mass energy of the LHC when operating at design specifications will lead to extreme experimental conditions. The ATLAS detector must not only be able to function continually with minimal degradation due to radiation damage caused by the conditions, but must also provide precision measurements over the entire course of the experiment. At the LHC, proton bunches will collide every 25 ns, with each bunch crossing containing an average of 20 interactions, leading to an interaction rate just below 1 GHz. Multiple interactions per bunch crossing mean that there are a large number of overlapping events, and ATLAS must have incredibly fine granularity detectors to separate out particles. Furthermore, with such small bunch separation, the detectors must have rapid response and integration times to minimise overlap from events produced in neighbouring bunch crossings. Finally, the data write-out frequency of ATLAS is limited to 200 Hz, so an incredibly efficient triggering system is required to accurately select interesting event types while reducing the total event rate by a factor $\mathcal{O}(10^{-7})$.

---

[1]TOTEM is designed to measure the total cross section of elastic scattering and diffractive processes and shares Point 5 with CMS.

[2]LHCf has two detectors 140 m either side of the ATLAS collision point designed to investigate cosmic ray physics by measuring the energy and number of neutral pion decays coming from the interaction point.

The philosophy behind the design of the ATLAS detector is to maximise the sensitivity of the detector to the largest range of signals coming from new phenomena that one could observe at the TeV scale. The implementation is performed by optimising the detector performance to a set of *benchmark processes*. The benchmark processes are designed to form a representative sample that covers the majority of possible signals. These can be divided into two main groups: Higgs boson searches, and searches for physics beyond the Standard Model (BSM searches). Explicit details on the benchmark processes can be found in the ATLAS TDR [41, 42], and more recent updates of the analyses can be found in the ATLAS CSC notes [36]. However, despite the vast array of physical signatures, most processes can be observed by the accurate reconstruction of electrons, photons, muons, hadronic jets[1] and missing energy. The quality of reconstruction is closely related to the performance of specific sub-detectors in ATLAS.

3.2.1   Basic design

Each of the ATLAS sub-detectors plays an important role in the reconstruction of particles. The sub-detectors are arranged in layers leading out from the interaction point. Closest to the beam pipe is the tracking chamber, used to reconstruct the trajectory of charged particles. It is enclosed by a solenoid, which provides a magnetic field for the chamber that bends the paths of the charged particles allowing a measurement of their momentum and charge. The electromagnetic calorimeter encloses the tracking chamber and is designed specifically to measure the energy of electrons and photons. Outside the electromagnetic calorimeter is the hadronic calorimeter, which measures the energy of hadronic particles. Finally, the calorimeters are enclosed by the muon spectrometer designed specifically to reconstruct and identify muons. The spectrometer houses large toroidal magnets to deflect the path of muons, combined with tracking chambers to make precise measurements of momentum and charge.

The efficiency of signal selection in analyses is highly dependent on the spatial coverage of the detector. The *detector acceptance* is a commonly used term to quantify this coverage and is defined for a given event-type as the efficiency to reconstruct that event-type due to the coverage of the detector. To maximise the acceptance, each

---

[1]Quarks and gluons do not exist on their own in nature, and when produced in the LHC, hadronise into *jets* of hadronic particles.

sub-detector comprises a central cylindrical barrel region, closed off at each end by end-caps. The acceptance of the calorimeters is particularly important for an accurate measurement of missing energy, so their coverage is extended as close to the beam pipe in the forward and backward directions as possible. A diagram of the ATLAS detector can be seen in Figure 3.2.
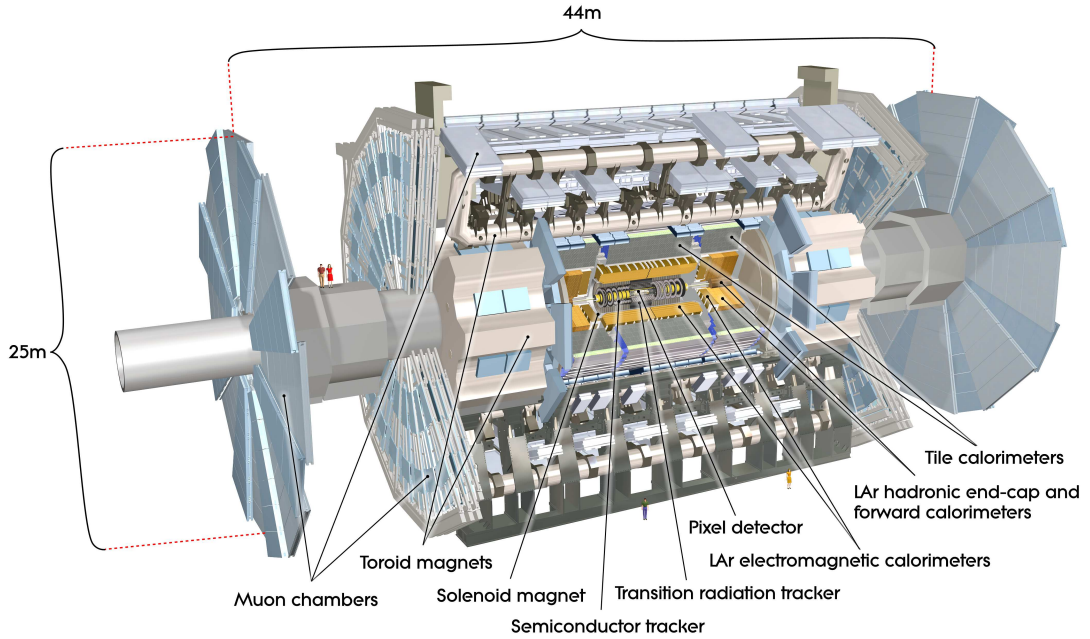
Figure 3.2: Cut-away view of the ATLAS detector [39].

3.2.2 Coordinate system

To aid with the description of the detector, a brief summary of the coordinate system and nomenclature is given. The nominal interaction point is defined as the origin of the coordinate system. The z-axis is parallel to the beam and the x and y axes are perpendicular to the beam forming a right-handed cartesian coordinate system where x points towards the centre of the LHC ring and y points upward. The x-y plane is called the *transverse plane*. The azimuthal angle, ϕ, is measured around the z-axis and the polar angle, θ, is measured from the z-axis. Kinematic quantities are often measured in the transverse plane (p_T and E_T) because the initial momentum of the interacting partons in the z direction is unknown. This means that the missing energy

can only be determined by momentum balance in the transverse plane. The missing transverse energy $\vec{\not{E}}_T$, is a 2-dimensional vector defined in the transverse plane such that the vectorial sum of the transverse energy of all particles in an event and $\vec{\not{E}}_T$ sum to zero ($\vec{\not{E}}_T = -\sum_{i\in\text{particles}} \vec{E}_{Ti}$). The pseudorapidity, defined as $\eta = -\ln\tan(\theta/2)$, is often used as a polar coordinate, since at hadronic colliders increments of $\Delta\eta$ are lorentz invariant in rate of particles, which is important for detector design. The transverse plane corresponds to $\eta = 0$, with the forward and backward directions ($+z$ and $-z$) corresponding to $\eta = +\infty$ and $\eta = -\infty$. The η-θ correspondence is shown in Table 3.2 for a representative selection of angles. The distance ΔR in η-ϕ space is defined as $\Delta R = \sqrt{\Delta\eta^2 + \Delta\phi^2}$.

Pseudorapidity

η	$-\infty$	0	1	2	3	5	$+\infty$
θ	180°	90°	40°	15°	6°	0.8°	0°

Table 3.2: Correspondence of η (the pseudorapidity) and θ (the polar angle measured from the $+z$-direction).

3.2.3 Tracking

The tracking chamber is the innermost system of the ATLAS detector, designed to reconstruct the tracks of charged particles. The chamber consists of a series of concentric detector layers surrounded by a solenoid, which provides a 2 T magnetic field parallel to the beam axis. As charged particles travel from the interaction point to the edge of the chamber they cross a number of detector layers where space-point measurements are made. Using pattern recognition, the tracks of the charged particles are reconstructed. The magnetic field bends the trajectory of charged particles in the transverse plane, and the curvature of the track is used to measure the p_T, and also to determine the sign of the particles charge. The tracks are described by five parameters which are estimated from the reconstruction: $1/p_T$, ϕ, θ, d_0 and z_0. The impact parameters d_0 and z_0, measure the closest approach to the nominal interaction point in the transverse plane and the beam axis respectively. Secondary vertices are reconstructed by identifying sets of tracks that originate from a common spatial point displaced from the interaction point. Both the reconstruction of secondary vertices and the measurement of the

impact parameters are important to the tagging of hadronically decaying tau-leptons and b-quark initiated jets.

Measurements in the tracking chamber are made by three distinct sub-detectors. The inner two detectors are the Pixels and the Semiconductor Tracker, both made from semiconductor technology. These detectors provide discrete high-resolution measurements close to the beam pipe, which are essential for an accurate estimate of the impact parameters. Outside the semiconductor trackers is the Transition Radiation Tracker, which consists of gas filled straw-tube drift chambers that provide a large number of track measurements at large radii. Charged particles traversing the straws ionise a xenon-based gas mixture and the resulting charge is collected on a wire in the middle of the straw providing space-point measurements of the charge particle's track. In addition, radiators are placed between the straws, which induce the radiation of soft low-angle photons from traversing charged particles. The radiators are made from foam and foils of high-refractive indices (to maximise radiation) and low atomic numbers (to minimise reabsorbtion of the low energy photons). The photons are then absorbed efficiently in the straws by the xenon, which has a high atomic number. The probability of radiation is dependent on the relativistic gamma factor, $\gamma = E/m$, so the amount of transition radiation provides discrimination between pions and electrons. The combination of measurements from all three sub-detectors provides robust track reconstruction with high-precision parameter estimation. A cut-away view of the tracking system is given in Figure 3.3.

3.2.4 Calorimeters

The ATLAS calorimeters are designed to make energy and position measurements of a range of particles over the pseudorapidity region $|\eta| < 4.9$. In general, when particles enter the calorimeter they interact with material layers causing a shower of lower energy particles to develop. Energy deposited by these particles in the sensitive medium of the calorimeter is measured. By integrating the energy deposition of a shower, the total energy of the particle can be measured. The most important performance requirements of the ATLAS calorimeters are: high precision electron and photon measurements in the central region, the ability to reconstruct hadronic jets as close to the beam pipe in the forward and backward directions as possible, and an excellent measurement of the
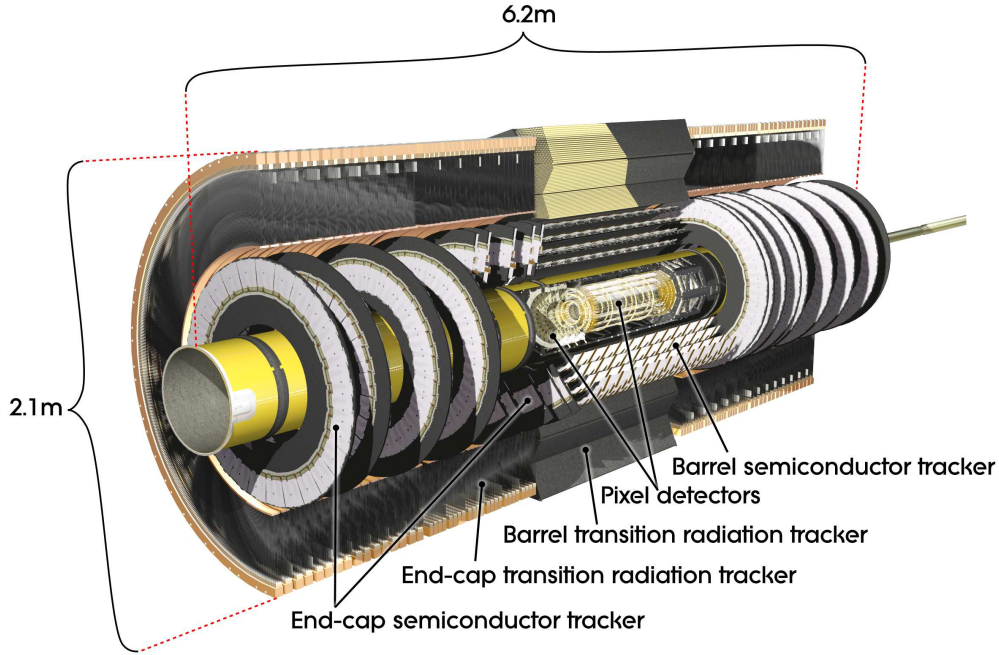
Figure 3.3: Cut-away view of the ATLAS tracking chamber [39].

missing transverse energy. To achieve these performance requirements ATLAS uses a variety of calorimetric technology over different regions of the detector.

The electromagnetic calorimeter is designed specifically to measure the energy of electrons and photons, and is situated directly outside the tracking chamber. High granularity is used in the central region matched to the tracking chamber, for high precision measurements. The hadronic calorimeter is designed to measure the energy of hadronic particles, and is positioned outside the electromagnetic calorimeter. The regions very close to the beam axis in the forward and backward direction are covered by the forward calorimeter, which combines a mixture of electromagnetic and hadronic calorimetry. Such fine granularity is not required for the measurement of hadronic jets, rather the focus is directed toward extending the coverage of the calorimeter to maximise both the acceptance of jet reconstruction and the measurement precision of the missing transverse energy. A cut-away view of the ATLAS calorimeters is given in Figure 3.4.

While a variety of technologies are used to meet the performance requirements in the different regions of the detector, all the calorimeters used in ATLAS are sampling
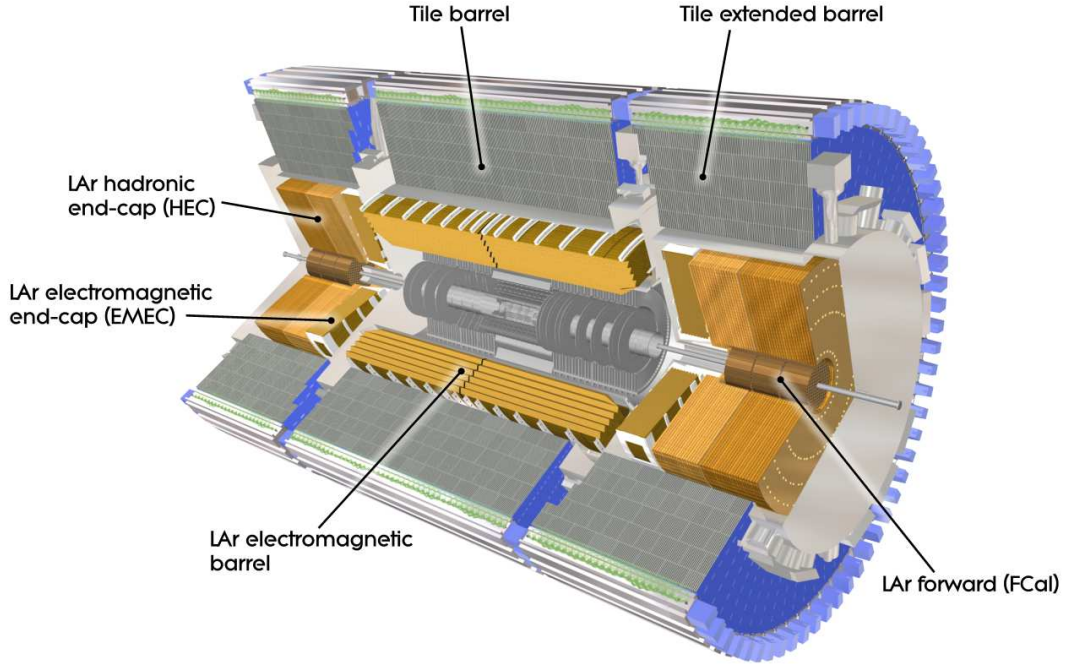
Figure 3.4: Cut-away view of the ATLAS calorimeters [39].

calorimeters. They consist of alternating absorber and detector layers, where particle showers are initiated by interactions in a high density absorber material, and energy deposits from particles in the showers are measured in a sensitive detector medium. The choice of absorber material is made to maximise the rate of either electromagnetic or hadronic shower development. To avoid bias on the energy measurement and penetration of particles into the muon spectrometer, the total integrated thickness of absorber throughout the calorimeters must be large enough to contain the showers.

The electromagnetic calorimeter is a high granularity electromagnetic sampling calorimeter, which alternates between lead absorber layers and liquid-argon (LAr), which is the sensitive medium. As electrons and photons pass through the lead, they initiate bremsstrahlung chains with high efficiency due to the high atomic number of the lead. As the radiated particles traverse through the alternating layers, an electromagnetic shower develops, which is measured from ionisation in the LAr layers. The electromagnetic calorimeter is divided into a barrel section ($|\eta| < 1.475$) and two end-cap sections ($1.375 < |\eta| < 3.2$), each housed in individual cryostats.

In the central region, hadronic calorimetry is performed by the scintillation-tile calorimeter, which uses steel as an absorber and scintillation tiles as the active material. As particles traverse the steel, nuclear interactions cause hadronic showers to develop. When the particles in these showers cross the scintillating medium they emit radiation, which is directed into photomultiplier tubes and measured. Outside this region the hadronic calorimeter uses the same LAr technology used in the electromagnetic calorimeter. Two hadronic end-cap wheels sit directly behind the electromagnetic calorimeter end-caps, sharing a common cryostat. The wheels are built from 32 identical wedge-shaped modules alternating between copper absorbing plates and LAr gaps, extending to $|\eta| < 3.2$. Beyond this is the forward calorimeter, which provides both electromagnetic and hadronic measurements in the region up to $|\eta| < 4.9$. The forward calorimeter shares the same cryostat as the end-cap calorimeters, and is split into three modules consisting of a metal matrix of concentric rods and tubes, filled with LAr. The first module is made from copper and is optimised for electromagnetic calorimetry, while the second two modules are optimised for hadronic calorimetry and are made from tungsten.

3.2.5   Muon spectrometer

Muons are extremely useful in searches for new physics at hadronic colliders. They do not interact via the strong force, and can only be produced via electroweak interactions. The presence of high-p_T muons is a clean signal that can be the result of heavy particle decays. Furthermore, muons are minimum ionising particles and can pass through the entire ATLAS calorimeter with very little energy loss. All other interacting particles shower in the calorimeters where they are well contained, and the observation of a particle outside the calorimeter is an extremely efficient way to identify muons. However, as muons deposit little energy in the calorimeter it is impossible to directly measure muon energy. Instead, muon 4-momentum must be determined solely from tracking. The tracking provided by the inner-tracker alone is insufficient to provide good momentum resolution and charge determination at high p_T due to limitation in the bending power. The muon spectrometer is designed specifically to measure the tracks of muons that pass through the calorimeter, providing good muon identification, momentum resolution and charge determination over a large range of muon momenta. To achieve adequate bending power the muon system uses huge superconducting air-core toroid

magnets, split into a large barrel region closed off by two end-caps. Precision measurements of the track coordinates in the principal bending direction are made by drift tubes filled with an ionising gas mixture of Ar/CO_2. The tubes are organised into three chambers forming concentric cylindrical layers in the barrel region and wheels in the end-cap region.

The muon spectrometer also has the capacity to trigger on particles exiting the calorimeter within the region $|\eta| < 2.4$. As the response of the drift tubes is too slow to be used in a triggering system, additional chambers with more rapid response are inserted between the drift tubes. A cut-away view of the ATLAS muon spectrometer is given in Figure 3.5.
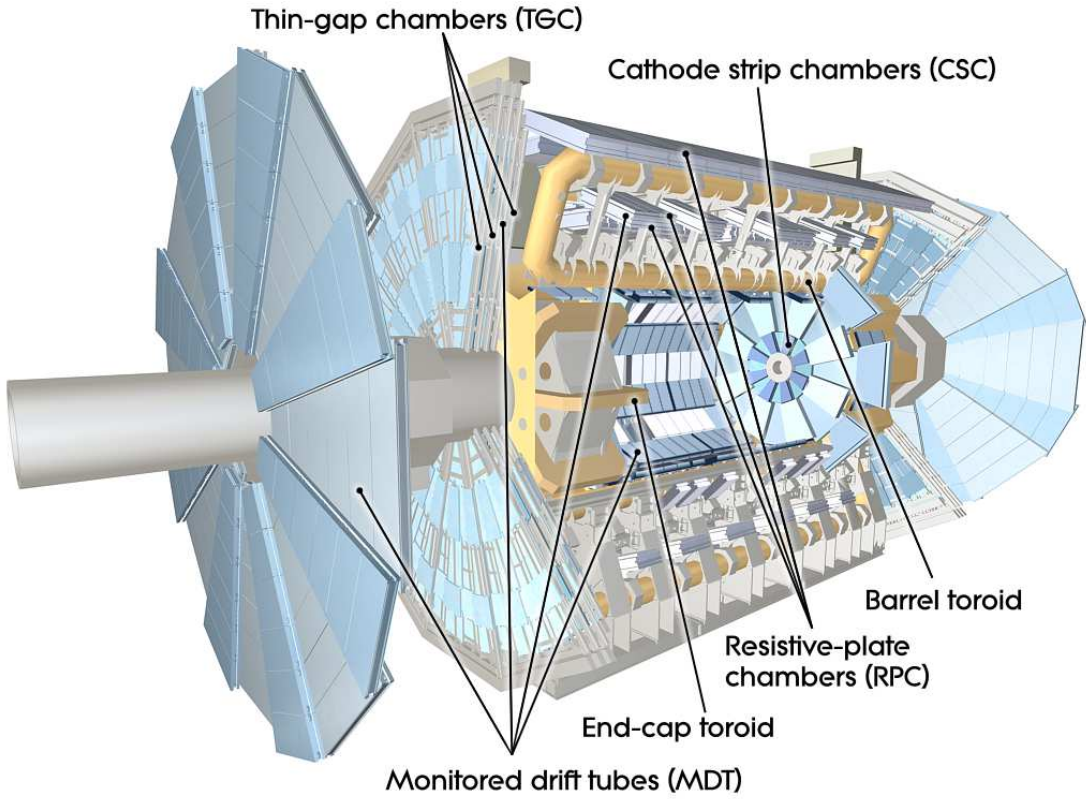
Figure 3.5: Cut-away view of the ATLAS muon spectrometer [39].

3.2.6 Trigger and data acquisition

The inelastic p-p interaction rate of the LHC at design luminosity is almost 1GHz, however, the total data recording rate of ATLAS is limited to 200 Hz. ATLAS employs a three-level trigger system, designed to maximise the selection efficiency of interesting physics signals, while reducing the huge production rate of the LHC to a writable frequency. The first level is the L1 trigger, where high p_T muons are identified from the muon trigger, and regions of high energy density are identified using reduced-granularity information from the calorimeters. A decision is made in less than 2.5 μs whether to keep or discard the event. The decision is controlled by the thresholds on the muons and calorimeter objects, which are tuned to reduce the rate to 75 kHz. *Regions of Interest* in the η-ϕ plane are identified by the L1 trigger, and passed on to the L2 trigger. The L2 trigger uses all the available detector data at full granularity inside the regions, combined with a *menu*[1] of interesting physics signatures, to reduce the rate to 3.5 kHz, within an average decision time of $\sim$40 ms. The final stage of the trigger is the event filter, which uses the full detector information and more complicated offline analysis procedures, with an average event processing time of four seconds, to reduce the rate to the final write-out frequency of 200 Hz. The data acquisition system takes care of transfer and buffering of the data between the different trigger levels. Finally, events passing the full trigger chain are transferred by the data acquisition system to CERN's Tier-0 computing facility where it is processed and recorded.

3.2.7 Data processing and distribution

The data output from the event filter is in a "byte-stream" format, containing information directly from the detector readout channels. The format is unintended for analysis by users. When the data arrives at the Tier-0 it is processed, which involves the execution of the standard ATLAS reconstruction algorithms including:

- Tracking - track reconstruction in the inner detector

- e/γ - reconstruction of electrons and photons

---

[1] A trigger menu contains a list of predefined conditions, including combinations of calorimeter and muon thresholds that will be accepted, designed to match the signatures of new or useful physics processes.

- Muon reconstruction

- Hadronic Tau Reconstruction

- Jet/Missing Transverse Energy reconstruction

- B-Tagging

All reconstruction is run within the ATLAS software framework, ATHENA. Details on the reconstruction algorithms can be found in [39]. These algorithms produce containers of reconstructed objects for each event, and also summarise detector readouts into object-orientated formats such as track hit containers in the inner tracker or cell energy maps in the calorimeter. Data processing can produce a number of output data formats with varying levels of detail for various levels of user-analysis. Due to the huge volume of data processing required in ATLAS, and the need to share access to the processed data fairly amongst the many institutes in different countries, ATLAS has adopted a distributed computing model. The different levels of data processing are distributed over the ATLAS Computing Grid, which is setup in a series of computing centres called *Tiers*, so that data flows from the Tier0 centre at CERN, through Tier1, Tier2 and Tier3 sites distributed across the globe. At each centre reprocessing can be performed.

The data processing performed by the ATLAS Computing Grid completes the full cycle of high energy physics data production in the ATLAS experiment, beginning from the production of physics events by the LHC. From this point the data must be analysed to make measurements or to search for evidence of new physics.

3.2.8 Commissioning

As of September 2008, all sub-systems of the ATLAS detector were successfully installed and commissioned, including: the inner tracker, the calorimeters, the muon spectrometer and the trigger and data acquisition system. All components were found to be operational and a general assessment of the performance was made. The commissioning and additional testing was performed on a series of data taking runs during 2008 and 2009, including: the collection of 7.6 million cosmic ray events, a number of single beam runs, and the first collisions from the LHC in December 2009, where nearly 400k events at a collision energy of 0.9 TeV and 36k events at 2.36 TeV, were recorded.

The cosmic ray events were particularly useful in the commissioning of the inner tracker [43] and the muon spectrometer [44], where performance tests of the detectors (checking the coverage, efficiency and resolution), triggers and the data acquisition and monitoring systems was possible. Calibration of the detectors was also performed along with an initial alignment of the detector modules. In both cases the detectors were shown to be fully operational and produced results close to design performance after optimisation. Most importantly, the performance of both sub-systems indicated they were ready to collect data from LHC collisions. The electronic performance and the quality of the cell energy reconstruction in the calorimeters was also extensively tested using calibration pulses, randomly triggered events, cosmic ray muons and beam splash events [45]. This allowed in depth characterisation of the ATLAS calorimeter system. It was also verified that the best noise suppression is achieved using the topological clustering algorithm (see Section 6.2.5).

A more thorough test of the complete detector was possible during the first collision runs of the LHC [46]. In this period, the overall data-taking efficiency of ATLAS was reported at 90%, with the sub-detectors typically 99% operational and the entire computing infrastructure of the trigger and data acquisition systems immediately operational. The inner tracker and the electromagnetic calorimeters were extensively tested, allowing good checks of electron, photon and vertex reconstruction. Importantly, the results were typically in good agreement with Monte Carlo simulations, indicating that the detector has been well modelled in the current MC performance studies. Reconstruction of hadronic jets and taus was also tested and the basic kinematic and flavour tagging quantities were shown to be in good agreement with MC simulation. The missing energy resolution predicted from MC was found to be in very good agreement with that observed in the collision data, demonstrating good overall calorimeter performance. Very few muons were produced in the collisions, which were predominantly low-energy soft parton scattering events. However, within the limited precision of the small sample of muons recorded, the performance of the muon spectrometer was in good agreement with MC predictions. Finally, although the p_T spectrum of the particles produced in the collisions was well below the range for which ATLAS was designed, the performance of the detector was found to be remarkably good. The outcome of the ATLAS commissioning has led to greater confidence in the results of MC performance studies and the capabilities of the detector.

4

Hadronic tau reconstruction

Accurate and efficient reconstruction of tau-leptons will be vital to many analyses in ATLAS. The tau is the heaviest of the known leptons, which significantly increases its coupling strength to the Higgs boson. Consequently, the $qqH \rightarrow qq\tau\tau$ channel is important for sensitivity to a SM Higgs boson signal in the low-mass region [36]. In the MSSM, Higgs boson coupling to the charged leptons is often enhanced, while coupling to the heavy gauge bosons is either suppressed or absent, making many of the SM Higgs boson searches ineffective. In this chapter, a brief description of hadronic tau reconstruction in the ATLAS experiment is given. However, full details can be found in [36, 39].

Taus are unstable particles with a lifetime of $c\tau = 87.11$ μm, and will decay long before reaching any of the ATLAS detectors. Therefore, they must be reconstructed from the detection of their decay products. Tau decays are categorised into leptonic (35.2%) and hadronic (64.8%) modes, each of which contain at least one neutrino that will appear only as missing transverse energy in the ATLAS detector. Feynman diagrams of the decay modes are given in Figure 4.1. In ATLAS it is very difficult to distinguish a leptonic tau decay from a prompt lepton (e.g. $W \rightarrow e\nu$ or $Z \rightarrow \mu\mu$) at the level of individually reconstructed objects, and there is no dedicated reconstruction algorithm for leptonically decaying taus. On the other-hand, hadronically decaying taus provide a unique signature and two algorithms dedicated to the reconstruction of hadronically decaying taus have been developed in ATLAS. As such, it is common

in ATLAS to use the word *tau* when referring specifically to hadronically decaying tau-leptons and this convention has been adopted unless otherwise specified.

(a) leptonic (35.2%)   (b) hadronic (64.8%)
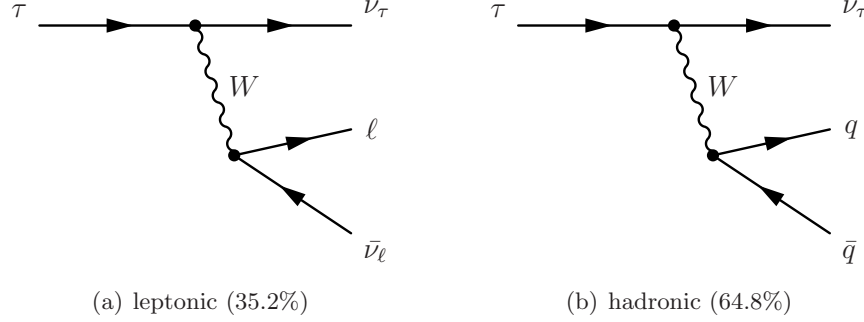
Figure 4.1: Tau-Lepton decay modes. In the leptonic mode, only the lepton is visible in the detector, and the decay is difficult to distinguish from a prompt lepton (e.g. $W \to e\nu$). In the hadronic mode the quarks hadronise into a number of charged and neutral hadrons that provide a unique signature in the detector. In both cases neutrinos are created which will only be detected as missing transverse energy.

Hadronic tau decays consist of a mixture of neutral and charged hadrons (predominantly $\pi^{\pm}$ and π^0), produced in the hadronisation of the quark anti-quark pair from the weak decay (Figure 4.1(b)). Charge conservation requires an odd number of charged hadrons, and the decays are categorised by their charged content into two modes:

- 1-prong (77%): $\tau^{\pm} \to h^{\pm} + n(h^0)$

- 3-prong (23%): $\tau^{\pm} \to 3h^{\pm} + n(h^0)$

where h represents any hadrons kinematically available to the decay and $n \geq 0$ is the number of neutral hadrons. The case where five charged hadrons are produced accounts for $< 0.2\%$ of hadronic decays and is not considered. The charged hadrons leave tracks in the inner tracker and deposit most of their energy into the hadronic calorimeter, while the π^0s decay into photon pairs, which leave clusters in the electromagnetic calorimeter. The reconstruction algorithms use a combination of calorimeter and tracking information to reconstruct taus. Unfortunately, quarks and gluons produced via strong interactions also hadronise into *jets* of charged and neutral hadrons, which can be difficult to distinguish from hadronic tau decays. These jets (often called QCD jets), are produced in copious quantities at the LHC[1] and form a significant background for

---

[1]QCD jet production can be up to $\mathcal{O}(10^{10})$ larger than signal production containing hadronic taus in many analyses, see Figure 3.1.

processes involving hadronically decaying taus. Fortunately, hadronic tau decays have a number of distinctive features that are exploited for discrimination against QCD jets. In signal processes, taus usually originate from heavy particle decay and are highly boosted in the frame of the detector. The jets from tau decays are therefore usually narrow collimated jets, with a low track multiplicity (1 or 3). On the other hand, QCD jets are formed via strong interactions and are typically wide with a large track multiplicity. Furthermore, the tau lifetime results in a measurable displacement from the interaction point that can be used to discriminate against QCD jets, which hadronise spontaneously at the interaction point. The two reconstruction algorithms were constructed to exploit these characteristic differences and provide complementary tau detection in the low and high E_{T} regions. They are called 'calo-based' and 'track-based' reconstruction.

There are two critical elements in the reconstruction of taus: accurate measurement of the visible hadronic energy-momentum vector[1] and exceptional discrimination between tau jets and QCD jets. These two processes are generally split into two separate procedures: 1. *Reconstruction*, where a list of all tau candidates in an event is defined, their kinematic properties measured, and a set of discriminating variables calculated, and 2. *Identification*, where selection based on the discriminating variables is applied to reject candidates from QCD jets.

4.1 Performance

The performance of the reconstruction algorithms is often evaluated using Monte Carlo simulated samples of taus and QCD jets, where the true origin of a tau candidate is known. In this way it is possible to determine the overall performance of an algorithm, characterised by the:

1. Resolution of the kinematic measurements.

2. Efficiency to reconstruct tau candidates.

3. Level of discrimination between tau jets and QCD jets.

---

[1]The visible hadronic energy-momentum vector for the tau is defined as $p_{\mu,\tau}^{\mathrm{vis}} = p_{\mu,\tau} - \sum_{\mathrm{neutrinos}} p_{\mu,\nu}$, where $p_{\mu,\tau}$ is the complete 4-momentum of the tau and $p_{\mu,\nu}$ are the 4-momenta of all neutrinos in the tau decay.

In these evaluations, the terms *real tau* and *fake tau* are used to distinguish between identified tau candidates originating from a true hadronic tau decay, and those originating from a QCD jet, respectively. Details regarding the determination of tau candidate origin can be found in Appendix A. The level of discrimination is usually indicated by comparing the identification efficiency of real taus and the rejection factor against fake taus that can be achieved. For most discriminants, the level of efficiency vs. rejection can be tuned by altering the selection on the discriminant. The values of the various efficiencies and rejections are dependent on their definitions, which are given below and used unless otherwise stated.

1. Reconstruction efficiency:

$$\epsilon_{\text{reco}}^{\text{REAL}} = \frac{\text{number of reconstructed tau candidates}}{\text{number of true hadronic taus}} \tag{4.1}$$

$$\epsilon_{\text{reco}}^{\text{FAKE}} = \frac{\text{number of reconstructed tau candidates}}{\text{number of true QCD jets}} \tag{4.2}$$

2. Identification efficiency:

$$\epsilon_{\text{ID}} = \frac{\text{number of reconstructed and identified tau candidates}}{\text{number of true hadronic taus}} \tag{4.3}$$

3. Rejection Factor:

$$R = \frac{\text{number of true QCD jets}}{\text{number of reconstructed and identified tau candidates}} \tag{4.4}$$

While the identification efficiency and the rejection factor are usually calculated against truth objects, they can also be calculated directly with respect to the reconstructed tau candidates. The convention is always stated in each case. Finally, whenever the denominator and numerator contain truth and reconstructed objects, the reconstructed object is required to match within a specified radius, ΔR, to the truth object. The efficiencies and rejections are often calculated as a function of the properties of the denominator. The reconstruction efficiency of the calo-based algorithm is shown in Figure 4.2 as a function of E_{T} and η.

Large rejection against fake candidates from QCD jets is vital due to the huge production rates for QCD processes at the LHC. Furthermore, good performance in both reconstruction and identification is required over a large range of transverse tau energies, from 10-15 GeV to beyond 500 GeV, to accommodate the detection of taus in a wide range of different processes.
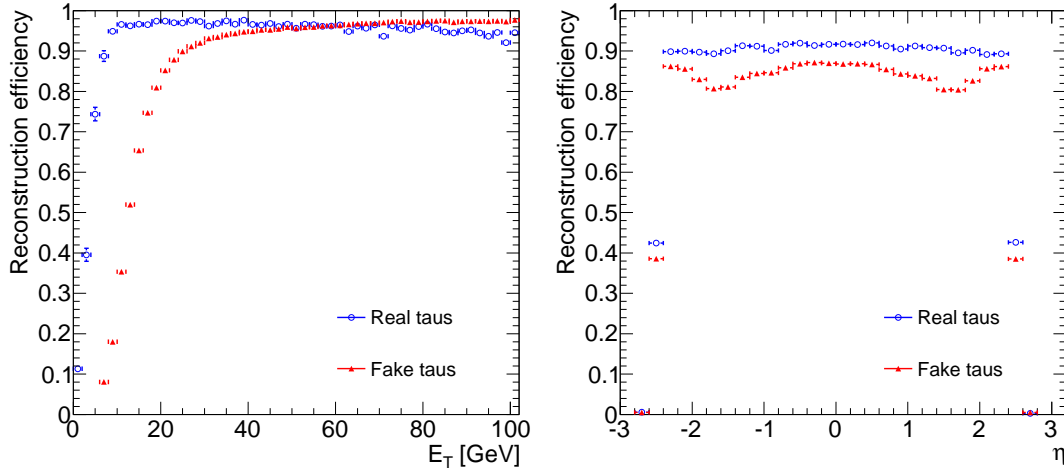
Figure 4.2: Reconstruction efficiency of the calo-based tau reconstruction algorithm for real and fake taus as a function of E_T (left) and η (right).

4.2 Calo-based reconstruction

The calo-based reconstruction is seeded by calorimeter clusters, which are reconstructed by the standard ATLAS jet cone algorithm with $\Delta R < 0.4$ [39]. Jet algorithms are discussed in more detail in Section 6.2.5. All clusters above a given E_T threshold are accepted as candidates[1]. The jet algorithm applies an H1-style energy calibration [47], which accounts for: 1. the differing response of the calorimeter to electromagnetic and hadronic particles (as the ATLAS calorimeter system is non-compensating), 2. the energy lost in dead material and 3. a correction for the jet energy deposited outside the reconstruction cone. An additional correction specific to hadronic taus is applied as the calibration is designed for regular hadronic jets and overestimates tau energy. As mentioned previously, the reconstruction efficiency for the calo-based algorithm can be seen in Figure 4.2. The efficiency for real candidates increases rapidly with respect to the true visible energy and reaches a maximum of $\sim 98\%$ at $E_T \sim 10$ GeV. The E_T of fake taus is underestimated due to the tau-specific energy correction and causes a lag in the rise of the reconstruction efficiency for fake candidates, which plateaus at

---

[1]Prior to Athena release 14, tau seeds were taken from jet reconstruction starting from the energy deposited in calorimeter towers with an E_T threshold of 15 GeV, however, a move was made to jets starting from topoclusters with a threshold of 10 GeV, which are clusters built using a topological clustering algorithm (designed to reduce the effect of calorimeter noise).

~ 30 GeV. The small drop in efficiency for real taus after 40 GeV is due to an increase in the number of candidates falling outside the η acceptance.

After reconstructing the cluster, the kinematic quantities and discriminating variables are calculated. The energy and position are taken directly from the calorimeter cluster. Tracks with $p_{\mathrm{T}} > 2$ GeV within $\Delta R < 0.3$ of the candidate are associated to the candidate. A number of variables with discriminating power against QCD jets are constructed using the tracking information and the calorimeter information in a cone of $\Delta R < 0.4$ around the candidate. A detailed description of the variables is given in [36]. The variables that provide the best discrimination are then combined into a one-dimensional likelihood ratio. The discriminating power of the Log-Likelihood ratio is shown in Figure 4.3. The level of rejection vs. signal efficiency is tuned by optimising selection on the discriminator for specific analyses.
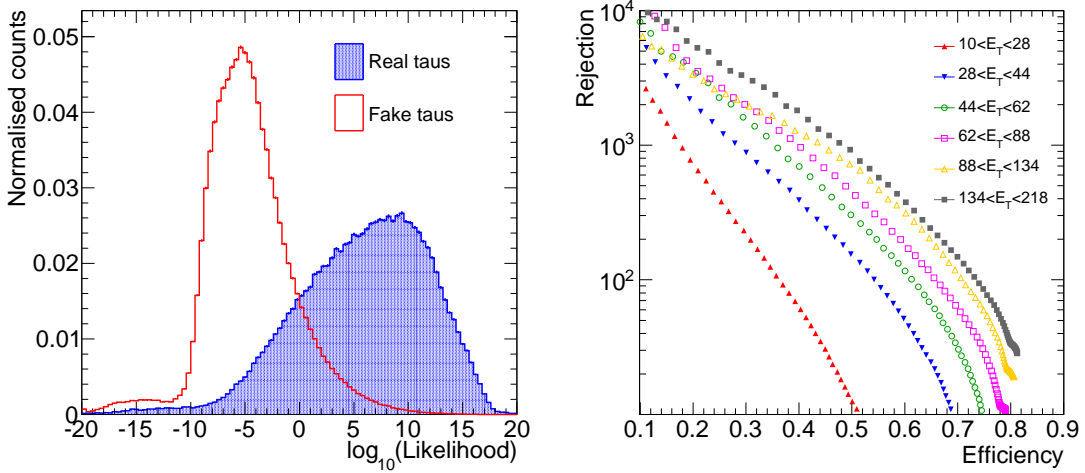
Figure 4.3: Discriminating power of the calo-based tau reconstruction using the Log-Likelihood discriminator. On the left are the Log-Likelihood distributions for real and fake taus, and on the right is the rejection factor vs. identification efficiency in a number of E_{T} regions. Rejection factors of 100 - 1000 can be achieved over the E_{T} range while still retaining 50%-60% of the real taus.

4.3   Track-based reconstruction

The track-based reconstruction is seeded by high quality tracks with $p_{\mathrm{T}} > 6$ GeV. Up to six additional tracks are allowed within a solid cone $\Delta R < 0.2$ around the leading track. The direction of the candidate is defined as the p_{T}-weighted barycentre of all associated tracks. The energy of the tau candidate is calculated using an *energy-flow* algorithm [36], which adds the p_{T} from charged hadrons measured in the tracking chamber to the E_{T} deposited in the electromagnetic calorimeter from π^0 decays. The method requires accurate separation of the calorimeter energy associated to the charged tracks and the energy deposited by π^0 decays, to avoid either underestimating the π^0 energy or double-counting the charged hadron energy. The resulting energy measurement is very good for real tau candidates as they are predominantly comprised of pions, however, the omission of an energy measurement from the hadronic calorimeter causes a severe underestimate of QCD jet energy due to a missing neutral hadronic component. This causes a large fraction of low p_{T} QCD jets to fail reconstruction. Finally, the summed charge of the associated tracks is required to be -1, 0 or 1. This sequence of reconstruction already provides quite good rejection against QCD jets. The reconstruction efficiencies of the track-based reconstruction for both real and fake taus are shown in Figure 4.4. Identification variables are also defined to increase rejection power. Most discriminator quantities are calculated in a *core-region* defined as the solid cone $\Delta R < 0.2$ around the candidate. An *isolation-region* is also defined as the annulus $0.2 < \Delta R < 0.4$ around the candidate. A detailed description of the discriminating variables is given in [36]. A number of discriminants are constructed using combinations of the most powerful variables. The most commonly used are: a basic one-dimensional cut-based discriminant, a cut-based discriminant optimised using the multi-variate analysis package TMVA [48] and a neural network discriminant. The discriminating power of the track-based reconstruction using the neural network discriminant is shown in Figure 4.5

4.4   Change over time

The ATLAS reconstruction software is frequently updated, with minor releases occurring every few months and major releases approximately every year. Both the
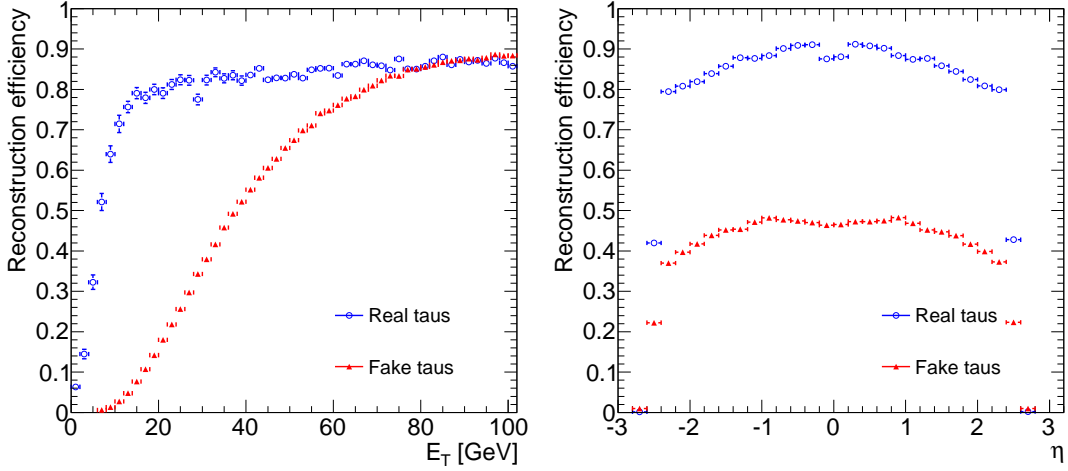
Figure 4.4: Reconstruction efficiency of the track-based tau reconstruction algorithm for real and fake taus as a function of E_T (left) and η (right). Good discrimination is already achieved after the reconstruction step, causing a lower reconstruction efficiency for fake tau candidates.

calo-based and track-based algorithms have changed substantially in the last few major releases, and have undergone significant restructuring. The information from the track-based and calo-based reconstruction is now merged into a single container of tau candidates. In reality both the algorithms are still run, however, information on whether a candidate is seeded by the track-based, calo-based or both algorithms is stored. Whenever possible, directional information is supplied by the track-based algorithm, and energy information is supplied by the calo-based algorithm. All the information calculated by an algorithm is still stored as long as a candidate is seeded by that algorithm. On top of this large structural change, the various discriminants are also frequently re-optimised with the software releases. The software releases used in Section 5.3 and Section 5.4 are prior to the major structural changes in the tau reconstruction, while the software used in Chapter 6 contains the merged tau reconstruction. Specific details of the tau reconstruction related to the software release are described in the sections where they are used.
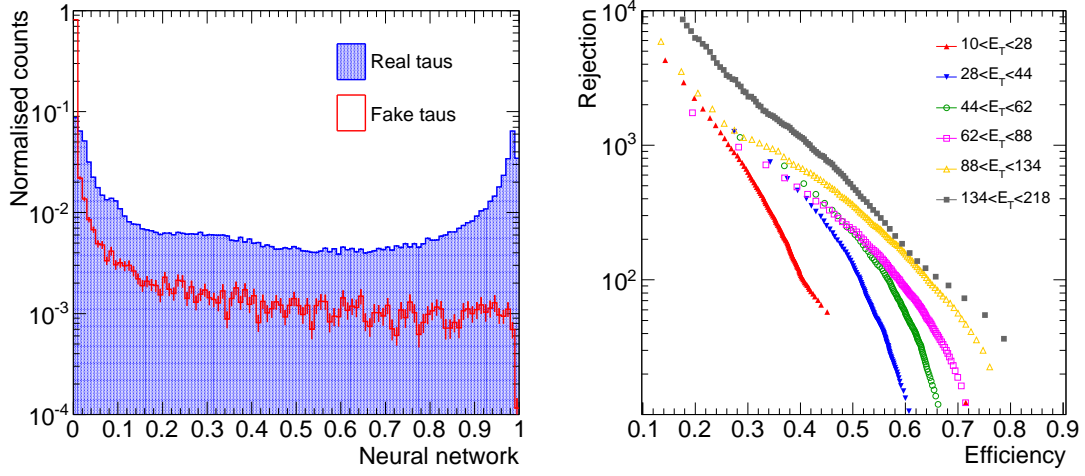
Figure 4.5: Discriminating power of the track-based tau reconstruction using the neural network discriminator. On the left are the neural network distributions for real and fake taus, and on the right is the rejection factor vs. identification efficiency in a number of E_T regions.

4.5 Summary

The two reconstruction algorithms provide complimentary reconstruction in the low and high p_T region. The track-based reconstruction works well in the low-p_T region, while the calo-based reconstruction works well in the high-p_T region. The discriminants calculated by both algorithms provide large rejection against fake taus while retaining a large fraction of the real taus.

5

ATLAS simulation

In this chapter a brief summary of the ATLAS Monte Carlo simulation is given, however, a full description can be found in [49]. In particular, the need for fast simulation software is discussed, and the fast simulation packages ATLFAST-I and ATLFAST-II are described. Following this introduction, a complete account of the author's contribution towards the development of hadronic tau simulation within these packages is given.

5.1 Production of simulated events in ATLAS

Monte Carlo (MC) simulations are an extremely important tool for High Energy Physics. They provide a tremendous aid in the understanding of detector response and performance, and the development of particle reconstruction, especially in the construction phase before data collection. They also provide a method to evaluate and optimise an experiment's sensitivity to specific physics processes. After the construction phase, simulations are relied on for continual evaluation of detector performance and are essential for an accurate interpretation of the data.

Monte Carlo simulations in collider experiments generally consist of the random generation of a scattering process, called an *event*, followed by a detailed simulation of the detector response to that event. The simulation of the detector response involves numerous particle interactions, which are computed by randomly sampling known dis-

tributions. The statistical nature of both the event generation and detector simulation demand large statistical samples to obtain accurate results.

ATLAS has developed a simulation-chain to produce MC simulated events, which is fully integrated into the ATLAS software framework, ATHENA. The chain is split into three distinct stages: event generation, simulation and digitisation. The multi-stage chain allows for a great degree of freedom in the integration of specialised third party software. Furthermore, the chain produces simulated events in a data-format identical to the output of the detector. This provides an excellent platform to compare MC simulated data and real collision data, as both formats can be processed by the standard ATLAS reconstruction software. The integration of the chain into ATHENA also allows the software to be run easily on the LHC Computing Grid, which is exploited in large scale production of official ATLAS MC datasets.

5.1.1 Truth particle record

In both event generation and simulation, particles are created and annihilated either through interactions with material in the detector or by decay. These particles eventually deposit energy into sensitive media in the detector. The energy depositions are converted into digital signals to emulate the detector readout. The final result is a detailed simulation of the detector's response to a given physics event. Although a detailed description of detector response is the final goal of the simulation, it is extremely useful to keep a record of all the particles created and annihilated in an event. This record is called the *truth particle record* and the particles it contains are called *truth particles*. The record allows the detector response to various truth particles to be assessed, and is extremely important for performance studies and analysis optimisation.

5.1.2 Event generation

ATLAS employs a number of event generators, most of which are developed by third parties and interfaced into the ATHENA framework via wrapper scripts. The generator begins by producing an interaction between partons in the colliding protons. The process is specified in the input, and is usually chosen to be a hard scattering process. Any unstable particles produced in the interaction that will decay before reaching a material layer in the ATLAS detector ($c\tau < 10$ mm) are forced to decay by the generator. Radiation from the initial and final particles in the interaction is generated

and finally, the hadronisation of free quarks and gluons into jets of hadronic particles is performed. Specialised external software is often used in the hadronisation and radiation steps due to the complexity of the models required. As well as selecting the initial interaction, a filter can be applied to select only events with specific properties (e.g. events containing a leptonic decay, or more complicated requirements such as angular separations of decay products). The generation step is extremely fast compared to the entire simulation-chain, and filters are particularly useful in reducing the total computational expense of the production by only selecting events that are likely to be useful. The final output is a set of truth particles created in the various processes coordinated by the generator.

5.1.3 Simulation

The simulation begins by reading in the truth particle record from the event generation. Each particle is propagated through a geometric model of the ATLAS detector by GEANT4 [50], which provides detailed models of physics interactions and the infrastructure to propagate particles through material layers. As the particles are propagated through the detector layers they may decay or radiate causing the generation of new particles, which are themselves propagated by the simulation. In particular, interactions in the calorimeters often lead to the development of large particle showers, and a typical event can contain $\mathcal{O}(50k)$ particles. Finally, energy deposited by particles in the sensitive regions of the detector are recorded as *hits* containing information on energy deposition, position, and time.

5.1.4 Digitisation

The digitisation begins by reading in the hit output from the simulation. Detector noise is added to the energy depositions and the decisions from the L1 trigger are evaluated and recorded, however no events are discarded. The energy depositions in the various detector components are converted into voltages and currents. In the real detector these signals are converted into digital output via Read Out Drivers. In the digitisation, the performance of these drivers is emulated to obtain a final data-format identical to the output of the real detector, allowing it to be processed by the standard ATLAS reconstruction.

5.1.5   Summary

The full ATLAS production chain including event generation, simulation, digitisation and reconstruction is extremely computationally expensive. While use of the LHC Computing Grid is made in official production of simulated physics samples, a maximum of approximately one million events per day can be produced. For comparison, $p\bar{p} \rightarrow W \rightarrow \ell\nu$, which has a rather modest cross section of $\sim$20 μb, will be produced at the order of 10 million events per day of LHC running at full luminosity. QCD jet production[1], which forms a large background for many analyses, can have rates as large as one billion events per day at the LHC.

One of the main uses of MC simulated event samples is to estimate the contributions of particular background processes in analyses of the data recorded by an experiment. In this case, the statistical size of the MC simulated event sample must be at least comparable to the size of the sample expected in the data, otherwise the estimate will suffer large statistical uncertainty. For many physics processes it will be impossible to produce sufficient numbers of MC simulated events with the standard ATLAS production chain. In reality, the vast majority of computational time in the production chain is spent in the GEANT4 simulation. To combat this problem, ATLAS has developed a number of fast simulation software packages to compliment the full GEANT4 simulation (commonly called "full simulation"), each of which is useful in different scenarios.

5.2   Fast simulations

ATLAS has three dedicated fast simulation packages: ATLFAST-I, ATLFAST-II and Fast G4, each of which trade-off the level of detail in simulation for a reduction in computational expense. ATLFAST-I was the first developed and exhibits the largest reduction in computational time. It is designed for physics parameter space scans and studies that require very large statistical samples, but not the level of detail provided by the full simulation. One major trade-off is that instead of providing a set of *hits* like the full simulation, ATLFAST-I provides its own 'reconstructed' particles as a set of 4-momentum vectors and cannot be processed by the standard ATLAS reconstruction. ATLFAST-II has recently been developed and was designed to minimise computational

---

[1]QCD jet production with $E_T > 100$ GeV will produce $\sim$1 billion events per day at full luminosity, see Figure 3.1 on page 24.

expense, while keeping the level of detail required to execute the standard ATLAS reconstruction. It is very useful for supplementing analyses that use full simulation samples. ATLFAST-II is comprised of two components: Fast Calorimeter Simulation (FastCaloSim) and Fast ATLAS Tracking Simulation (Fatras). The most accurate fast simulation is the Fast G4 simulation, which uses the regular GEANT4 simulation, but replaces low energy electromagnetic particles in the calorimeter with pre-simulated showers. However, this only offers a marginal reduction in computational expense compared to the other fast simulators.

5.2.1 ATLFAST-I

ATLFAST-I performs an extremely fast simulation of the ATLAS detector, including its own 'reconstruction'. Rather than using a detailed detector simulation to propagate particles through the material layers of the detector, parameterised detector resolution functions are applied directly to the truth particles. In general, reconstruction efficiencies and misidentification rates are not modelled. True particles are reconstructed with 100% efficiency, overestimating the real reconstruction efficiency. Furthermore, fake particles arising from the misidentification of various detector objects are not modelled at all, with two exceptions: the tagging of hadronic tau jets and b-jets. Here the tagging and mistagging rates are extracted from full simulation event samples, parameterised, and applied in ATLFAST-I as weights. Thus simulation of fake taus and b-jets is included in ATLFAST-I. The reconstruction efficiencies of all other particles are left to the user to apply in their analysis if necessary. As particles aren't propagated through detector material, studies requiring detail at the detector level (e.g. track hits or calorimeter cell information) are impossible.

Despite these limitations, ATLFAST-I is an invaluable tool for many analyses since it reduces simulation time by factor of ~1000. This makes it possible to perform parameter space scans, and analyses which require simulation of huge numbers of background events. It will also be useful for making quick estimates of systematic uncertainties in early data analyses, and estimating uncertainties from event generators.

5.2.2 ATLFAST-II

ATLFAST-II provides a much more detailed simulation of the detector than ATLFAST-I, and has the distinct advantage that its output can be processed by the standard AT-

LAS reconstruction. To achieve this, both the fast calorimeter simulation (FastCaloSim) and the fast tracking simulation (Fatras) simulate input directly into the standard ATLAS reconstruction, bypassing the digitisation step. In both cases, the simulation time is reduced by using the simplified geometric detector model adopted by the standard ATLAS reconstruction algorithms.

ATLFAST-II also supports the use of GEANT4 in the simulation of any of the sub-detectors. By default, ATLFAST-II uses GEANT4 to simulate the inner tracker and the muon spectrometer, and FastCaloSim to simulate the calorimeter. The label 'ATLFAST-IIF' is used when Fatras is run for the tracking.

5.2.2.1 FastCaloSim

FastCaloSim (and the Fast G4 simulation) takes advantage of the fact that the vast majority of time spent in GEANT4 simulation of the ATLAS detector is taken up by particle shower simulation in the calorimeters. In particular, electromagnetic showers account for ~75% of the total simulation time. Instead of simulating these showers, FastCaloSim takes all the interacting truth particles at the end of the inner tracker volume, and uses a parameterisation of the longitudinal and lateral shower energy profile to deposit energy directly into the calorimeter cells.

The shower parameterisation is extracted from GEANT4 simulated single photon and single charged pion events. The photon parameterisation is used for electromagnetic showers of both electrons and photons, and the charged pion parameterisation is used for the showers of all hadronic particles. The simulation time for a single particle is a few μs, and a typical $t\bar{t}$ event takes a few seconds. The default ATLFAST-II setup reduces simulation time by a factor of 10 compared to the full simulation. When Fatras is substituted for the tracking simulation, the total simulation time can be reduced by a factor ~100 with respect to the full simulation.

5.3 Parameterisation of the calo-based tau reconstruction for ATLFAST-I

In this section the parameterisation of the calo-based tau reconstruction for use in ATLFAST-I is presented. The parameterisation is the complete work of the author.

To accurately model hadronically decaying taus in ATLFAST-I a parameterisation of the tau reconstruction performance is needed. The performance of the calo-based tau reconstruction algorithm was parameterised in [51], however, this parameterisation was extracted from full simulated data produced with an old version of the ATLAS software (Athena release 11). Numerous changes to the tau reconstruction were made in subsequent software releases, the most dramatic being a change in the calorimeter clustering algorithm, which was implemented in release 14. In this section, the extraction of a new parameterisation using the calo-based tau reconstruction in Athena release 14 is described.

5.3.1 Datasets

The parameterisation was performed prior to the official release of Athena 14, so that it could be included in the release. At this time there were no official MC simulated datasets produced with Athena 14. However, the calo-based tau reconstruction for use in Athena 14 was finalised and could be run as a patch over the previous release. To perform the parameterisation, the patched calo-based reconstruction was used to process the existing simulated datasets. Datasets from the ATLAS computing system commissioning (CSC) production [36] were used, as they are thoroughly validated and contain large event samples. The same datasets were also processed with ATLFAST-I, allowing comparisons between reconstructed objects from ATLFAST-I and full simulation. Datasets containing a representative sample of real and fake taus over a large energy range were chosen. Table 5.1 lists the background samples containing fake taus and Table 5.2 lists the signal samples containing real taus. The QCD di-jet production was used for the main parameterisation of the rejection, however, fake taus from a $t\bar{t}$ sample were also studied to investigate the effect of jet origin on rejection.

List of QCD di-jet samples

Process Name	Generator Cut [GeV]	Cross Section [mb]	Sample Size [k]
J0	$8 - 17$	17	199
J1	$17 - 35$	1.4	99.5
J2	$35 - 70$	9.3 E-2	93.8
J3	$70 - 140$	5.9 E-3	99.0
J4	$140 - 280$	3.1 E-4	99.0
J5	$280 - 560$	1.2 E-5	98.0
J6	$560 - 1120$	3.6 E-7	99.2
J7	$1120 - 2280$	5.7 E-9	98.9
J8	> 2280	2.4 E-11	98.8
$t\bar{t}$	-	8.33 E-7	198

Table 5.1: QCD di-jet samples, providing fake taus up to ∼4 TeV. QCD di-jet production is divided into samples to provide adequate statistical precision over the whole energy spectrum. A generator cut is applied to p_T generated in the hard $2 \rightarrow 2$ scattering process. A $t\bar{t}$ sample was also included to study the effect of jet origin on the fake tau rejection factor. The sample sizes are listed in thousands of events.

List of signal samples

Process Name	Sample Size [k]
$Z \rightarrow \tau\tau$	99.9
$A(800 \text{ GeV}) \rightarrow \tau\tau$	198

Table 5.2: Signal Samples, providing real taus up to ∼1 TeV.

5.3.2 Reconstruction performance

The first step towards modelling the calo-based tau reconstruction in ATLFAST was to ensure that the kinematic reconstruction of tau candidates was reproduced correctly. Although ATLFAST-I applies resolution functions to the direction and energy of particles to account for detector effects, there is a slight difference between the jet reconstruction algorithm used in ATLFAST-I and full simulation. The difference arises from the energy calibration schemes used in each reconstruction.

The jet reconstruction uses an energy calibration to account for hadronic energy mismeasurement. However, the standard H1 calibration applied to jets, results in an overestimate of hadronic tau energy. Therefore, when the jets are passed to the calo-

based tau reconstruction, an additional correction is applied. While this results in a good estimate of the energy of real taus, it causes an underestimate of the energy of fake taus coming from QCD jets. It is impossible to correctly reproduce the energy of both real and fake tau candidates with a single H1-style hadronic energy calibration. On the other hand, since ATLFAST-I takes its energy directly from truth particles, no calibration is needed, and in all cases it reproduces the correct energy. This results in a discrepancy between the energy measurement of ATLFAST-I and the calo-based tau reconstruction for fake candidates originating from QCD jets. A useful variable for assessing the reconstruction of kinematic variables is the resolution defined as:

$$\text{reso}(x) = \frac{x_{\text{reco}} - x_{\text{true}}}{x_{\text{true}}} \tag{5.1}$$

where $x \in \{E_{\text{T}}, \eta, \phi\}$. The core of the kinematic resolution is often Gaussian distributed (due to the detector resolution). In this case it is described by its *scale* (mean of the Gaussian) and its *resolution* (standard deviation of the Gaussian). Figure 5.1 gives a comparison of the E_{T} resolution of the standard ATLAS jet reconstruction, the calo-based tau reconstruction, and ATLFAST-I jets for QCD jets and hadronic tau jets. For real taus, good agreement in the E_{T} scale between TauRec and ATLFAST was found, while for fake taus there was a large discrepancy. For both real and fake candidates the resolution was underestimated by ATLFAST. Figure 5.2 gives a comparison of the η and ϕ resolutions. Agreement between TauRec and ATLFAST was found to be very good in ϕ and adequate in η.

To correctly model fake tau candidates from the calo-based reconstruction the ATL-FAST jet energy had to be adapted. To do this, the difference in energy scale, $\Delta \bar{x}(E_{\text{T}})$ and resolution, $\Delta \sigma(E_{\text{T}})$ of the fake tau candidates was extracted in nine E_{T} bins (15, 20, 25, 30, 45, 65, 90, 120, 200, 1000 GeV). The scale and resolution difference are defined as:

$$\Delta \bar{x} = \bar{x}_{\text{tau}} - \bar{x}_{\text{atl}}, \tag{5.2}$$

and

$$\Delta \sigma^2 = \sigma_{\text{tau}}^2 - \sigma_{\text{atl}}^2, \tag{5.3}$$

where $\bar{x}_{\text{tau}}$, $\bar{x}_{\text{atl}}$, σ_{tau} and σ_{atl} are the mean and standard deviation of the energy resolution from the calo-based tau reconstruction and the ATLFAST jets respectively. The parameters $\bar{x}$ and σ were extracted by fitting a single Gaussian around the peak
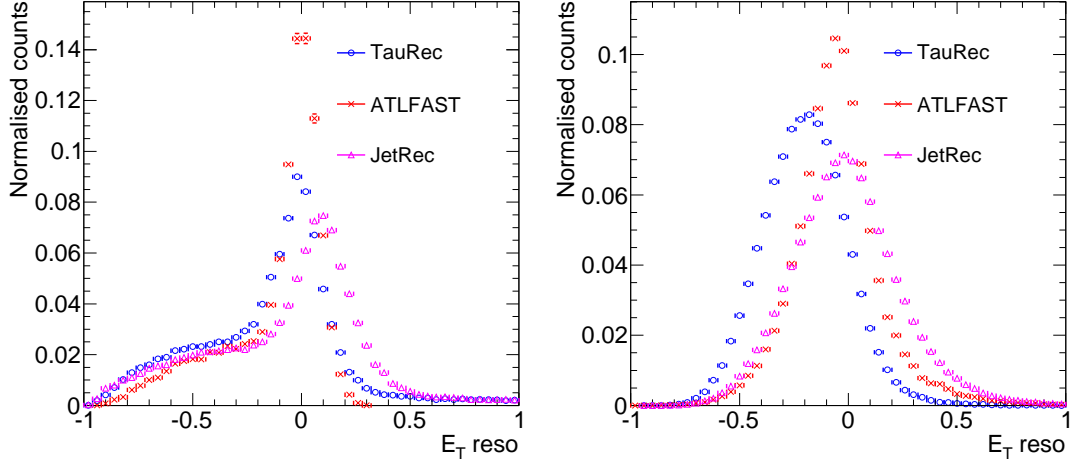
Figure 5.1: Comparison of the E_{T} resolution for calo-based tau reconstruction (TauRec), jet reconstruction (JetRec), and ATLFAST-I jet reconstruction (ATLFAST) for real tau candidates (left) and fake tau candidates (right). For real taus, good agreement in the E_{T} scale between TauRec and ATLFAST is found, while for fake taus there is a large discrepancy. For both real and fake candidates the resolution is underestimated by ATLFAST.

of the energy resolution. Figure 5.3 shows $\Delta\bar{x}$ and $\Delta\sigma$ as functions of E_{T}. A Gaussian resolution function was then constructed from the extracted parameters,

$$f(E_{\mathrm{T}}) = \mathrm{Gauss}(\; E_{\mathrm{T}} \;\mid\; \Delta\bar{x}(E_{\mathrm{T}}), \;\; \Delta\sigma(E_{\mathrm{T}}) \;) \tag{5.4}$$

and applied to the ATLFAST jets. Figure 5.4 shows the corrected energy resolutions.

Typically, in an analysis, a threshold of at least 15 GeV is placed on the energy of the reconstructed tau. This results in a gradual rise of the reconstruction efficiency as a function of the true energy near the threshold. Figure 5.5 shows a comparison of the reconstruction efficiency of fake taus reconstructed by the calo-based tau reconstruction and ATLFAST with and without the energy correction. A good match is seen after the correction is applied. Finally, the E_{T} and η distributions for fake taus are given in Figure 5.6, showing very good agreement between calo-based taus and corrected ATL-FAST jets. A small drop in reconstruction efficiency occurs around $|\eta| = 1.5$, known as
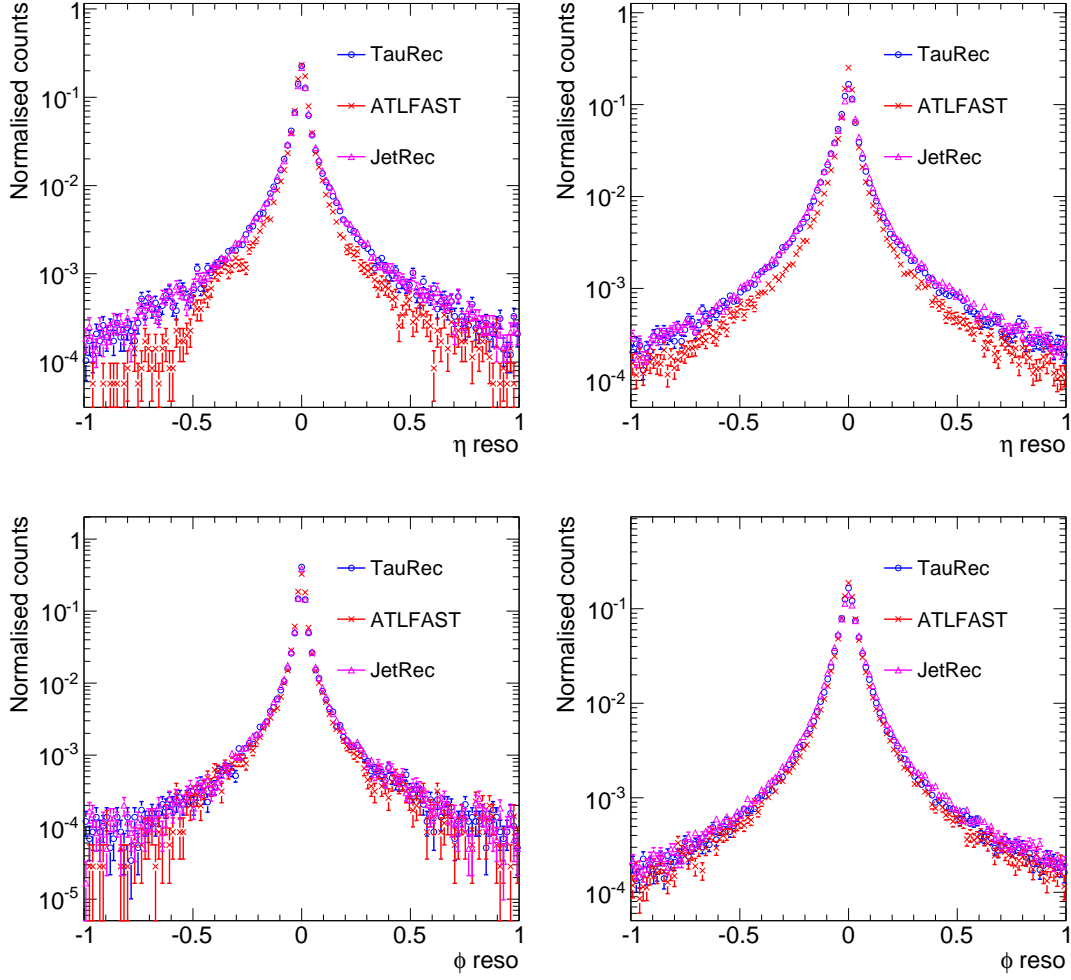
Figure 5.2: Comparison of the η (top) and ϕ (bottom) resolution for calo-based tau reconstruction (TauRec), jet reconstruction (JetRec), and ATLFAST-I jet reconstruction (ATLFAST) for real tau candidates (left) and fake tau candidates (right). Agreement between TauRec and ATLFAST is very good in ϕ and adequate in η.
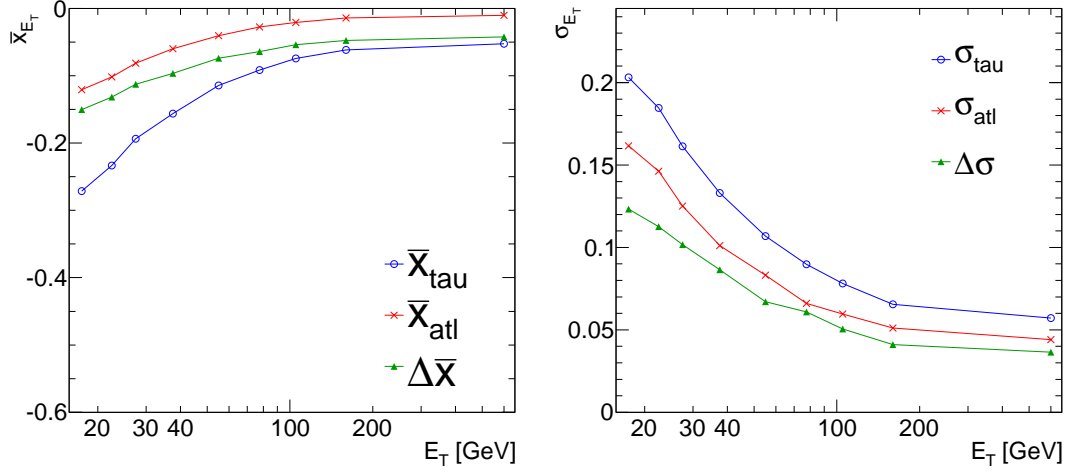
Figure 5.3: The E_T Scale ($\bar{x}$) and resolution (σ) as a function of E_T for fake taus reconstructed with the calo-based tau algorithm and ATLFAST. The difference between the two, used to construct the resolution function, is also shown.
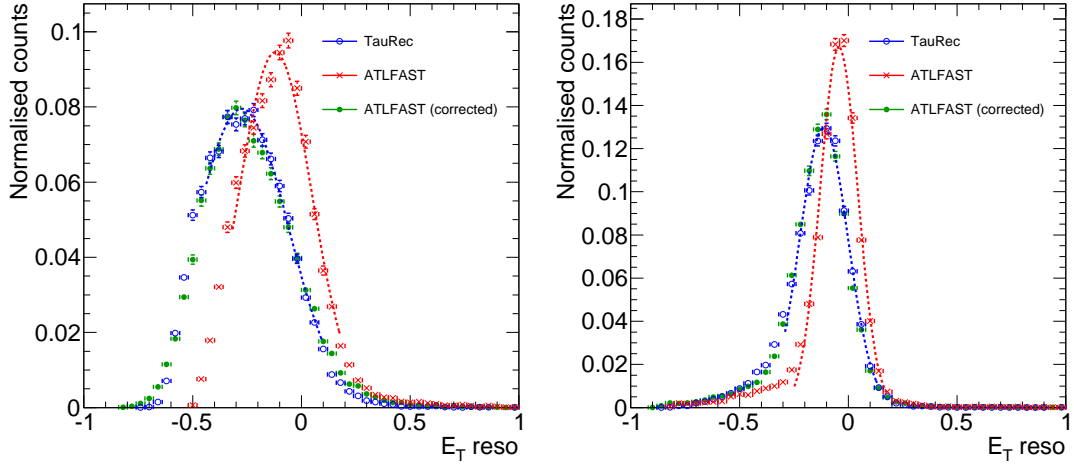
Figure 5.4: Comparison of the E_T resolution of fake tau candidates reconstructed by the calo-based tau reconstruction and ATLFAST with the tau-energy correction applied. The resolution in two E_T bins are shown: 15-20 GeV (left) and 45-65 GeV (right). Very good agreement is achieved over the whole E_T range.

the *crack-region*[1], which is not modelled by ATLFAST. However, the agreement in the general shape of the η distributions is adequate for use in ATLFAST. As the kinematic resolutions of real taus in ATLFAST were already found to be in good agreement with the calo based reconstruction, no correction was applied for real taus.
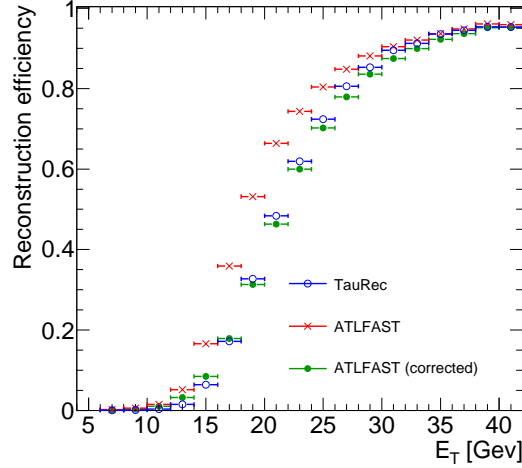
Figure 5.5: Comparison of the reconstruction efficiency for fake candidates reconstructed with the calo-based tau reconstruction and ATLFAST with and without the energy correction applied. After the correction is applied, good agreement is found between tau reconstruction and ATLFAST.

5.3.3 Identification performance

A good description of the identification process used to discriminate against fake taus from QCD jets is crucial for a model of the tau reconstruction. Specifically, this requires a good parameterisation of the identification efficiency of real hadronic taus, ϵ and an excellent parameterisation of the rejection factor against fakes from QCD jets, R, which can be $\mathcal{O}(1000)$ in some regions of phase space. The jets in ATLFAST are then weighted[2] according to their label, so that:

$$N_{\tau-\text{tagged}} = \epsilon \cdot N_\tau + \frac{1}{R} \cdot N_{\text{other}}, \tag{5.5}$$

---

[1]In this region there is a gap in the calorimeter where the barrel and end-cap sections meet. There is a large increase in dead-material due to the presence of cabling for detector readout, which is fed through the gap, resulting in a degradation of the performance in this region.

[2]Jets can also be randomly tagged if desired by the user.
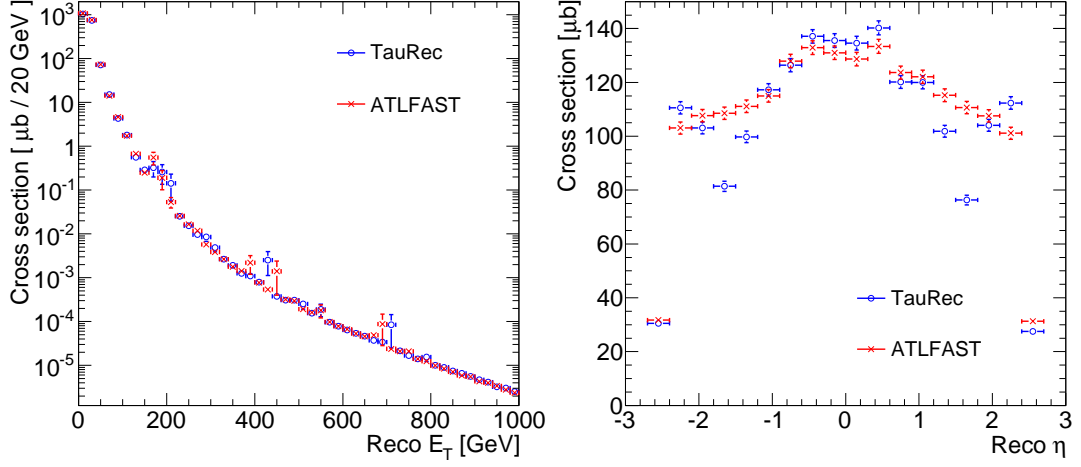
Figure 5.6: Comparison of the E_{T} and η distributions for fake taus reconstructed by calo-based tau reconstruction and ATLFAST with energy corrections applied. Very good agreement is found. A small drop in reconstruction efficiency occurs around $|\eta| = 1.5$, known as the *crack-region*, which is not modelled by ATLFAST. However, the general shape of the η distribution is in good enough agreement for use in ATLFAST.

where $N_{\tau-\mathrm{tagged}}$ is the number of jets tagged as hadronic taus, N_τ is the number of jets labelled as a true tau and N_{other} is the number of jets labelled as something other than a true hadronic tau.

5.3.3.1 Identification efficiency

To evaluate the identification efficiency for real taus, the identification efficiency as defined in eqn. (4.3) (page 42), was used. Identification was performed by applying selection to the Likelihood discriminator (constructed by the calo-based tau reconstruction). The identification efficiency was extracted as a function of the properties of the true hadronic tau (e.g. $\epsilon(E_{\mathrm{T,true}})$ or $\epsilon(\eta_{\mathrm{true}})$).

It is known that the Likelihood, although binned in E_{T}, retains some residual dependence on E_{T} [51], and a single cut on the Likelihood will neither result in optimal performance nor provide a flat identification efficiency. In light of this, a set of cuts on the Likelihood discriminator was defined so that the signal efficiency was flat across the whole E_{T}-η range. An arbitrary identification efficiency of 55% was chosen as a

Cuts on Log-Likelihood for flat identification efficiency

E_{T}[GeV]	$|\eta|$						
	Bin 1	Bin 2	Bin 3	Bin 4	Bin 5	Bin 6	Bin 7
15 - 20	4.42	3.96	3.56	3.40	2.80	2.52	2.04
20 - 25	5.14	5.32	4.46	3.88	3.12	3.22	2.72
25 - 30	5.90	5.68	5.10	4.98	3.66	3.66	3.44
30 - 45	6.44	5.94	4.94	4.62	3.70	3.96	3.78
45 - 65	7.18	6.74	5.32	4.46	3.22	3.26	3.04
65 - 90	7.60	7.00	5.38	3.84	2.34	2.28	1.76
90 - 120	7.32	6.74	4.94	3.18	1.32	1.86	1.00
120 - 200	6.60	6.00	3.90	2.24	0.56	1.04	-0.18
200 - 1000	5.64	4.94	2.98	0.94	-0.78	-0.22	-0.86

Table 5.3: Cuts on the Log-Likelihood required for a flat 55% identification efficiency in E_{T} and $|\eta|$. The E_{T} bins are constructed to contain similar statistical precision, and 7 bins of equal width span the region $0 < |\eta| < 2.5$.

working point. The cuts on the Log-Likelihood required for a flat 55% identification efficiency are given in Table 5.3.

This set of cuts is then used to extract the rejection factor as a function of E_{T} and η. The rejection is also extracted as a function of the identification efficiency, so that the E_{T}-η parameterisation can be scaled to a given user-selected input efficiency. Thus, by defining a set of Likelihood cuts to obtain a flat identification efficiency where the user can select the overall value, a parameterisation of the identification efficiency against E_{T} and η is no longer necessary. Instead, each ATLFAST jet labelled as a true tau is weighted with the user-selected input efficiency (ϵ_{user}), and the contribution to eqn. (5.5) is simply $\epsilon_{\mathrm{user}} \cdot N_{\tau}$, which is independent of E_{T} and η.

5.3.3.2 Rejection

To evaluate the rejection factor for fake taus the rejection factor as defined in eqn. (4.4) (page 42), was used, with the exception that the denominator was chosen as calo-based tau candidates. In addition, candidates matched to a true hadronic tau or electron within $\Delta R < 0.3$ were discarded from the calculation. It was important to remove fake candidates from electrons as they can significantly bias the rejection when applying only the Likelihood discriminator, which is optimised against hadronic jets. A separate discriminator has been developed to reject electron fakes and will efficiently reject

these candidates in an analysis. In ATLFAST, calorimeter cell deposits matched to true electrons are removed from the cell collection used to reconstruct jets, preventing any tau fakes from electrons.

The large rejection factors exhibited by the Likelihood discriminator severely limit the sample size of misidentified jets available to calculate the rejection itself. Although the ideal parameterisation method would calculate the rejection using a complete two-dimensional parameterisation with fine binning in both E_T and η, this was not possible. Instead, the rejection was extracted against: E_T in two η-regions (0, 1.43, 2.5), and $|\eta|$ in four E_T-regions (15, 20, 30, 90, 1000 GeV). The rejection functions in each of the regions are shown in Figure 5.7. The rejection in E_T was fitted with the combination of an error function and Landau of the form:

$$R(E_T) = p_0 \cdot \mathrm{Landau}(E_T | p_1, p_2) + p_3 \cdot \left[1 + \mathrm{erf}\left(\frac{(E_T - p_1)}{p_4} \right) \right]. \tag{5.6}$$

The rejection in η was fitted with a degree 4 symmetric polynomial of the form:

$$R(\eta) = p_0 + p_1 \cdot \eta^2 + p_2 \cdot \eta^4. \tag{5.7}$$

A linear interpolation between the one-dimensional functions was used to construct the two-dimensional rejection function, shown in Figure 5.8. In the interpolation, the η functions were cutoff at 2.25 to remove edge-effects from the fitting procedure.

Finally, the rejection was extracted against the identification efficiency in 12 E_T-regions (15, 20, 25, 30, 45, 65, 90, 135, 220, 280, 335, 435, 1000 GeV) shown in Figure 5.9 (left). Exponential functions were fitted to the rejection in each of the regions and were normalised to unity at 55% identification efficiency, shown in Figure 5.9 (right). The final parameterisation can be written as:

$$R(E_T, \eta, \epsilon) = C_{\mathrm{INT}} \cdot f(R_i(E_T), R_j(\eta)) \cdot R_k^{\mathrm{norm}}(\epsilon), \tag{5.8}$$

where $f(R_i(E_T), R_j(\eta))$ is the linear interpolation between the fitting functions in E_T and η, $R_k^{\mathrm{norm}}(\epsilon)$ are the rejection functions in efficiency normalised to unity at 55%, i, j and k are iterators over the various E_T and η regions, and C_{INT} is a correction factor needed after applying the interpolation. Figure 5.10 shows the E_T and η distributions of fake taus. The figure shows fake taus reconstructed and identified with the calo-based tau reconstruction, and fake taus reconstructed as ATLFAST jets, including the tau energy correction described in Section 5.3.2, and weighted by the parameterised
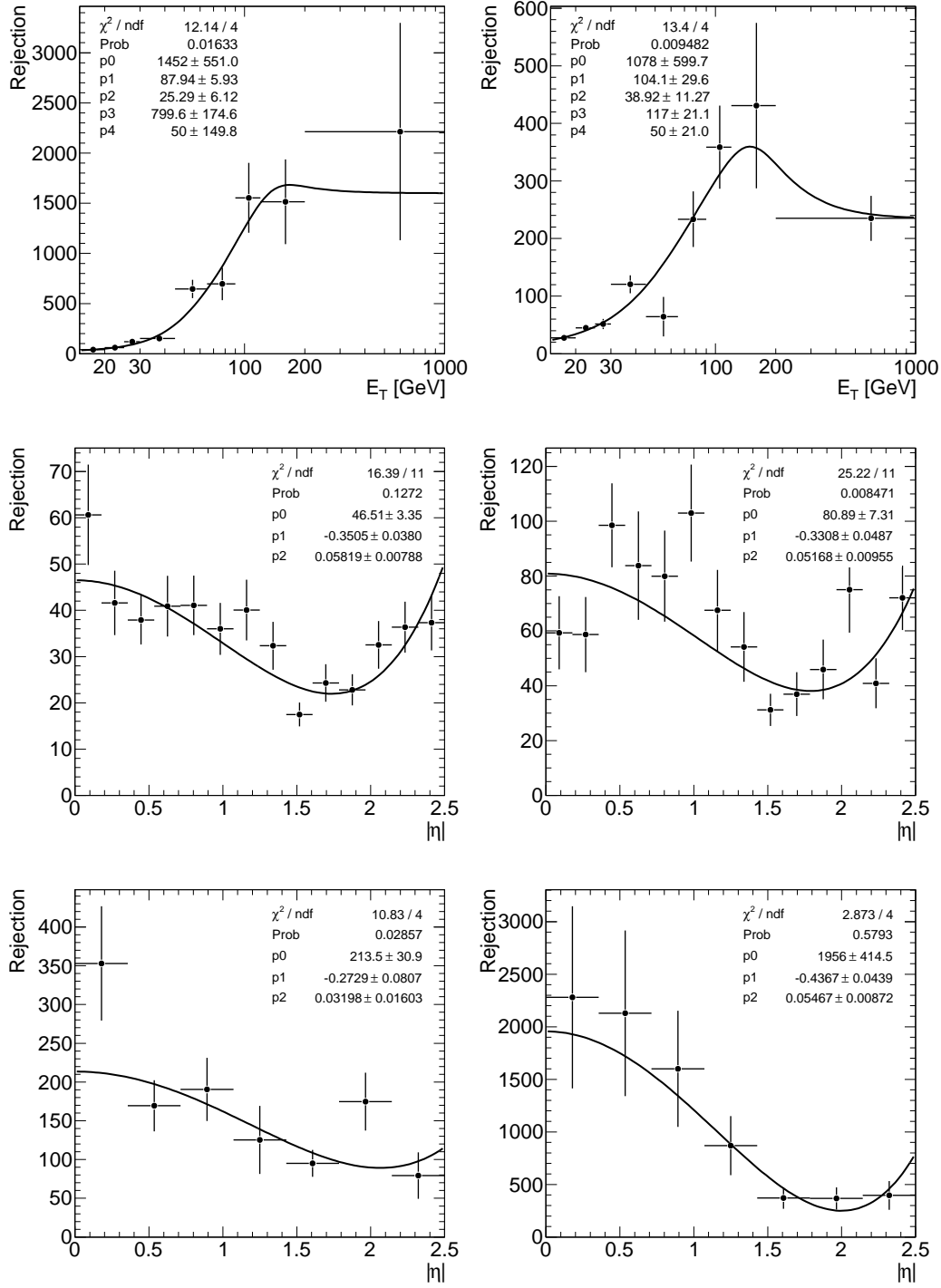
Figure 5.7: Rejection functions in E_T and η.
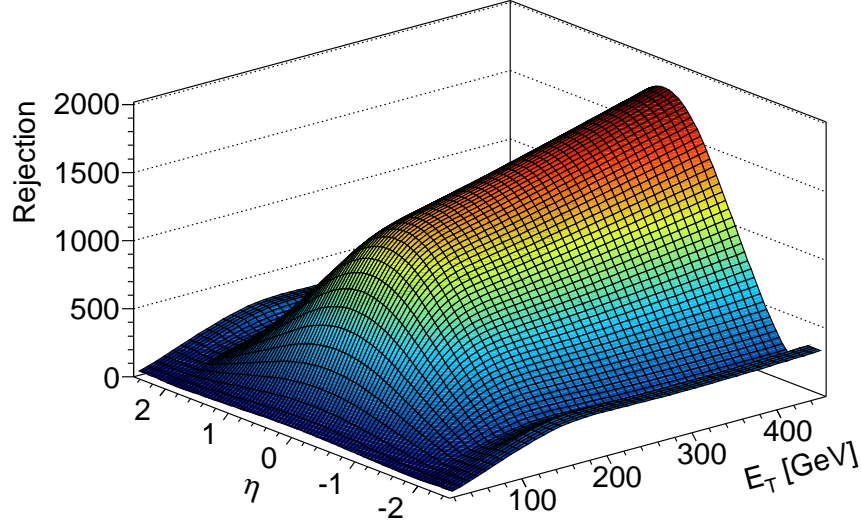
Figure 5.8: Two-dimensional Rejection function vs E_T and η. The two-dimensional function is a linear interpolation between the corresponding one-dimensional functions.

rejection function. Comparisons are made at the nominal identification efficiencies 30%, 55% and 70%, and good agreement is found in both E_T and η for all cases.

5.3.3.3 Jet-type parameterisation

In the previous section a parameterisation of the tau identification was extracted from QCD di-jet events. The parameterisation was shown to accurately reproduce the performance of the tau identification in the QCD di-jet events themselves, however, there is no guarantee that the parameterisation will be valid for other event types. In the past, parameterisations of the tau performance for ATLFAST-I have been used primarily to generate large samples for the evaluation of the QCD background. Therefore a QCD specific parameterisation was sufficient. However, as the LHC enters its first operational phase, the ability to rapidly generate large MC samples will become increasingly important, not only to guide analyses, but especially for the evaluation of systematic uncertainties. A parameterisation that can reproduce the performance of
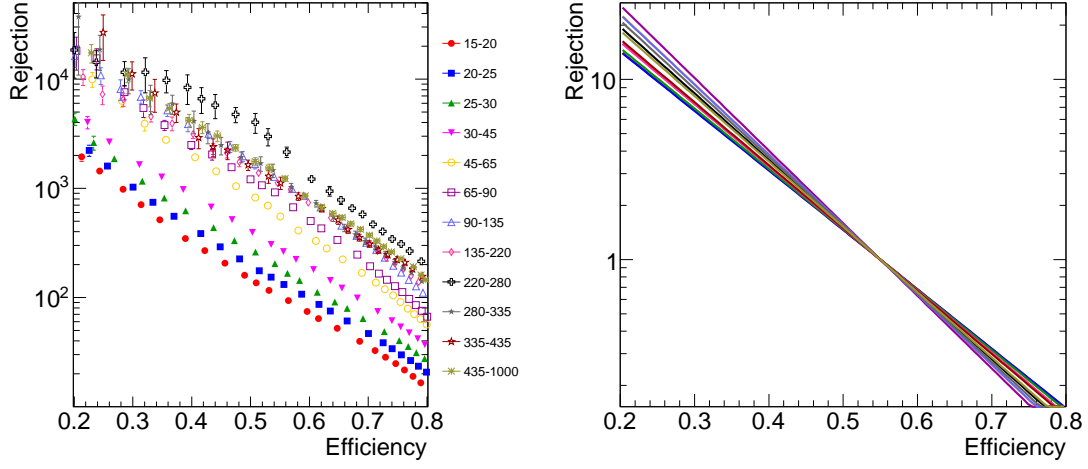
Figure 5.9: Rejection vs. Efficiency in 12 bins of E_T (left), and the corresponding fitted functions normalised to unity at 55% efficiency (right).
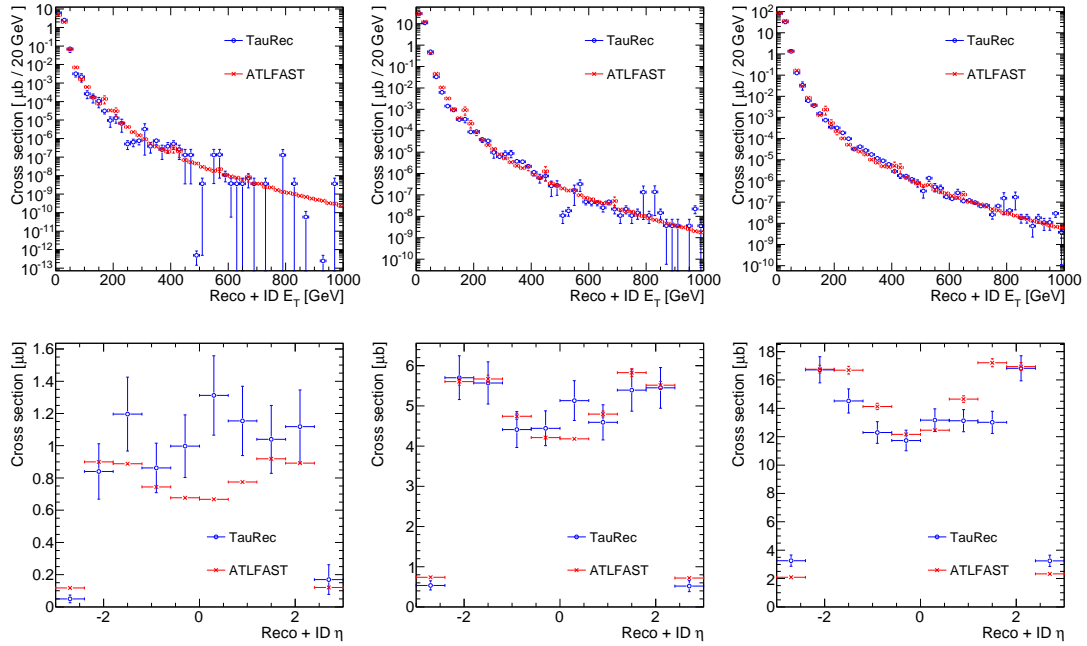
Figure 5.10: Performance of the ATLFAST tau parameterisation for fake taus as a function of E_T (top) and η (bottom). The performance was evaluated at 30% (left), 55% (middle) and 70% (right) identification efficiency. Excellent agreement was achieved.

the tau reconstruction independent of the event type would be necessary for such a task.

The performance of the tau identification is very sensitive to the origin of fake candidates, which can vary depending on the production process. In fact, even if the parameterisation is restricted to hadronic jets alone (disregarding fakes from electrons) there is still a large diversity in the types of jets that can be produced. The diversity stems from the fragmentation and hadronisation processes in which a free parton will dissipate energy via radiation and form a jet of stable hadrons. The fragmentation is dominated by low angle radiation of quarks and gluons from the free partons. As the higher energy partons continue to lose energy through radiation, a large number of partons are generated and eventually hadronise into jets of stable hadronic particles. The number, type and lateral energy distribution of hadrons in the jets is highly variable. Furthermore, the radiated partons are occasionally emitted at higher angles, which can result in the formation of additional jets. As the allowed set of partons produced in the fragmentation may be quite different to the set of partons available in the initial interaction (e.g. $W \rightarrow q\bar{q}'$, which cannot include gluons), the fragmentation itself can alter the composition of jet origin in a sample. As the tau identification works primarily on jet shape information to discriminate between regular hadronic jets and hadronic tau decays the fragmentation can lead to a large range of behaviour.

Although the fragmentation of an individual parton is largely non-deterministic, the identity of the parton has a large bearing on the outcome. Firstly, gluons have a higher tendency to radiate than quarks due to the difference in their colour charge ($C_A = 3$ for gluons and $C_S = 4/3$ for quarks). Thus gluon-initiated jets tend to exhibit higher particle multiplicities with a softer energy spectrum compared to quark-initiated jets [52]. As hadronic tau decays form low multiplicity jets where the particles by definition carry large fractions of the total energy, gluon-initiated jets are expected to exhibit much higher rejection factors than quark-initiated jets. Secondly, if the initial parton is a heavy quark, then it will decay via the weak interaction at some point after the fragmentation. Weak decays have very distinct properties compared to the surrounding hadronic activity. Not only can the decays occur at a distance from the initial production vertex (due to the lifetime of the heavy quark), but they can also result in the production of leptons, which have a very different signature in the detector. For b-quarks, which have large mass, the decays can occur at significant angle

to the axis of the jet, creating a wide energy distribution. The specific characteristics of gluon, light-quark and heavy-quark initiated jets leads to very different rejection factors from the tau identification algorithms.

Figure 5.11 shows the ratio of the rejection factor measured from QCD events for light-quark, b-quark and gluon initiated jets with respect to the mean rejection. As expected, gluon jets exhibit high rejection factors, while light-quark jets exhibit considerably lower rejection factors. This indicates that a sample must have very similar jet composition to QCD for the standard parameterisation to be valid. Figure 5.12 shows the performance of the standard parameterisation on $t\bar{t}$ events. While the kinematic distribution of the tau candidates match very well before identification is applied, the distributions after identification is applied show that the parameterisation clearly underestimates the fake-rate. The origin of the discrepancy lies in the jet composition, which is much different in $t\bar{t}$ events than in QCD di-jet events. Table 5.4 summarises the composition of fake tau candidates in each sample before and after the identification was applied. As the b-quark rejection is approximately equal to the mean rejection from the QCD samples, the largest difference comes from the dramatic change in the ratio of candidates from gluons and light-quarks. At this point it should also be mentioned that the QCD samples themselves have very different fractions of light-quark and gluon initiated candidates depending on the E_T generated in the hard $2 \rightarrow 2$ scattering process, shown in Figure 5.13. This means that is very important to correctly normalise the samples to their production cross section when extracting the parameterisation to ensure the correct composition of fake candidates. However, in doing so, the advantage of dividing the samples into regions of generated E_T is diminished due the increased statistical uncertainty from the highly weighted low E_T samples. Therefore, a successful jet-type parameterisation may negate the need to normalise the samples, increasing the statistical accuracy of the parameterisation. Finally, Figure 5.14 shows the kinematic distributions for identified fake tau candidates in $t\bar{t}$, where the rejection in ATLFAST was taken from the standard QCD parameterisation and the ratios from Figure 5.11 used to correct for jet-type. With the inclusion of the jet-type correction, reasonable agreement between ATLFAST and the calo-based tau reconstruction was achieved. The result could probably be improved with the addition of an η dependent jet-type correction, however, this was not considered in the current study.
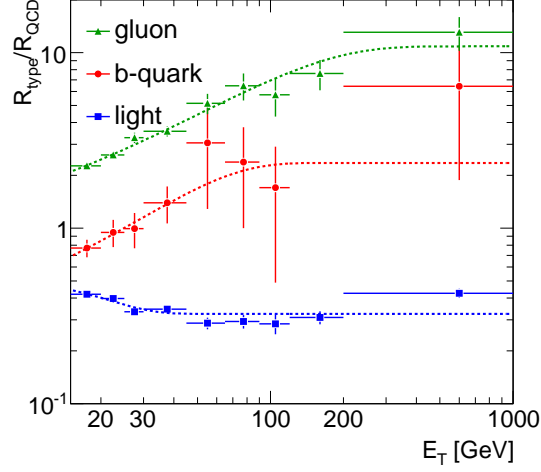
Figure 5.11: Ratio of the rejection factor for light-quark, b-quark and gluon initiated jets with respect to the mean rejection from the QCD samples. The rejection for gluon initiated jets is much higher than for light-quark initiated jets.

Composition of fake tau candidates

Jet-type	QCD		$t\bar{t}$	
	Reco [%]	ID [%]	Reco [%]	ID [%]
light-quark	40.4	67.7	36.4	76.2
gluon	57.4	30.7	19.7	8.6
b-quark	2.0	1.6	43.8	15.0
Total	1.87 mb	41.8 μb	3.09 nb	33.9 pb

Table 5.4: Composition of fake tau candidates in QCD di-jet and $t\bar{t}$ events before (Reco) and after (ID) the tau identification was applied. As the b-quark rejection is quite similar to the overall rejection from QCD, the largest difference is caused by the dramatic change in the ratio of light-quark and gluon initiated candidates.
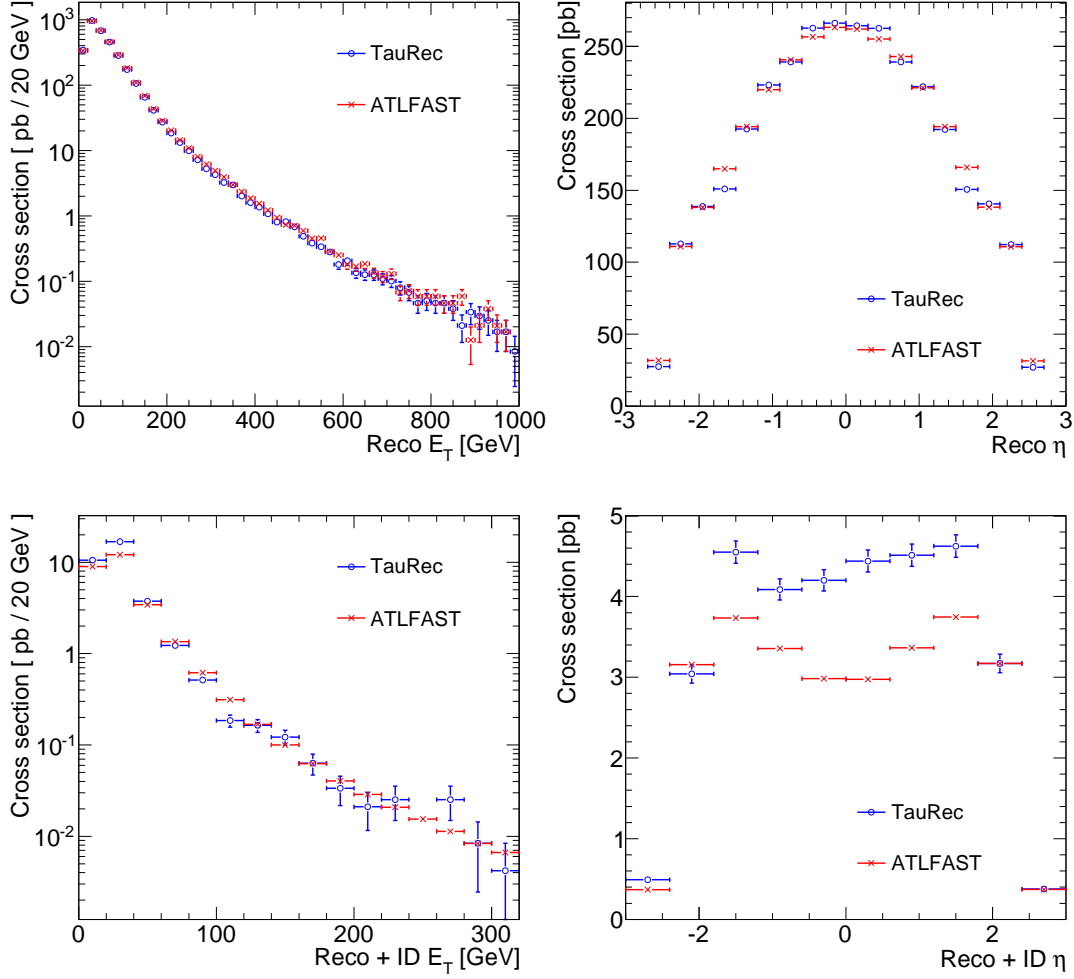
Figure 5.12: Comparison of the E_T and η distributions for fake tau candidates in $t\bar{t}$ events. Distributions for calo-based candidates and ATLFAST candidates with the energy corrections applied are given. The distributions when no selection is applied (top) are in very good agreement, however, the distributions including selection on the Likelihood with 55% signal efficiency (bottom) show some discrepancy.

71
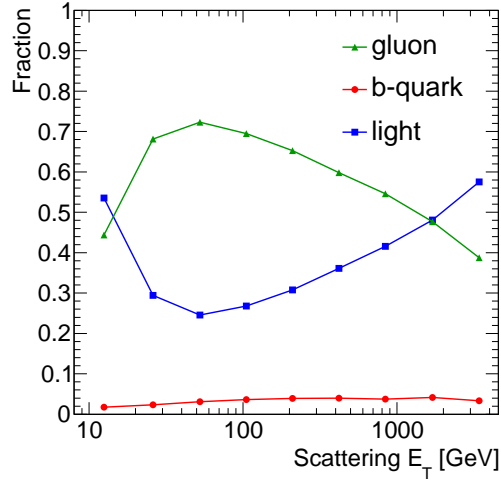
Figure 5.13: Composition of tau candidates in QCD events vs the E_T generated in the hard $2 \rightarrow 2$ scattering process. The discrete points correspond to the individual QCD samples.
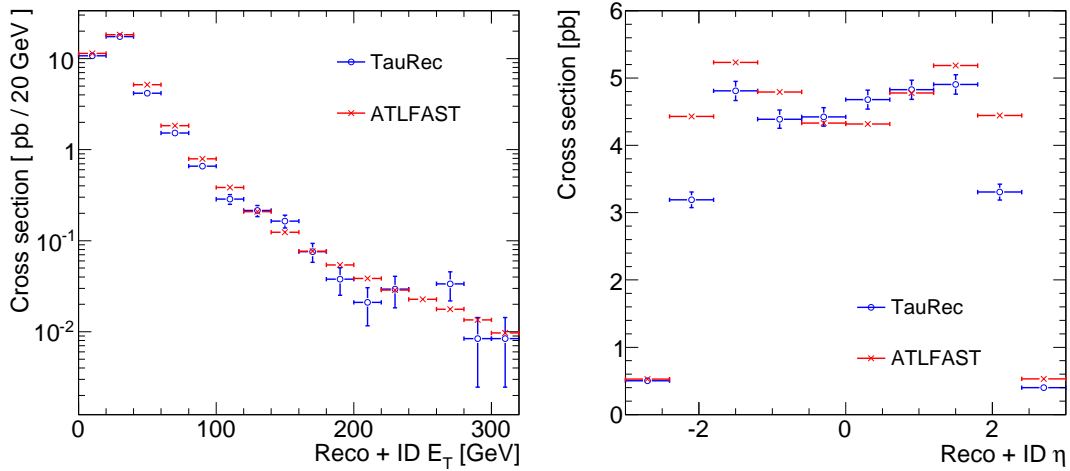
Figure 5.14: Kinematic distributions of reconstructed and identified fake taus in $t\bar{t}$. The rejection for ATLFAST jets is taken from the standard QCD parameterisation and a correction is applied for the jet-type. With the inclusion of the jet-type correction, reasonable agreement between ATLFAST and the calo-based tau reconstruction was achieved.

Unfortunately, the jet-type corrections rely on the definition used to categorise the origin of the tau candidates, which can present problems since gluons and quarks are not themselves physically observable objects. In this study, tau candidates were categorised by a match to truth particles within a cone of $\Delta R < 0.4$. If a b-quark was found, the jet was labelled as a b-quark initiated candidate, otherwise the highest p_{T} light-quark (u, d, s or c) or gluon was used to label the candidate. While the distinction of b-quark jets in this fashion is independent of the hadronisation model, a problem arises since the categorisation of light-quark and gluon initiated jets by the leading p_{T} truth parton depends on the hadronisation model used. Therefore, a parameterisation that uses such a categorisation is not independent of the event generator. To develop a jet-type parameterisation that is completely independent of the hadronisation model, physically observable quantities should be used. A selection of variables were investigated for their discriminating power between light-quark and gluon initiated jets. The two most effective variables were:

1. $N_{\text{particle}}^{\Delta R < 0.1}/N_{\text{particle}}^{\Delta R < 0.4}$ - the ratio of the number of stable truth particles in cones of $\Delta R < 0.1$ and $\Delta R < 0.4$ around the candidate, with $p_{\mathrm{T}} > 1$ GeV.

2. $\Sigma E_T^{\Delta R < 0.1}/\Sigma E_T^{\Delta R < 0.4}$ - the ratio of the total summed E_{T} of stable truth particles in cones of $\Delta R < 0.1$ and $\Delta R < 0.4$ around the candidate, with $p_{\mathrm{T}} > 1$ GeV.

Figure 5.15 shows distributions of the variables for light-quark and gluon initiated candidates. While good separation is displayed, the most encouraging property in regard to constructing an event type independent parameterisation is that the rejection factor is very sensitive to both variables, and both variables have minimal correlation to E_{T} and η, which are already used in the parameterisation. Despite the encouraging features of the variables, the implementation of such a parameterisation is much more complicated than the basic jet-type correction. The extraction of a single parameterisation that is independent of both the event type and the event generator remains a goal of the author.
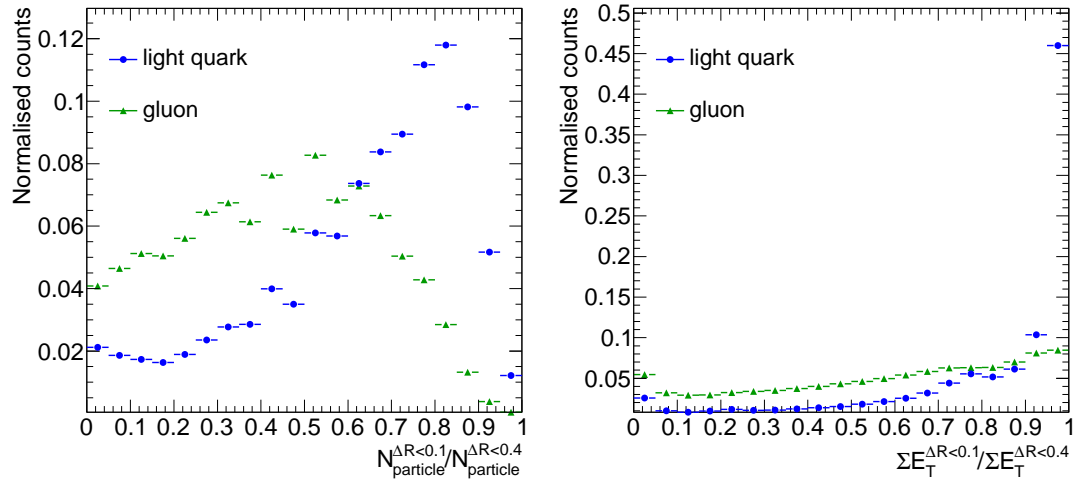
Figure 5.15: Physical observables for discrimination between light-quark and gluon initiated jets.

5.4 Validation of the track-based tau reconstruction for FastCaloSim

At the time of this work the fast calorimeter simulation software, FastCaloSim, had only recently been developed and was implemented as the first fast-simulator of the ATLFAST-II project. Fatras had not been developed, and GEANT4 was used to simulate the inner tracker and muon chambers. For such a new form of simulation, validation of the performance of the various reconstruction algorithms with respect to the full simulation was extremely important. The ATLFAST-II conveners decided that, in addition to the validation, correction factors should be supplied for the main reconstruction algorithms to match the performance in full simulation, as they were expected to be very small. In this section the validation of the track-based tau reconstruction is presented, as well as the extraction of the correction factors. All content is the complete work of the author, and has been published in an internal ATLAS note [53].

5.4.1 Outline of the validation

The validation for the track-based tau reconstruction was performed for signal ($Z \rightarrow \tau\tau$) and background (QCD di-jets[1]) samples. A privately produced ATLFAST-II sample of $\sim$75k events was used for the signal. An officially produced ATLFAST-II sample containing $\sim$650k events was used for background. All full simulation samples were official CSC datasets [36] of comparable size to the fast simulated samples.

For the signal samples, a comparison of the resolution in E_T, η and ϕ was made. For both signal and background, the reconstruction and identification efficiencies as functions of E_T and η were compared. The efficiencies vs. η were split into two E_T regions $10-35$ GeV and $35-100$ GeV. The validation of the efficiencies was done in two steps. The aim was to first compare the reconstruction efficiency, applying corrections if necessary and then to compare the identification efficiency. Three discriminants from the track-based reconstruction were used in the comparison of the identification efficiencies: 1. B_cut – a basic 1-D cut-based discriminant, 2. B_TMVA – a cut-based discriminant optimised using the multivariate analysis package, TMVA, and 3. C_NN – a neural network discriminant. The differences between ATLFAST-II and full simulation

---

[1]The di-jet sample had a generator cut requiring the p_T generated in the hard $2 \rightarrow 2$ scattering process to be within $70 < p_\mathrm{T} < 140$ GeV.

for the track-based tau reconstruction were expected to be small, as the full GEANT4 simulation was used in ATLFAST-II to simulate the tracking.

5.4.2 Resolutions

The resolutions in ϕ, η and E_T are shown in Figure 5.16 for 1-prong and 3-prong candidates for full simulated samples and ATLFAST-II samples. The resolutions are shown for track-based candidates matched to a true hadronic tau (within a cone of $\Delta R < 0.3$), and also for matched and identified candidates where B_cut is used for identification. The kinematic resolution for track-based taus in ATLFAST-II was found to be in very good agreement with full simulation. The result is not surprising since η and ϕ of the candidate are calculated directly from tracking and the energy-flow algorithm used to calculate E_T uses minimal calorimeter information.

5.4.3 Reconstruction efficiency

The reconstruction efficiencies for real and fake candidates were calculated using the standard definitions: eqn. (4.1) and eqn. (4.2). All efficiencies were calculated with respect to the kinematic quantities of the denominator (i.e. truth variables). The reconstruction efficiencies as functions of E_T and η are shown in Figure 5.17. In general, very good agreement was found between ATLFAST-II and full simulation. The agreement for signal was within 2-3% across E_T and η, while for background the agreement was slightly poorer, with a difference of up to $\sim$10% in the high E_T, high η region. Despite some differences in specific regions of phase space, the overall agreement between ATLFAST-II and full simulation was very good and corrections to the reconstruction efficiency were not required.

5.4.4 Identification efficiency

The identification efficiency was calculated as in eqn. (4.3), using tau candidates as the denominator. Therefore all efficiencies are shown as functions of the track-based tau reconstructed kinematic variables. As corrections were required to be applied with respect to the reconstructed variables, it was important to use tau candidates in the denominator and not truth particles. Furthermore, no match to truth particles was performed to determine the true identity of the candidates as the MC datasets already

(a) 1P ϕ-resolution

(b) 1P η-resolution

(c) 1P E_{T}-resolution

(d) 3P ϕ-resolution

(e) 3P η-resolution

(f) 3P E_{T}-resolution
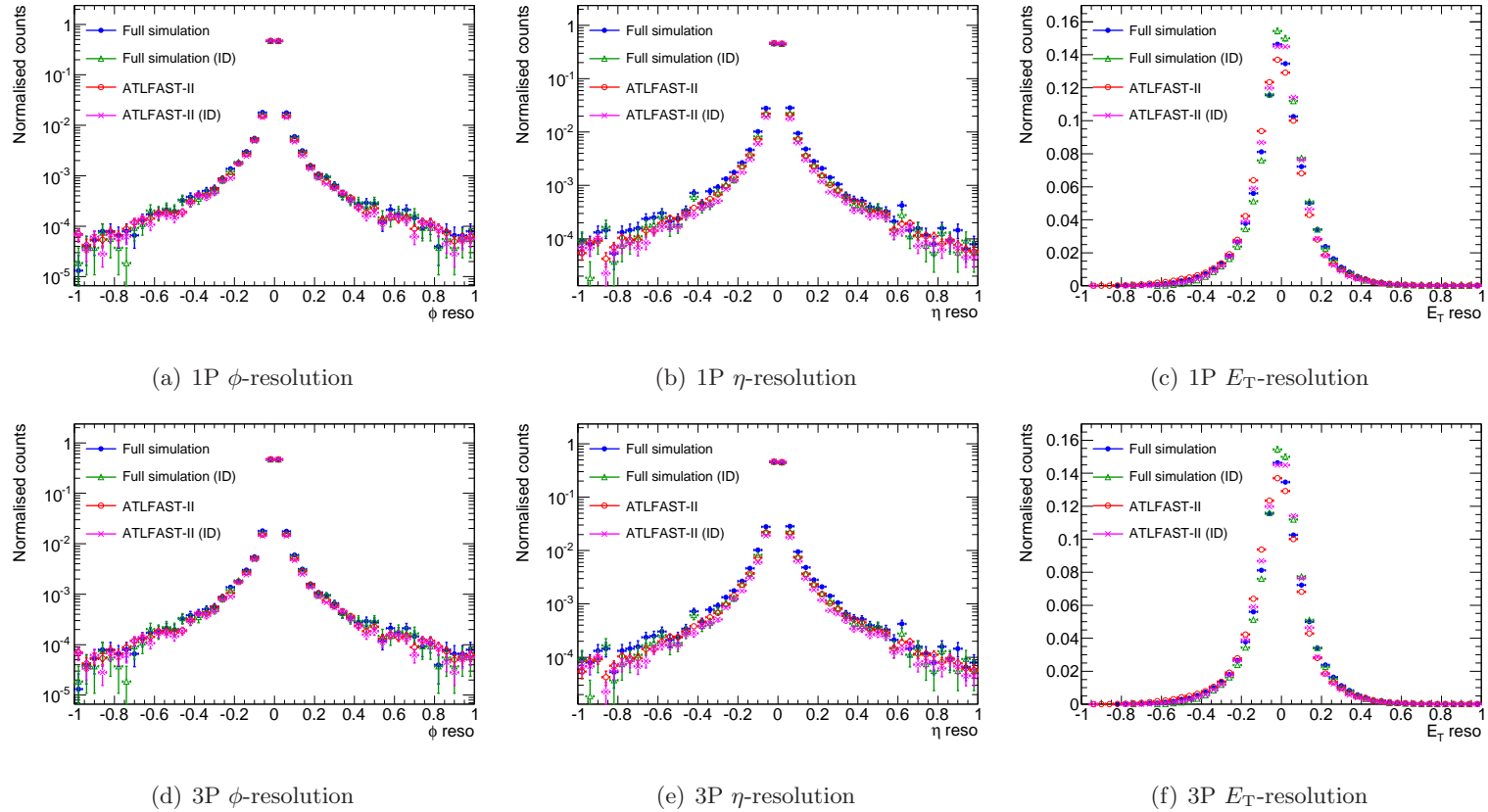
Figure 5.16: Resolutions for ϕ, η and E_{T} for signal 1-prong (top) and 3-prong (bottom) candidates. The resolutions are given for track-based candidates matched to true hadronic taus, and also for matched and identified candidates where B_{cut} is used for identification. The agreement in the kinematic resolutions between full simulation and ATLFAST-II is very good.

(a) Signal

(b) $10 - 35$ GeV

(c) $35 - 100$ GeV

(d) Background

(e) $10 - 35$ GeV

(f) $35 - 100$ GeV
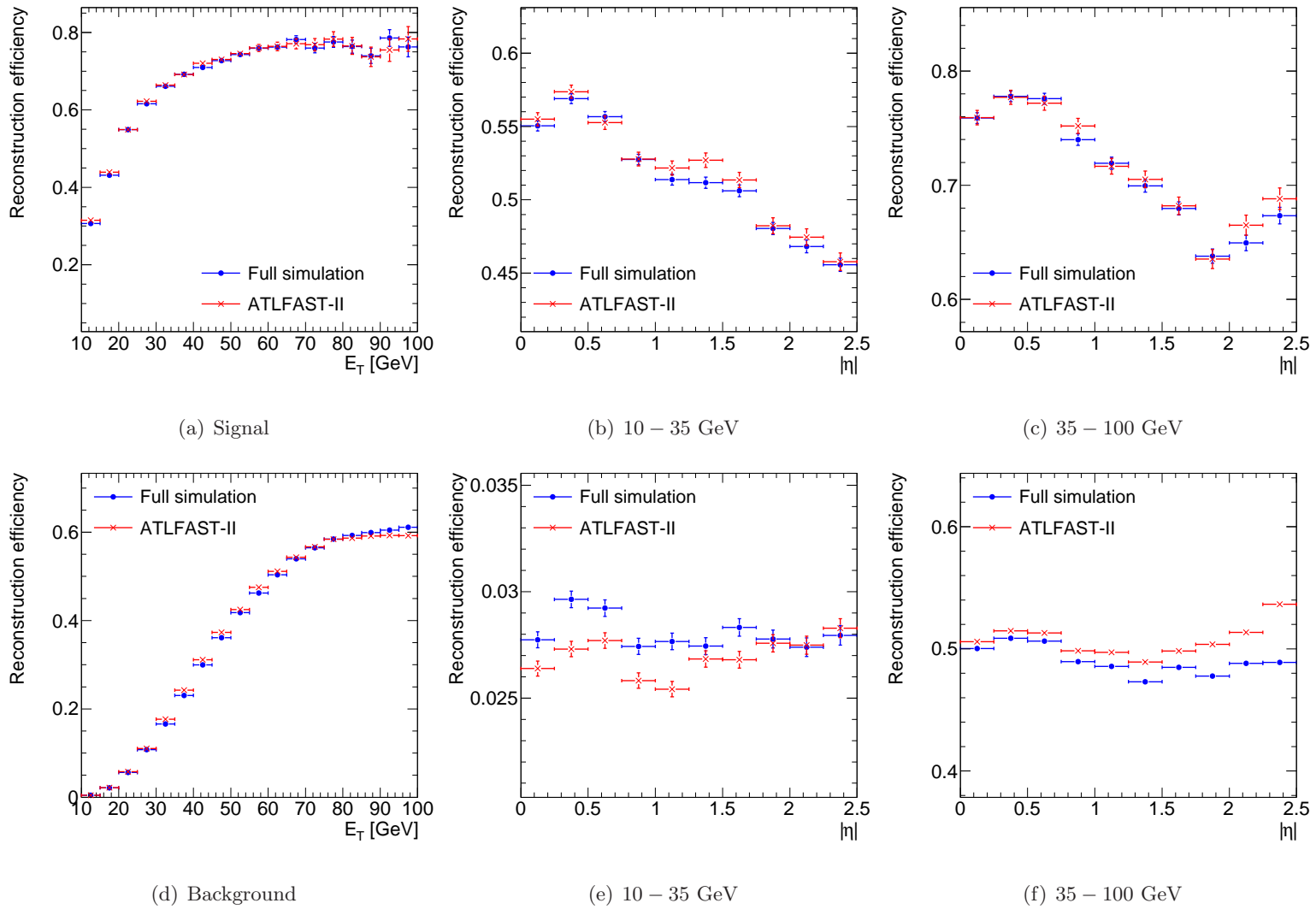
Figure 5.17: Reconstruction Efficiencies for signal (top) and background (bottom) against truth variables. The agreement between reconstruction efficiency for ATLFAST-II and full simulation is very good. Differences for the signal are generally less than $2 - 3\%$. For the background they are slightly larger with a variation of up to $\sim 10\%$ at very high E_{T} and $|\eta|$.

provided very clean samples of real and fake taus. Also, only the relative differences in the efficiencies were of concern, not the absolute values. Three discriminants were used for identification of the tau candidates. They were split into two categories: 1. *Boolean* – where the discriminant returns either a pass or fail for any given candidate (B_{cut} and B_{TMVA}), and 2. *Continuous* – where the discriminant forms a continuous distribution and selection can be tuned to alter the level of rejection vs. identification efficiency for real and fake candidates (C_{NN}). For the boolean discriminants a single comparison of the efficiency against E_{T} and η was sufficient. However, for C_{NN}, a more complex comparison was required.

Figures 5.18 to 5.20 show the identification efficiencies using each discriminant for track-based tau candidates in ATLFAST-II and full simulation. Significant differences can be seen in both E_{T} and η. The discrepancies are generally ∼10-20% and can be up to ∼50% in some regions. For C_{NN}, the efficiency when requiring $C_{\mathrm{NN}} > 0.3$ is shown, however, selection at different values shows similar (or larger) discrepancies. It was deemed necessary to apply an E_{T} and η dependent correction to each of the discriminants. The following sections describe the correction technique applied to each tau identification discriminant.

5.4.5 Correcting boolean discriminants

The boolean discriminants were corrected by altering the identification state (from 0 to 1 or vice versa) of a randomly selected sample of candidates. Ultimately, this would be performed in a complete set of two-dimensional bins spanning E_{T} and η. However, the sizes of the MC samples did not permit such a method. Instead, the discriminants were corrected in a two-step process. Firstly, a correction against E_{T} was extracted and applied. Secondly, the remaining difference in η was extracted (in the two E_{T} regions) and applied as a correction. In each step the following ratio was extracted:

$$R(x) = \epsilon_{\mathrm{Full}}(x)/\epsilon_{\mathrm{Fast}}(x), \tag{5.9}$$

where ϵ_{Full} and ϵ_{Fast} are the identification efficiencies found in full simulation and ATLFAST-II, respectively, and x can be either E_{T} or η. This ratio was then used to correct the ATLFAST-II discriminant, B, using the following procedure in both the E_{T} and η steps. Firstly, for each ATLFAST-II candidate, a random number, r, with flat distribution between 0 and 1 was drawn. Then, the candidate was classified into

(a) Signal

(b) $10 - 35$ GeV

(c) $35 - 100$ GeV

(d) Background

(e) $10 - 35$ GeV

(f) $35 - 100$ GeV
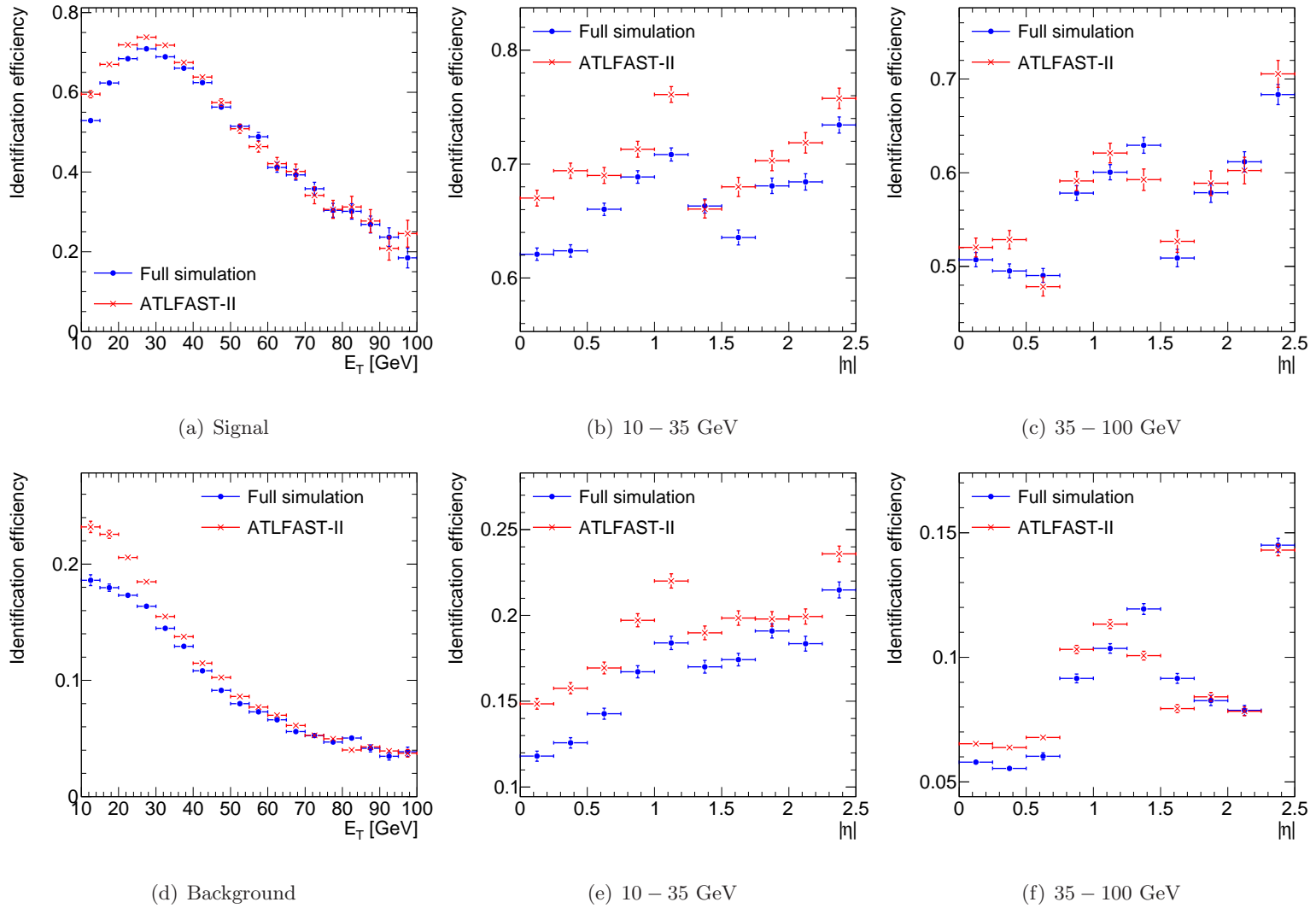
Figure 5.18: Identification efficiencies against reconstructed variables for signal (top) and background (bottom) using $B_{\mathrm{cut}} = 1$.

(a) Signal

(b) $10 - 35$ GeV

(c) $35 - 100$ GeV

(d) Background

(e) $10 - 35$ GeV

(f) $35 - 100$ GeV
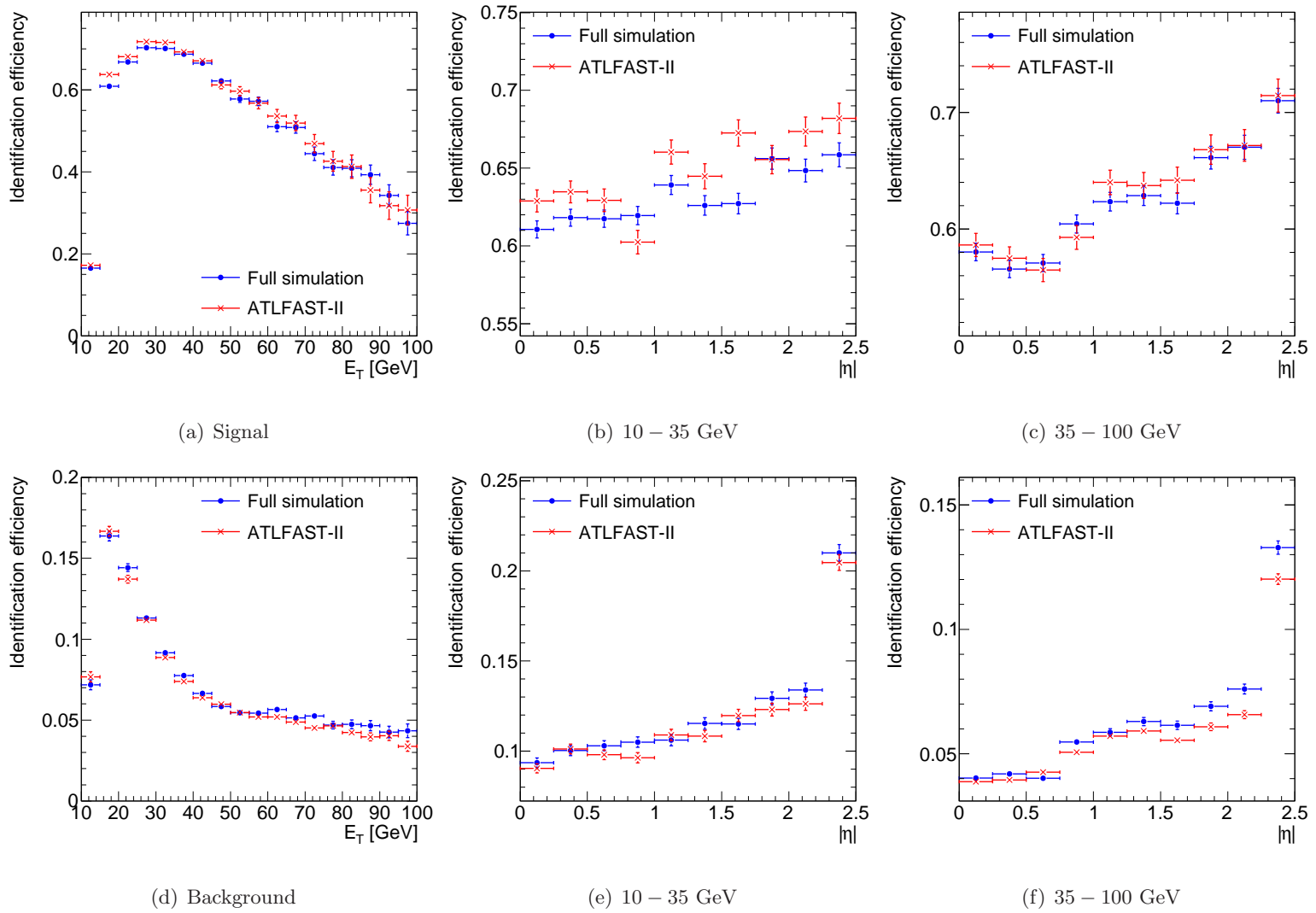
Figure 5.19: Identification efficiencies against reconstructed variables for signal (top) and background (bottom) using $B_{\mathrm{TMVA}} = 1$.

(a) Signal

(b) $10 - 35$ GeV

(c) $35 - 100$ GeV

(d) Background

(e) $10 - 35$ GeV

(f) $35 - 100$ GeV
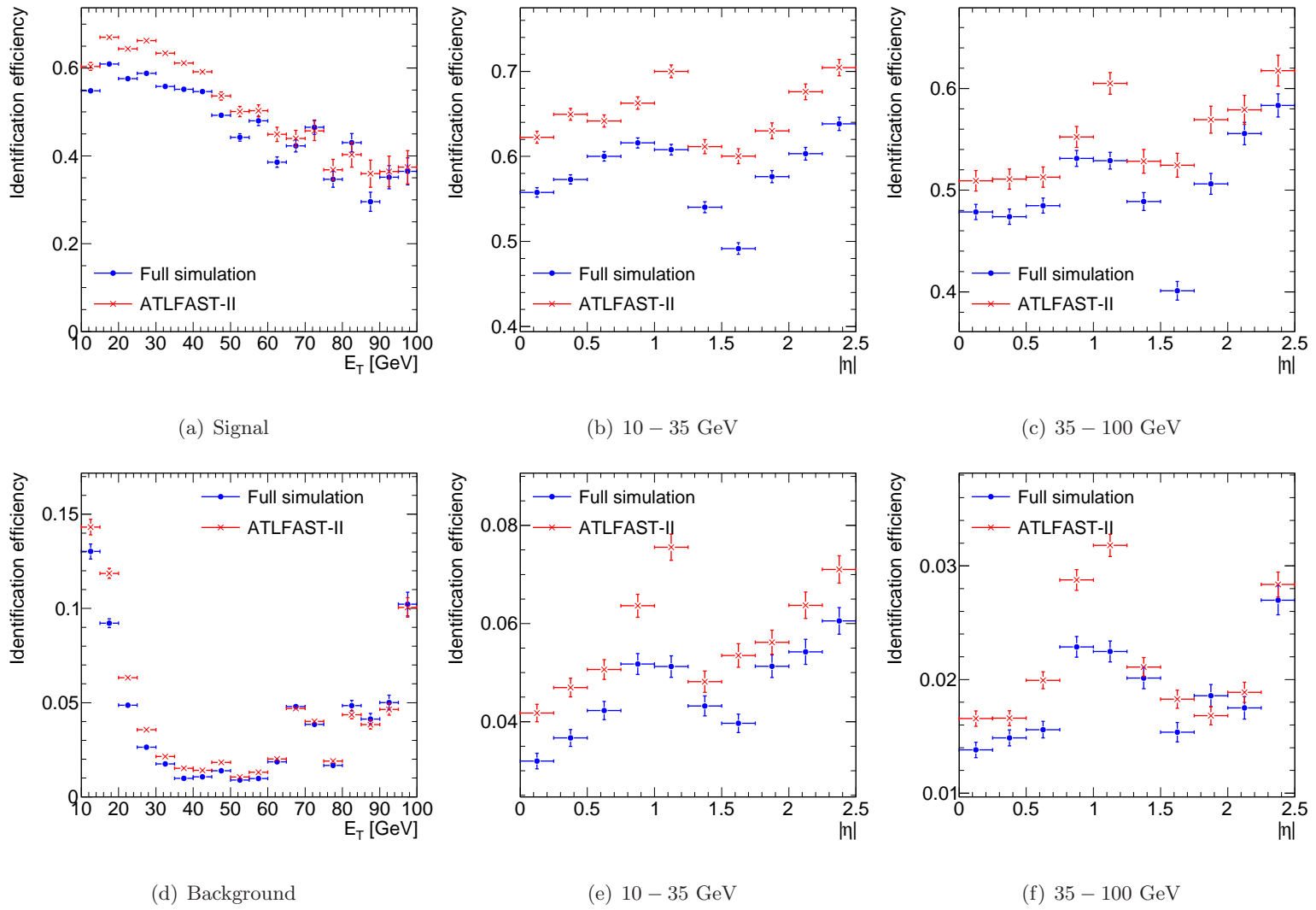
Figure 5.20: Identification efficiencies against reconstructed variables for signal (top) and background (bottom) using $C_{\mathrm{NN}} > 0.3$.

one of two categories depending on whether the identification efficiency in ATLFAST-II was found to be higher or lower than in full simulation for the region of phase space occupied by the candidate. If the identification efficiency in ATLFAST-II was higher and the identification state of the candidate was set to 1, then if $r > R(x)$ the identification state was switched to 0, reducing the efficiency in ATLFAST-II in that region. Conversely, if the identification efficiency in ATLFAST-II was lower, a more complicated procedure had to be applied. Firstly, the ratio $R(x)$ was transformed to $D(x) = \frac{R(x)-1}{e(x)^{-1}-1}$, where $e(x)$ is the ATLFAST-II efficiency, to act on failed candidates ($B = 0$). Then, if the identification state of the candidate was set to 0 and $r < D(x)$, the identification state was switched to 1, increasing the efficiency in ATLFAST-II in that region.

The results after these corrections were applied are shown in Figures 5.21 and 5.22. The corrections for signal were very good and resulted in an identification efficiency within ∼3% of full simulation in all E_T and η bins. The corrections for background weren't as successful and despite giving much improved matches in E_T (within ∼2%), the differences in η were only corrected to within ∼9-10% with a noticeable over-correction. The two-step method has a clear disadvantage with respect to a full two-dimensional parameterisation as correlations between E_T and η are largely neglected. If larger MC samples were to become available in the future it would be worth investigating a complete two-dimensional parameterisation, however, the results of the two-step corrections are still very good.

5.4.6 Correcting continuous discriminants

The continuous discriminant, C_NN, was corrected by applying a shift to the distribution in ATLFAST-II so that it would match the distribution in full simulation. Rather than adopting a two-step procedure as for the Boolean corrections, a complete two-dimensional approach was taken to correctly account for correlations, however, the statistical precision in some regions of phase space was very limited. The shift was parameterised in 12 kinematic regions comprised of six E_T (10, 15, 20, 40, 60, 80, 100 GeV) and two $|\eta|$ (0, 1, 2.5) bins. Due to the lack of statistical precision, a direct comparison of the C_NN distributions was difficult. Instead, to extract the shift in the discriminant, the identification efficiency was calculated as a function of the threshold on the discriminant over the entire range $C_\text{NN} \in [0, 1]$ in steps of 1/1000.

(a) Signal

(b) $10 - 35$ GeV

(c) $35 - 100$ GeV

(d) Background

(e) $10 - 35$ GeV

(f) $35 - 100$ GeV
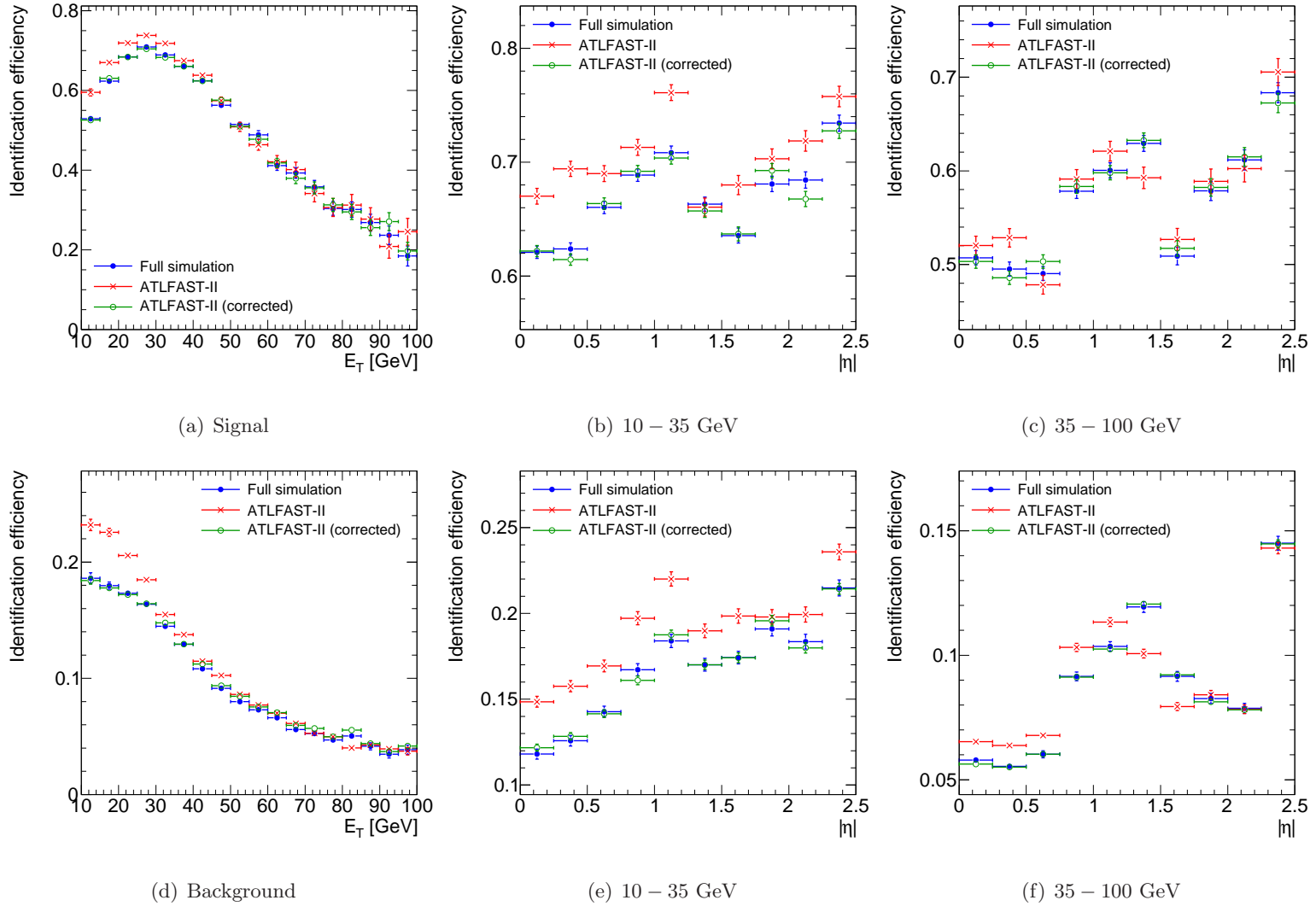
Figure 5.21: Corrected identification efficiencies for signal (top) and background (bottom) using $B_{\text{cut}} = 1$. The corrected signal is within ∼3% of FullSim for all bins in E_{T} and η. The background exhibits a slight over-correction, and lies within ∼10%.

(a) Signal   (b) $10 - 35$ GeV   (c) $35 - 100$ GeV

(d) Background   (e) $10 - 35$ GeV   (f) $35 - 100$ GeV
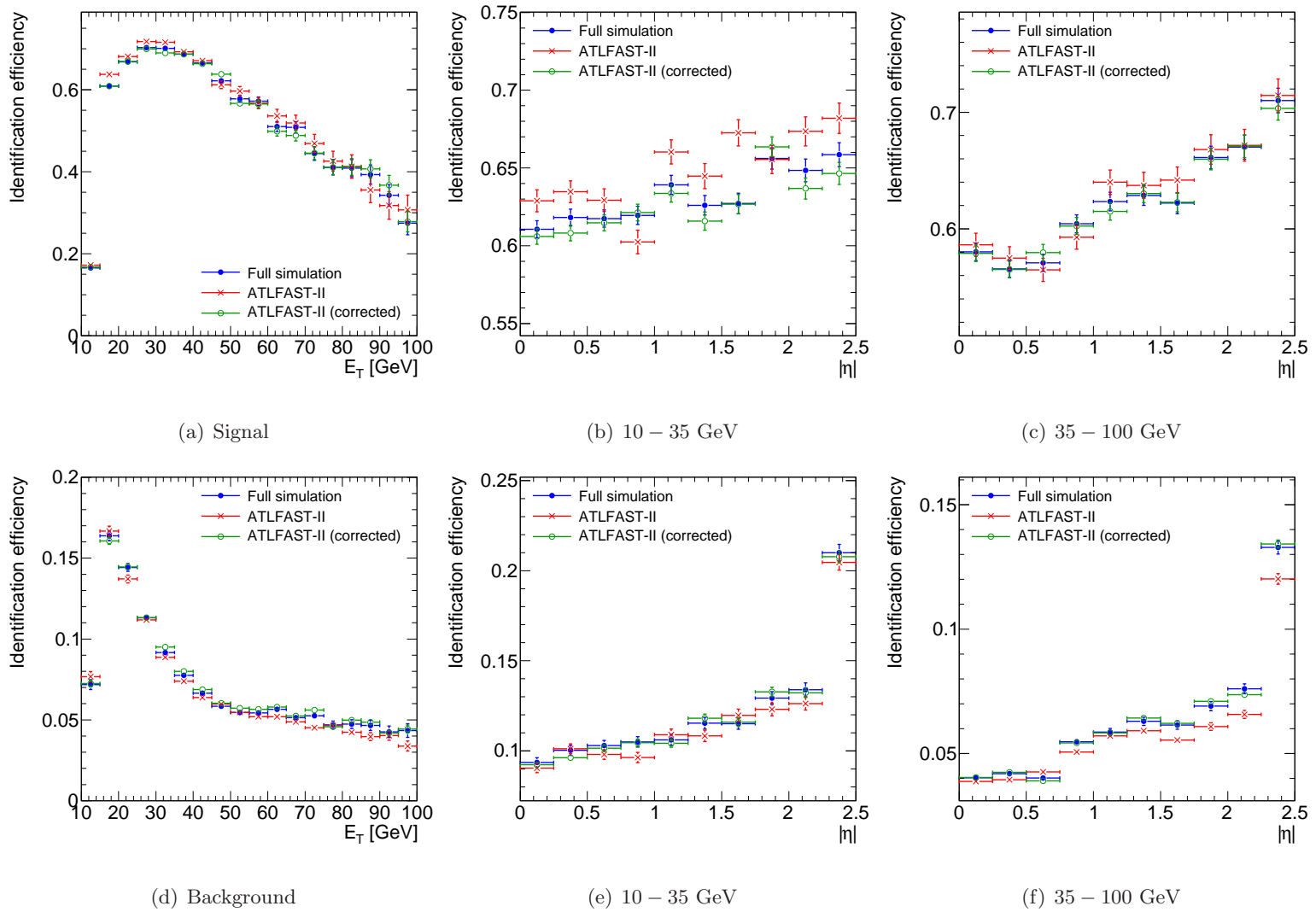
Figure 5.22: Corrected identification efficiencies for signal (top) and background (bottom) using $B_{\mathrm{TMVA}} = 1$. The corrected signal is within $\sim 1.5\%$ of FullSim for all bins in E_{T} and η. The background exhibits a slight over-correction, and lies within $\sim 9\%$.

This produced a monotonically increasing function that was much more well behaved. For each evaluation point in ATLFAST-II, the full simulation point that gave the closest match in efficiency was found. The difference between these two points gave the shift in the ATLFAST-II C_{NN} threshold (required to give the closest match in efficiency) as a function of the ATLFAST-II C_{NN} threshold itself. This function was then fitted with a 4th degree polynomial fixed to 0 at $C_{\mathrm{NN}} = 0$ and 1 (since there can be no difference between the efficiencies for these thresholds). The procedure was then repeated for each of the kinematic regions. The shift was then directly applied to the C_{NN} discriminant in the correction process. The results can be seen in Figure 5.23. The corrected signal is generally within ∼6% of full simulation, however, for one bin in E_{T} and another in η there are large over-corrections resulting in discrepancies of ∼20%. The background correction again performs slightly worse with discrepancies ranging from ∼12%-20%. Ultimately, the performance of the corrections for the background are limited by the statistical precision available in the tail of the C_{NN} distribution.

5.4.7 Summary

The agreement in the kinematic resolutions of track-based tau candidates between ATLFAST-II and full simulation is excellent. The reconstruction efficiency is found to be within 2-3% of full simulation in both E_{T} and η, and no corrections were required. The identification efficiencies were found to have discrepancies ranging from 10-50% with the low E_{T} region in most need of correction. The boolean corrections were found to be very successful, reducing the discrepancies to 2-3% for signal and 10% for background. For each of these corrections the match in E_{T} was very good, however the match in η was significantly poorer, due to the neglect of correlations when using the two-step method. Extracting the correction for the C_{NN} distribution was a much more difficult task, however, given the difficulty gave reasonable results. The corrections gave a match between 10-20%, with best results in the low-mid E_{T} range.

(a) Signal C_{NN} distribution   (b) Corrected ID Efficiency vs. E_T (c) Corrected ID Efficiency vs. $|\eta|$

(d) Background C_{NN} distribution   (e) Corrected ID Efficiency vs. E_T (f) Corrected ID Efficiency vs. $|\eta|$
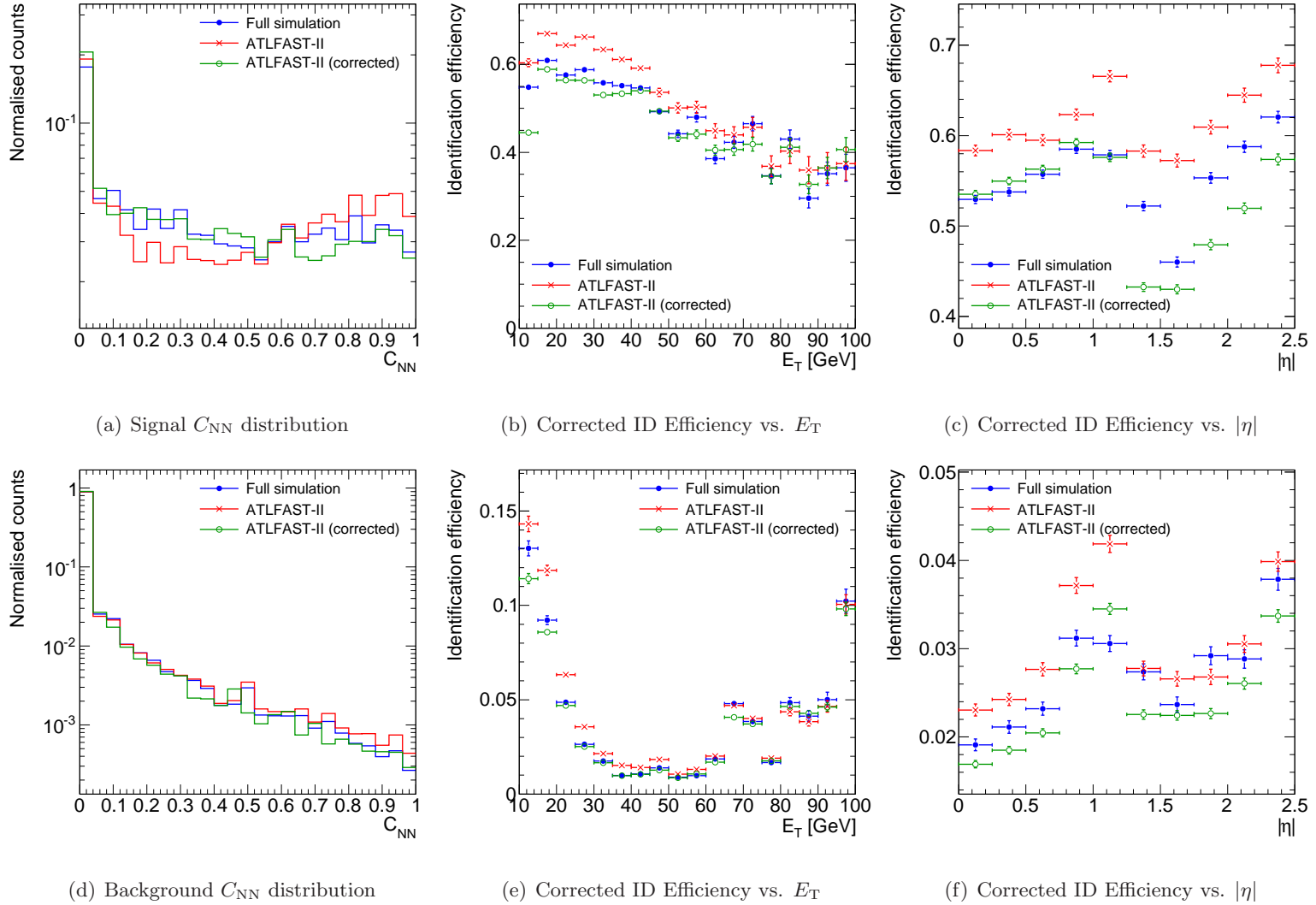
Figure 5.23: Corrected C_{NN} distribution and identification efficiencies for signal (top) and background (bottom) using $C_{NN} > 0.3$. The corrected signal is generally within ∼6% of full simulation, however, for one bin in E_T and another in η there are large over-corrections resulting in discrepancies of ∼20%. The background correction again performs slightly worse with in general, discrepancies ranging from ∼12%-20%. This is because the background correction is significantly harder to extract due to a much lower portion of statistics in the tail of the C_{NN} distribution.

6

Discovery potential for A/H in the ATLAS experiment

The main objective of the LHC experiments is to discover the mechanism for electroweak symmetry breaking. As discussed in Chapter 2, one of the favoured theoretical candidates for EWSB is the Higgs mechanism, which requires at least one additional scalar particle, the Higgs boson. While the Higgs mechanism is employed in the Standard Model with the minimal choice of scalar sector, the mechanism is also required in some beyond SM theories to facilitate EWSB, and in some cases a more complex sector can be required. There is also nothing preventing a more complex scalar sector within the SM itself. Thus, if a Higgs boson is found by the ATLAS experiment, correct identification of the particular model it belongs to will be crucial. It is therefore important for the ATLAS collaboration to develop searches for Higgs bosons in a number of different scenarios. In this chapter, a study of the discovery potential for neutral Higgs bosons in the Minimal Supersymmetric Standard Model at the ATLAS experiment is presented. The bosons were required to decay into a pair of tau-leptons, where one tau decays leptonically ($\ell = e, \mu$) and the other hadronically ($\ell\tau_h$-channel). The mass range $150 < m_A < 800$ GeV was considered. The study was aimed at 14 TeV proton-proton collisions with a maximum instantaneous luminosity of 10^{33} cm^{-2}s^{-1} and a total integrated luminosity of 30 fb^{-1} collected by the ATLAS experiment. All results were interpreted in the m_h-max scenario [27]. A counting experiment was performed to extract the sensitivity of the analysis, using the number of signal and background events

with a reconstructed mass inside a given window. The work was performed in collaboration with members of the ATLAS experiment and has been published in [1]. All the work presented in this chapter is the complete work of the author, unless otherwise stated. Data-driven background estimation procedures for the $t\bar{t}$ and $Z \to \tau\tau$ processes were developed by other members of the project and are not discussed, however details can be found in the publication.

In the MSSM, two complex Higgs doublets are required, resulting in five physical Higgs bosons: three neutral (h, H and A) and two charged ($H^{\pm}$). At tree-level all the properties of the Higgs sector, including the masses and couplings of the Higgs bosons can be described by two parameters, typically chosen as m_A and $\tan\beta$, where $\tan\beta$ is the ratio of the vacuum expectation values of the two Higgs doublets. In general the couplings of the bosons are quite different to the SM Higgs boson, in particular, the ZZ and WW decay modes that are relied upon in SM Higgs boson searches are no longer dominant. Instead, couplings to the down-type fermions are enhanced, and Higgs boson production and decay through pairs of b-quarks and tau-leptons is dominant. The two dominant production modes are b-quark associated production and gluon fusion. In most of the parameter space, neutral Higgs boson decay is dominated completely by the modes $\phi \to b\bar{b}$ ($\sim$90%) and $\phi \to \tau\tau$ ($\sim$10%), where ϕ denotes any of the neutral Higgs bosons ($A/H/h$). Although the $b\bar{b}$ mode has a much larger branching fraction, it is extremely difficult to separate from the overwhelming QCD di-jet background. On the other hand, the tau mode has more distinctive features for discriminating against QCD di-jets and provides much better signal sensitivity. The taus can either decay leptonically or hadronically forming three modes: $\ell\ell$ (12%), $\ell\tau_h$ (46%) and $\tau_h\tau_h$ (42%). The $\tau_h\tau_h$ mode suffers similar difficulties as the $b\bar{b}$, being very difficult to separate from the QCD background. On the other hand, the $\ell\ell$ mode, while providing good suppression of the QCD background, is limited by the branching fraction. The $\ell\tau_h$ mode has the largest branching fraction and can be adequately separated from the QCD background, providing the best sensitivity over a large range of the MSSM parameter space. In the mass range $m_A \geq 150$ GeV, m_A and m_H are degenerate to less than 1 GeV, while m_h is well below m_A. Therefore the signal from A and H sum together and can be searched for with a single analysis, however, the analysis is not sensitive to h.

The signature of the $\ell\tau_h$ channel in the ATLAS detector is not entirely unique and a number of Standard Model processes combine to form a background for the signal. When data from the ATLAS experiment is analysed, selection based on the information from the detector must be used to discriminate against the backgrounds to enrich the *signal purity* of the sample. To optimise the selection in the analysis, and to evaluate the discovery potential for ATLAS, Monte Carlo simulated event samples were produced for the signal and background processes. Using the standard production chain, it is impossible to produce all the MC samples with a sample size equivalent to what is expected in $30\,\mathrm{fb}^{-1}$ of data, so a number of measures were taken to increase the effective size of the MC samples. Firstly, ATLFAST-II was used for the simulation of all samples, increasing the production rate by a factor $\sim$10. Secondly, a Multi-Lepton-Filter was applied to all background samples in event generation to increase the yield of background events that pass the analysis selection (described in Section 6.1).

To accurately reconstruct the signal and achieve the required level of background rejection, the analysis demands excellent performance from all the ATLAS sub-detectors. Accurate reconstruction of muons, electrons, hadronic taus, hadronic jets and missing energy is necessary. In particular, excellent performance from the hadronic tau identification (Tau-ID) and large rejection from the Lepton Isolation will be required to control the QCD background. Excellent resolution on the missing transverse energy measurement is required for accurate reconstruction of the invariant tau-tau mass and a good understanding of b-jet tagging will be necessary to take advantage of the presence of b-quarks in the b-quark associated Higgs boson production mode. The analysis will be run on the data streams written out by single electron and muon triggers and the performance of the triggers is included in the study. However, as trigger simulation was not available in ATLFAST-II the performance of the triggers had to be extracted from full simulated signal samples. As well as applying strict identification to the reconstructed objects, selection on event properties was also required to achieve adequate discrimination against the backgrounds. To achieve the best sensitivity, after a basic set of event selection criteria were applied, the analysis was split into two completely orthogonal sub-analyses using the number of b-tagged jets. The final set of selection criteria were optimised for each sub analysis and at each mass hypothesis. A statistical combination of the results from each sub-analysis was performed to achieve the best signal sensitivity.

The discovery potential for the $\ell\tau_h$ channel has been evaluated in previous studies, demonstrating adequate sensitivity for discovery or exclusion over a large region of the parameter space [54]. However, these studies were performed using now outdated software, without an estimation of the expected impact of systematic uncertainties or the inclusion of data-driven background estimation procedures. In this study, the impact of systematic uncertainties on the discovery potential was evaluated, and data-driven background estimation techniques were developed for all the major backgrounds. Furthermore, weighting procedures were developed to deal with the lack of MC background events that passed the strict object identification. For these backgrounds, the contribution estimated from the MC incurs a large statistical uncertainty and an estimate without such procedures would have been impossible.

The chapter is organised as follows. Section 6.1 describes the signal and background processes and the production of MC simulated samples. Section 6.2 describes the particle reconstruction and identification. A brief description of the evaluation of the trigger is also given at the end of the section, however, the final parameterisation was performed by Uli Felzmann. Section 6.3 describes the event selection. Section 6.4 describes the Tau-ID and Lepton Isolation Weighting procedures. Section 6.5 describes the estimation of the impact of systematic uncertainties. Section 6.6 describes the data-driven W and QCD background estimation procedures. Section 6.7 shows the final results including the calculation of the discovery potential of the A/H Higgs bosons using the analysis.

6.1 Signal and background processes

In this section, the production mechanisms of the Higgs bosons are discussed along with the Standard Model processes that form the major background contribution to the analysis. Cross sections for all processes are given, including theoretical uncertainties. MC simulated event samples were produced for each process and details regarding the event generation and simulation are given.

Although it is possible that SUSY processes could themselves contribute as backgrounds, the production cross sections are (in general) much lower than for the major SM backgrounds. Furthermore, the parameter space for such processes is largely unconstrained and it would be difficult to justify the resources needed to evaluate the processes as backgrounds for an analysis. Rather, if the processes do exist, they are likely to be discovered well before the A/H bosons, at which point a more serious study of their contribution could be made.

All MC simulated event samples were produced without pileup, largely due to the limited availability of computing resources. However, the effects of pileup on the analysis were considered and a brief description is given in Section 6.7.6.

6.1.1 Higgs boson production

The masses and couplings of all the MSSM Higgs bosons are defined at tree-level by m_A and $\tan\beta$. Figure 6.1 shows the masses of the neutral Higgs bosons as a function of m_A at $\tan\beta = 10$ and $\tan\beta = 50$. Below $m_A \sim 100$ GeV, m_A and m_h are degenerate, while m_H is large. However, for the mass range considered in this analysis, $150 \leq m_A \leq 800$ GeV, m_A and m_H are degenerate (to within 1 GeV), while m_h is well below m_A. Therefore the cross sections of the A and H bosons are added to obtain the total Higgs boson production cross section and the contribution from h is omitted. Thus the analysis is sensitive to the combined contributions of A and H, but has no sensitivity to h. It should be noted that although there is a possibility of small contributions from the h boson to enter into the analysis at low mass (due to limited invariant mass resolution), the cross section for h in this region is much smaller than for A and H. The contribution from h would also suffer much lower selection efficiencies due to the thresholds on the reconstructed objects (described in Section 6.2). An accurate

evaluation of the contribution would require dedicated production of signal samples at the h mass and will almost definitely have negligible effect, so was not included.
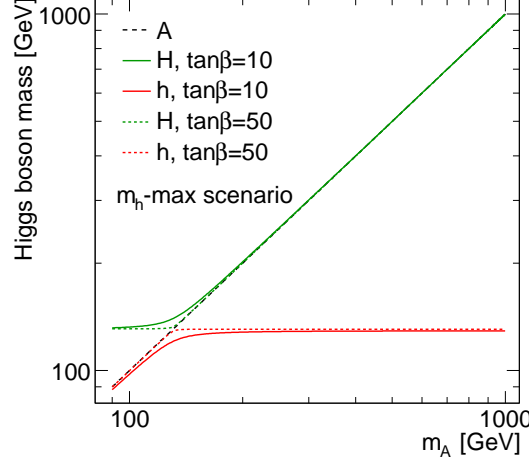
Figure 6.1: Masses of the neutral MSSM Higgs bosons as a function of m_A for values of $\tan\beta = 10$ and $\tan\beta = 50$. At low values of m_A, m_A and m_h are degenerate, while at high values of m_A, m_A and m_H are degenerate. The masses were calculated using the software `FeynHiggs 2.6.5` [55, 56, 57, 58].

Higgs boson production in the MSSM is dominated by b-quark associated production and gluon fusion. The Feynman diagrams contributing to each process are shown in Figure 6.2. Figure 6.3 shows the cross sections for each process in the m_h-max scenario as a function of m_A at $\tan\beta = 10$ and $\tan\beta = 50$. At small values of m_A both the b-quark associated and gluon fusion processes make similar contributions to the total cross section. However, the gluon fusion process falls more rapidly as m_A increases (especially at high $\tan\beta$) and becomes negligible above $m_A \sim 450$ GeV. Uncertainties on the signal cross sections are calculated in [1], which include uncertainties on the parton distribution functions and the factorisation and renormalisation scales. MC samples were generated for the b-quark associated signal production process at six mass hypotheses in the range 150 GeV $\leq m_A \leq 800$ GeV. Gluon fusion samples were produced at the four mass hypotheses with $m_A \leq 450$ GeV. Details on the samples are given in Tables 6.1 and 6.2.
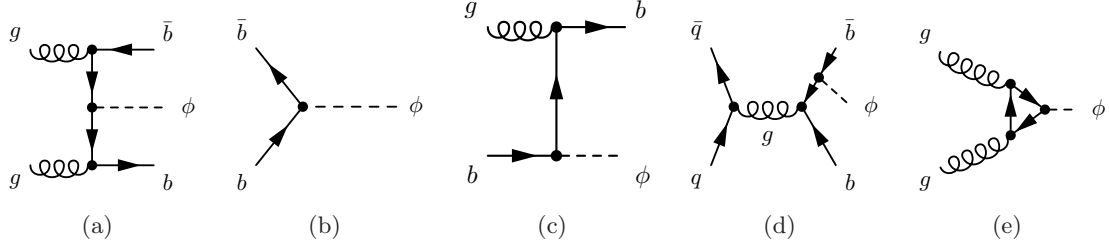
Figure 6.2: Feynman diagrams contributing to neutral MSSM Higgs boson production. Diagrams (a) through (d) contribute to the b-quark associated production and diagram (e) represents gluon fusion. In the diagrams ϕ represents any of the neutral Higgs bosons in the MSSM.
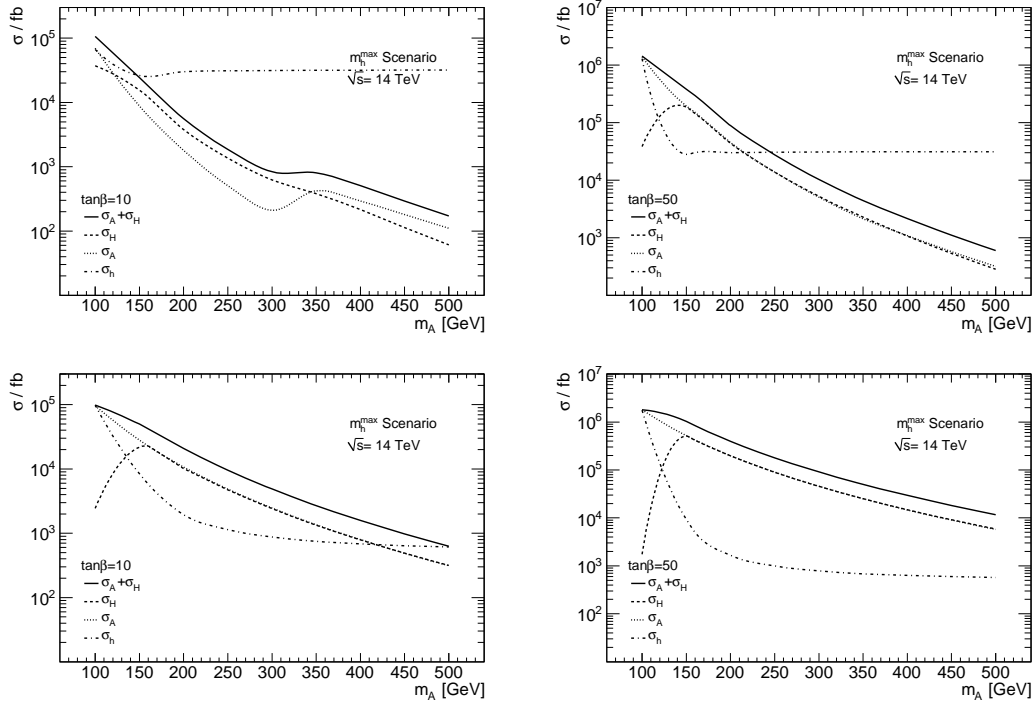
Figure 6.3: Production cross sections for the h (dash-dotted), H (dashed), and A (dotted) Higgs bosons as a function of m_A [1]. The combined cross section for the A and H bosons is also shown (solid). The cross sections for gluon fusion (top) and b-associated production (bottom) are given for $\tan\beta = 10$ (left) and $\tan\beta = 50$ (right).

Higgs boson samples (b-quark associated production)

DS-ID	m_A	σ_{prod} [pb]	$\Delta\sigma_{\mathrm{prod}}/\sigma_{\mathrm{prod}}$	$\sigma_{\mathrm{prod}} \times \mathcal{B}(\phi \to \tau\tau)$ [pb]	Events [k]
209500	150	199.22	0.196	18.61	600
209221	200	78.81	0.149	7.60	300
209123	300	18.16	0.101	1.61	60
209501	450	3.62	0.076	0.22	30
209502	600	1.04	0.064	0.048	30
209503	800	0.27	0.056	0.011	30

Table 6.1: Details for the signal samples where the Higgs bosons are produced via b-quark-associated production. The cross sections include contributions from both A and H and are calculated for $\tan\beta = 20$. $\Delta\sigma_{\mathrm{prod}}/\sigma_{\mathrm{prod}}$ is the total fractional theoretical uncertainty on the production cross section.

Higgs boson samples (gluon fusion)

DS-ID	m_A	σ_{prod} [pb]	$\Delta\sigma_{\mathrm{prod}}/\sigma_{\mathrm{prod}}$	$\sigma_{\mathrm{prod}} \times \mathcal{B}(\phi \to \tau\tau)$ [pb]	Events [k]
209510	150	77.77	0.120	7.27	300
209511	200	19.94	0.111	1.73	150
209512	300	2.06	0.103	0.19	30
209513	450	0.30	0.108	0.018	30

Table 6.2: Details for the signal samples where the Higgs bosons are produced via gluon fusion. The cross sections include contributions from both A and H and are calculated for $\tan\beta = 20$. $\Delta\sigma_{\mathrm{prod}}/\sigma_{\mathrm{prod}}$ is the total fractional theoretical uncertainty on the production cross section.

6.1.2 Background processes

This section describes the Standard Model processes that make up the major background for the analysis. Brief details of the MC simulated samples for each process are given and summarised in tables. The theoretical uncertainties on the production cross sections are given in Table 6.9.

$Z \to \tau\tau$

$Z \to \tau\tau$ is an irreducible background when the taus decay in the $\ell\tau_h$ mode. It is one of the largest backgrounds and suppression is ultimately limited by the invariant

mass resolution. However, there are typically no associated b-quarks. To cover the full mass range of the analysis with adequate statistical precision, three separate MC samples were simulated with a generator level filter applied to the invariant tau-tau mass requiring $m_{\tau\tau} > 60$ GeV, 150 GeV $< m_{\tau\tau} < 250$ GeV or 250 GeV $< m_{\tau\tau}$. Details on the samples are in given Table 6.3. A procedure was used to remove overlap between the samples, described in Section 6.7.2.

$t\bar{t}$

In $t\bar{t}$ events the top pair decays to $b\bar{b}$ and two on-shell W bosons with a branching fraction greater than 98%. The major contributions to the background of the analysis come from the irreducible $t\bar{t} \to b\bar{b}\ell\nu\tau\nu$ ($\mathcal{B} = 4.8\%$) and reducible $t\bar{t} \to b\bar{b}\ell\nu q\bar{q}$ ($\mathcal{B} = 28.8\%$) modes. A single fully inclusive MC simulated $t\bar{t}$ sample was produced. Details on the sample are given in Table 6.4.

W+jets

The $W \to e\nu, \mu\nu, \tau\nu$ modes contribute significantly to the analysis, forming the largest irreducible background. While the W decay provides a high p_T isolated lepton, a regular hadronic jet must be misidentified as a tau to mimic the signal. MC simulated samples for the three leptonic modes were produced. Details on the samples are given in Table 6.5.

QCD di-jets

The production of di-jet events through strong interactions in the proton-proton collisions at the LHC will occur at a rate $\mathcal{O}(10^{10})$ larger than the signal production. Although the typical signature of these events is very different to the signal, the sheer size of the background means that even small tail regions that mimic the signal can completely overwhelm it. Strict identification of both leptons and hadronic taus provides the best handle to suppress these events, by minimising contributions from fakes. An excellent understanding of the reconstruction algorithms will be critical in controlling the QCD background as even small uncertainties in the performance could lead to dangerous biases in the estimates of the background. Furthermore, it is impossible to simulate the equivalent number of di-jet events expected in $30\,\text{fb}^{-1}$ of ATLAS data.

To combat this, a number of techniques were used to obtain an accurate estimate of the QCD background. For the simulation, three different di-jet samples were produced. Firstly, generic unfiltered di-jet events were simulated. Although a complete estimate of the background from these events was impossible (as only a very small fraction of the total expected number of events could be produced), the events were used to evaluate the contribution from fakes. Secondly, di-jet events with a generator filter requiring at least one lepton with $p_\mathrm{T} > 15$ GeV were produced. These events comprise the vast majority of the QCD di-jet background, and were used to estimate the QCD di-jet background contribution. Finally, di-jet events containing the production of a $b\bar{b}$ pair were also simulated to improve the estimation of the background for the b-quark associated signal production. Each of the samples were divided into regions defined by the p_T generated in the hard $2 \to 2$ scattering process, which helps populate events with high transverse jet energies. Details on the samples are given in Tables 6.6 to 6.8.

$Z(\to \ell\ell)$+jets

$Z(\to \ell\ell)$+jets production creates a minor irreducible background to the analysis. Separate MC simulated samples for the e^+e^- and $\mu^+\mu^-$ channels were produced. Details on the samples are given in Table 6.3.

Single Top

Single top-quark production may contribute a minor background to the analysis, however, has not been considered for the analysis in the past and was not included in the MC production. Single top production can proceed through a number of channels including:

- $gb \to Wt$ ($\sigma_\mathrm{prod} = 66$ pb)

- t-channel $qb \to q't$ ($\sigma_\mathrm{prod} = 247$ pb)

- s-channel $q\bar{q} \to t\bar{b}$ ($\sigma_\mathrm{prod} = 11$ pb)

Details on the evaluation of single top are presented in Section 6.7.

Z samples

Process	Mass Range [GeV]	DS-ID	σ_{prod} [pb]	Filter	Efficiency [%]	Events [k]
$\gamma^*/Z \to ee$	$m_{ee} > 60$	209520	2015	MLF	79.90	2 000
$\gamma^*/Z \to \mu\mu$	$m_{\mu\mu} > 60$	209521	2015	MLF	78.94	2 000
$\gamma^*/Z \to \tau\tau$	$m_{\tau\tau} > 60$	209522	2015	MLF	15.20	2 000
$\gamma^*/Z \to \tau\tau$	$150 < m_{\tau\tau} < 250$	209523	7.21	MLF	29.19	200
$\gamma^*/Z \to \tau\tau$	$m_{\tau\tau} > 250$	209524	1.37	MLF	29.30	200

Table 6.3: Z samples.

$t\bar{t}$ samples

Process	DS-ID	σ_{prod} [pb]	Filter	Efficiency [%]	Events [k]
$t\bar{t}$	209550	833	MLF	49.259	7 000

Table 6.4: $t\bar{t}$ samples.

W samples

Process	DS-ID	σ_{prod} [pb]	Filter	Efficiency [%]	Events [k]
$W \to e\nu$	209530	20510	MLF	60.65	4 500
$W \to \mu\nu$	209531	20510	MLF	60.54	4 500
$W \to \tau\nu$	209532	20510	MLF	6.70	4 250

Table 6.5: W samples.

QCD di-jet samples (unfiltered)

Process	DS-ID	p_{T} range [GeV]	σ_{prod} [pb]	Filter	Efficiency [%]	Events [k]
QCD J2	205011	$35 - 70$	9.6 E7	NONE	–	400
QCD J3	205012	$70 - 140$	6.1 E6	NONE	–	400
QCD J4	205013	$140 - 280$	3.2 E5	NONE	–	400
QCD J5	205014	$280 - 560$	1.2 E4	NONE	–	400
QCD J6	205015	$560 - 1120$	3.4 E2	NONE	–	400

Table 6.6: Unfiltered QCD di-jet events. The p_{T} range indicates the generator cut on the p_{T} generated in the hard $2 \to 2$ scattering process.

QCD di-jet samples (filtered)

Process	DS-ID	p_T range [GeV]	σ_prod [pb]	Filter [k]	Efficiency [%]	Events [k]
QCD J2	209542	$35 - 70$	$9.6\,\mathrm{E}7$	MLF	0.24112	400
QCD J3	209543	$70 - 140$	$6.1\,\mathrm{E}6$	MLF	1.12106	200
QCD J4	209544	$140 - 280$	$3.2\,\mathrm{E}5$	MLF	2.89661	200
QCD J5	209545	$280 - 560$	$1.2\,\mathrm{E}4$	MLF	5.44532	200
QCD J6	209546	$560 - 1120$	$3.4\,\mathrm{E}2$	MLF	8.37902	200

Table 6.7: QCD di-jet events with Multi-Lepton-Filter (MLF). The p_T range indicates the generator cut on the p_T generated in the hard $2 \rightarrow 2$ scattering process.

$b\bar{b}$ QCD di-jet samples (filtered)

Process	DS-ID	p_T range [GeV]	σ_prod [pb]	Filter	Efficiency [%]	Events [k]
$b\bar{b}$ QCD J1	209641	$17 - 35$	$2.35\,\mathrm{E}7$	MLF	0.373	100
$b\bar{b}$ QCD J2	209642	$35 - 70$	$3.52\,\mathrm{E}6$	MLF	2.893	995
$b\bar{b}$ QCD J3	209643	$70 - 140$	$3.65\,\mathrm{E}5$	MLF	8.516	264
$b\bar{b}$ QCD J4	209644	$140 - 280$	$2.59\,\mathrm{E}4$	MLF	16.136	100
$b\bar{b}$ QCD J5	209645	$280 - 560$	$1.26\,\mathrm{E}3$	MLF	23.553	100
$b\bar{b}$ QCD J6x	209646	> 560	$4.03\,\mathrm{E}1$	MLF	29.635	100

Table 6.8: $b\bar{b}$ QCD di-jet events (MLF applied). The p_T range indicates the generator cut on the p_T generated in the hard $2 \rightarrow 2$ scattering process.

6.1.3 Event generation

A number of event generators were used in the production of the Monte Carlo samples. SHERPA 1.1 [59] was used to generate the signal samples and the W and Z backgrounds. PYTHIA 6.4.18 [60] was used to generate the QCD di-jet samples and MC@NLO 3.1 [61, 62] was used to generate the $t\bar{t}$ sample. All samples not generated with SHERPA used HERWIG 6.5.10 [63, 64] for the parton shower, TAUOLA [65] for tau decay and PHOTOS [66] for initial and final state radiation of photons. All event generation was run within ATHENA, release 14.2.25.6.

Theoretical uncertainties on background processes

Process	$Z(\rightarrow \ell\ell/\tau\tau)$	$W(\rightarrow \ell\nu/\tau\nu)$	$t\bar{t}$	QCD di-jets
$\Delta\sigma/\sigma$	0.03	0.03	0.12	0.50

Table 6.9: Theoretical uncertainties on the cross sections for the background processes.

6.1.4   Multi-Lepton Filter

A Multi-Lepton Filter (MLF) was applied to all backgrounds (except unfiltered QCD) in event generation. The filter requires at least one lepton (either e or μ) with $p_T > 15$ GeV (or 13 GeV for $t\bar{t}$) and $|\eta| < 2.7$ in the event. The filter can be applied since the overwhelming majority of background contributions to the analysis come from events containing a real lepton. The application of the filter reduces the production of useless background events, allowing the production of samples with an increased yield of events surviving the event selection in the given production time. The MLF was particularly useful in the evaluation of the QCD backgrounds, which would have been impossible otherwise.

6.1.5   Simulation

The simulation for all samples was performed with ATLFAST-II, run within ATHENA, release 14.2.25.8. The performance of ATLFAST-II has been extensively validated by the ATLFAST task-force [49], and has been shown to be in very good agreement with the standard GEANT4 simulation, especially in the energy regime of this analysis, which doesn't consider particles with E_T below 20 GeV. However, in the version of the ATLFAST-II software used for the production, simulation of the trigger system was not available. Two b-associated signal samples with $m_A = 150$ GeV and $m_A = 600$ GeV were produced with the full GEANT4 simulation to evaluate the trigger. The trigger menu for operation at $L = 10^{33}\,\mathrm{cm}^{-2}\mathrm{s}^{-1}$ was selected in the simulation.

6.2   Object selection

While the $A/H \rightarrow \tau(\rightarrow \ell\bar{\nu}_\ell\nu_\tau)\tau(\rightarrow \tau_h\nu_\tau)$ channel has a distinctive signature in the ATLAS detector, many Standard Model processes have similar signatures that form the background for the analysis. An accurate reconstruction of the signal with adequate suppression of the various backgrounds requires excellent performance from all ATLAS reconstruction algorithms. For this reason, this analysis has been used as a benchmark to evaluate the performance of the various reconstruction algorithms throughout the history of ATLAS.

The leptonic tau decay produces a high p_T lepton that is isolated from hadronic jet activity. The isolated lepton not only provides a trigger for the event, but also very strong discrimination against QCD di-jet events, where the only source of real leptons comes from the small fraction of events containing heavy quark decays. In these events, the lepton is usually surrounded by hadronic activity, so the degree of isolation can be used to control the size of the QCD background. The leptons are reconstructed with the standard ATLAS electron and muon reconstruction algorithms, and good performance is required to control contamination from fake and non-isolated leptons. The hadronic tau decay is reconstructed with the standard ATLAS hadronic tau reconstruction and excellent performance is required to discriminate against backgrounds containing fake taus. The neutrinos from the tau decays result in a large amount of missing transverse energy, which needs to be measured with exceptional precision by the ATLAS missing energy reconstruction algorithm to correctly reconstruct the invariant mass of the Higgs boson. The presence or absence of b-quarks in the signal can be used to discriminate against the backgrounds. The b-quarks are reconstructed by the standard ATLAS jet reconstruction and a flavour tagging algorithm is used to separate them from generic hadronic jets. A good understanding of the b-jet tagging and mistagging rates is required.

In this analysis, all objects including: muons, electrons, hadronic tau jets, jets and missing transverse energy were reconstructed using the standard ATLAS reconstruction algorithms. Selection was applied to the reconstructed candidates to minimise the contamination due to misidentification. In particular, the lepton and tau selection was optimised for high rejection against fake taus and fake and non-isolated leptons, which was crucial in reducing the overwhelming QCD background that can have a production

cross section $\mathcal{O}(10^{10})$ larger than the signal. This resulted in extremely large rejection factors for QCD and the other backgrounds that do not contain real taus (e.g. W+jets and $Z(\to \ell\ell)$+jets). As a consequence, many of these backgrounds contained little or no events after the lepton and tau selection was applied. Unfortunately, for many of the background processes it was impossible to produce equivalent numbers of MC simulated events as expected in $30\,\text{fb}^{-1}$ of collision data. For these processes, the statistical uncertainty on the estimate of the contribution following the event selection was far too large to make a direct evaluation. To combat this, a weighting procedure was developed where a looser selection was applied for leptons and taus in the analysis and the objects were weighted by the measured efficiency of the full selection. The procedure is described in Section 6.4. The electron, muon and tau selection described in this section is split into a loose set of criteria (pre-selection) and the remaining criteria (event-selection) accordingly.

6.2.1 Muon reconstruction

In ATLAS, a number of specialised tracking algorithms have been developed to reconstruct tracks in the muon spectrometer. These algorithms can be used for standalone muon reconstruction or can be combined with the standard track reconstruction in the inner detector. In this analysis, muons were reconstructed by the `STACO` reconstruction algorithm. `STACO` performs a statistical combination of tracks reconstructed in the muon spectrometer and tracks from the inner detector. Firstly, the tracks from the the muon spectrometer are extrapolated back to the impact point, then an attempt to merge the track to inner detector tracks is made using a statistical combination of their track parameters and covariance matrices. Tracks are merged if they pass a set of basic quality criteria. Only `STACO` candidates that were successfully merged and where the choice of inner detector track resulted in the best possible match with the muon spectrometer track were accepted, indicated by the `isCombined` flag. An additional criterion was applied to the quality of the merged candidate (as recommended by the combined muon performance group of ATLAS), requiring that the matching $\chi^2_{\text{match}}/\text{n.d.f}$, defined as the difference in the track parameters from the two measurements weighted by their covariance matrices and divided by the number of degrees of freedom, be less than eight. The candidates were required to have $p_{\text{T}} > 24$ GeV, which is largely bounded from below by the threshold on the muon trigger and also by

the need to suppress background contributions from QCD di-jets where the muon p_T distribution rises exponentially with decreasing p_T. The candidate was also required to have $|\eta| < 2.5$ so as to be within the inner detector tracking volume. This constituted the *pre-selection* applied to muons. On top of the *pre-selection*, strict isolation was applied in the *event-selection*, which is described in Section 6.2.3. The muon selection is summarised in Table 6.10. Figure 6.4 shows the performance of the muon selection for real isolated muons in the signal and non-isolated muons in QCD.

Muon selection		
Pre-selection	Kinematic	$p_\mathrm{T} > 24$ GeV, $|\eta| < 2.5$
	Quality	`isCombined`
		$\chi^2_\mathrm{match}/\mathrm{n.d.f} < 8$
Event-selection	Isolation	$E_\mathrm{T}^{\Delta R < 0.2}/p_\mathrm{T} < 0.1$
		$N_\mathrm{tracks}^{\Delta R < 0.3} < 2$

Table 6.10: Muon selection. A standard set of kinematic and quality requirements are applied in the pre-selection, while strict isolation is applied in event-selection for large rejection against the QCD di-jet background. The isolation variables are defined in Section 6.2.3.

6.2.2 Electron reconstruction

ATLAS employs a number of electron reconstruction algorithms with differing purposes. High p_T isolated electrons are best reconstructed with the standard electron reconstruction, which is seeded by electromagnetic calorimeter clusters reconstructed by a sliding window algorithm with an E_T threshold of 3 GeV [36]. Electron candidates were required to be reconstructed by the standard reconstruction, indicated by the `AuthorElectron` flag. Reconstructed tracks within a small distance in η-ϕ space are associated to the cluster and the closest is considered the best match. The tracking, shower shape and more general calorimeter information is combined to construct a cut based discriminant for rejection against fake electron candidates, in particular charged pions. The variable is called `isEM` and can be set at a number of discrete levels, which trade off real electron selection efficiency with fake electron rejection. In the pre-selection `isEM::ElectronMediumNoIso` was used, and in event-selection `isEM::ElectronTight` was used for large rejection against fake electron candidates
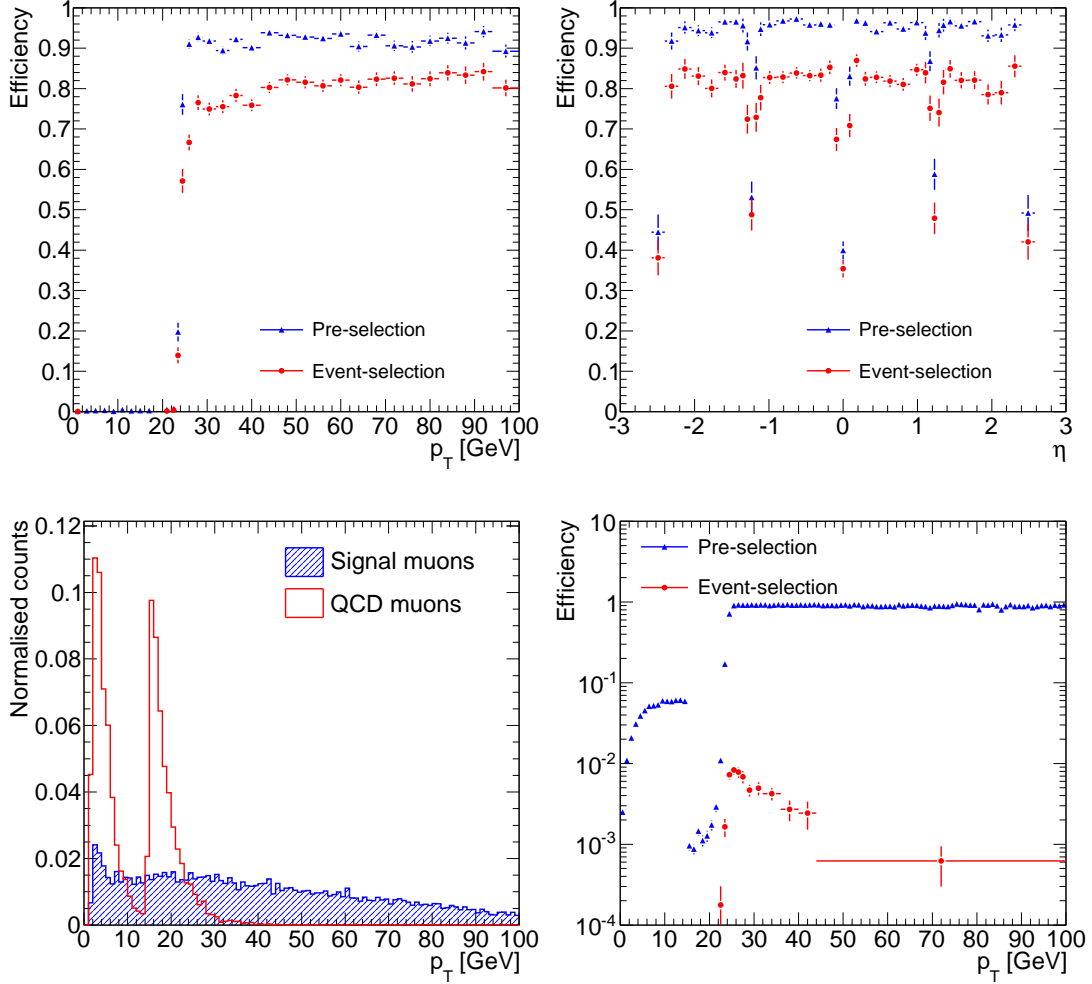
Figure 6.4: Muon reconstruction performance. The selection efficiencies for real isolated muons in the signal (top) are shown as functions of p_T (left) and η (right). The p_T distribution of muons that pass the event-selection in the signal and QCD samples is shown on the bottom-left (without the selection on p_T itself). The sharp rise at ∼15 GeV in QCD is caused by the MLF generator filter. The contribution from muons in QCD rises dramatically at low p_T and the 24 GeV threshold is crucial for the suppression of QCD. The selection efficiency for muons in QCD is shown on the bottom-right. Large suppression is achieved by applying the full muon event-selection.

in the QCD di-jet background. Kinematic cuts of $E_T > 24$ GeV and $|\eta| < 2.5$ were applied in pre-selection, and isolation similar to the muon isolation was applied in event-selection, described in Section 6.2.3. The electron selection is summarised in Table 6.11. Figure 6.5 shows the performance of the electron selection for real isolated electrons in the signal and non-isolated electrons in QCD.

Electron selection

Pre-selection	Kinematic	$E_T > 24$ GeV, $|\eta| < 2.5$
	Algorithm	`AuthorElectron`
	Quality	`isEM::ElectronMediumNoIso`
Event-selection	Isolation	$E_T^{\Delta R < 0.2}/p_T < 0.1$
		$N_{\text{tracks}}^{\Delta R < 0.3} < 2$
	Quality	`isEM::ElectronTight`

Table 6.11: Electron selection. A standard set of kinematic and quality requirements are applied in the pre-selection, while strict isolation is applied in event-selection for large rejection against the QCD di-jet background. The isolation variables are defined in Section 6.2.3

6.2.3 Lepton Isolation

The ability to control the overwhelming QCD background is essential in this analysis. While the signal has a cross section of order 1 pb for moderate values of $\tan \beta$, the cross section for QCD di-jet events[1] is approximately 10^8 pb. Thus, a huge suppression of the QCD events is required for any chance of observing the signal. By requiring at least one pre-selected lepton in the QCD events, the cross section is reduced to $\sim 10^4$ pb, however, this suppression alone is insufficient. In the remaining events, the lepton candidates are almost categorically due to real leptons produced in heavy quark decays, or fake electrons from charged pions.

The contribution from fake electrons can only be estimated from the unfiltered QCD samples. This presents a problem, as it is impossible to simulate an adequate number of unfiltered events to make a direct evaluation. Instead, the ratio of fake electrons (estimated from the unfiltered QCD samples) to real electrons (estimated from the filtered QCD samples) was used to scale the contribution from the filtered

---

[1] All QCD di-jet events with $p_T > 35$ GeV generated in the $2 \to 2$ scattering process.
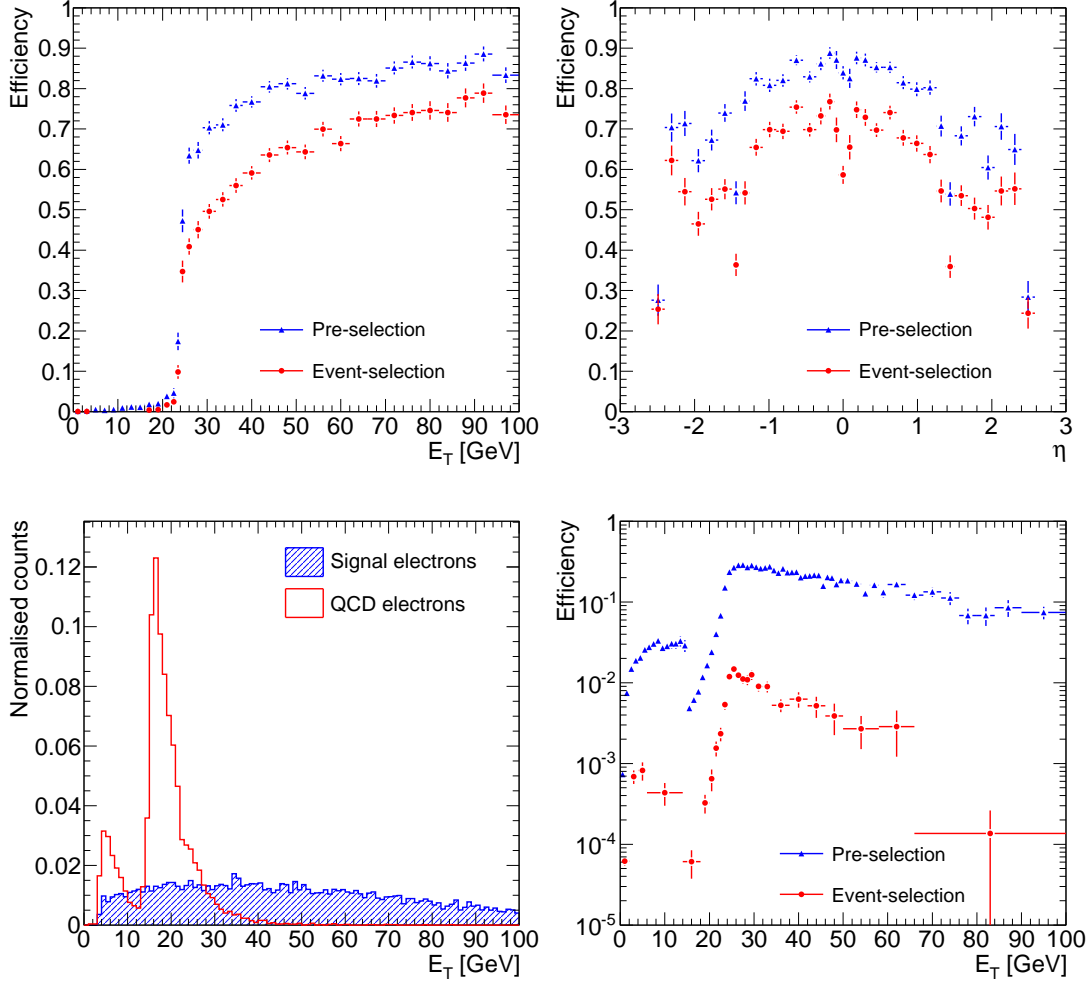
Figure 6.5: Electron reconstruction performance. The selection efficiencies for real isolated electrons in the signal (top) are shown as functions of E_T (left) and η (right). The E_T distribution of electrons in QCD that pass the event-selection is shown on the bottom-left (without the selection on p_T itself). The sharp rise at ∼15 GeV is caused by the MLF generator filter. The contribution from electrons in QCD rises dramatically at low E_T and the 24 GeV threshold is crucial for the suppression of QCD. The selection efficiency for electrons in QCD is shown on the bottom-right. Large suppression is achieved by applying the full electron event-selection.

QCD samples, which can be measured. Therefore controlling the fake contribution is extremely important, not only to suppress the QCD background, but also to keep the uncertainties from the scaling method as small as possible. Table 6.12 shows the number of real and fake electrons expected in $30\,\mathrm{fb}^{-1}$ from the unfiltered QCD di-jet events. The contribution from fake electrons can be strongly suppressed with the standard electron discriminant `isEM::ElectronTight`, and appears to be negligible after the isolation in the electron event-selection is applied, with real electrons contributing 99.9±0.1%. However, this fraction and its associated binomial uncertainty are misleading. The total sample size of real and fake electrons in the calculation was very small and the only fake electrons came from the higher E_{T} di-jet samples, which have much smaller weighting due to their lower cross sections. While this can cause the binomial uncertainty to be very small, a statistically independent sample of similar size at the lowest di-jet energy could contain one or more fake electrons that passed the event-selection causing a much different result. So as not to underestimate the fake electron contribution, the expected number of events in $30\,\mathrm{fb}^{-1}$ containing at least one pre-selected electron that also passed `isEM::ElectronTight` were counted in the filtered and unfiltered QCD samples. The filtered sample was found to account for 75% of the unfiltered sample. This conservative estimate was used to scale the result calculated from the filtered samples.

Fake electron contribution

Selection	$N_{\mathrm{Real}}(30\,\mathrm{fb}^{-1})$	[%]	$N_{\mathrm{Fake}}(30\,\mathrm{fb}^{-1})$	[%]
Pre-Selection	(4.8 ± 0.5)E8	44±4	(6.0 ± 0.6)E8	56±4
`isEM::ElectronMedium`	(2.7 ± 0.4)E8	53±5	(2.4 ± 0.4)E8	47±5
`isEM::ElectronTight`	(2.1 ± 0.4)E8	83±6	(4.2 ± 1.6)E7	17±6
Event-Selection	(2.9 ± 1.4)E7	99.9±0.1	(2.7 ± 2.3)E4	0.1±0.1

Table 6.12: Number of real and fake electrons expected in $30\,\mathrm{fb}^{-1}$ from unfiltered QCD di-jet events. The numbers correspond to the total number of reconstructed electrons that pass the pre-selection, `isEM::ElectronMedium`, `isEM::ElectronTight` and the event-selection, applied in succession. The fraction of the total contribution is also given. After applying the `isEM::ElectronTight` identification the fake contribution is reduced to 17%, and after the full isolation in the event-selection is applied, the contribution from fakes is negligible.

As mentioned previously, leptons produced in heavy quark decay are usually surrounded by large amounts of hadronic activity, while leptons produced in leptonic tau-decays are usually well isolated in the detector. To suppress the contribution from leptonic quark decay, two types of isolation criteria were considered, each of which measure the amount of activity inside a cone around the lepton candidate:

1. calorimeter isolation

2. track isolation.

In the calorimeter isolation the E_T of cells within a cone was summed and cells associated to the candidate were subtracted to improve discrimination. For muons, calorimeter cells above a 3.6σ noise threshold within the cone were included, while cells within a small cone $\Delta R < 0.05$ around the track were associated to the candidate and excluded from the calculation. For electrons, all cells within the cone were included, except those from the 3rd layer of the hadronic tile calorimeter and a core region of 7×5 cells in η-ϕ space associated to the candidate.

In the track isolation, the number of tracks within a cone around the candidate were counted. The tracks were required to pass the following set of quality criteria:

$$
\begin{aligned}
p_\mathrm{T} &> & 1\,\mathrm{GeV} \\
d_0^\mathrm{IP} &< & 10\,\mathrm{mm} \\
z_0^\mathrm{IP} &< & 10\,\mathrm{mm} \\
n(\text{silicon hits}) &\geq & 4
\end{aligned}
$$

where d_0^IP and z_0^IP are the impact parameters measured with respect to the primary vertex of the candidate and $n(\text{silicon hits})$ is the number of hits in silicon tracking detectors associated to the track. For electrons, the candidate track was not included when counting, however, for muons the candidate track was included[1]. A number of other isolation discriminants can be calculated with the track information, such as the sum of track p_T or the p_T sum weighted by the distance from the candidate, however, these quantities are highly correlated to the two chosen variables and add almost no extra discrimination.

---

[1]The different treatment of muon and electron candidates was merely an artefact of the tool used for track isolation and has no physical motivation.

Figure 6.6 shows the performance of the track and calorimeter isolation for a number of different cone sizes. The two isolation criteria provide complimentary performance for discrimination against non-isolated leptons. While the calorimeter isolation is sensitive to both charged and neutral particles, it is highly susceptible to contamination from extra detector activity. It is expected that the performance of the calorimeter isolation will be significantly degraded at high luminosity due to pile-up. In particular, the larger cone sizes suffer much larger levels of contamination. On the other hand, the track quality selection used in the track isolation allows the selection of tracks based on their separation from the candidate track at the impact point. This is extremely useful for removing tracks from overlapping events, as the longitudinal distance over which interactions occur is Gaussian distributed with a standard deviation of 5.6 cm, meaning that most overlapping collisions will be well separated in the z direction. Figure 6.7 shows the separation in the z direction of adjacent $p\bar{p}$ bunch crossings at the LHC for two luminosity settings, taken from [67]. The publication indicates that the probability of two adjacent bunch crossings to be separated by less than $z_0^{\mathrm{IP}} = 5$ mm is $\sim 10\%$ for $L = 2 \times 10^{33}\,\mathrm{cm^{-2}s^{-1}}$. Therefore the selection used in the track isolation should control the contamination from pile-up reasonably well as the analysis is only intended to run up to a maximum luminosity of $10^{33}\,\mathrm{cm^{-2}s^{-1}}$. Thus it is possible to use a larger cone size and stricter selection criteria for the track isolation. However, as the track isolation is only sensitive to charged particles, a combination of both track and calorimeter isolation gives the best performance. To avoid significant loss of signal, a small cone size of $\Delta R < 0.2$ was chosen for calorimeter isolation, while a cone size of $\Delta R < 0.3$ was chosen for track isolation. Figures 6.8 and 6.9 show the isolation variables for muons and electrons, respectively. The calorimeter isolation is normalised by the p_{T} of the candidate, which not only provides better discrimination than the unnormalised quantity, but also more constant performance over a large range of candidate p_{T}. A track isolation criteria of $N_{\mathrm{tracks}}^{\Delta R < 0.3} < 2$ and a calorimeter isolation of $E_{\mathrm{T}}^{\Delta R < 0.2}/p_{\mathrm{T}} < 0.1$ were found to be optimal for both muon and electron candidates.

6.2.4 Hadronic tau reconstruction

ATLAS has developed two complimentary hadronic tau reconstruction algorithms, as described in Chapter 4. In the Athena release used for the reconstruction of the MC simulated samples, the two algorithms were merged. The merged algorithm begins by
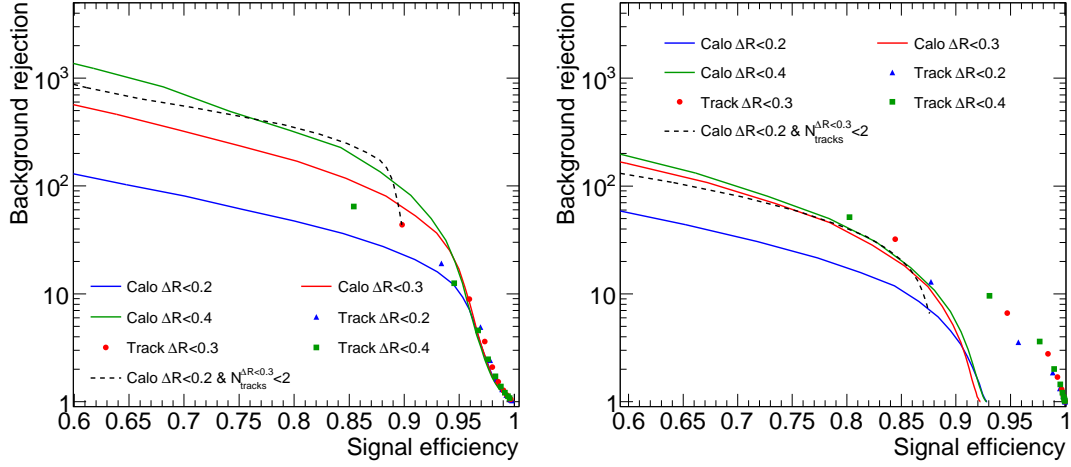
Figure 6.6: Performance of the track and calorimeter isolation for a number of cone sizes, for muons (left) and electrons (right). Performance improves with increasing cone size, however, the larger cones will suffer larger degradation in performance due to pile-up. The dashed line indicates the combination of the $N_{\text{track}}^{\Delta R < 0.3} < 2$ selection used in the analysis with selection on $E_T^{\Delta R < 0.2}/p_{\text{T}}$. By combining track and calorimeter isolation with smaller cone sizes, good suppression of non-isolated leptons in QCD events can be obtained, which should be robust under pile-up conditions. The performance for muons is much better than for electrons. In fact, a significant number of signal electrons have p_{T} lower than the summed energy from the calorimeter isolation, causing an $\sim 8\%$ signal loss whenever the calorimeter isolation is used.
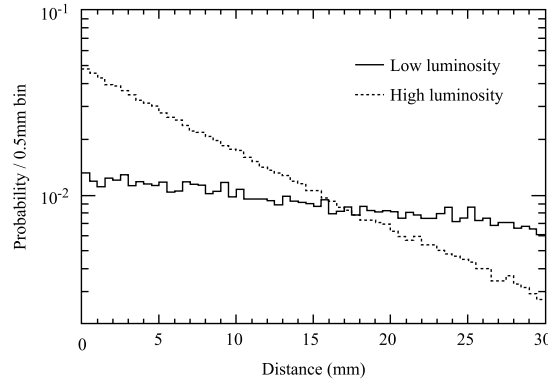
Figure 6.7: Separation of adjacent $p\bar{p}$ collisions in the z direction at low luminosity $(2 \times 10^{33}\,\text{cm}^{-2}\text{s}^{-1})$ and high luminosity $(10^{34}\,\text{cm}^{-2}\text{s}^{-1})$ for bunch crossings with two or more interactions [67].

111
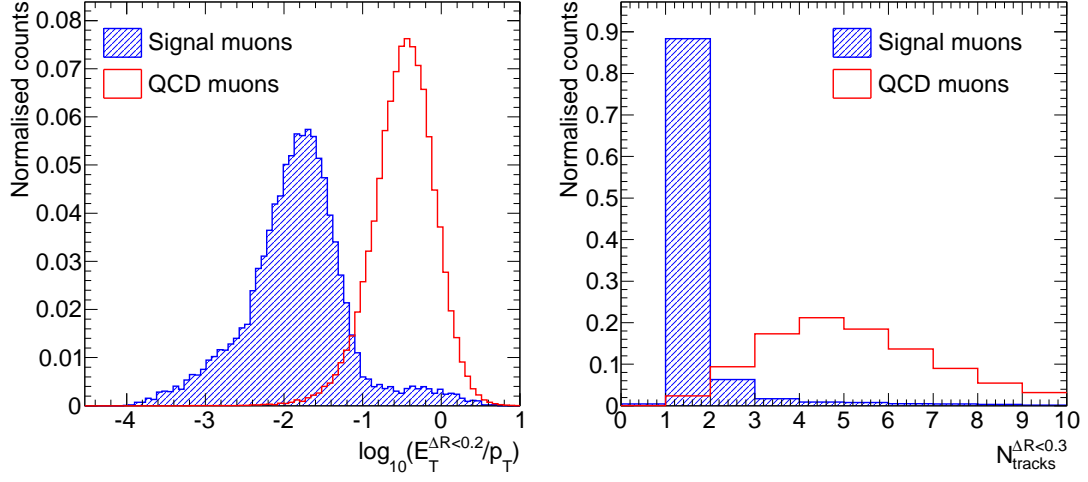
Figure 6.8: Muon isolation variables. The calorimeter isolation using a cone size of $\Delta R < 0.2$ is shown on the left and the track isolation using a cone size of $\Delta R < 0.3$ is shown on the right.
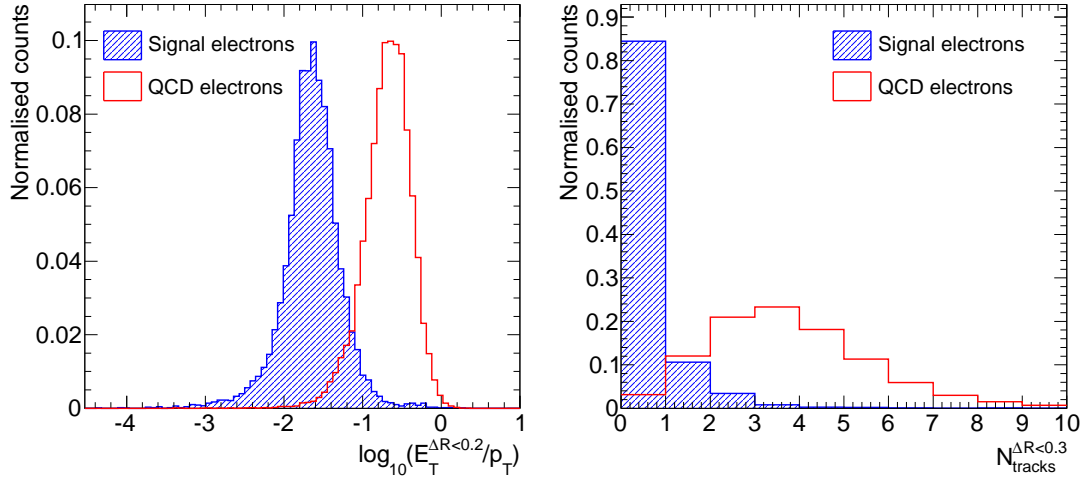
Figure 6.9: Electron isolation variables. The calorimeter isolation using a cone size of $\Delta R < 0.2$ is shown on the left and the track isolation using a cone size of $\Delta R < 0.3$ is shown on the right.

defining a set of good quality tracks (with $p_\mathrm{T} > 6$ GeV) and topological calorimeter clusters (with $E_\mathrm{T} > 10$ GeV) as seeds. The track-based reconstruction is run first (over the track-seeds), providing a set of track-based candidates. A search for calo-seeds within a cone of $\Delta R < 0.2$ around the candidate is performed. If no match is found the candidate is a track-based only candidate. If a match is found, the calo-based reconstruction is also run creating an overlap candidate. Finally, the calo-based reconstruction is run over the remaining unmatched calo-seeds, creating a set of calo-based only candidates. For the track-only and calo-only candidates all the information from reconstruction is calculated and stored as usual. However, for the overlap candidates, the E_T is taken from the calo-based reconstruction and the η, ϕ, charge and number of associated tracks are taken from the track-based reconstruction. In addition, a new likelihood function for discrimination against QCD jets is defined for overlap candidates, which uses information from both the track-based and calo-based algorithms.

For this analysis, tau candidates were required to be reconstructed by both algorithms, which provides good discrimination against QCD jets (especially near the E_T threshold) and allowed the use of the new combined likelihood. Candidates were required to pass a loose kinematic selection, including $E_\mathrm{T} > 24$ GeV and $|\eta| < 2.5$, and were also required to have a charge magnitude of one. Dedicated vetoes were used to remove fakes from electrons and muons. The selection thus far, called *loose pre-selection*, was applied to all candidates. From this point the selection was divided into two further classifications: tight pre-selection and event-selection, required to perform the Tau-ID Weighting procedure described in Section 6.4. In the tight pre-selection, candidates were required to have either one or three charged tracks, and pass a flat selection on the likelihood of $\log_{10}(\mathrm{Likelihood}) > 3$. In the event-selection, an E_T-dependent threshold on the likelihood was applied to achieve a relatively flat 70% signal identification efficiency with respect to the loose pre-selection. The optimisation was performed in the same bins used to construct the likelihood function itself. Table 6.13 summarises the hadronic tau selection. Figure 6.10 shows the performance of the tau selection for real taus in the signal and fake taus in QCD.

In addition to the generic hadronic tau selection described here, stricter selection was used throughout the analysis to achieve increased discrimination against the various backgrounds. This included increased thresholds on the tau E_T and the use of only 1-prong taus, which have much lower contamination from fakes.
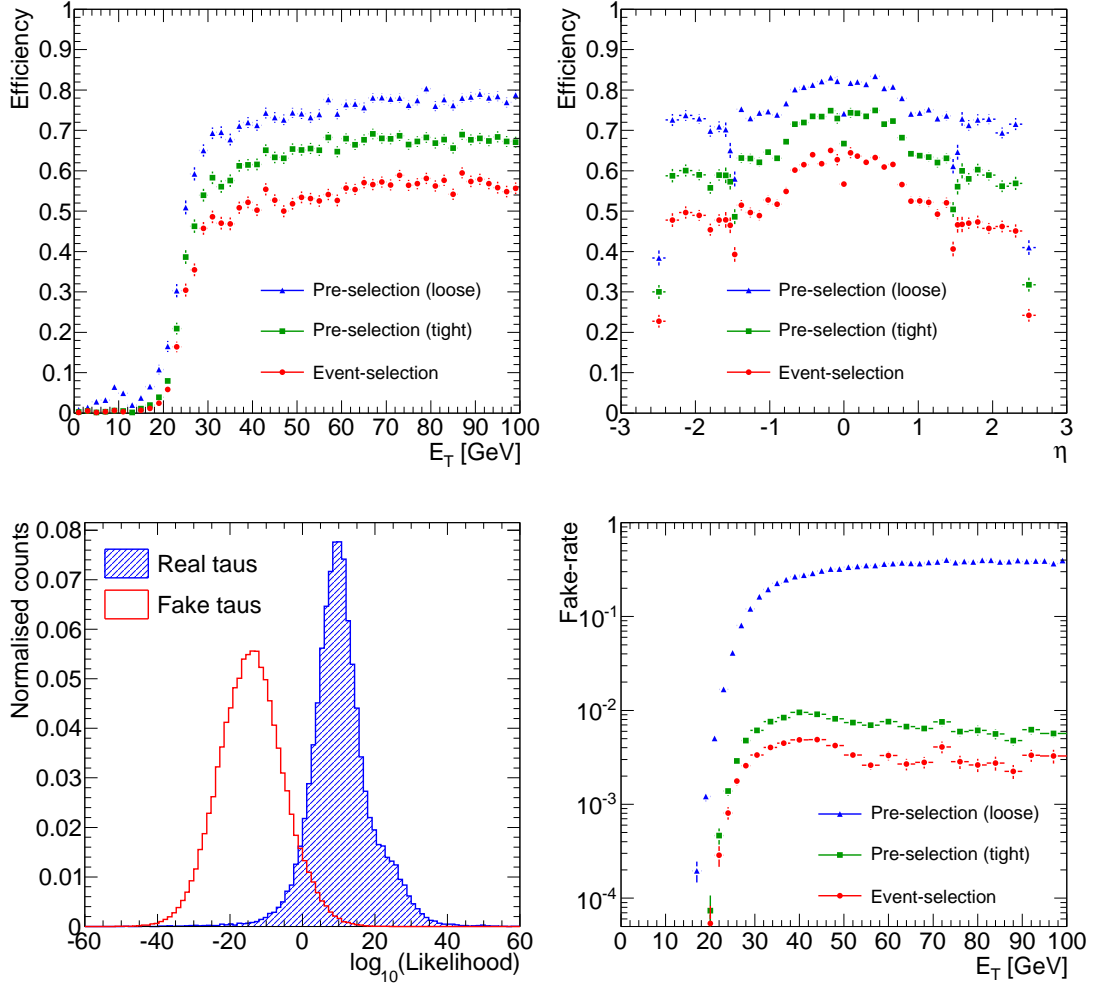
Figure 6.10: Hadronic Tau reconstruction performance. The selection efficiencies for real taus in the signal (top) are show as functions of E_T (left) and η (right). The likelihood distribution for real and fake taus is shown on the bottom-left. The selection efficiency for taus in QCD is shown on the bottom-right. Large suppression was achieved by applying the full tau event-selection.

		Hadronic tau selection
Pre-selection (loose)	Kinematic	$E_\mathrm{T} > 24$ GeV, $|\eta| < 2.5$
	Algorithm	track-based & calo-based
	Vetoes	`ElectronVeto` & `MuonVeto`
	Quality	$|\mathrm{charge}| = 1$
Pre-selection (tight)	Quality	1 or 3 tracks
		LLH > 3
Event-selection	Quality	24 GeV $< E_\mathrm{T} < 45$ GeV: LLH > 5.5
		45 GeV $< E_\mathrm{T} < 70$ GeV: LLH > 6.7
		70 GeV $< E_\mathrm{T} < 100$ GeV: LLH > 6.0
		100 GeV $< E_\mathrm{T}$: LLH > 7.5

Table 6.13: Hadronic tau selection. The selection is split into three levels to accommodate the Tau-ID Weighting procedure. The loose pre-selection is applied to all candidates, while the further selection is parameterised and applied as weights in some event samples. The event-selection includes the E_T dependent selection on the log-likelihood (LLH).

6.2.5 Jet reconstruction

Jets of hadronic particles are produced in copious quantities at the LHC. The jets are formed in the hadronisation of quarks and gluons, which do not exist as free particles at low energy densities. The only way to access these particles is to reconstruct their hadronic jets. In particular, jet reconstruction was used in this analysis to reconstruct b-quarks, and also as a means of discrimination against processes with large jet activity, such as $t\bar{t}$.

Jet reconstruction in ATLAS is divided into three stages. Firstly, the calorimeter cells are combined into *towers* or *topoclusters*. The tower combines the cells from all calorimeter layers within a fixed size window defined in η-ϕ space (of fixed dimension 0.1×0.1), resulting in a rigid two-dimensional structure. On the other hand, the *topological* clustering algorithm creates a dynamic three-dimensional cluster by grouping cells based on their nearest neighbour relations and on the significance of their energy content with respect to the cell noise, σ_noise (including electronic noise and eventually pile-up noise). The topoclusters are seeded by cells where the energy deposited is above the threshold $|E_i| > 4\sigma_\mathrm{noise}$. Neighbouring cells with $|E_i| > 2\sigma_\mathrm{noise}$ are added iteratively and finally, all neighbours of the accumulated cells are added to obtain the final cluster.

The topological clustering algorithm reflects the shape of showers in the calorimeter more accurately and provides much better suppression of calorimeter noise than the tower algorithm. The topological clustering algorithm superseded the tower algorithm and is now widely used as the default algorithm in ATLAS. The switch from the use of tower jets to topological jets as seeds to the calo-based tau reconstruction was the main motivation to re-parameterise the performance of the calo-based algorithm for ATLFAST-I, as described in Section 5.3.

The clusters are then used as input to jet finding algorithms, which attempt to combine clusters into well defined jets that accurately represent the contributions from the initial partons. In this analysis, topological clusters were used as input to a seeded iterative cone jet finding algorithm with cone size $\Delta R < 0.4$. The algorithm uses high E_T clusters as seeds. A cone is defined around the seed, and an attempt is made to merge other clusters within the cone above a given E_T threshold. After a new cluster is merged, the position of the cone is recalculated, and the procedure repeated until no more clusters above threshold are found in the cone. Seeded cone algorithms have been widely used in ATLAS, since their fixed size makes them easy to use in an experimental environment. However, seeded cone algorithms have a number of unfavourable attributes which have led the ATLAS collaboration to abandon them in favour of the new anti-k_t algorithm [68], which will be used for the analysis of the first data from the LHC [69]. Although a change in the jet finding algorithm will be required when the current analysis is performed on collision data, the effect is expected to be minimal as a detailed treatment of jets is not crucial to the analysis. On the other hand, the calo-based tau reconstruction will also change to be seeded by the anti-k_t algorithm, which may have a larger effect on the analysis.

The final stage of jet reconstruction is a hadronic energy calibration (see Section 4.2). In this analysis an H1-style energy calibration was used, which weights the cell energy according to the cell energy density and applies a final correction to ensure that the jet energy is properly reconstructed. The jets were then required to have $E_T > 20$ GeV and $|\eta| < 5$.

6.2.6 *b*-tagging

The identification of jets that originate from the fragmentation and hadronisation of *b*-quarks (*b*-tagging) can help discriminate against various backgrounds. When *b*-quarks

are produced in interactions they fragment to form b-hadrons. Due to the lifetime of the b-quark, the b-hadron travels an average distance of $3\,\mathrm{mm}$ before decaying. The b-quark decays through the weak interaction preferentially into a c-quark, forming a c-hadron with an additional W boson decay. Due to the large mass of the b-quark the decay products can have large momentum transverse to the b-hadron flight path providing a very distinct signature. In contrast, jets initiated by light quarks or gluons (light jets) generally hadronise into stable particles at the interaction point, and don't contain the rich structure of the b-decay chain. The ATLAS b-tagging algorithms use tracking information to try and discriminate between the two signatures.

Track impact parameters can provide very good identification of b-jets. In particular, the significance of the transverse and longitudinal impact parameters, $d0/\sigma_{d0}$ and $z0/\sigma_{z0}$, provide the best discrimination. The IP3D b-tagging algorithm combines the significance of the longitudinal and transverse impact parameters of all the tracks inside a jet into a discriminant. The reconstruction of the b-hadron vertex can also provide good identification of b-jets. The SV1 secondary vertexing algorithm attempts to reconstruct the decay chain of the b-hadron including the subsequent decay of the c-hadron daughter. From the reconstruction three parameters are built to discriminate against light jets. PDFs of the parameters constructed by both the IP3D and SV1 algorithms are constructed by training on b-jet and light jet samples. The PDFs are used to construct a likelihood ratio, w, called the *heavy flavour weight*, which was used in the analysis for the selection of b-jets. Pre-selected jets with a heavy flavour weight, $w > 4$ were tagged as b-jets. Figure 6.11 shows the performance of the b-tagging. The selection provides $\sim 50\%$ b-tagging efficiency with a rejection of ~ 700 for light jets. Table 6.14 summarises the selection for jets and b-tagging.

<div align="center">

Jet selection and b-tagging

Pre-selection	Kinematic	$E_\mathrm{T} > 20$ GeV, $|\eta| < 5$
	Clustering	topological
	Jet Finding	seeded cone $\Delta R < 0.4$
	Calibration	H1-style
b-tagging	IP3D+SV1	$w > 4$

</div>

Table 6.14: Jet selection and b-tagging.
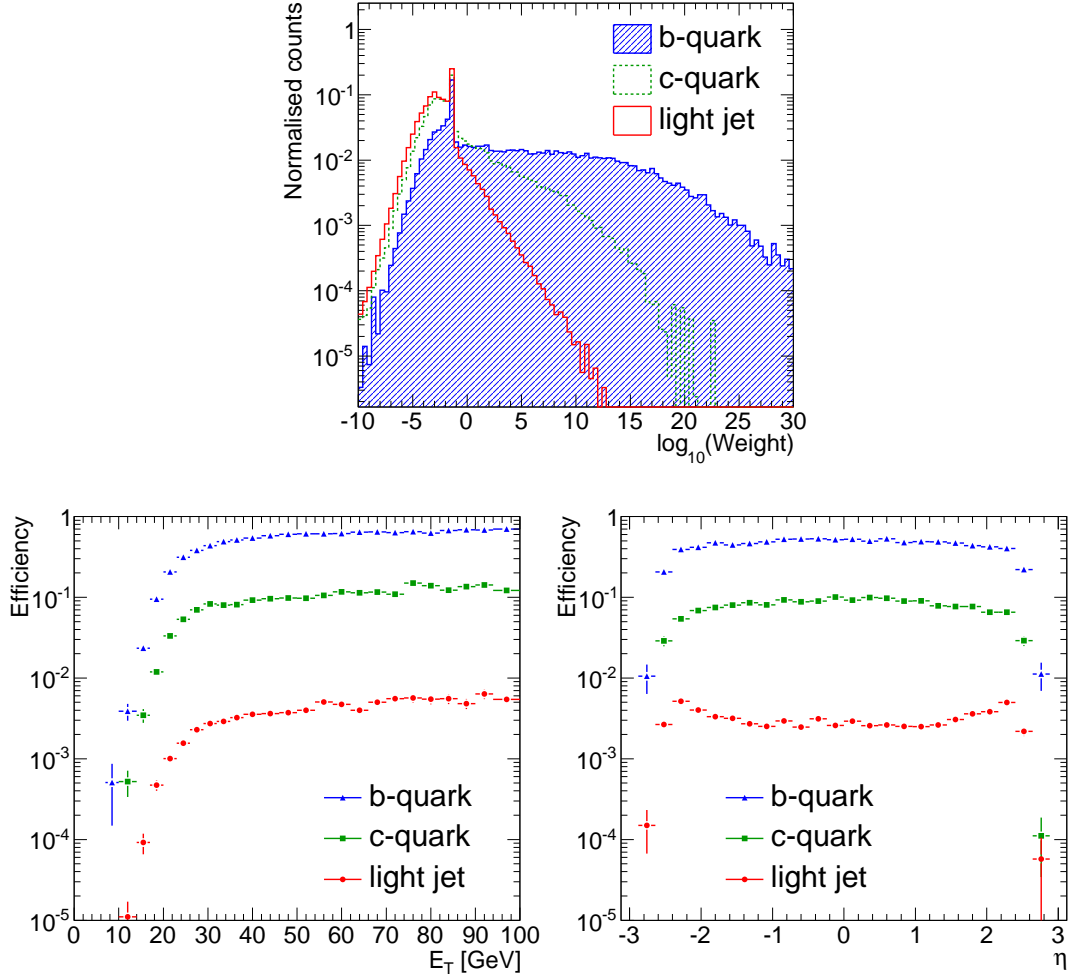
Figure 6.11: *b*-tagging performance. The *b*-tagging weight calculated from a combination of the IP3D and SV1 algorithms is shown for *b*-quark and *c*-quark initiated jets and light jets (top). The tagging efficiency for *b*-quark initiated jets and the mistagging rates for light jets and *c*-quark initiated jets are shown as functions of E_T (bottom-left) and η (bottom-right). Good suppression of light jets and moderate suppression of *c*-quark initiated jets was achieved.

6.2.7   Missing energy reconstruction

An excellent measurement of the missing transverse energy ($\not{E}_T$) is required to reconstruct the invariant mass of the Higgs boson due to the neutrinos in the tau decays. In fact, the invariant mass resolution is dominated by the $\not{E}_T$ resolution, which is discussed in Section 6.3.2.

The standard ATLAS missing energy reconstruction performs a cell level calculation of the missing transverse energy with the inclusion of muons from the spectrometer. Firstly, a topoclustering algorithm is run over all cells in the calorimeter. Only the cells within clusters are used by the reconstruction, which achieves large suppression of the calorimeter noise. A global hadronic calibration is then performed by applying H1-style weights to the cells in the topoclusters. The energy of the cells is then summed vectorially in the transverse plane to calculate the missing transverse energy vector. Good quality muons matched to inner detector tracks are added to the calculation. The standalone p_T measurement from the spectrometer is used to avoid double counting of the muon energy loss in the calorimeter. A correction term is included to account for energy loss in the cryostat, which is fitted between the EM barrel calorimeter and the Hadronic Tile Calorimeter. The cryostat introduces approximately half an interaction length of material, which can cause significant energy loss for high p_T hadronic jets. At this point very good $\not{E}_T$ reconstruction is already achieved. However, a final refinement to the cell energy calibration is performed by associating cells to high p_T reconstructed objects. For cells that are associated to electrons, photons, hadronic taus, jets and muons, chosen in that order, a specific calibration dependent on the object type is applied, which gives much better precision than the global calibration. The final measurement of the missing transverse energy, called `MET_RefFinal` was used in the analysis. The performance of the $\not{E}_T$ reconstruction is characterised by the *linearity* and the *resolution* defined as:

$$\text{Linearity} = (\not{E}_T^{\text{True}} - \not{E}_T^{\text{Reco}})/\not{E}_T^{\text{True}} \tag{6.1}$$

and

$$\text{Resolution} = \sigma(\not{E}_{x,y}^{\text{True}} - \not{E}_{x,y}^{\text{Reco}}) \tag{6.2}$$

where σ represents the width of the distribution. The resolution is a function of the total E_T in an event, and can be described by $\sigma = a \cdot \sqrt{\sum E_T}$, where a has a value

around 0.5 depending on the event topology. Above $\not{E}_{\mathrm{T}}^{\mathrm{True}} = 40$ GeV the linearity is less than 1-2%, however becomes rapidly non-linear below $\not{E}_{\mathrm{T}}^{\mathrm{True}} = 20$ GeV due to the limited $\not{E}_{\mathrm{T}}$ resolution [36].

6.2.8   Overlap removal

In each event, pre-selection was performed on the containers of reconstructed objects to define a set of pre-selected candidates. However, it is possible for a single physics object to be reconstructed by multiple algorithms. This creates an ambiguity in terms of the real identity of overlapping candidates. In this case a procedure must be defined to remove the overlapping candidate and resolve the ambiguity.

The prescription used to remove overlapping candidates was to define a preferential order for object selection, starting from the simplest and most accurately reconstructed objects. Each pre-selected object was required not to overlap with any previously selected object within a cone of $\Delta R < 0.2$, otherwise it was removed. The order of selection was:

1. Muons

2. Electrons

3. Hadronic Taus

4. Jets

6.2.9   Trigger

For an event to be written out by the ATLAS data acquisition system, it must pass a complete trigger decision chain including a Level 1, Level 2 and Event Filter trigger decision. Accordingly, a large number of trigger chains have been optimised to accept 'interesting' events with high efficiency. For a given luminosity setting of the LHC, a menu of trigger chains is defined so that the total write out frequency is $\sim$200 Hz. Therefore, there is only limited bandwidth allocated for trigger chains, and not all can be included, especially at higher luminosities. Because there is only a limited selection of chains available in a given menu, it is important to choose a chain that maximises signal selection efficiency. A number of feasible trigger chains exist for the analysis in the menu for $L = 10^{33}\,\mathrm{cm}^{-2}\mathrm{s}^{-1}$, including single lepton triggers and combined triggers.

Table 6.15 lists a small selection of the feasible trigger chains. Generally, single object triggers are more favourable than combined triggers since it is easier to measure their performance. However, combined triggers exhibit lower individual thresholds and may retain higher signal efficiencies. In this analysis, the threshold on the offline lepton selection was chosen to be 24 GeV, which was set to control the QCD di-jet background and could not be lowered. Since the single lepton trigger thresholds were already below the offline lepton thresholds there was no advantage in using the combined filter chains, and the `mu20` and `e20_medium1` were chosen.

Trigger chains

Level 1	Level 2	Event Filter	Description
		Single Lepton Chains	
L1_MU20	L2_mu20	EF_mu20	20 GeV muon
L1_EM18	L2_e20_medium1	EF_e20_medium1	20 GeV isolated electron
		Combined Chains	
L1_2TAU9I_EM13I	L2_tau20i_e15i	EF_tau20i_e15i	20 GeV isolated tau and 15 GeV isolated electron
L1_EM13_XE20	L2_e15_xe20	EF_e15_xe20	15 GeV electron and 20 GeV $\not{E}_T$
L1_TAU11I_MU10	L2_tau20i_mu10	EF_tau20i_mu10	20 GeV isolated tau and 10 GeV muon

Table 6.15: Feasible trigger chains for the $\ell\tau_h$ channel at $L = 10^{33}\,\mathrm{cm}^{-2}\mathrm{s}^{-1}$.

As simulation of the trigger was not available in the version of ATLFAST-II used for production, the trigger performance was parameterised and used to weight the ATLFAST-II events. Two additional signal samples with $m_A = 150$ GeV and $m_A = 600$ GeV were simulated with the full GEANT4 simulation to evaluate the trigger over a large range of lepton p_T. To correctly account for the trigger performance when applied as a weight in the analysis, the trigger efficiency was measured with respect to the leading lepton that passed the full offline lepton selection, including isolation. It was especially important to include the offline isolation when measuring the efficiency of the electron trigger, since although the trigger includes a small level of isolation itself, the requirement is much looser than the offline isolation. In addition to the decision of the trigger chain, the object constructed by the event filter was required to match the leading p_T pre-selected lepton within $\Delta R < 0.2$. In the regions of overlapping lepton p_T between the two signal samples, no difference was found in the trigger efficiencies, so

the samples were combined to increase the statistical precision of the parameterisation. Figure 6.12 shows the efficiency of the electron and muon triggers with respect to the p_T of the offline lepton.

The trigger efficiency was parameterised as a function of the offline lepton p_T using a function of the form:

$$f(p_T) = \frac{1}{2} p_2 \left[1 + \mathrm{erf} \left(\frac{p_T - p_0}{\sqrt{2} p_1} \right) \right] \tag{6.3}$$

where p_0 is the p_T when the trigger efficiency reaches half its maximum, p_1 is the slope and p_2 is the maximum efficiency. The maximum efficiency of the triggers were found to be $(97.7 \pm 0.3)\%$ for electrons and $(81.1 \pm 0.4)\%$ for muons. In each case, the triggers were very close to reaching maximum efficiency at the 24 GeV threshold applied to offline leptons. The trigger parameterisation was performed by Uli Felzmann and results are taken from [1].
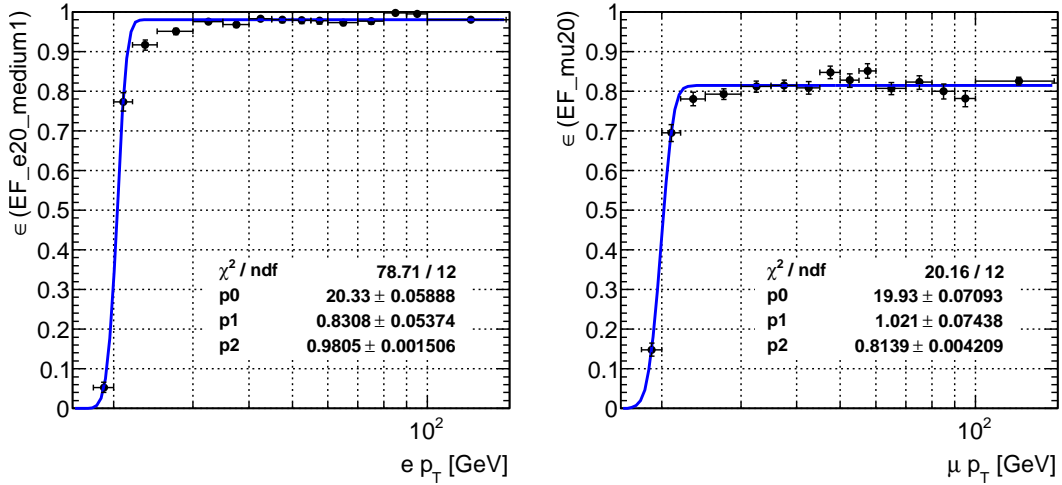
Figure 6.12: Trigger performance extracted from signal samples for electrons (left) and muons (right). The results are taken from [1], where the performance was parameterised by Uli Felzmann.

6.3 Event selection

The main backgrounds for the $A/H \to \tau(\to \ell\bar{\nu}_\ell\nu_\tau)\tau(\to \tau_h\nu_\tau)$ channel are:

- reducible: $W(\to \ell\bar{\nu}_\ell)$+jets, $W(\to \tau\bar{\nu}_\tau \to \ell\bar{\nu}_\ell\nu_\tau\bar{\nu}_\tau)$+jets, $Z(\to \ell\ell)$+jets, $t\bar{t}$ (excluding $t\bar{t} \to b\bar{b}\ell\nu_\ell\tau\nu_\tau$) and QCD di-jets

- irreducible: $Z \to \tau\tau$ and $t\bar{t} \to b\bar{b}\ell\nu_\ell\tau\nu_\tau$.

Strict object pre-selection and Lepton Isolation provide large discrimination against fake taus and fake and non-isolated leptons, which largely suppresses the reducible backgrounds. However, further suppression is required to observe the signal, especially for the irreducible backgrounds. In this section the event selection is described, which exploits the characteristic signature of the $\ell\tau_h$ channel to suppress the various backgrounds.

The event selection was divided into three stages: *baseline selection*, *b-tagging split* and *analysis-dependant selection*. The baseline selection comprised of a basic set of selection criteria that were always applied and achieved large suppression against the reducible backgrounds. The analysis was then divided into two completely orthogonal sub-analyses using the number of b-tagged jets. This helped to separate out the major backgrounds. Finally, a select few cuts were applied at the end of the analysis, which were optimised separately for the two sub-analyses and for each Higgs boson mass hypothesis. This procedure was found to give the best sensitivity to the Higgs boson signal.

6.3.1 Baseline selection

In this section each of the cuts in the baseline selection are described. The distributions of the selection variables for signal and background are shown in Figure 6.13.

Pre-selected lepton ($n_{\mathrm{leptons}} > 0$)

At least one pre-selected lepton was required in the event. In the case where multiple leptons passed pre-selection, the leading lepton (highest p_{T}) was chosen for use in all following calculations in the event selection. This choice resulted in the correct selection of the lepton from the leptonic tau decay in $> 99\%$ of signal events. Due to the lepton p_{T} threshold used in pre-selection, large suppression of the QCD background was achieved.

Typically, the requirement of exactly one lepton is used to suppress all backgrounds containing multiple leptons. However, since the lepton selection was divided in two stages to allow weighting on QCD events, no isolation was applied in the pre-selection. Consequently there were a significant number of additional pre-selected leptons from semi-leptonic b-quark decays in the signal. Consequently, the selection on the number of pre-selected leptons was relaxed to $n_{\text{leptons}} > 0$, since requiring exactly one lepton caused an additional reduction in signal efficiency of 6%, 11% and 17% for the 150, 300 and 800 GeV mass hypotheses, respectively.

Z-mass veto (Z-Veto)

Selection on an invariant lepton-lepton mass was used to suppress $Z \to \ell\ell$ events. An algorithm was devised to suppress $Z \to \ell\ell$ events with the highest rejection achievable while keeping the signal loss below 1%. The algorithm iterates through all electron and muon pair combinations applying much looser lepton selection than applied in the pre-selection. If a combination had an invariant mass within a window around the Z boson mass peak of (91 ± 10) GeV, the event was rejected. No kinematic requirements were applied to the leptons. For electron pairs, one electron was required to pass the `isEM::ElectronMediumNoIso` and `AuthorElectron` flags and the other the `isEM::Loose` flag, to reduce signal loss from combinations of fakes. For muons no selection was applied.

Lepton Isolation

The Lepton Isolation described in Section 6.2 was applied to the leading lepton. In QCD di-jet events the Lepton Isolation was applied as a weight, and no events were removed by the selection. Very large suppression of QCD di-jet events was achieved.

Trigger

The trigger parameterisation (described in Section 6.2.9) was used to weight the event as a function of the p_{T} of the leading lepton. Although the trigger requirement would typically appear at the start of the event selection, in this case it had to be applied after the lepton selection as it was parameterised as a function of the p_{T} of the leading pre-selected lepton.

Missing transverse energy ($\not{E}_\text{T} > 20$ GeV)

The reconstructed $\not{E}_\text{T}$ was required to be greater than 20 GeV. There are two reasons for the choice of the threshold. Firstly, the signal events contain a moderate amount of missing energy due to the neutrinos in the tau decays, while QCD di-jet and $Z \to \ell\ell$ events only contain fake $\not{E}_\text{T}$, due mainly to jet energy mismeasurement or non-reconstructed muons. Good suppression of the QCD and $Z \to \ell\ell$ backgrounds was achieved with the 20 GeV threshold. At the same time, the $\not{E}_\text{T}$ plays an extremely important role in the reconstruction of the invariant tau-tau mass. Since the $\not{E}_\text{T}$ measurement rapidly becomes non-linear under 20 GeV, the threshold is required to achieve a good mass reconstruction.

Transverse mass: ($m_\text{T} < 25$ GeV)

The transverse mass, m_T, was used to discriminate against events containing on-shell W bosons. It is reconstructed from the p_T of the leading lepton and the missing energy, such that:

$$m_\text{T} = \sqrt{2 \cdot p_\text{T}^\ell \cdot \not{E}_\text{T} \cos(1 - \phi)} \tag{6.4}$$

where ϕ is the angle between the $\not{E}_\text{T}$ vector and the lepton in the transverse plane. For the $W \to \ell\nu$ backgrounds the $\not{E}_\text{T}$ is due entirely to the neutrino from the W decay. In this case, the transverse mass will form a Jacobian peak with an endpoint at the W mass (including some broadening from detector resolution). However, in the signal m_T peaks at zero. By requiring $m_\text{T} < 25$ GeV, very large suppression of the $W \to \ell\nu$ background and also moderate suppression of $t\bar{t}$ was achieved.

Pre-selected tau ($n_\tau = 1$)

Exactly one pre-selected tau (including loose and tight pre-selection) was required in the event. For backgrounds where Tau-ID Weighting was used, only loose pre-selection was applied. This increases the statistical precision of the background estimate by increasing the number of pre-selected candidates. However, in this case the standard selection must be relaxed to $n_\tau \geq 1$, otherwise the background rejection is overestimated. As a result there may be multiple tau candidates in each event, and a loop on all pre-selected taus must be made, as described in Section 6.4.2.

Tau Identification (Tau-ID)

The tau event-selection (as in Table 6.13) was applied to the pre-selected tau. For backgrounds where Tau-ID Weighting was used, no selection was applied and each pre-selected tau in the event was weighted by the measured Tau-ID efficiency. The Tau-ID achieves large suppression of the reducible backgrounds.

Physical mass ($m_{\tau\tau} > 0$)

The invariant mass reconstructed using the collinear approximation was required to be physical, as described in Section 6.3.2.

Opposite sign (OS)

The selected tau and lepton were required to have opposite sign charges. In the signal, the lepton and tau should always have opposite charges due to charge conservation. However, in the reducible backgrounds the charges are uncorrelated as either the tau or lepton (or both) are fake.

6.3.2 Mass reconstruction

The tau decays in the $\ell\tau_h$ channel contain a total of three neutrinos that will not be detected by ATLAS. Assuming massless neutrinos, each neutrino has three unknown momentum components, totalling nine degrees of freedom. The only measure of the neutrino momenta comes from the two components of the $\not{E}_T$ vector in the transverse plane. With only two independent measurements, it is impossible to directly reconstruct the individual neutrino Lorentz vectors, making it impossible to reconstruct the invariant mass of the tau-tau system.

Historically, the collinear approximation [70] has been used in analyses of the $\ell\tau_h$ channel to allow the reconstruction of the invariant mass. The assumption is made that all the decay products of the tau have the same direction, which is valid when the taus are highly boosted. This is the case for the $\ell\tau_h$ channel since the mass of the taus are negligible compared to the mass of the resonance. As the two neutrinos in the leptonic tau decay have the same direction they can be described by a single Lorentz vector. This leaves only the magnitudes of the two neutrino Lorentz vectors as the degrees of freedom, allowing the system to be solved using the two $\not{E}_T$ components.
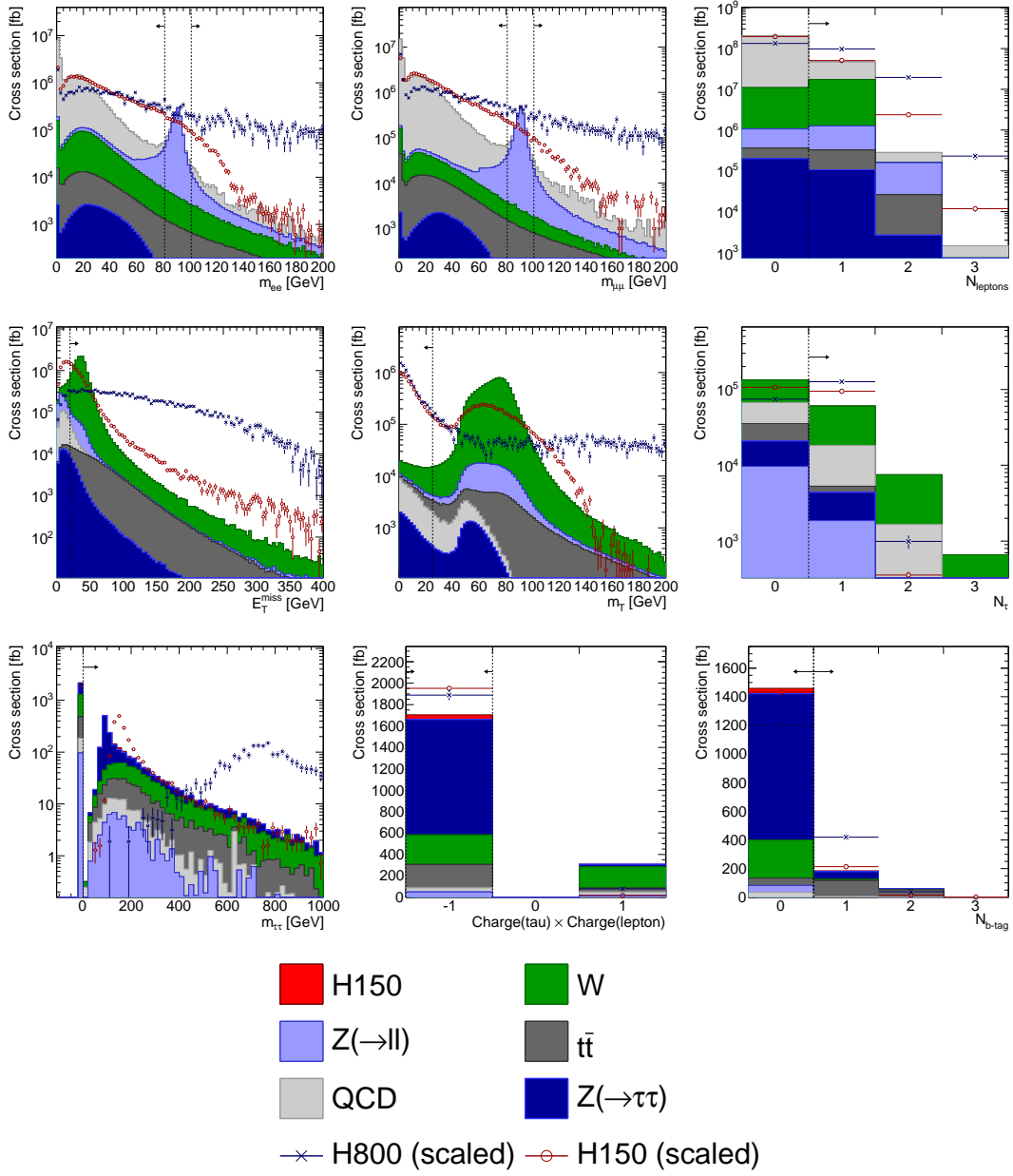
Figure 6.13: Baseline selection. The contributions are normalised to the expected cross section in fb. In each figure the background contributions are stacked from smallest to largest and the total signal contribution for the $m_A = 150$ GeV hypothesis is stacked on top. As the signal is barely visible the distributions for the $m_A = 150$ GeV and $m_A = 800$ GeV hypotheses are also overlaid, normalised to the total background contribution. Dashed lines indicate the selection, which is made in the direction of the arrows.

127

Two formulations to calculate the solutions for the neutrino energies exist, [70] and [54], however, both give identical results with the correct constraints. In this study the latter formulation was used, and is described briefly. The mass of the tau-tau system is calculated as:

$$m_{\tau\tau} = \sqrt{2(E_1 + E_{\nu 1})(E_2 + E_{\nu 2})(1 - \cos\Delta\phi)} \qquad (6.5)$$

where E_1 and E_2 are the energies of the visible tau decay products, $E_{\nu 1}$ and $E_{\nu 2}$ are the energies of the corresponding neutrino Lorentz vectors and $\Delta\phi$ is the angle between the visible decay products in the transverse plane. $E_{\nu 1}$ and $E_{\nu 2}$ are obtained by solving the system of linear equations:

$$\not{E}_i = E_{\nu 1} \cdot \hat{p}_{1,i} + E_{\nu 2} \cdot \hat{p}_{2,i}, \quad i \in \{x, y\} \qquad (6.6)$$

where $\not{E}_i$ are the components of the $\not{E}_T$ vector and $\hat{p}_1$ and $\hat{p}_2$ are unit vectors in the direction of the visible decay products. Both $E_{\nu 1}$ and $E_{\nu 2}$ are required to be positive, which can only be true if the $\not{E}_T$ vector lies between the visible decay products in the transverse plane. This requirement is indicated as the *Physical Mass* ($m_{\tau\tau} > 0$) requirement in the baseline selection. The solution is unstable in the region $\Delta\phi \sim \pi$, where the visible decay products are back-to-back in the transverse plane. Figure 6.14 shows the invariant mass vs. $\Delta\phi$ for signal events with $m_A = 150$ GeV and for $Z \to \tau\tau$ events. The back-to-back region must be removed to suppress contributions from poorly reconstructed $Z \to \tau\tau$ events in the signal mass window. The resolution of the reconstructed mass is affected not only by the selection on $\Delta\phi$, but also by the energy resolution of the reconstructed lepton, tau and $\not{E}_T$. Figure 6.15 shows the reconstructed mass for signal events with $m_A = 150$ GeV. By far the most dominant contributions to the achievable mass resolution are the $\not{E}_T$ resolution and the selection on $\Delta\phi$.

6.3.3 b-tagging split

Depending on the signal production process, the Higgs boson may be accompanied by either 0, 1 or 2 b-quarks. In contrast, $t\bar{t}$ typically contains two b-quarks, and all the other backgrounds typically contain no b-quarks. After the baseline selection was applied, the analysis was divided into the two cases where either exactly zero b-jets were reconstructed, the *non b-tagged analysis*, or at least one b-jet was reconstructed, the *b-tagged analysis*. By dividing the analysis in this way the major backgrounds could
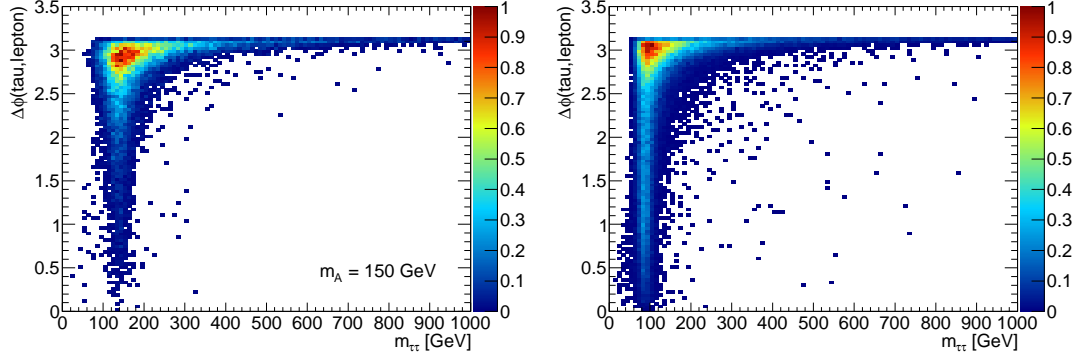
Figure 6.14: Invariant mass vs. the angular separation of the tau and lepton in the transverse plane ($\Delta\phi$), for signal (left) and $Z \rightarrow \tau\tau$ (right). An arbitrary normalisation was used for the colour scale. In the region $\Delta\phi \sim \pi$, the collinear approximation breaks down and there is a large tail up to high $m_{\tau\tau}$. This region must be removed to suppress contributions from poorly reconstructed $Z \rightarrow \tau\tau$ events.

be isolated, improving the suppression by exploiting their distinct features. Figure 6.13 includes the distribution of the number of b-jets for the signal and background processes.

6.3.4 Analysis dependant optimisation

In the final stage, the selection was optimised to exploit the distinct features of the isolated backgrounds. The optimisation was performed separately for each mass hypothesis, and for the b-tagged and non b-tagged analyses. Numerous variables were studied to suppress the $t\bar{t}$ background in the b-tagged analysis (discussed in the following section, Section 6.3.4.1). In the end, selection on the number of jets was found to give the best discrimination. In the non b-tagged analysis, the W+jets background becomes important for mass hypotheses $m_A \geq 300$ GeV as the $Z \rightarrow \tau\tau$ contribution becomes less dominant. The selection of only 1-prong tau candidates significantly reduces the contribution from fake taus and was used in the non b-tagged analysis to suppress the W+jets background in this mass range. To achieve the best discrimination over the entire Higgs mass range, selection on a few variables that exhibited the largest discrimination was optimised. In both the b-tagged and non b-tagged analyses, increased thresholds on the $\not{E}_T$ and the E_T of the selected tau were found to give the best discrimination. Selection on the angle between the tau and lepton in the transverse plane was applied to remove the region where the mass reconstruction breaks

(a) Generator mass

(b) True τ, ℓ and $\not{E}_T$

(c) Reconstructed τ and ℓ, true $\not{E}_T$

(d) Reconstructed τ, ℓ and $\not{E}_T$
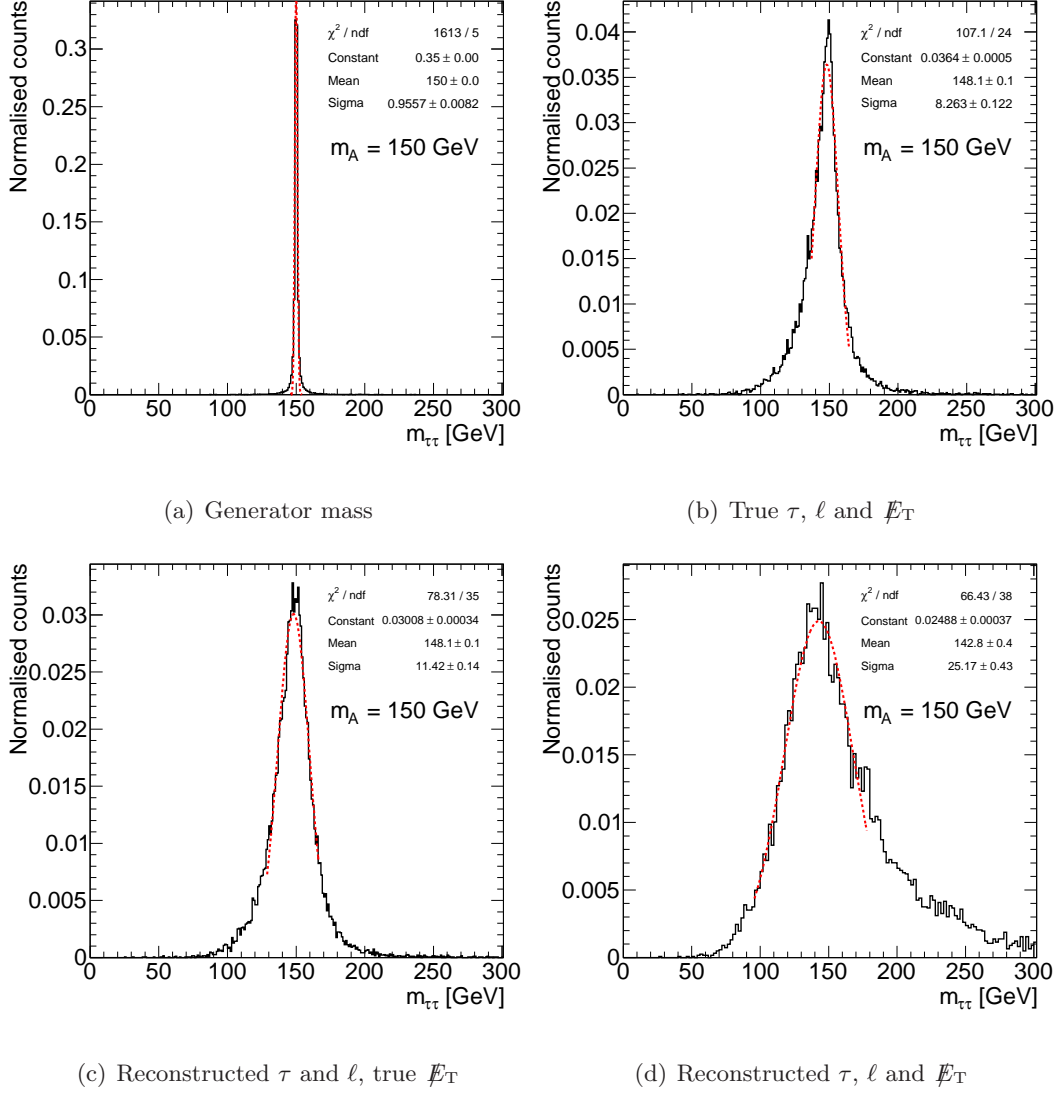
Figure 6.15: Invariant tau-tau mass for signal events with $m_A = 150$ GeV. Events were required to have at least one pre-selected lepton and tau that were matched to their respective truth particles and separated by $\Delta\phi < 3.0$ in the transverse plane. The tau-tau mass from the event generator is shown in (a). Figures (b)-(d) show the reconstructed mass using the collinear approximation. In Figure (b) the tau and lepton momenta are taken from the matched truth particles and the $\not{E}_T$ is also taken from truth. In Figure (c) the tau and lepton momenta are replaced by the reconstructed quantities, and in Figure (d) all quantities are taken from reconstruction. Each distribution was fitted with a Gaussian function in the core region. The use of the collinear approximation causes a significant increase in the mass resolution, highly dependant on the selection applied to $\Delta\phi$. The energy resolution of the reconstructed lepton and tau cause almost no extra degradation in the mass resolution. By far the most dominant contribution to the mass resolution is the resolution of the reconstructed $\not{E}_T$.

down. Finally, a window on the reconstructed invariant mass was applied, defined as $[\mu - 1.5\sigma, \mu + 1.5\sigma]$, where μ and σ are the mean and standard deviation of the invariant mass distribution. The parameters μ and σ were extracted by fitting the signal-only mass distribution with a single Gaussian. Table 6.16 shows the parameters for the mass window.

Higgs boson mass windows

m_A [GeV]	μ [GeV]	σ [GeV]	low edge [GeV]	high edge [GeV]
150	154	22	121	187
200	200	36.6	145	255
300	290	53.3	210	370
450	440	66.6	340	540
600	580	106.6	420	740
800	730	123.3	545	915

Table 6.16: Higgs boson mass windows chosen for each mass hypothesis. A single Gaussian with mean μ and standard deviation σ was fitted to the signal-only mass distribution. The window was taken as $[\mu - 1.5\sigma, \mu + 1.5\sigma]$.

6.3.4.1 Discrimination against $t\bar{t}$

To obtain signal sensitivity in the b-tagged analysis, good discrimination against the dominant $t\bar{t}$ background is essential. A number of discriminating quantities were investigated to try and suppress $t\bar{t}$, including:

- N_{jet} – the number of pre-selected jets in the central region $|\eta| < 3.2$.

- $\max[E_{\mathrm{T}}(b-\mathrm{jet})]$ – largest E_{T} from a b-jet.

- $\sum E_{\mathrm{T}}$ – scalar sum of E_{T} measured in the calorimeters, reconstructed in the same way as the $\not{E}_{\mathrm{T}}$, which is instead a vectorial sum.

- $\min[\Delta R(\ell, b-\mathrm{jet})]$ – minimum separation in ΔR between the leading lepton and a b-jet.

- *Circularity* – event shape variable defined as:

$$C = \frac{2\lambda_1}{\lambda 1 + \lambda 2},$$
(6.7)

131

where $\lambda_1 < \lambda_2$ are the eigenvalues of the matrix

$$M^{\alpha\beta} = \sum_i p_i^\alpha p_i^\beta. \qquad (6.8)$$

$M^{\alpha\beta}$ is a 2×2 matrix defined by the components of particle momenta in the transverse plane, where $\alpha, \beta \in \{x, y\}$. The sum runs over all particles in the event including the $\not{E}_{\mathrm{T}}$ vector.

- $m_{t\bar{t}}$ – reconstructed mass of the $t\bar{t}$ pair. The event topology of the semi-leptonic decay mode was assumed, where one W decays leptonically, and the other hadronically. The mass of the $t\bar{t}$ system was reconstructed from the leading lepton, the neutrino and up to four accompanying jets. The transverse momentum components of the neutrino were taken from the $\not{E}_{\mathrm{T}}$ vector. The p_z component was calculated by requiring the invariant mass of the ℓ-ν system to equal the W mass. A quadratic equation must be solved for p_z and the smaller of the two solutions was taken, which resulted in the correct value in $\sim 70\%$ of cases. If no real solution exists $p_z = 0$ was used.

Figure 6.16 shows the distributions of the discriminating quantities before the event selection is applied for $t\bar{t}$ and signal events at three mass hypotheses. The variables that exhibit the largest discriminating power are N_{jet} and *circularity* and also $\sum E_{\mathrm{T}}$ and $m_{t\bar{t}}$ for the low mass hypotheses. Unfortunately, most of the variables are highly correlated with the event selection and provide little discrimination after the baseline selection. Only the N_{jet} variable (and to some extent $\sum E_{\mathrm{T}}$ for $m_A = 150$ and 200 GeV) retained adequate discriminating power. A selection of $N_{\mathrm{jet}} < 3$ was chosen as it provides good discrimination over the full mass range. Figures showing the discriminating power of each of the variables after the baseline selection including $N_{b-\mathrm{tag}} > 0$ and the invariant mass window are given in Appendix B.1

The discrimination from the *circularity* is further degraded by the $\Delta\phi(\ell, \tau)$ selection used to improve the mass reconstruction, as both operate in the transverse plane. In this respect, a three-dimensional event shape variable such as *spherocity*[1] may exhibit improved discrimination, however, was not considered. The $m_{t\bar{t}}$, although showing some discrimination in the low mass region, is essentially just a basic reconstruction of

---

[1]Spherocity is calculated as $S = \frac{3}{2}(\lambda_2 + \lambda_3)$, where λ_2 and λ_3 are the lower two eigenvalues of the tensor $M^{\alpha\beta}$ calculated in three dimensions.

the mass produced in the event, which provides little discrimination for m_A around the $t\bar{t}$ threshold. To pursue this path, a more detailed comparison of the decay chains in $t\bar{t}$ and the signal would have to be made. In particular, the topology of the irreducible $t\bar{t} \to b\bar{b}\ell\nu_\ell\tau\nu_\tau$ mode should be studied, as this mode contributes ~70% of the total $t\bar{t}$ background after the full event selection is applied, whereas the semi-leptonic mode only contributes ~30%.
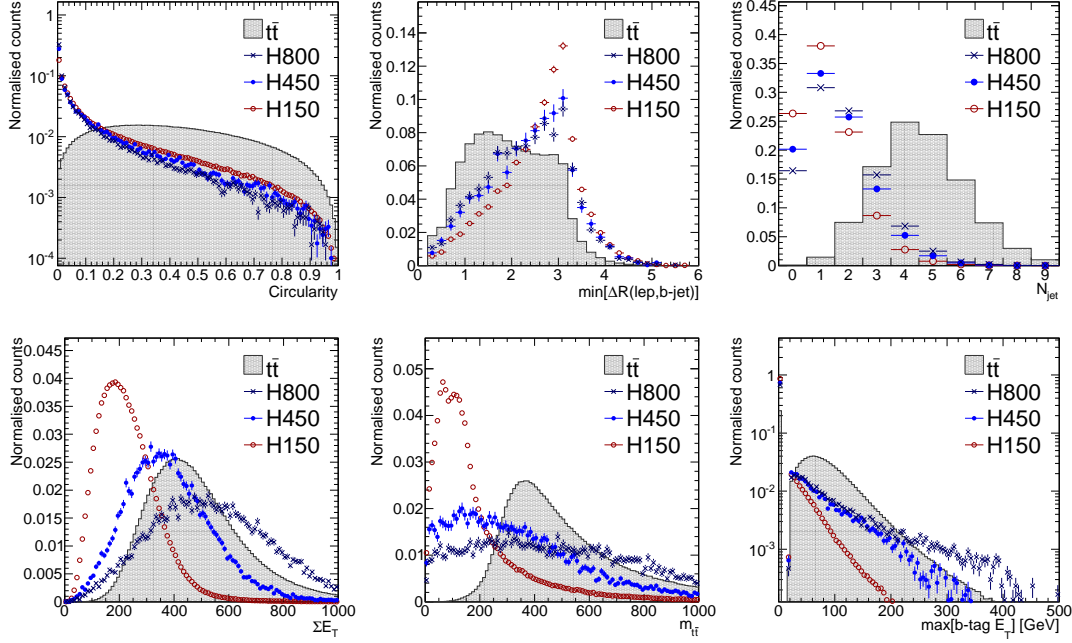
Figure 6.16: $t\bar{t}$ discriminating variables.

6.3.4.2 Optimisation of selection

As the Higgs boson mass hypothesis is increased, so too is the energy of the decay products. By increasing the thresholds on the E_T of the selected tau and on the $\not{E}_T$ (which is due to the neutrinos in the tau decays), large discrimination against the backgrounds was achieved. To remove the region where the collinear approximation breaks down, an upper cut on the angle between the tau and lepton was also applied. In addition, a lower cut on the angle was applied in the b-tagged analysis to suppress the contribution from $Z \to \tau\tau$ in the $t\bar{t}$ background estimation procedure. A similar cut was not applied in the non b-tagged analysis as $Z \to \tau\tau$ events with small angular

separation result in very good mass reconstruction, and are removed by the selection on the mass window.

The final selection was optimised by iterating sequentially through the variables and choosing the threshold for each that maximised the significance of the analysis. In this process the significance was estimated using the simple approximation:

$$S = \frac{N_S}{\sqrt{N_B}}, \tag{6.9}$$

where N_S and N_B are the expected number of signal and background events in $30\,\mathrm{fb}^{-1}$ of data. For analyses with very small numbers of expected events, the Poisson formula

$$S = \sqrt{2 \cdot \left((N_\mathrm{S} + N_\mathrm{B}) \cdot \log \left(1 + \frac{N_\mathrm{S}}{N_\mathrm{B}}\right) - N_\mathrm{S} \right)}, \tag{6.10}$$

was used. However, the choice of significance calculation had little effect on the choice of cut. For the analyses at higher mass hypotheses, this method often resulted in extreme choices for cuts, leaving few or no MC simulated background events. For backgrounds where fewer MC simulated events were available than the number of events expected in data, a large statistical uncertainty was introduced. The choice of such cuts severely degrades the accuracy of the estimation of the discovery potential and for these cases the cuts were relaxed to reduce the impact from the lack of MC simulated events. In this sense the lack of MC simulated events ultimately limits the maximum significance obtainable by the analysis. However, until larger MC simulated samples become available, further tuning of the cuts is not useful. The method also ignores the contribution from systematic uncertainties in the significance calculation, the effect of which is discussed in Section 6.8. Figures 6.17 to 6.22 show the optimised selection for the b-tagged and non b-tagged analyses at each mass hypothesis. The selection for the non b-tagged analysis is summarised in Table 6.17 and the selection for the b-tagged analysis is summarised in Table 6.18. The optimisation of the non b-tagged analysis was the complete work of the author, however, the optimisation of the $\slashed{E}_\mathrm{T}$, tau E_T and $\Delta\phi$ for the b-tagged analysis was done by Jana Schaarschmidt. Further figures showing the individual contributions from the backgrounds in the optimised selection, and the invariant mass distribution after each cut can be found in Appendix B.2.
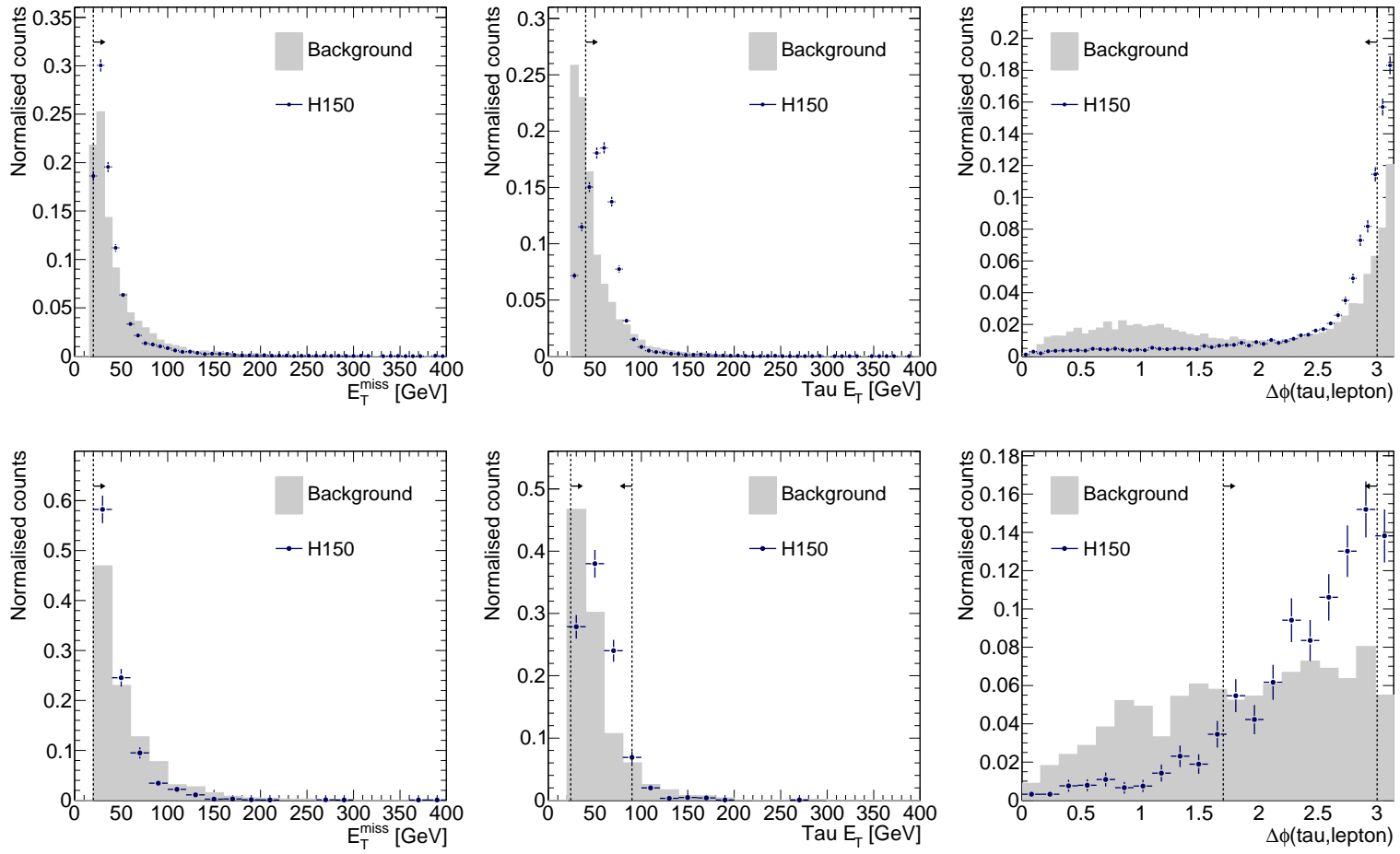
Figure 6.17: Optimised selection at $m_A = 150$ GeV for the non b-tagged (top) and b-tagged (bottom) analyses. The selected regions span from the dashed lines in the direction of the arrows.
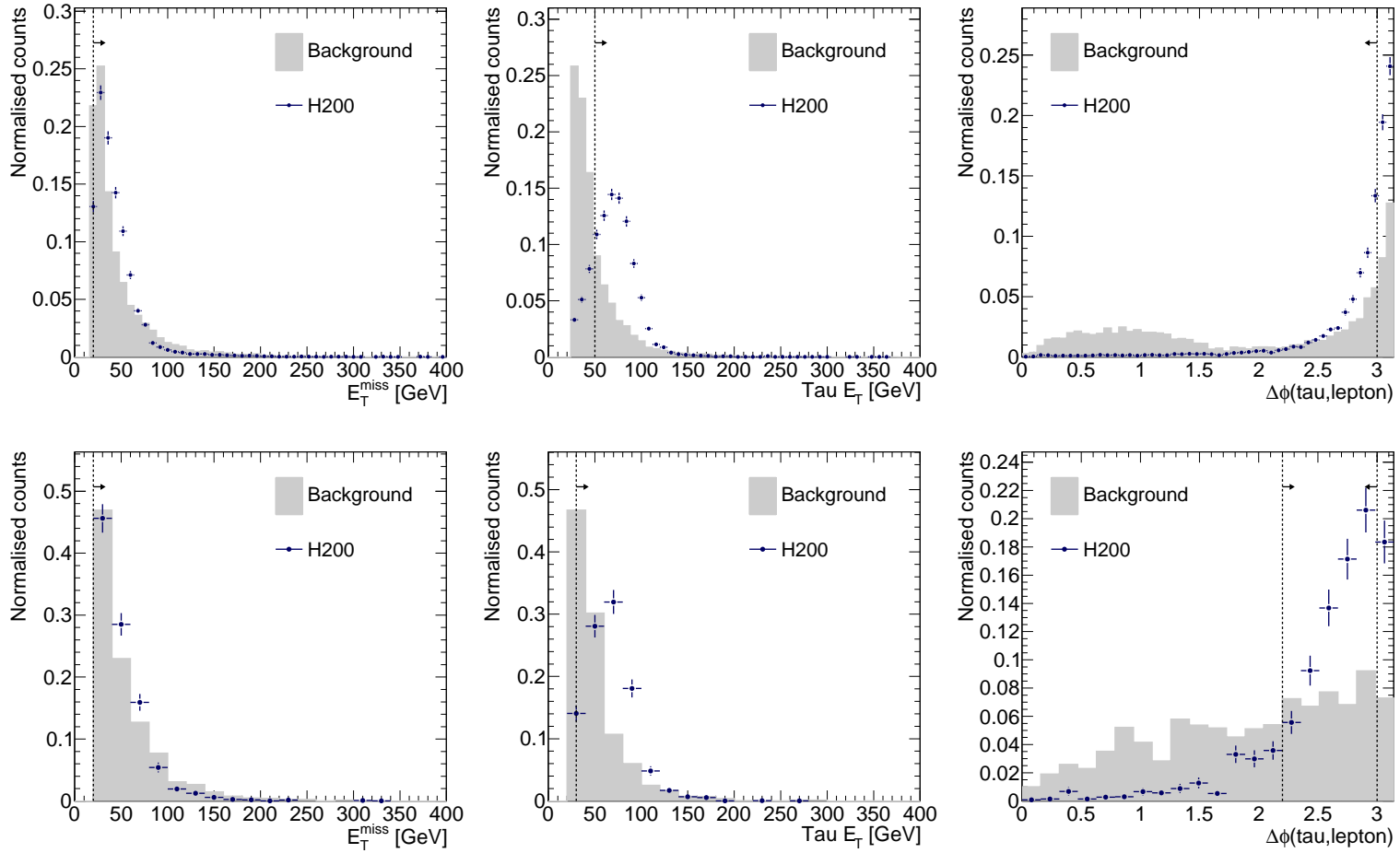
Figure 6.18: Optimised selection at $m_A = 200$ GeV for the non b-tagged (top) and b-tagged (bottom) analyses. The selected regions span from the dashed lines in the direction of the arrows.
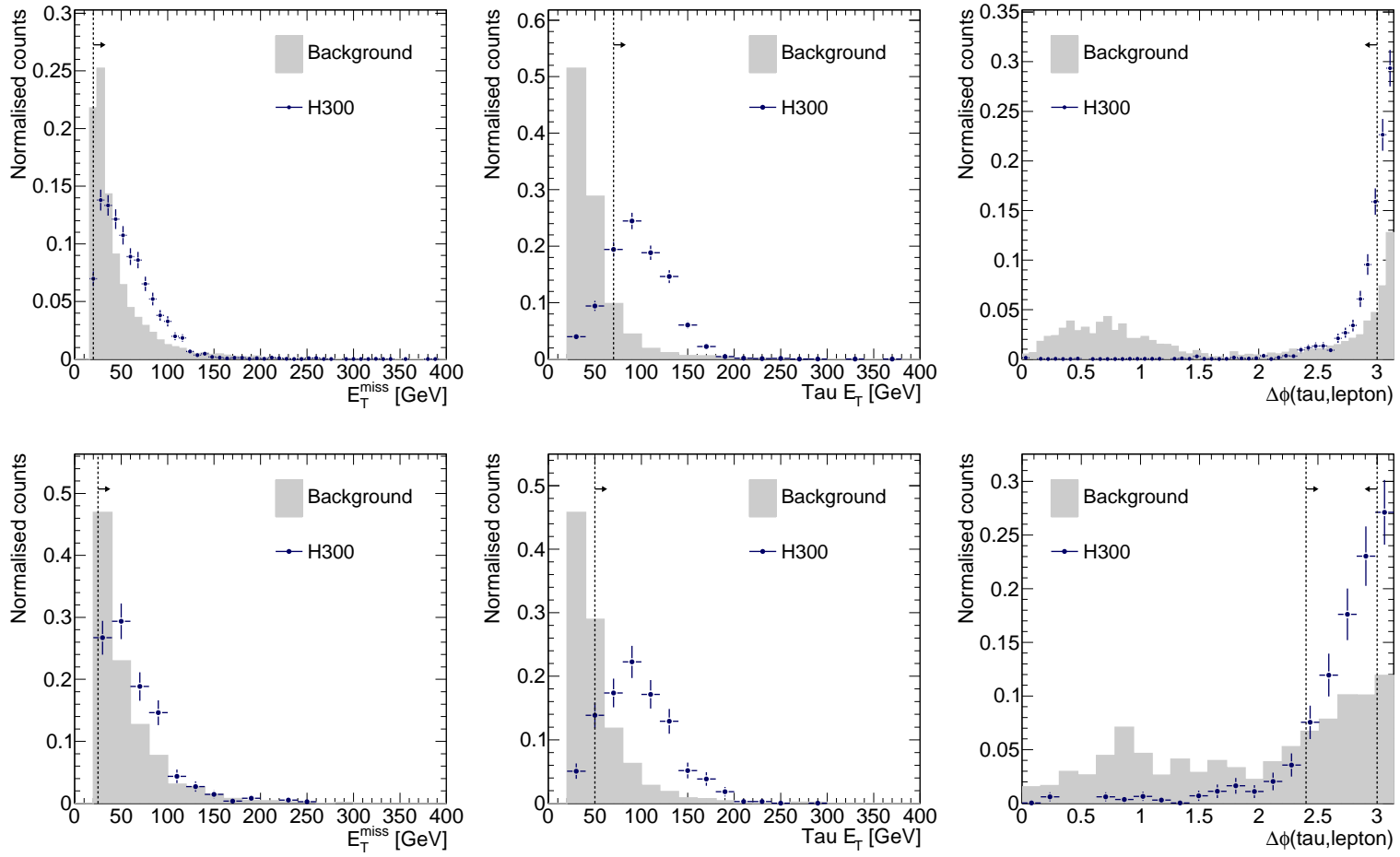
Figure 6.19: Optimised selection at $m_A = 300$ GeV for the non b-tagged (top) and b-tagged (bottom) analyses. The selected regions span from the dashed lines in the direction of the arrows.
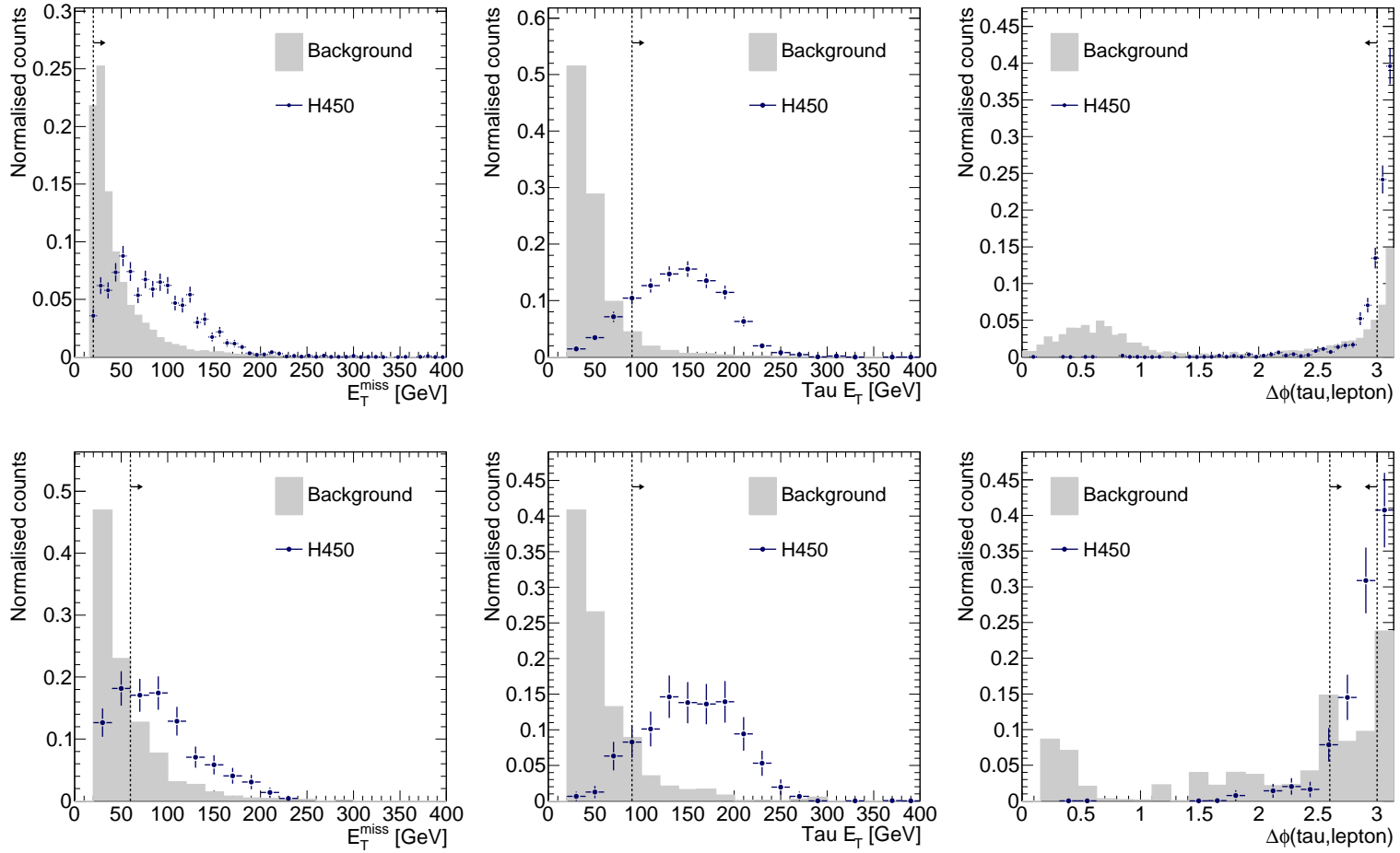
Figure 6.20: Optimised selection at $m_A = 450$ GeV for the non b-tagged (top) and b-tagged (bottom) analyses. The selected regions span from the dashed lines in the direction of the arrows.
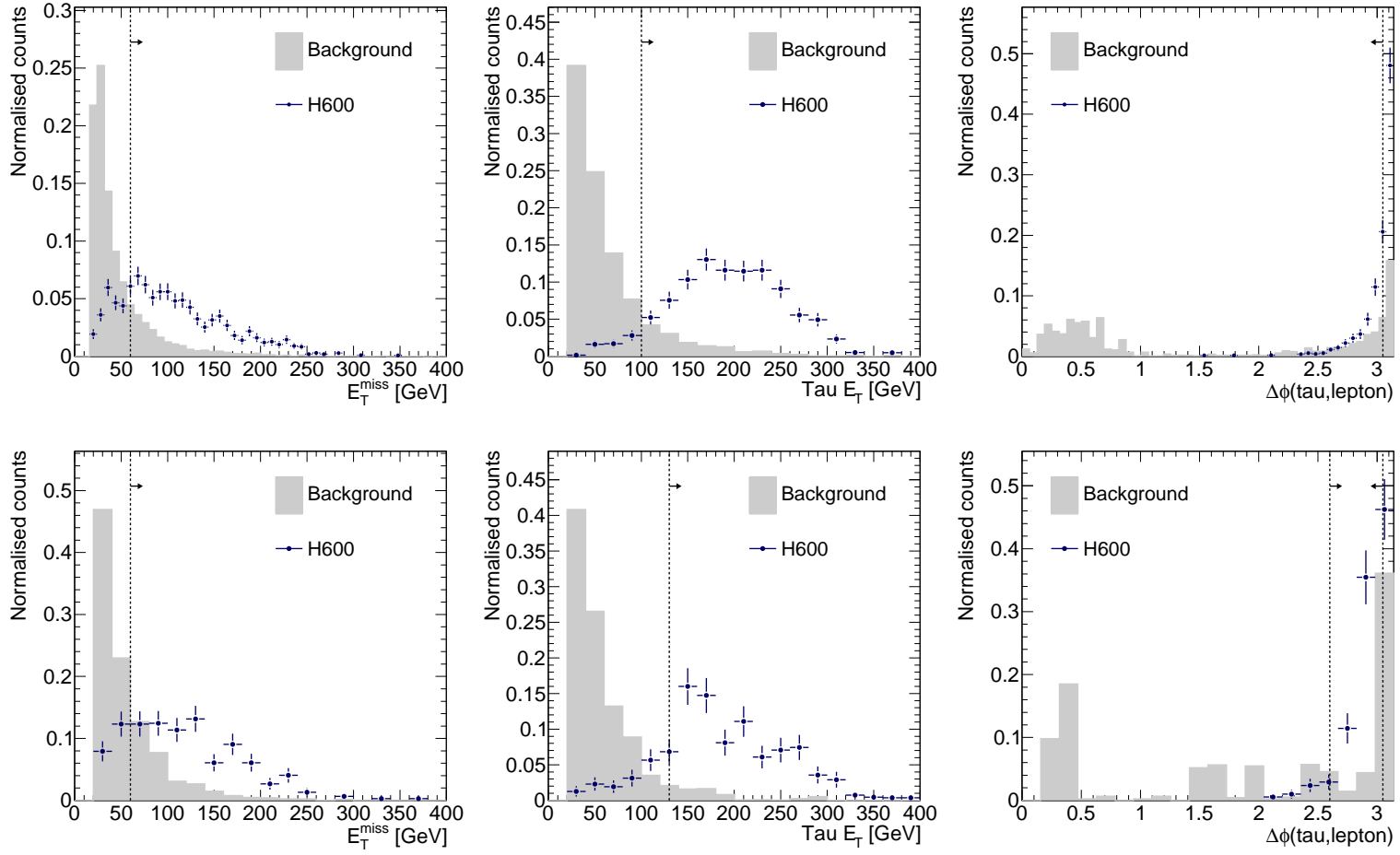
Figure 6.21: Optimised selection at $m_A = 600$ GeV for the non b-tagged (top) and b-tagged (bottom) analyses. The selected regions span from the dashed lines in the direction of the arrows.
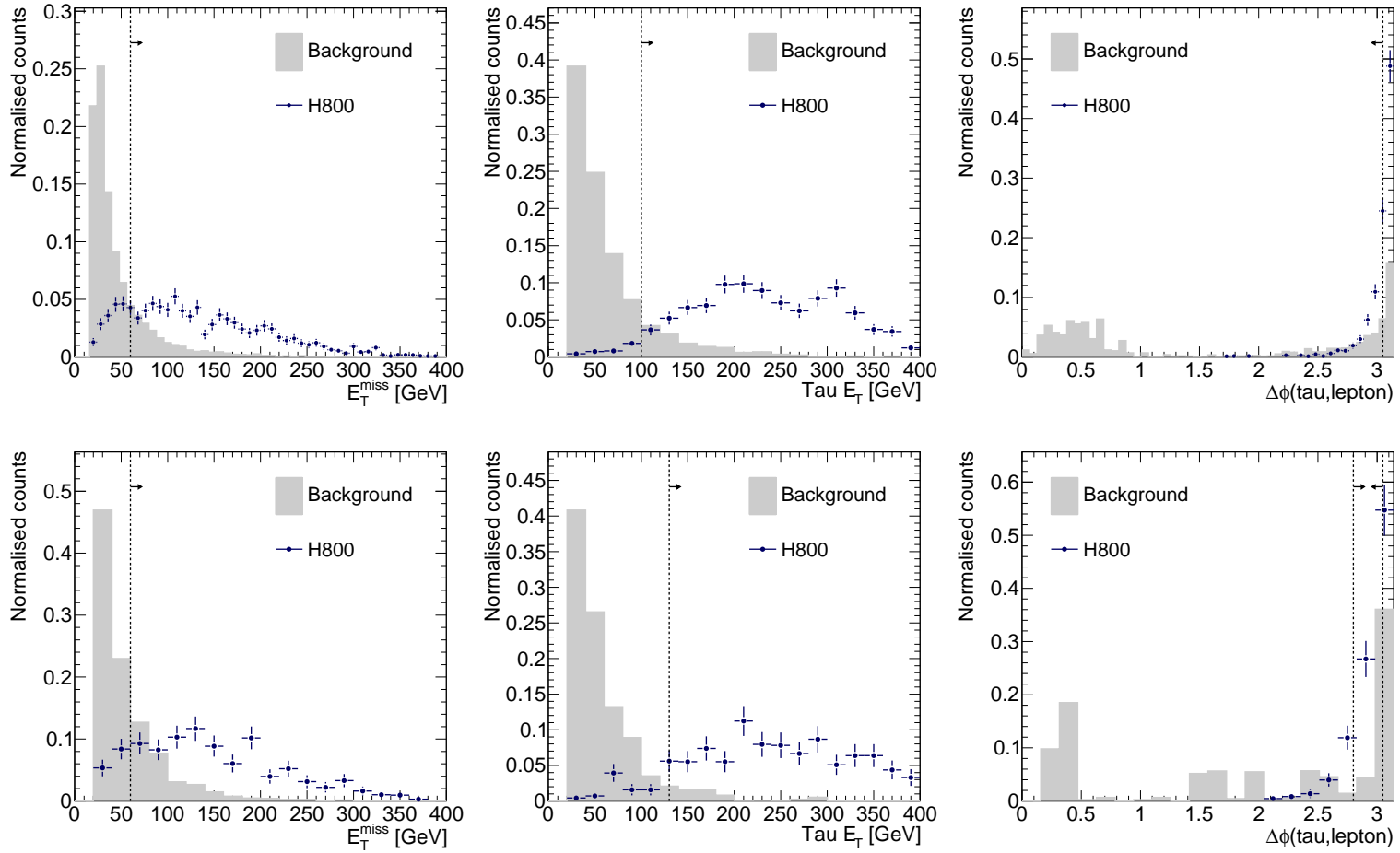
Figure 6.22: Optimised selection at $m_A = 800$ GeV for the non b-tagged (top) and b-tagged (bottom) analyses. The selected regions span from the dashed lines in the direction of the arrows.

Analysis-dependent cuts for the non *b*-tagged analysis

m_A [GeV]	150	200	300	450	600	800
$\not{E}_T$ [GeV]	> 20	> 20	> 20	> 20	> 60	> 60
n^τ_tracks	$-$	$-$	$= 1$	$= 1$	$= 1$	$= 1$
E^τ_T [GeV]	> 40	> 50	> 70	> 90	> 100	> 100
$\Delta\phi$ [rad]	< 3.0	< 3.0	< 3.0	< 3.0	< 3.05	< 3.05

Table 6.17: Analysis-dependent cuts for the non *b*-tagged ($n_{b-\text{tags}} = 0$) analysis.

Analysis-dependent cuts for the *b*-tagged analysis

m_A [GeV]	150	200	300	450	600	800
$n_\text{light jets}$	< 3	< 3	< 3	< 3	< 3	< 3
$\not{E}_T$ [GeV]	> 20	> 20	> 25	> 60	> 60	> 60
E^τ_T [GeV]	< 90	> 30	> 50	> 90	> 130	> 130
$\Delta\phi$ [rad]	< 3.0	< 3.0	< 3.0	< 3.0	< 3.05	< 3.05
$\Delta\phi$ [rad]	> 1.7	> 2.2	> 2.4	> 2.6	> 2.6	> 2.8

Table 6.18: Analysis-dependent cuts for the *b*-tagged ($n_{b-\text{tags}} > 0$) analysis.

6.4 Tau Identification and Lepton Isolation Weighting

The evaluation of the backgrounds in the $\ell\tau_h$ channel has always been limited by the ability to produce large MC simulated samples. To combat this, the MLF filter was used on all background samples giving an effective increase in the number of events up to a factor of 400. ATLFAST-II was also used for the simulation of all MC samples, increasing the production rate by a factor $\sim$10 [49]. Despite this, many of the samples have far fewer events than expected in $30\,\mathrm{fb}^{-1}$. Table 6.19 shows the event weight for each of the background samples when scaled to $30\,\mathrm{fb}^{-1}$, calculated as:

$$w = \frac{\sigma \cdot L \cdot \epsilon_{\mathrm{filter}}}{N_{\mathrm{MC}}}, \tag{6.11}$$

where σ is the production cross section of the process, L the integrated luminosity, $\epsilon_{\mathrm{filter}}$ the event filter efficiency and N_{MC} the number of MC simulated events. For many of the backgrounds the event weight is much greater than one. In this case a large statistical uncertainty is introduced from the MC and a realistic estimate of the background is impossible. In this analysis 'Object Weighting' was used to increase the statistical precision of some of the Monte Carlo samples. This means that instead of applying the full identification for some objects, a looser selection was applied and the object was weighted with a predetermined identification efficiency. Table 6.19 also shows the event weight for each background after the Object Weighting procedure was applied, calculated by multiplying the event weight by the Tau-ID and Lepton Isolation efficiencies averaged over the entire sample. With the inclusion of this procedure, a reasonable estimation of all background contributions was possible.

6.4.1 General procedure

The procedure used for Object Weighting is as follows:

- The object selection is split into loose and tight criteria.

- The identification efficiency for loose objects to pass the tight criteria is measured independently of the event selection.

- When running the analysis, objects are selected with the loose criteria and the event is weighted by the measured efficiency.

Object Weighting was considered for the Tau-ID and the Lepton Isolation. Table 6.20 indicates which Object Weighting was applied to each of the backgrounds. The Object Weighting cannot be used if there are large correlations between the tight criteria and the event selection. Therefore, the Tau-ID Weighting procedure was used only on backgrounds containing no real tau decays, and the Lepton Isolation Weighting was used only on QCD events.

6.4.2 Tau Identification Weighting procedure

The reducible backgrounds that contribute to the $\ell\tau_h$ channel contain no real hadronic tau decays. In these backgrounds an object (usually a QCD jet) is misidentified as a hadronic tau jet (fake tau). Figure 6.23 shows the fake-rate for loose pre-selected tau candidates to be misidentified as tight candidates (passing both tight pre-selection and tau event-selection) for the backgrounds where the Tau-ID Weighting procedure was used. In addition, the fake-rates were measured for the two cases where either a one-track only (left), or three-track only (right) requirement was included in the tight identification. This was necessary to accommodate the selection used in the analysis, where either a one or three track selection was used or a one-track only selection was used (see Table 6.17). For the three-track only case, the origin of the fakes is predominantly hadronic QCD jets, so a similar fake-rate is seen from all samples. However, for the one-track only case, there is a large contribution from lepton fakes, causing a difference in the fake-rates from QCD, W and $Z(\rightarrow \ell\ell)$, as the samples

Event weights for samples when scaled to $30\,\text{fb}^{-1}$

Event Weight	$W \rightarrow e\nu$	$W \rightarrow \mu\nu$	$W \rightarrow \tau\nu$	$Z \rightarrow ee$	$Z \rightarrow \mu\mu$	$Z \rightarrow \tau\tau$	$t\bar{t}$
W/o Weighting	83	83	10	24	24	4.7	1.8
(with weighting)	1.8	1.5	0.2	1.6	1.3	-	-

Event Weight	J2 (MLF)	J3 (MLF)	J4 (MLF)	$b\bar{b}$ J2	$b\bar{b}$ J3	$b\bar{b}$ J4
W/o Weighting	8500	9900	1300	3100	3500	1300
(with weighting)	3.2	0.31	0.0069	0.66	0.11	0.0083

Table 6.19: Event weights for samples when scaled to $30\,\text{fb}^{-1}$. Event weights are calculated before and after Object Weighting is applied. Object Weighting is not used in $Z \rightarrow \tau\tau$ and $t\bar{t}$, as discussed in Section 6.4.1.

Object Weighting used on the background samples

	QCD	$W \to \ell\nu$	$W \to \tau(\ell\nu)\nu$	$Z \to \ell\ell$	$Z \to \tau\tau$	$t\bar{t}$
Tau ID	YES	YES	YES	YES	NO	NO
Lepton Isolation	YES	NO	NO	NO	NO	NO

Table 6.20: Summary of the Object Weighting used on each of the background samples.

typically contain 0, 1 or 2 leptons, respectively. The fake-rate ranges from 10% to 0.1% for the different samples over the whole E_T range. In contrast, the ID efficiency for real loose tau candidates to pass the tight criteria can be seen in Figure 6.24. The summed efficiency for requiring either 1-prong or 3-prong tau candidates is roughly 70% with respect to the loose selection.
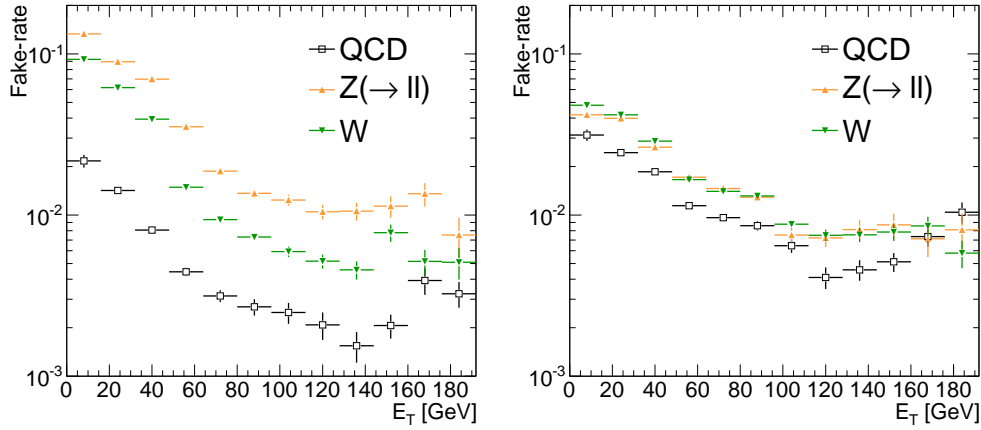
Figure 6.23: Fake-rates for loose tau candidates passing the tight ID vs. the E_T of the candidate. In the left plot the tight ID requires that the tau has exactly one charged track, and on the right exactly three. The increase in the 1-prong fake-rate for $Z \to \ell\ell$ compared to $W \to \ell\nu$ is due toelectron fakes.

6.4.2.1 Tau selection

In the standard analysis, both the loose and tight tau pre-selection are applied, then only events containing exactly one pre-selected tau are accepted. On the other hand, when the Tau-ID Weighting procedure is used, only the loose pre-selection is applied, to increase the number of pre-selected candidates. If the $n_\tau = 1$ selection is applied to the
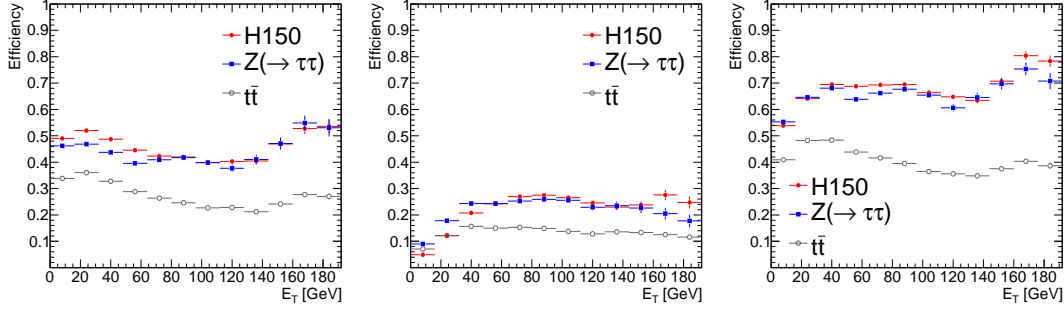
Figure 6.24: Identification efficiencies for loose tau candidates passing the tight ID vs. the E_T of the tau. The tau candidate was required to be matched within a cone of $\Delta R < 0.2$ to a generator-level hadronically decaying tau. In the left plot the tight ID requires that the tau has exactly one charged track, in the middle exactly three, and on the right either one or three.

number of loose pre-selected candidates, the efficiency of the cut will be underestimated as there can often be more than one pre-selected candidate. One solution is to actively separate the loose and tight pre-selection in the analysis. In this case one would always apply just the loose pre-selection at the object selection stage, make a choice of which pre-selected tau to use in the analysis (if there were multiple taus in the event), and then apply the tight pre-selection to the chosen tau in the event selection. The selection $n_\tau = 1$ must then be relaxed to $n_\tau \geq 1$ to avoid signal loss from additional loose pre-selected fake candidates. The advantage of such a procedure is that the event-selection can be treated in exactly the same way, regardless of whether the weighting is applied or not. Unfortunately, a difficulty arises in the choice of which pre-selected tau to use in the analysis. In previous analyses of the $\ell\tau_h$ channel, the highest p_T pre-selected tau was chosen. If this method is applied using the tight pre-selection, then in $> 99\%$ of signal events a correct choice of the hadronic tau from the Higgs boson decay is made. However, choosing the highest p_T loose pre-selected tau causes a large drop in the signal efficiency due to incorrectly selected tau candidates, as can be seen in Figure 6.25. The efficiency loss comes from choosing an object other than the tau coming from the Higgs boson when only the loose pre-selection is applied (usually a QCD jet initiated by one of the associated b-quarks) as this object is likely to fail the tight Tau-ID. Since this procedure cannot be used, the regular tight tau pre-selection and $n_\tau = 1$ selection was used in the standard analysis, and the loose tau pre-selection combined with the

relaxed cut $n_\tau \geq 1$ was used with the Tau-ID Weighting procedure. In addition, when using the Tau-ID Weighting procedure, all tau candidates had to be considered, and each combination of a tau candidate with the event kinematics was passed through the event selection. The final estimate was then calculated as the weighted sum of all the possible combinations.
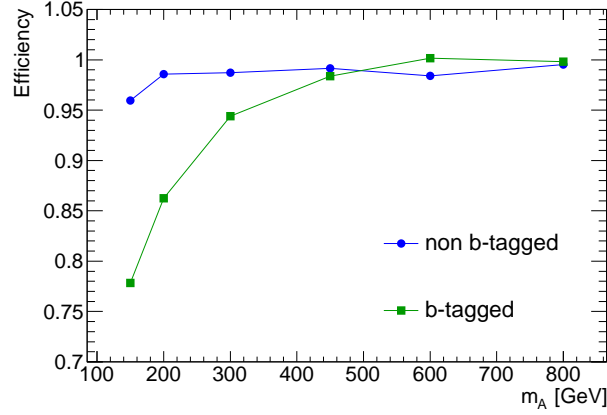
Figure 6.25: Efficiency for signal when choosing the highest E_T loose tau with respect to the highest E_T tight tau, at each Higgs boson mass hypothesis. The efficiency loss comes from choosing an object other than the tau coming from the Higgs boson when only the loose Tau-ID is applied (usually a QCD jet initiated by one of the associated b-quarks) as this object is likely to fail the tight Tau-ID. The efficiency loss increases as the tau E_T threshold is lowered since the b-quarks are soft. The b-tagged analysis suffers the most since it exhibits the lowest tau E_T thresholds.

6.4.2.2 Categorised Tau-ID Weighting

Although the majority of loose tau candidates come from light-quark and gluon-initiated QCD jets, some background samples also contain large numbers of electrons, muons and heavy-flavour quark jets. For samples such as QCD, these extra contributions are relatively low, and a simple treatment with no differentiation between tau candidate origin was sufficient. However, for other samples such as $Z \rightarrow ee$ (where electrons make a significant contribution), the separation of fakes into categories was essential.

The following categories for tau candidates were considered: muon, electron, semi-leptonic b-quark decay, hadronic b-quark decay and other, which consists mainly of light-quark and gluon-initiated QCD jets. The category for a tau candidate was determined by a spatial match to truth particles with a cone of $\Delta R = 0.2$ for leptons and $\Delta R = 0.3$ for b-quarks. Leptonic b-quark decays were distinguished from hadronic decays by requiring an additional match to either a muon or an electron. The first matching category was selected with the following order: leptonic b-quark, hadronic b-quark, muon, electron. If no match was found, the category 'other' was used. A p_T threshold of 15 GeV was applied to the generator particles. Further details regarding the categorisation can be found in Appendix B.3.

6.4.2.3 Tau fake-rate parameterisation

In Section 6.2 the optimisation of the tau likelihood cut in different E_T bins was described. This results in a relatively flat signal efficiency for the combined sum of 1-prong and 3-prong tau candidates, in the range of the optimisation 25 GeV $< E_T <$ 100 GeV, see Figure 6.24 (right). Above 100 GeV, the E_T dependence remains, since there is only one bin (100 GeV $< E_T$). On the other hand, the fake-rates shown in Figure 6.23 have a large E_T dependence over the entire tau E_T range. To obtain a sufficiently accurate description of the tau fake-rate for use in the Tau-ID Weighting procedure, the fake-rate was calculated in E_T bins (the same bins used for the likelihood optimisation). Furthermore, since the fake-rate includes a cut on the number of tracks, two separate parameterisations were made to accommodate the event selection where either one track (1P) is required, or either one or three tracks are required (1P3P). Thus the final tau fake-rate was parameterised in five E_T bins, for 1P and 1P3P selection and

in five generator level matched categories. A separate parameterisation was made for each background sample.

6.4.2.4   Summary of Tau-ID Weighting

Figure 6.26 shows the invariant mass distribution for a number of background samples directly after the Tau-ID was applied in the event selection. As a test of the Tau-ID Weighting procedure, the figure includes distributions where Tau-ID Weighting was not applied, when Tau-ID Weighting was applied using the fake-rate calculated only on 'other' candidates (as an approximation for all candidates) and where Tau-ID Weighting was applied with fully categorised tau candidates. For $Z \to ee$, the categorised procedure shows a significant improvement. Table 6.21 shows a comparison of the W+jets and $Z(\to \ell\ell)$+jets contributions, estimated with and without the Tau-ID Weighting procedure. The overall agreement is within statistical uncertainty.

<div align="center">

Cross check of the Tau-ID Weighting procedure

Sample	Cross Section [pb]	
	Without Weighting	With Tau-ID Weighting
W+jets	285 ± 23	276 ± 4
$Z(\to \ell\ell)$+jets	53 ± 6	48 ± 3

</div>

Table 6.21: Comparison of the estimated cross sections for W+jets and $Z(\to \ell\ell)$+jets when no Object Weighting was used, and when Tau-ID Weighting was used. The comparison was made after the *Opposite Sign* selection was applied, which includes as much of the event selection as possible while retaining sufficient statistical precision. For both samples the agreement is within the statistical uncertainty.
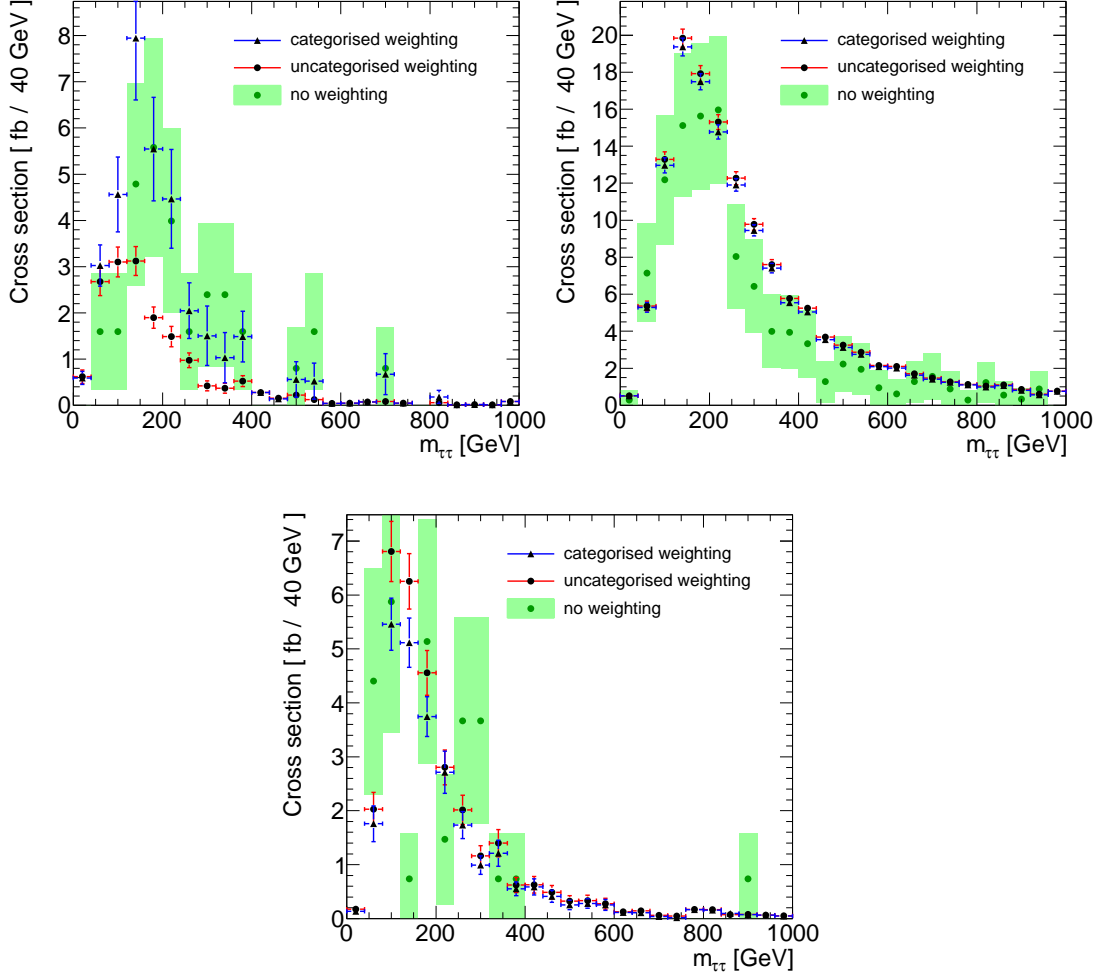
Figure 6.26: Invariant tau-tau mass distributions directly after the Tau-ID in the event selection. A comparison of the distribution is made when the Tau-ID Weighting was not applied and when the Tau-ID Weighting was applied with categorised and un-categorised weighting for $Z \rightarrow ee$ (top left), $W \rightarrow \tau\nu$ (top right), and $b\bar{b}$ J2 QCD (bottom) events.

6.4.3   Lepton Isolation Weighting

In the previous section the Tau-ID Weighting procedure was introduced. The method reduces the average event weight by $\mathcal{O}(100)$ (the average rejection factor for the tight Tau-ID). For W and $Z \to \ell\ell$ this was enough to reduce the event weight to approximately unity. However, for the QCD backgrounds the event weights were still much too large. For these backgrounds an additional method was required. Here, the Lepton Isolation is considered for weighting in a very similar way to the Tau-ID of the previous section.

The lepton selection is broken up into loose and tight criteria, where all the selection other than the isolation is applied in the loose selection and the isolation is applied in the tight selection (as described in Section 6.2).

6.4.3.1   Lepton selection

In the standard analysis, the highest p_T pre-selected lepton was chosen in the event-selection and the Lepton Isolation was applied in a separate step. Therefore no ambiguity arose in the selection of the lepton when applying the Lepton Isolation Weighting. This was important, since it meant that a loop over the loose leptons was not required.

6.4.3.2   Lepton Isolation parameterisation

The Lepton Isolation efficiency was defined as the rate at which loose leptons passed the tight isolation criteria. For a number of reasons the parameterisation of the Lepton Isolation efficiency was much simpler than for the Tau-ID. The lepton selection was not analysis dependent. No match to generator level objects was needed, since the loose lepton composition was made almost entirely of leptons. Finally, the Lepton Isolation efficiency was much less sensitive to the lepton p_T than the Tau-ID. Figure 6.27 shows the Lepton Isolation efficiencies for electrons and muons against p_T. Although for the $b\bar{b}$ J2 QCD events there was a visible correlation between efficiency and p_T the rest of the samples were relatively flat within statistical uncertainty. A single number for the overall efficiency of each sample was considered adequate, the efficiencies are listed in Table 6.22. Figure 6.28 shows good agreement in the transverse mass distribution for QCD events, with and without the use of Lepton Isolation Weighting before selection on m_T was applied in the event selection.
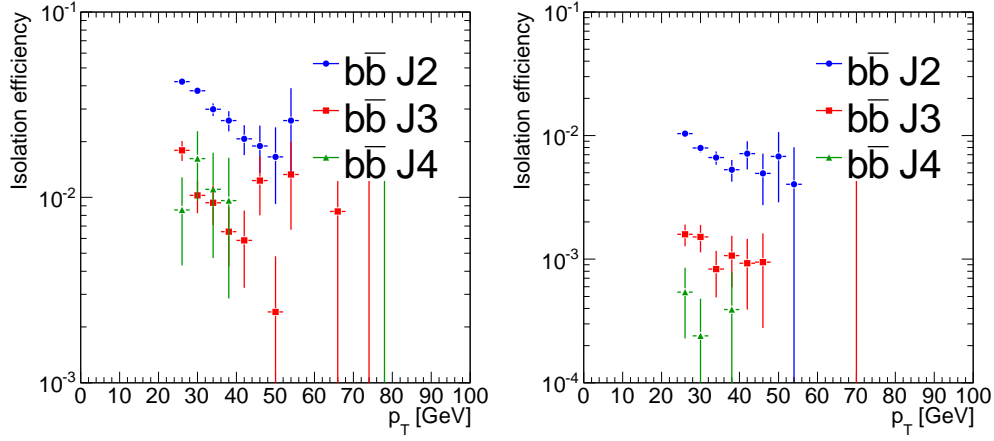
Figure 6.27: Lepton Isolation efficiencies against p_T for $b\bar{b}$ QCD samples for electrons (left) and for muons (right).
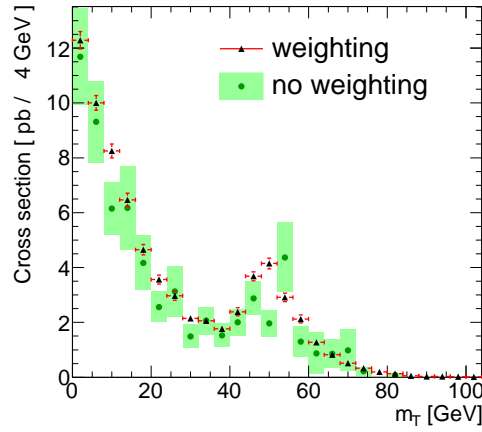
Figure 6.28: Transverse mass for QCD background, with and without the use of Lepton Isolation Weighting before the cut on m_T is applied in the event selection.

151

Lepton Isolation efficiencies for QCD samples

	J2 (MLF)	J3 (MLF)	J4 (MLF)	J5 (MLF)	J6 (MLF)
Muon	(1.0 ± 0.6)E-2	(1.3 ± 0.2)E-3	(2.9 ± 0.8)E-4	(4.1 ± 2.9)E-5	(2.4 ± 2.4)E-5
Electron	(4.5 ± 0.2)E-2	(1.2 ± 0.1)E-2	(6.8 ± 1.4)E-3	(6.4 ± 1.8)E-3	(9.7 ± 2.6)E-3
	$b\bar{b}$ J2	$b\bar{b}$ J3	$b\bar{b}$ J4	$b\bar{b}$ J5	$b\bar{b}$ J6x
Muon	(8.9 ± 0.3)E-3	(1.2 ± 0.2)E-3	(2.0 ± 0.9)E-4	(2.4 ± 0.9)E-4	(6.8 ± 4.8)E-5
Electron	(3.7 ± 0.1)E-2	(1.1 ± 0.1)E-2	(6.2 ± 1.7)E-3	(5.9 ± 2.2)E-3	(9.0 ± 3.2)E-3

Table 6.22: Summary of Lepton Isolation efficiencies for QCD samples.

A comparison of the QCD contribution estimated with and without Lepton Isolation Weighting is shown in Table 6.23. A small positive bias of $\sim$15%, corresponding to two standard deviations, was found following selection on the transverse mass after Lepton Isolation Weighting was applied. The table also includes an estimate for the QCD dijet background when both the Lepton Isolation and Tau-ID Weighting procedures were applied. In this case, the addition of the Tau-ID Weighting causes a small negative bias just outside one standard deviation. The total uncertainty on the QCD estimate from the use of both the Tau-ID and Lepton Isolation Weighting procedures was assumed to be $\lesssim$ 20%, which occurred with no more than a two standard deviation bias.

6.4.4 Summary of the Object Weighting procedure

By including the Object Weighting procedure in the analysis, a reasonable estimate of the background contributions was possible with the available Monte Carlo samples. Comparisons of the background contributions with and without the use of Tau-ID and Lepton Isolation Weighting, such as those in Figures 6.26 and 6.28, show reasonable agreement. Comparisons were also made at all points in the event selection, and a summary of the agreement is given in Tables 6.21 and 6.23, in Appendix B.3.1. For samples where only the Tau-ID Weighting was used, no bias outside statistical uncertainty was observed when applying the weighting method. For QCD, where both the Tau-ID and Lepton Isolation Weighting procedures were applied, a small bias of $\lesssim$ 20% was found, occurring at no more than two standard deviations.

Finally, it is expected that after the collection of $30\,\mathrm{fb}^{-1}$ of collision data, Monte Carlo samples large enough to directly estimate all background contributions (other

Cross check of the Lepton Isolation Weighting procedure

| | Cross Section [pb] | | | |
| | Without Weighting | With Weighting | | |
Cut		Tau-ID	Lepton Isolation	Both
Transverse Mass	40300 ± 3100	–	46000 ± 600	–
Tau-ID	*	126 ± 17	187 ± 51	161 ± 6
Invariant Mass	*	70 ± 14	134 ± 50	72 ± 4
Opposite Charge	*	43 ± 11	104 ± 48	39 ± 2

Table 6.23: Comparison of the estimated cross section for QCD (including both di-jet and $b\bar{b}$ processes) when no Object Weighting was used, and when Tau-ID Weighting or Lepton Isolation Weighting or Both were used. It was impossible to make a direct comparison between the No Object Weighting scenario and the Both Object Weighting scenario, as there were very few QCD events remaining after applying both tight Tau-ID and Lepton Isolation. Instead, a comparison was made at a number of points in the event selection so that individually, both weighting methods could be validated, and then the validation of their combination inferred. The cross sections at the Transverse Mass cut indicate a small positive bias outside of statistical uncertainty for the Lepton Isolation Weighting ($\lesssim 15\%$) at the level of two standard deviations. On the other hand, the cross sections after the last three selection criteria show a negative bias when applying Tau-ID Weighting compared to Lepton Isolation Weighting, which is just outside of statistical uncertainty. It is probably safe to assume that the combined bias for the combination of both weighting methods in QCD events is $\lesssim 20\%$, which occurs at most at the level two standard deviations. The cells marked * have too few events remaining for comparison, and the cells marked – are not included since the Tau-ID has not been applied at this point in the event selection.

than QCD) will be available. For these backgrounds the Object Weighting procedure will no longer be required. For QCD, either the data-driven background estimation technique developed in this study, or a more advanced technique will be used to estimate the background contribution. Therefore the small uncertainty introduced by the Object Weighting procedure was not included in the calculation of the discovery potential.

6.5 Systematic uncertainties

In this section the systematic uncertainty on the estimates of the signal and background contributions is evaluated. The treatment of systematic uncertainties was based on the prescription given in [36]. The method from the $A \rightarrow \tau\tau \rightarrow \ell\ell$ channel was used (with the addition of adapted techniques for uncertainties related to tau candidates), so that a statistical combination of both results would be valid. The uncertainties calculated in this section apply to direct MC estimates of the various contributions. While some of the minor backgrounds are estimated directly from MC, data-driven background estimation methods have been developed for all of the major backgrounds. The systematic uncertainties of these methods are evaluated and discussed in [1], and the W+jets and QCD estimation, which is the work of the author, is also discussed in Section 6.6. All other backgrounds were estimated directly from Monte Carlo samples. For these backgrounds the total uncertainty must be calculated by including: the full experimental uncertainties, the luminosity uncertainty and the theoretical uncertainty on the production cross section.

6.5.1 Experimental uncertainties

Experimental uncertainties refer to the uncertainty on any of the quantities measured by the detector. These include uncertainties associated with the reconstruction of the various particles used in the analysis: electrons, muons, tau leptons and jets, and the integrated luminosity recorded by the detector. For this analysis, an uncertainty of 3% on the integrated luminosity was assumed [36], which is directly propagated to the uncertainty on the MC estimates. The uncertainties associated with particle reconstruction are summarised in Table 6.24 and include uncertainties on the energy scale, energy resolution and reconstruction efficiency of the reconstructed candidates. To evaluate the effect of these uncertainties on the result of the analysis, the complete analysis was run independently varying each of the parameters. The result was then compared to the standard result to estimate the uncertainty. The implementation was performed as follows:

- Scale: The analysis was run twice, scaling the Lorentz vectors of the corresponding particles up and then down by ΔE. An average of both variations was taken as the uncertainty.

- Resolution: The analysis was run once, smearing the Lorentz vectors of the corresponding particles by randomly drawing an energy shift, ΔE, from a Gaussian of mean, $\mu = 0$ and width, $\sigma = \sigma(E)$, where $\sigma(E)$ is the resolution smearing required.

- Efficiency: The analysis was run once, randomly removing a fraction ($\Delta\epsilon$) of the corresponding particles. A random number ($rand \in [0, 1]$) was generated with a flat distribution. If $rand < \Delta\epsilon$ then the particle was discarded. The up and down variation was assumed to be the same and the uncertainty was taken as the magnitude of the down variation.

- b-tagging Efficiency: The analysis was run once, randomly un-tagging a fraction ($\Delta\epsilon_{b-\text{tag}}$) of the b-tagged jets. The method is exactly the same as for the other efficiencies except a $\Delta R < 0.2$ match to a generator-level b-quark was required.

- Light jet rejection: First, the light jet fake-rate, 'f' was extracted for each sample. Then, the analysis was run once, randomly tagging a fraction ($\Delta f_{\text{l-jet}}$) of the light jets as b-jets. The light jets were tagged only if they failed a $\Delta R < 0.2$ match to generator b-quarks and if $rand < f \cdot \Delta f_{\text{l-jet}}$.

For both the scale and resolution variations the change in the particle momentum vector,

$$\Delta\vec{p} = \vec{p}\,' - \vec{p} \tag{6.12}$$

was propagated to the $\vec{\not{E}}_\text{T}$ vector. The adjusted $\not{E}_\text{T}$ was calculated as:

$$\not{E}_\text{T}{}' = \not{E}_\text{T} - \sum_i \Delta p_i \tag{6.13}$$

where i runs over all scaled momentum vectors in an event. The energy scale correction for jets and taus is currently not used in the calculation of $\not{E}_\text{T}$. This is mainly due to the difficulty of separating out hadronic corrections and corrections for out-of-cone energy, which are already accounted for by the $\not{E}_\text{T}$ reconstruction. However, there are plans to incorporate such corrections in the future. Therefore, for the jet and tau energy scale variations, only 5% of $\Delta\vec{p}$ was propagated to $\not{E}_\text{T}{}'$. The propagation was only performed for particles that passed the object selection defined in Section 6.2, which loosely matches the selection used in the $\not{E}_\text{T}$ reconstruction.

The implementation of the above method is straightforward, however, the procedure requires large Monte Carlo samples to obtain reasonable estimates of the individual variations. For most of the MC samples in this analysis there were only a handful of events remaining by the end of the event selection. This made it impossible to obtain an accurate estimate of the individual variations by simply counting the events remaining at the end of the event selection. In the $A \to \tau\tau \to \ell\ell$ analysis [36], very large samples were produced with ATLFAST-I for the purpose of studying the systematics. Similar samples were not available for this study. Instead, a new method was developed to estimate systematic uncertainties with small statistical samples.

6.5.2 Evaluation of systematic uncertainties

Although there were often very few events remaining after applying the entire event selection, each systematic uncertainty usually only affected the efficiency of a few of the selection criteria. To determine which criteria were affected, each of the systematic uncertainties was evaluated after each criterion in the event selection. By studying the systematic effect as a function of the event selection, it was possible to find a point in the event selection for each individual systematic where all the following variations were only statistical fluctuations. If sufficient events remained at this point, and it could be verified that there really were no significant correlations with the remaining selection, then a reasonable estimate of the systematic uncertainty could be made. The systematics were broken up into three distinct categories defined by their level of correlation to the event selection: efficiency, b-tagging and scale or resolution. Finally, the study was repeated a second time with a re-ordered event selection as a cross-check.

Experimental systematic uncertainties

	Scale	Resolution	Efficiency
Electron	$\Delta E_\mathrm{T} = 0.2\%$	$\sigma(E_\mathrm{T}) = 0.00073 \cdot E_\mathrm{T}$	$\Delta\epsilon_e = 0.2\%$
Muon	$\Delta p_\mathrm{T} = 1.0\%$	$\sigma\left(\frac{1}{p_\mathrm{T}}\right) = \left(\frac{0.001}{p_\mathrm{T}}\right) \oplus 0.00017$	$\Delta\epsilon_\mu = 1.0\%$
Tau	$\Delta E_\mathrm{T} = 3.0\%$	$\sigma(E) = 0.45\sqrt{E}$	$\Delta\epsilon_\tau = 5.0\%$
Jet	$\Delta E = 3.0\%(|\eta| < 3.2)$	$\sigma(E) = 0.45\sqrt{E}(|\eta| < 3.2)$	$\Delta\epsilon_{b-\mathrm{tag}} = 5.0\%$
	$\Delta E = 10\%(|\eta| > 3.2)$	$\sigma(E) = 0.63\sqrt{E}(|\eta| > 3.2)$	$\Delta f_{\mathrm{light-jet}} = 10.0\%$

Table 6.24: Summary of experimental systematic uncertainties. All energy and momenta are in units of GeV.

Efficiency and *b*-tagging systematic variations

	$\Delta\epsilon_e$	$\Delta\epsilon_\mu$	$\Delta\epsilon_\tau$	$\Delta\epsilon_{b-\text{tag}}$	$\Delta f_{l-\text{jet}}$
Signal	0.1	0.5	5	0.5 (2.3)	0.3 (1.0)
$W \to e\nu$	0.2	-	5	0.0 (2.0)	0.1 (5.0)
$W \to \mu\nu$	-	1.0	5	0.0 (2.0)	0.1 (5.0)
$W \to \tau\nu$	0.2	0.5	5	0.0 (0.8)	0.1 (4.3)
$Z \to ee$	0.2	-	5	0.0 (1.8)	0.2 (6.0)
$Z \to \mu\mu$	-	1.0	5	0.0 (1.5)	0.2 (5.5)
$Z \to \tau\tau$	0.1	0.5	5	0.0 (1.8)	0.4 (3.2)
QCD	0.2	0.5	5	2.0 (3.0)	1.0 (3.0)
$t\bar{t}$	0.2	0.5	5	5.0 (2.0)	4.0 (1.5)

Table 6.25: Summary of efficiency and *b*-tagging systematic variations (%). Numbers in parentheses indicate the variations for the *b*-tagged analysis when different from the non *b*-tagged analysis.

6.5.3   Evaluation of efficiency systematics

The efficiency systematics were straightforward to calculate since there was little correlation between randomly removing a particle and the event selection. Figure 6.29 shows the muon efficiency systematic variation for two samples as a function of the regular event selection (top) and the re-ordered selection (bottom). For $W \to \tau\nu$ the systematic variation is shown for the selection used at each mass point. The plots give a specific example of how the efficiency variations were calculated. They also show how the reordered event selection was used to cross-check the variations calculated with the regular event selection. The methods used in this specific example were applied to all the datasets and repeated for the electron and muon efficiencies. For the QCD samples the Lepton Isolation was found to have a large effect on the lepton efficiency variation. All other samples were checked and were consistent with a flat lepton systematic variation after the Lepton Isolation. A similar behaviour was seen in the tau efficiency systematic uncertainty, where the variation was found to stabilise after the Tau-ID was applied. A summary of the systematic efficiency variations is given in Table 6.25.
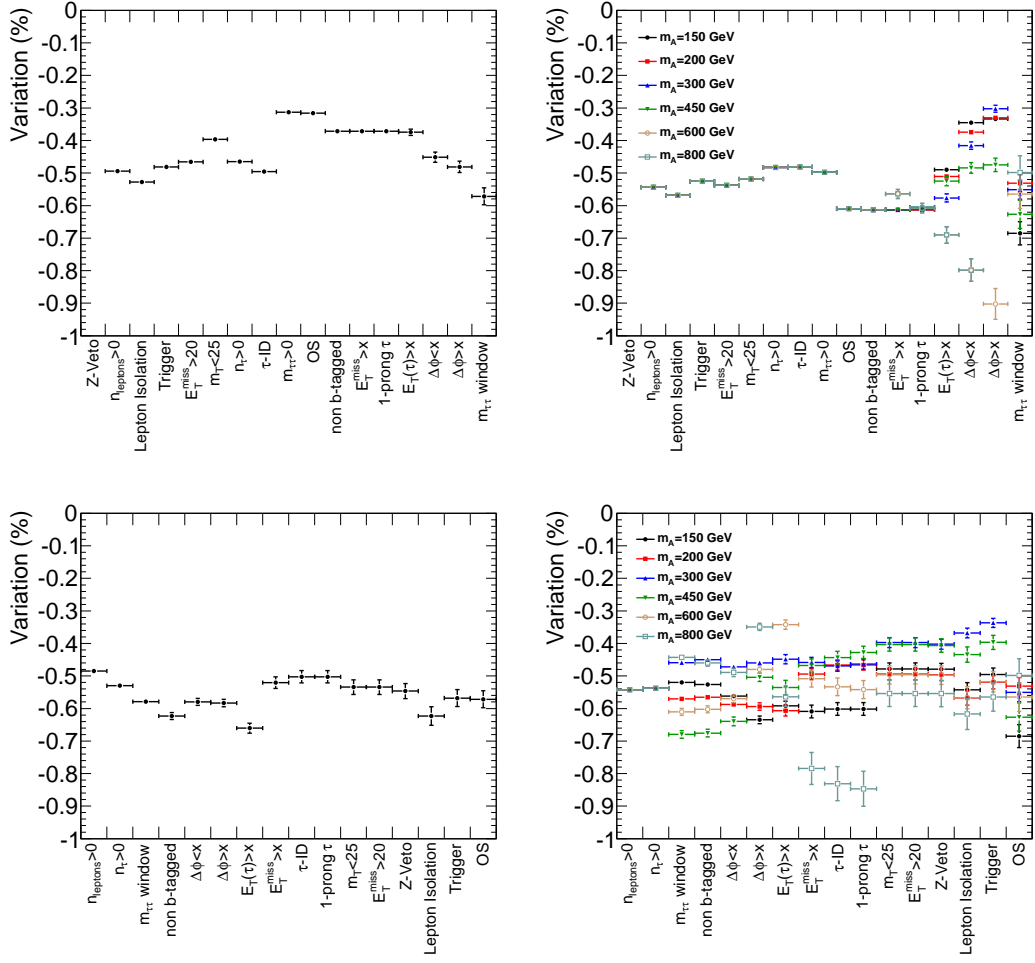
Figure 6.29: Muon efficiency systematic variation for the $m_A = 150$ GeV signal sample (left) and $W \to \tau\nu$ (right). The variation is given as a function of the event selection. Selection criteria where the variable, 'x' is used rather than a specific value, take the values defined in Section 6.3.4.2 for each specific mass point. The top plots correspond to the regular event selection and the bottom plots to the reordered event selection. For the signal an initial variation of -0.5% can be seen after the loose lepton selection. Although there are some small fluctuations around the initial value the variation remains relatively constant. The reordered event selection shows a small fluctuation in the opposite direction of the regular selection, however is still consistent with the central value of -0.5%. For $W \to \tau\nu$ a variation of -0.5% can also be seen after the Lepton Isolation, however, some correlation is also seen at the opposite-sign selection which pushes the variation to $\sim -0.6\%$. The effect of the analysis dependent selection is difficult to determine from the regular ordered selection, however, in the reordered event selection the different sets of selection form a distribution that is centred around the original value from the regular event selection. A central value of -0.5% was taken as the variation.

6.5.4 Estimation of *b*-tagging systematics

The technique used to estimate the efficiency variations had to be modified slightly for the *b*-tagging efficiencies. This is because the *b*-tagging only takes effect at the point when the analysis is split into the *b*-tagged and non *b*-tagged analyses. In the regular ordered event selection, the split is very close to the end of the selection. There were often too few events remaining to evaluate the systematic variation at this point and the variation due to the preceding variables also couldn't be measured. Instead, the ratio of *b*-tagged and non *b*-tagged events was calculated at a selected number of points in the event selection. These were: 'Start' (before the event selection was applied), 'Tau-ID' (after the Tau-ID was applied) and 'Split' (just before the analysis split). The ultimate goal was to predict the systematic variation at the point of the Split. The numbers for all samples at the three points are shown in Table 6.26. The samples marked with a dagger, had too few events to properly evaluate the *b*-tagging variation at the point of the Split. However, for all the other samples, a good agreement was found between the numbers after the Tau-ID and the numbers at the Split. The correlation between *b*-tagging and Tau-ID was expected, due to the close interplay between the Tau-ID and *b*-jets. Since the same correlation was seen in all samples, and there was no good reason to believe that any additional correlations would arise in the low event samples, the systematic variation calculated at the Tau-ID point was used to estimate the *b*-tagging systematic variations. This procedure was then checked by changing the order of the event selection, where the *b*-tagging split was moved close to the start of the analysis. Good agreement was found in both of the results. Figure 6.30 shows the *b*-tag efficiency variation as a function of the reordered event selection. The procedure gives different variations for the *b*-tagged and non *b*-tagged analyses and was used to evaluate both the *b*-tagging efficiency and light-jet rejection. This procedure assumes that the efficiency and rejection systematic variations are uncorrelated, however, this not necessarily true and should be investigated in the future.

6.5.5 Estimation of scale and resolution systematics

The scale and resolution systematics were the most difficult to evaluate. This is because the kinematics of the particles are highly correlated with the event selection. This made it quite difficult to predict the behaviour of the systematic variation when

event numbers were small. To evaluate the scale and resolution uncertainties the event selection method used to evaluate the efficiencies was used with the addition of the following techniques:

- Trends in samples with lower statistical uncertainty were studied and used as a guide for evaluating samples with higher statistical uncertainty.

- Some selection criteria were loosened in samples with very high statistical uncertainty to identify the main sources of variation.

- Both the up and down scale variations were compared to cross-check for statistical fluctuations.

- The study was performed twice, once with the standard event selection and once with a reordered event selection to cross-check the results.

- When large variations were seen for selection criteria that were known to have little correlation with a systematic effect, the variation was assumed to be a statistical fluctuation.

The most powerful technique to determine if an effect was due to statistical fluctuation was the reordering of the event selection. By shifting criteria from the end of the regular selection to the start of the reordered selection, it was possible to gauge the systematic variation for each of the selection criteria in at least one statistically significant location.

Evaluation of b-tagging systematic variations

	bbA	ggA	$W \to e\nu^{\dagger}$	$W \to \mu\nu^{\dagger}$	$W \to \tau\nu$	$Z \to ee^{\dagger}$	$Z \to \mu\mu^{\dagger}$	$Z \to \tau\tau$	$t\bar{t}$
Start	0.4	0.02	0.03	0.02	0.04	0.05	0.05	0.03	5.0
Tau-ID	0.5	0.02	0.04	0.06	0.03	-	0.001	0.1	5.8
Split	0.6	0.02	0.1	0.06	0.02	-	-	0.1	7.1

Table 6.26: The b-tagging systematic variations (%) at three points in the event selection. The samples marked with a dagger had too few events remaining to evaluate the variation at the split point. For the other samples a good agreement can be seen between the variation at the Tau-ID and Split. The variation corresponds to the change in the number of events going into the non b-tagged analysis.
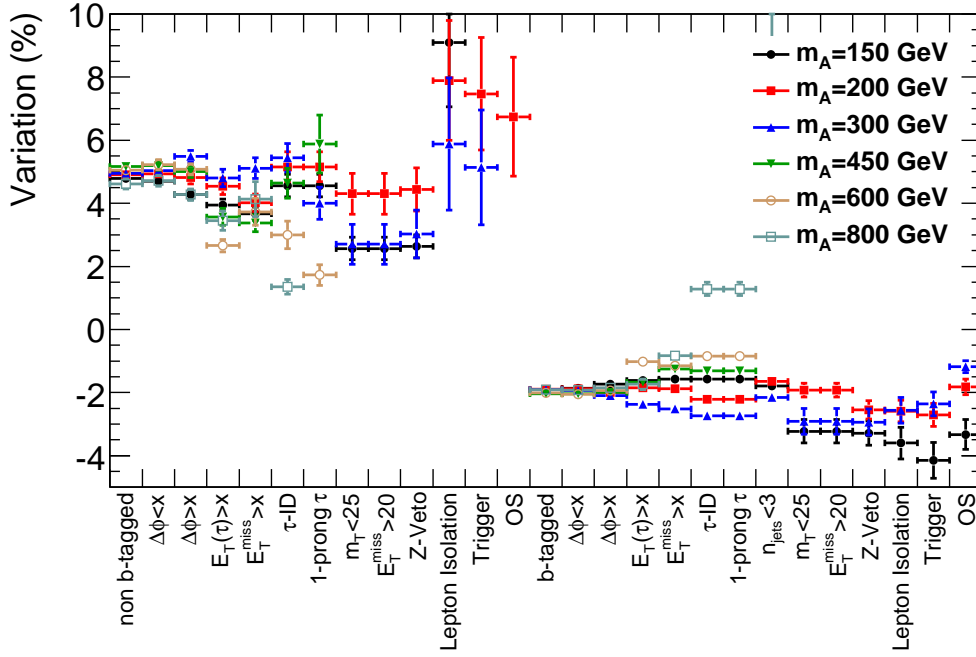
Figure 6.30: b-tagging efficiency variation for $t\bar{t}$ as a function of the reordered event selection. Criteria where the variable 'x' is used rather than a specific value take the values defined in Section 6.3.4.2 for each specific mass point. The first set of points corresponds to the non b-tagged analysis and the second to the b-tagged analysis. The random un-tagging causes an out flux from the b-tagged analysis and an influx into the non b-tagged analysis. In each case a common variation is seen in all analyses directly after the analysis split. Large statistical fluctuations develop further into the event selection, however, the initial value of the variation is consistent with the value obtained in Table 6.26.

Using all of the above techniques the scale and resolution systematics were evaluated manually for each particle type and on each sample. Wherever ambiguity arose in the estimation of a variation, a conservative estimate was given. The complete evaluation was performed using the regular event selection, and then repeated using the reordered selection. For the majority of systematic effects a consistent estimation was obtained from both the regular and reordered event selection. The cases where a match was not obtained were due to severe lack of Monte Carlo data. For these cases, a comparison of the two results was made to determine the non-statistical variations, and the largest

of these variations was taken to be the systematic uncertainty. A complete summary of the scale and resolution systematics is given in Table 6.27.

Scale and resolution systematic variations

	Jet			τ			e			μ		
	ΔE↑	ΔE↓	$\Delta\sigma$(E)	ΔE↑	ΔE↓	$\Delta\sigma$(E)	ΔE↑	ΔE↓	$\Delta\sigma$(E)	Δp_T↑	Δp_T↓	$\Delta\sigma p_\mathrm{T}$
Signal	0 (1)	0 (1)	1 (1)	1	2	2	0.5	0	0	0.5	0.5	0.5
$W \to e\nu$	0.5	0.5	1	< 5	< 6	2	1	1	0	2	3	0
$W \to \mu\nu$	0.5	0.5	1	< 5	< 6	2	1	1	0	2	3	0
$W \to \tau\nu$	0 (0.5)	0 (1)	1 (5)	< 5	< 6	1	0.5	0.5	0	0.5	0.5	0
$Z \to ee$	2	2	5	3	3	1	2	1	1	-	-	-
$Z \to \mu\mu$	0 (2)	0 (2)	3	< 6	< 7	2	-	-	-	5	5	0
$Z \to \tau\tau$	1	0	1	5	10	4	1	0.5	0	1	1	0.5
QCD	1 (3)	1 (2)	5	5	5	2	1	1	1	2	2	0
$b\bar{b}$-QCD	1 (3)	1 (2)	5	5	5	2	1	1	1	2	2	0
$t\bar{t}$	2 (3)	1	3	< 6 (< 10)	5 (< 7)	2	1	0	0	1	2	0

Table 6.27: Summary of scale and resolution systematic variations (%). Numbers in parentheses indicate the variations for the *b*-tagged analysis when different from the non *b*-tagged analysis.

6.6 Data-driven W+jets and QCD estimation

In this section, the development of data-driven estimation procedures for the W and QCD backgrounds is described. A control region that is very pure in W events is used to estimate the background contribution in the data-driven W estimation procedure. The method was developed on the non b-tagged analysis where W events comprise a significant proportion of the total background. In principle, the result could also be scaled to the b-tagged analysis by accurately measuring the ratio of b-tagged to non b-tagged events for W. However, as W makes only a small contribution to the b-tagged analysis, this procedure was not developed. The Opposite-Sign/Same-Sign (OS/SS) subtraction method is employed in the data-driven estimation procedure for the QCD background. Both data-driven techniques estimate the number of events expected in the final mass window, rather than accurately predicting the shape of background distributions. This is sufficient as the analysis is a counting experiment, where the signal is extracted by looking for an excess of events over the expected background within a mass window.

6.6.1 Estimation of the background from W+jets

6.6.1.1 Control region

A control region was defined where W events could be accurately measured from data. The number of events found in the control region (N_W^{con}) is then scaled back to estimate the number of events expected in the signal region (N_W^{sig}):

$$N_W^{\text{sig}} = R \cdot N_W^{\text{con}}. \tag{6.14}$$

The ratio 'R' was taken from MC since no technique to extract the ratio from data has been found so far. Values for R at each Mass point are given in Table 6.28 including its experimental systematic uncertainty, which is calculated later in this section. The choice of the control region was made based on the following requirements:

- Large number of events - $N_W^{\text{con}} \gg N_W^{\text{sig}}$, so that the statistical uncertainty in the control region is negligible.

- High purity - any contamination in the control region will bias the estimate of N_W^{sig}.

- Close to signal region - the control region must be as close to the signal region in phase space as possible. This is important since the ratio 'R' is taken from MC, and differences in the kinematics between the two regions will make the method susceptible to experimental uncertainties.

The first and last requirement can create a tension in the choice of control region. While moving the control region closer to the signal region reduces the experimental uncertainty of the method, it often significantly reduces the size of the sample in the control region, increasing the statistical uncertainty. A balance between the two must be reached.

The control region was then defined by changing a small number of criteria from the regular event selection in order to satisfy these requirements. The following choice of the control region was found to be optimal:

1. The *baseline* selection was applied, as described in Section 6.3.

2. The $m_{\tau\tau} > 0$ requirement was removed (physical solution to invariant mass reconstruction).

3. The $m_T < 25$ GeV requirement was removed (transverse mass selection).

4. The transverse mass was required to be in the window 60 GeV $< m_T < 90$ GeV.

The justification for this selection is given below.

W control region ratio

m_A [GeV]	Ratio [$\times 10^{-3}$]	Uncertainty [%]
150	2.0	3.4
200	1.7	3.3
300	0.30	3.8
450	0.17	5.0
600	0.089	7.4
800	0.049	6.3

Table 6.28: Ratio from the W control region to the signal region for W+jets calculated from MC at each mass point. The experimental systematic uncertainty is also included.

The baseline selection was applied so that the region of phase space occupied by the control region was close to the signal region. The remaining selection was not included since it contains tight selection on the tau E_T and $\not{E}_\mathrm{T}$ that can severely reduce the number of events in the control region. Figure 6.31 shows the tau E_T and $\not{E}_\mathrm{T}$ distributions for W. The optimised thresholds on these variables for different mass points can be up to 130 GeV and 60 GeV, respectively, which severely decreases the statistical size of the control sample.
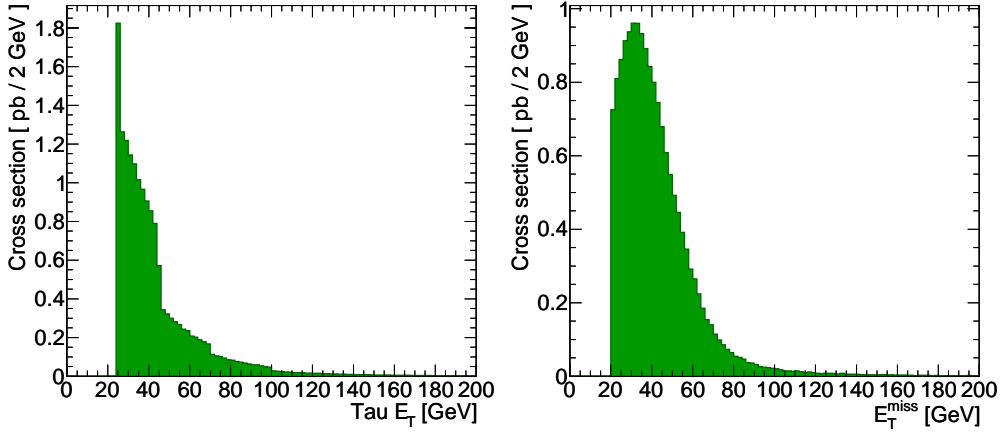
Figure 6.31: Tau E_T and $\not{E}_\mathrm{T}$ distributions for W events in the W control region. The optimised selection on tau E_T and $\not{E}_\mathrm{T}$ have thresholds up to 130 GeV and 60 GeV, respectively, which strongly depletes the number of W events. These criteria must be dropped from the control region.

There is a large correlation between the mass reconstruction and the transverse mass in W events. The collinear approximation used in the mass reconstruction assumes that the neutrinos are in the same direction as the visible decay products. To obtain a physical solution, the missing energy vector must lie in between the tau and lepton vectors in the transverse plane. In W events the neutrino and lepton tend to be in the same hemisphere with a recoiling jet misidentified as a tau. Figure 6.32 shows the angular distribution between the sum of the tau and lepton vectors $(\vec{p_\ell} + \vec{p_\tau})$ and the $\not{E}_\mathrm{T}$ vector in the transverse plane. For signal, the $\not{E}_\mathrm{T}$ and the decay products share the same hemisphere in roughly half of the events, whereas for W they occupy opposite hemispheres in almost all the events. This means that in most of the W events a

physical mass will not be reconstructed. The selection requiring that the reconstructed mass be physical was therefore removed from the control region.
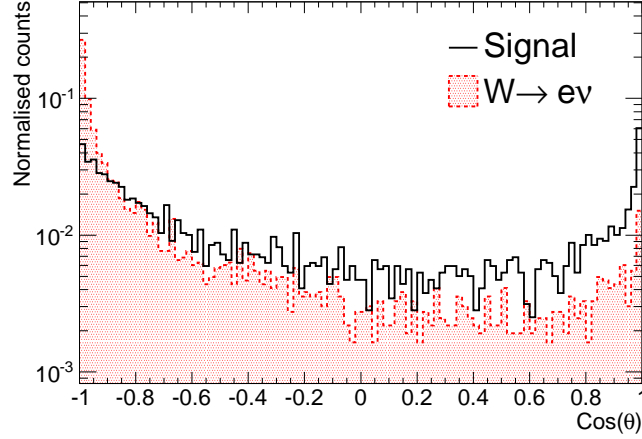
Figure 6.32: Distribution of $\cos\theta$, where θ is the angle in the transverse plane between the vector sum of the lepton and tau momenta $(\vec{p}_\ell + \vec{p}_\tau)$ and the missing transverse energy. Events where the missing transverse energy is in the opposite direction of the tau and lepton fail the mass reconstruction since the neutrinos are assumed to be in the same direction as the decay products. Requiring a real solution to the mass reconstruction suppresses a large fraction of $W \to \ell\nu$ events, so the criterion must be dropped from the control region.

The transverse mass exhibits large discriminating power against events containing real W bosons. Figure 6.33 (left) shows the transverse mass distribution just before the $m_{\mathrm{T}} < 25$ GeV criterion was applied in the event selection. The criterion was used specifically to discriminate against the W background. By removing this selection and applying a window around the W transverse mass peak (60 GeV$< m_{\mathrm{T}} < 90$ GeV), a very pure sample of W events was obtained. Figure 6.33 (right) shows the transverse mass distribution for the control region (without the window applied), which retains a sharp peak with a large number of events. Figure 6.34 shows the $m_{\tau\tau}$ mass spectrum for W+jets events in the signal and control region. Although the method does not require good agreement between the two distributions to be used in this analysis (as only a single number estimate of the number of W events in the final mass window is required), the level of agreement indicates that the method could also be used in an analysis where the shape was required.

Figure 6.33: Transverse mass distribution just before selection on the transverse mass is made in the analysis (left) and in the control region without the transverse mass window applied (right).

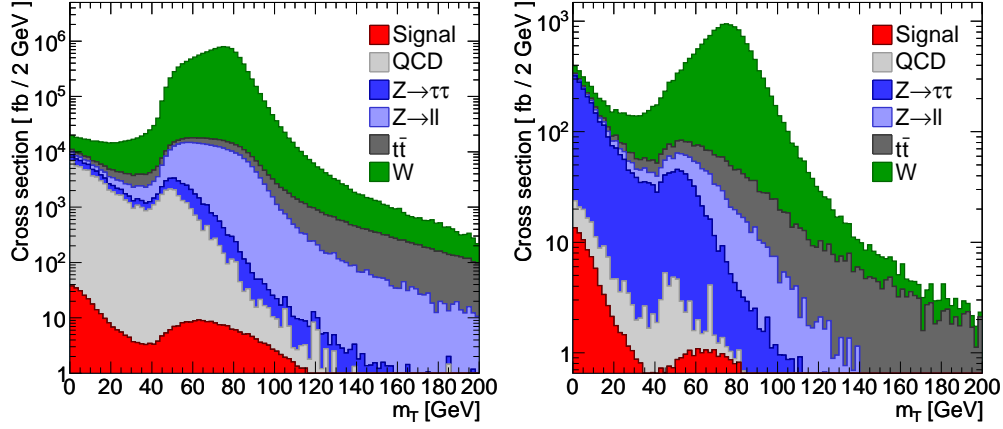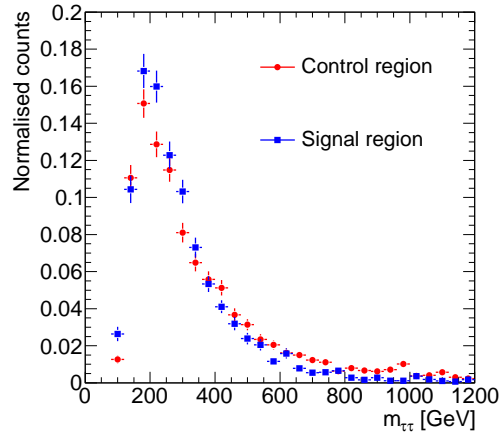**Figure 6.34:** Invariant $m_{\tau\tau}$ distributions in the control and the signal regions. The distributions are in good agreement.

167

The composition of the control region can be seen in Table 6.29. The region contains sufficient events, however the purity is only 92.8 %. This causes a bias of 8% in the estimate of W in the signal region ($N_{W,\text{est}}^{\text{sig}}$). A large fraction of the contamination in the control region comes from $t\bar{t}$ ($N_{t\bar{t}}$), and the removal of this contamination can significantly reduce the bias.

6.6.1.2 Removing $t\bar{t}$ contamination

By requiring $n_{b-\text{jet}} = 2$ rather than $n_{b-\text{jet}} = 0$, a second control region was defined, which had 99% $t\bar{t}$ purity. Figure 6.35 shows the number of b-tagged jets in W and $t\bar{t}$ events (left) and the transverse mass distribution for the control region when $n_{b-\text{jet}} = 2$ (right). The b-tagging efficiency will be measured very accurately by the top group. Hence the ratio of $n_{b-\text{jet}} = 0$ to $n_{b-\text{jet}} = 2$ events in $t\bar{t}$ is expected to be known to high precision. This ratio can be used to scale the number of $t\bar{t}$ events measured from the $n_{b-\text{jet}} = 2$ control region back to the W control region to remove the $t\bar{t}$ contamination. After the $t\bar{t}$ contamination in the control region was subtracted, the bias was reduced to 4% (see Table 6.30). The remaining contamination was almost entirely due to $Z \to \ell\ell$ events where one lepton escaped the detector. These events look exactly the same as

Composition of the W control region

	$N_{\text{exp}}(30\,\text{fb}^{-1})$	[%]
	control region	
N_{ALL}	336100	
N_W	311700	93
$N_{t\bar{t}}$	11750	3.5
	signal region	
N_W^{sig}	616	
$N_{W,\text{est}}^{\text{sig}}$	664	
Bias		+7.8%

Table 6.29: Composition of the W control region. The numbers correspond to the expected number of events in $30\,\text{fb}^{-1}$. N_{ALL} is the total contribution from all processes in the control region and N_W and $N_{t\bar{t}}$ are the contributions from the W+jets and $t\bar{t}$ processes, respectively. N_W^{sig} is the number of W+jets events in the signal region, and $N_{W,\text{est}}^{\text{sig}}$ is the estimated number of W+jets events obtained by scaling N_{ALL} by R. The statistical size of the region is very large, however there is a large bias caused mainly by $t\bar{t}$ contamination.

$W \to \ell\nu$ events. A data-driven estimate of this contamination would be difficult as one has to somehow reproduce a reconstructed lepton outside the detector acceptance. However, with sufficiently large MC samples, an estimate adequate for the purpose of removing this small contamination could be made.
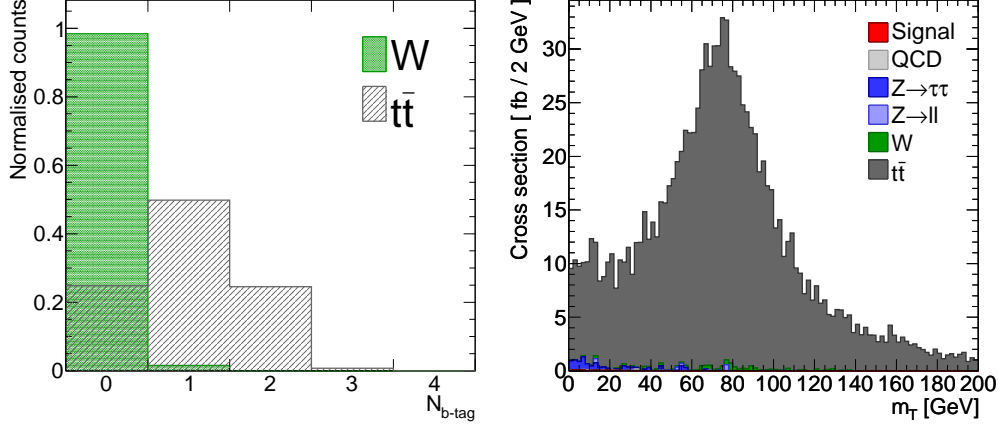
Figure 6.35: Number of b-tagged jets for W and $t\bar{t}$ (left). Transverse mass for the double b-tagged control region (right).

6.6.1.3 Uncertainty on W estimation

As well as the inherent bias (ΔS_{Bias}) of the data-driven W estimation procedure, the procedure also suffers from experimental systematic uncertainties (ΔS_{Sys}), as described in Section 6.5, and statistical uncertainties (ΔS_{Stat}) from the control regions. To calculate the full uncertainty on the method, each of these uncertainties are added in quadrature:

$$\Delta S = \Delta S_{\mathrm{Bias}} \oplus \Delta S_{\mathrm{Sys}} \oplus \Delta S_{\mathrm{Stat}}. \tag{6.15}$$

The method used to calculate the experimental uncertainties on the data-driven W estimation procedure is very similar to the method described in Section 6.5. To emulate the effect of experimental uncertainties on the data-driven method, variations were applied in the calculation of all numbers that will be obtained from data, while the ratio, R, that is taken from MC was kept constant. The uncertainty for each effect was then calculated as follows:

$$\Delta S_{\mathrm{Sys},\,i} = (N_{W,\,i}^{\mathrm{est}} - N_{W,\,i}^{\mathrm{MC}})/N_{W,\,i}^{\mathrm{MC}} - \Delta S_{\mathrm{Bias}} \tag{6.16}$$

where $N_{W,i}^{\text{est}}$ is the data-driven estimate of the number of W events in the signal region and $N_{W,i}^{\text{MC}}$ is the MC estimate, for the ith systematic variation. A summary of the detector systematic effects can be seen in Table 6.31. The systematic uncertainty tends to increase with increasing mass. This can be explained by the increasing thresholds of the tau E_{T} and $\not{E}_{\text{T}}$ selection for the higher mass analyses, which create a larger difference in phase space between the signal and control region. The uncertainties are summarised in Table 6.32. The W background can be estimated with a level of accuracy of 5% to 9% over the range of mass hypotheses.

Composition of the double b-tagged control region

	$N_{\text{exp}}(30\,\text{fb}^{-1})$	[%]
double b-tagged control region		
$N_{\text{ALL}}^{\text{C2}}$	12460	
$N_{t\bar{t}}^{\text{C2}}$	12300	99
W control region		
$N_{\text{ALL}}^{\text{C1}} - N_{t\bar{t},est}^{\text{C1}}$	324200	
N_{W}^{C1}	311700	96
signal region		
$N_{\text{W}}^{\text{sig}}$	616	
$N_{\text{W},est}^{\text{sig}}$	641	
Bias		+4.0%

Table 6.30: Composition of the double b-tagged $t\bar{t}$ control region (C2) and the W control region (C1) with the $t\bar{t}$ contamination removed. The numbers correspond to the expected number of events in $30\,\text{fb}^{-1}$. $N_{\text{ALL}}^{\text{C2}}$ is the total contribution from all processes in the double b-tagged control region and $N_{t\bar{t}}^{\text{C2}}$ is the contribution from $t\bar{t}$. $N_{\text{ALL}}^{\text{C1}}$ is the total contribution from all processes in the W control region, $N_{t\bar{t},est}^{\text{C1}}$ is the contribution from $t\bar{t}$ in the W control region estimated by scaling $N_{\text{ALL}}^{\text{C2}}$ by the $n(b-\text{jet}=0)/n(b-\text{jet}=2)$ ratio measured for $t\bar{t}$ events and N_{W}^{C1} is the number of W events in the W control region. N_{W}^{sig} is the number of W+jets events in the signal region, and $N_{W,\,\text{est}}^{\text{sig}}$ is the estimated number of W+jets events obtained by scaling $(N_{\text{ALL}} - N_{t\bar{t},est}^{\text{C1}})$ by R. The purity of the double b-tagged control region is very high, allowing an accurate removal of the $t\bar{t}$ contamination in the W control region. The final bias on the estimate of W events in the signal region is reduced to 4.0%.

Scale and resolution variations

m_A [GeV]	jet ΔE↑	jet ΔE↓	jet $\Delta\sigma$	e ΔE↑	e ΔE↓	e $\Delta\sigma$	μ ΔE↑	μ ΔE↓	μ $\Delta\sigma$	τ ΔE↑	τ ΔE↓	τ $\Delta\sigma$	Total
150	0.6	0.7	1.4	-1.0	1.3	-0.08	-1.2	1.2	0.2	1.6	1.0	2.7	3.8
200	-0.5	0.09	-2.3	-0.1	1.4	0.3	-2.2	1.7	-0.09	1.8	-0.4	0.6	3.4
300	-0.1	0.07	-1.9	-1.0	0.3	-0.3	-1.8	0.5	0.2	0.6	-3.5	-2.1	3.8
450	-0.2	0.7	4.3	-0.6	1.1	1.1	-1.1	0.4	0.2	4.3	-1.4	0.8	5.5
600	0.7	1.3	-3.9	-0.3	1.0	0.7	-1.7	0.3	-0.7	8.3	-2.3	3.6	7.7
800	1.6	-1.2	-1.4	-0.3	0.7	-0.02	-1.4	0.6	-1.1	9.1	-3.3	-0.9	6.8

Table 6.31: Summary of scale and resolution systematic variations (%) on the W background procedure. These numbers include the uncertainty on R.

Summary of the systematic uncertainties for the data-driven W estimate

m_A [GeV]	ΔS_{Bias}	ΔS_{Stat}	ΔS_{Sys}	ΔS
150	4.0	0.2	3.8	5.5
200	4.0	0.2	3.4	5.2
300	4.0	0.2	3.8	5.4
450	4.0	0.2	5.5	6.7
600	4.0	0.2	7.7	8.6
800	4.0	0.2	6.8	7.8

Table 6.32: Complete summary of the systematic uncertainties on the data-driven W background estimation procedure. ΔS_{Bias} is the inherent bias of the method, ΔS_{Stat} is the statistical uncertainty from the control region, ΔS_{Sys} is the experimental uncertainty (including the uncertainty from using R) and ΔS is the total systematic uncertainty of the method, obtained by summing the individual terms in quadrature.

6.6.1.4 Impact of single top on W estimation

MC simulated single top samples were not included in the production for the analysis. However, it is important to consider the effect of single top on the analysis. An estimate of the single-top background contribution for the main analysis is described in Section 6.7. The contribution is given as a fraction of the $t\bar{t}$ contribution, where a conservative upper limit of 10% was found that includes a 50% uncertainty on the single-top estimate. The most dominant contribution comes from the irreducible $Wt \to \ell\nu b\tau\nu$ mode. Since the mode contains only one b-quark, it will not be present in the $n_{b-\text{jet}} = 2$ control region used to subtract $t\bar{t}$ contamination from the W control region. Since the $t\bar{t}$ contamination in the W control region is 3.5%, a 10% Wt contribution would only

result in an additional 0.35% bias to the method. Furthermore, this bias could be considerably reduced if the Wt contamination was removed using an MC estimate. The effect of single top on the W estimation was therefore considered to be negligible.

6.6.2 Estimation of the QCD background

The QCD background can be estimated by counting the number of events surviving the event selection where the tau and lepton have the same charge (Same-Sign or SS events) instead of opposite charge (OS events). For QCD, the ratio of OS to SS events is expected to be close to unity, while for the signal there are almost no SS events. By using the SS events, a sample that has very little contamination from the signal can be obtained. The contribution from all backgrounds other than QCD in the SS region is then subtracted from the total number of SS events recorded in data ($n_{\mathrm{DATA}}^{\mathrm{SS}}$) to obtain the number of SS QCD events ($n_{\mathrm{QCD}}^{\mathrm{SS}}$)

$$n_{\mathrm{QCD}}^{\mathrm{SS}} = n_{\mathrm{DATA}}^{\mathrm{SS}} - \sum_i n_i^{\mathrm{SS}}, \tag{6.17}$$

where $i \in$ all backgrounds other than QCD. The number of QCD events in the signal region is then estimated using the ratio of OS to SS events for QCD ($R^{\mathrm{OS/SS}}$):

$$n_{\mathrm{QCD}}^{\mathrm{OS}} = R^{\mathrm{OS/SS}} \cdot n_{\mathrm{QCD}}^{\mathrm{SS}}. \tag{6.18}$$

From MC the ratio is 1.2 ± 0.1, however this will need to be verified with data. The invariant mass distribution for SS events in the non b-tagged analysis is shown in Figure 6.36. The analysis selection optimised for the 150 GeV mass point was used. The region is dominated by W events, not QCD events, which limits the accuracy of a QCD estimate through the background subtraction procedure.

Table 6.33 summarises the QCD background estimation when the SS contribution of all the backgrounds other than QCD were estimated directly from MC. The complete uncertainty on these contributions was folded into the final uncertainty on the QCD estimate, including the experimental uncertainties explained in Section 6.5 and the theoretical uncertainties on the cross sections given in Table 6.9. The absolute uncertainty on the QCD estimation ($\Delta n_{\mathrm{QCD,est}}^{\mathrm{SS}}$) is very small compared to the statistical and experimental uncertainties of the other backgrounds. Furthermore, in the most problematic case where the QCD background is larger in data than estimated
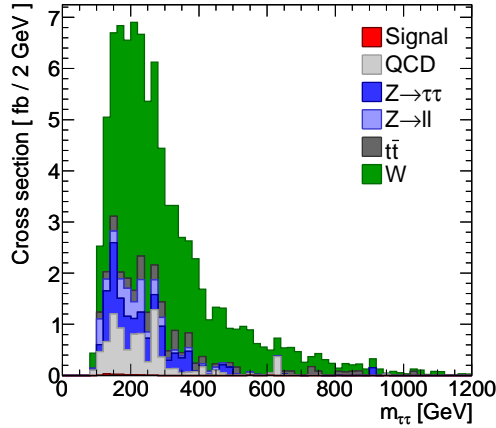
Figure 6.36: Invariant Mass distribution in the non b-tagged analysis for events where the tau and lepton have the same sign charge (SS events). The event selection optimised for the 150 GeV mass point was used. The region is dominated by W events, not QCD events, which limits the accuracy of a QCD estimate through the background subtraction procedure.

from MC, the estimate of the QCD background using this procedure will become more accurate.

Data-driven estimations of the other SS background contributions could also be used to reduce the uncertainty on the QCD estimate. As the SS region is dominated by W events, the most significant improvement is likely to result from the reduction in the uncertainty on the W contribution. Table 6.34 summarises the QCD estimate with the inclusion of the data-driven W estimation, where the SS contribution is estimated using the same technique as described in Section 6.6.1. The absolute uncertainty on the QCD estimate is reduced for almost all of the mass points with respect to the previous method. Although the estimate can result in quite large fractional uncertainties for the QCD alone, mainly due to the very small size of the QCD contribution, the uncertainties are small compared to those from the dominant backgrounds.

Although the method employed to estimate the QCD contribution in this study is a basic subtraction technique using MC estimates, it is very useful for a number of reasons. Firstly, the theoretical uncertainty from the MC on the QCD samples is much larger than for all the other samples. This means that the MC subtraction technique can actually reduce the uncertainty on the estimate with respect to a direct MC estimate.

Data-driven QCD estimate

$N_{\text{exp}}(30\,\text{fb}^{-1})$	m_A [GeV]					
	150	200	300	450	600	800
$N_{\text{QCD}}^{\text{SS}}$	90	60	5	1	0.04	0.008
$N_{\text{DATA}}^{\text{SS}}$	620	494	101	46	28	20
$N_{\text{OTHER}}^{\text{SS}}$	528	431	95	44	27	19
$N_{\text{QCD,est}}^{\text{SS}}$	92 ± 31	63 ± 27	5.7 ± 5.5	1.7 ± 3.2	0.6 ± 2	0.8 ± 1.6

Table 6.33: Expected numbers in $30\,\text{fb}^{-1}$ for the data-driven QCD estimation in the non b-tagged analysis at each Higgs boson mass hypothesis. In the estimate of the QCD contribution all backgrounds other than QCD are taken directly from MC. $N_{\text{QCD}}^{\text{SS}}$ is the number of QCD events in the SS region, $N_{\text{DATA}}^{\text{SS}}$ is the total contribution from all processes, $N_{\text{OTHER}}^{\text{SS}}$ is the total contribution from all processes other than QCD, and $N_{\text{QCD,est}}^{\text{SS}} = N_{\text{DATA}}^{\text{SS}} - N_{\text{OTHER}}^{\text{SS}}$, where $N_{\text{OTHER}}^{\text{SS}}$ includes the complete systematic uncertainty for a direct MC estimation. For the low masses where the QCD contribution is non-negligible the uncertainty can be significantly reduced with respect to a direct MC estimate.

Data-driven QCD estimate (including data-driven W)

$N_{\text{exp}}(30\,\text{fb}^{-1})$	m_A [GeV]					
	150	200	300	450	600	800
$N_{\text{QCD}}^{\text{SS}}$	90	60	5.3	0.8	0.04	0.008
$N_{\text{DATA}}^{\text{SS}}$	620	494	101	46	28	20
$N_{\text{OTHER}}^{\text{SS}}$	539	441	97	45	28	20
$N_{\text{QCD,est}}^{\text{SS}}$	81 ± 24	53 ± 19	4 ± 4	0.7 ± 2.6	-0.1 ± 2.2	0.3 ± 1.4

Table 6.34: Expected numbers in $30\,\text{fb}^{-1}$ for the data-driven QCD estimation in the non b-tagged analysis at each Higgs boson mass hypothesis. In the estimate of the QCD contribution the SS contribution for W is estimated using the data-driven W estimation procedure described in Section 6.6.1. All other backgrounds are taken directly from MC. The calculation of $N_{\text{QCD,est}}^{\text{SS}}$ includes the complete systematic uncertainty on $N_{\text{OTHER}}^{\text{SS}}$, coming from the uncertainty on the data-driven W estimation and the uncertainty on the direct MC estimations of the other backgrounds. By including the data-driven W estimation the uncertainty on the QCD estimate is reduced.

Secondly, it will be impossible to produce a sufficient number of MC simulated QCD events to reduce the statistical uncertainty of a direct MC estimate to a level that can actually be used. Inevitably, some type of weighting method would have to be used. Such a method will always introduce some degree of systematic uncertainty, which will increase the overall uncertainty of the direct MC estimate.

6.7 Results

In this section, the results obtained following the event selection are presented for both the b-tagged and non b-tagged analyses at each of the mass points. Both the Tau-ID and Lepton Isolation Weighting procedures were employed when necessary in the estimation of the background contributions. The cut-flows and mass plots are normalised to the cross section in fb and correspond to electron and muon events inclusively. The combination of the QCD and $Z \rightarrow \tau\tau$ samples, and the estimate of the background contribution from single top production are described. Finally, the expected significance and the discovery potential as a function of m_A and $\tan\beta$ are presented. The significance calculation includes the full systematic uncertainty on the contributions either from direct MC estimates or the data-driven techniques.

6.7.1 Evaluating QCD

Three QCD samples were simulated: filtered and unfiltered generic QCD events and $b\bar{b}$ QCD events. The QCD background was estimated by summing the contributions from both the filtered QCD samples and the $b\bar{b}$ QCD samples. In the unfiltered QCD samples none of the events passed the complete event selection, so they were not used in the final estimation. However, the unfiltered samples were used to evaluate the contribution from fake electrons detailed in Section 6.2.3. A scaling factor of 1.33 was applied to the electron contribution from the filtered QCD and $b\bar{b}$ samples accordingly. To account for the overlap of $b\bar{b}$ events in the filtered QCD and $b\bar{b}$ QCD samples, events containing two or more generator b-quarks were removed from the filtered QCD samples.

6.7.2 Combining $Z \rightarrow \tau\tau$ samples

To accurately estimate the $Z \rightarrow \tau\tau$ background over the entire m_A range, three samples were generated with selection on the invariant tau-tau mass of $m_{\tau\tau} > 60$ GeV, $150 < m_{\tau\tau} < 250$ GeV and $m_{\tau\tau} > 250$ GeV. Overlap occurs between the samples since there is no upper limit on the low-mass sample. To account for the overlap, events in the low mass sample where $m_{\tau\tau} > 150$ GeV were removed.

6.7.3 Estimating single top

Single top-quark production may contribute a minor background to the analysis, however, has not been considered for the analysis in the past and was not included in the MC production. Single top production can proceed through a number of channels including:

- $gb \to Wt$ ($\sigma_{\mathrm{prod}} = 66\,\mathrm{pb}$)

- t-channel $qb \to q't$ ($\sigma_{\mathrm{prod}} = 247\,\mathrm{pb}$)

- s-channel $q\bar{q} \to t\bar{b}$ ($\sigma_{\mathrm{prod}} = 11\,\mathrm{pb}$)

Both the t-channel and s-channel processes cannot contain both an isolated lepton and a hadronic tau in the final state, so they are reducible. These processes will be highly suppressed by the tau and lepton selection. The Wt process will make the largest contribution in the irreducible $Wt \to \ell\nu b\tau\nu$ final state. In the ATLAS note describing the study [1], the single top contribution was estimated as a fraction of the $t\bar{t}$ contribution, and was not the work of the author. The estimate was performed by looking at the only available samples for the single top, each of which had very few events. The samples used for the estimate included the t-channel process and an exclusive Wt process that did not contain the $Wt \to \ell\nu b\tau\nu$ final state. Corrections had to be applied to account for the lack of hadronic taus in the Wt sample and cut-factorisation was used due to the small number of MC events. The final conclusion was that single top contributed an additional 3-10% of the $t\bar{t}$ component of the total background in the b-tagged analysis for the $m_A = 150, 200$ and 300 GeV mass hypotheses and was negligible at higher masses. These numbers include a 50% inflation, which acts as a safety margin to account for the uncertainties of the estimate. The contribution in the non b-tagged analysis was assumed to be the same as in the b-tagged analysis, however, was almost negligible compared to the other background contributions. The numbers were used to scale the $t\bar{t}$ contribution in the current analysis.

At the time of the estimate, there was a large fully inclusive Wt sample available produced at a collision energy of 10 TeV. Use of the sample in the official ATLAS analysis was disfavoured, however, comparisons between Wt and $t\bar{t}$ at 10 TeV can give a very good idea of the expected relative Wt contribution at 14 TeV. The following

evaluation of the Wt contribution using 10 TeV samples is the complete work of the author.

Again there were not enough events in the Wt sample to run the full analysis. To make a comparison, selection requiring at least one pre-selected tau and lepton was applied to both samples. Then a comparison was made of the distributions of each of the variables used in the event selection. The only variables which showed any statistically significant differences were $N_{b-\text{tag}}$ and N_{jet}, shown in Figure 6.37. Comparisons of the other variables are shown in Figure B.20, see Appendix B.4. The difference in the distributions arises since there is one less b-quark produced in Wt than in $t\bar{t}$. This causes a drop in the efficiency of the $N_{b-\text{tag}} > 0$ selection, but an increase in the efficiency of the $N_{\text{jet}} < 3$ selection. The overall effect is a drop of only $\sim 4\%$ in the selection efficiency of Wt with respect to $t\bar{t}$. After the baseline selection was applied to each sample and the numbers were scaled to the production cross sections at $\sqrt{s} = 10$ TeV, the Wt sample was found to contribute at the level of 8% with respect to $t\bar{t}$. As this comparison does not even consider single top production via the t-channel process, this would indicate that the level of single top may be considerably larger than estimated in the official analysis, even with the 50% safety factor included. Differences were also found in the selection efficiency of the final mass window ranging from 0-50%, but only at two standard deviations. If the effect of the mass window is included, the Wt contribution is reduced to $\sim 4\%$ at the highest mass point, however, is not negligible.
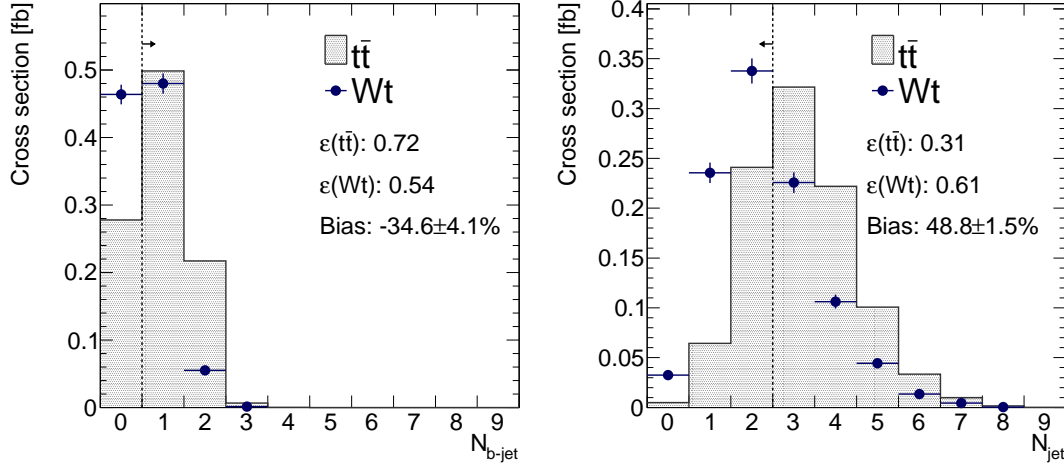
Figure 6.37: Comparison of Wt and $t\bar{t}$ distributions generated at a collision energy of 10 TeV. Events were required to have at least one pre-selected tau and lepton. The selection applied in the b-tagged analysis is indicated by the dashed line. The efficiency of the selection in each sample is also given, as well as the bias $(1 - \epsilon_{t\bar{t}}/\epsilon_{Wt})$.

6.7.4 Event selection cut-flows and $m_{\tau\tau}$ mass distributions

Tables 6.35 to 6.40 list the cross section in fb at each mass point for the signal and background processes after each of the criteria is applied in the event selection. After the Opposite Sign (OS) selection, the cut-flow is split into the b-tagged and non b-tagged analyses. The numbers for the MC samples are combined where appropriate into inclusive samples. The number of expected events for a given integrated luminosity L, can be obtained by multiplying the numbers in the tables by L in fb^{-1}. The discovery potential calculated later in this section uses the value $L = 30$fb^{-1}.

Figures 6.38 to 6.43 show the invariant mass distributions of the tau-tau system for all mass points in the analysis. The mass window is marked on the plots by vertical black lines. Due to the large contribution at the $Z \to \tau\tau$ mass peak in the non b-tagged analysis, an inlay figure zoomed in to the signal mass peak was included.

Event Selection for $m_A = 150$ GeV

	Associated	Fusion	W+jets	$Z(\to \ell\ell)$+jets	$Z(\to \tau\tau)$+jets	$t\bar{t}$	QCD
Total	4.3 E3	9.7 E2	2.6 E7	3.2 E6	3.1 E5	4.5 E5	2.2 E8
Z-Veto	4.3 E3	9.7 E2	2.6 E7	1.8 E6	3.1 E5	4.4 E5	2.2 E8
$n_{leptons} > 0$	8.3 E2	2.8 E2	1.6 E7	1.1 E6	1.1 E5	2.6 E5	3.0 E7
Lepton Isolation	7.1 E2	2.4 E2	1.5 E7	9.5 E5	9.8 E4	1.9 E5	4.5 E5
Trigger	6.2 E2	2.1 E2	1.3 E7	8.5 E5	8.6 E4	1.7 E5	4.2 E5
$E_{\mathrm{T}}^{\mathrm{miss}} > 20$ GeV	3.4 E2	1.2 E2	1.2 E7	2.7 E5	3.2 E4	1.5 E5	7.3 E4
$m_T < 25$ GeV	1.5 E2	80	1.1 E5	1.2 E4	1.4 E4	1.7 E4	4.6 E4
$n_\tau = 1$	70	37	4.9 E4	2.1 E3	2.5 E3	9.9 E2	1.4 E4
Tau-ID	57	29	1.3 E3	1.6 E2	1.9 E3	6 E2	1.6 E2
$m_{\tau\tau} > 0$	28	17	4.8 E2	65	1.1 E3	2.8 E2	72
OS	28	17	2.8 E2	49	1.1 E3	2.4 E2	39
non b-tagged	22	16	2.7 E2	48	1 E3	56	35
$E_T(\tau) > 40$ GeV	19	12	1.7 E2	22	4.9 E2	36	15
$\Delta\phi < 3.00$	10	9.3	1.2 E2	18	3.9 E2	32	11
$m_{\tau\tau}$ window	6.7	7.6	29	8.3	52	5.8	4.1
b-tagged	5.7	0.39	9.5	1.3	58	1.8 E2	4.5
$n_{jets} < 3$	4.7	0.2	6.5	0.92	39	46	3
$E_T(\tau) < 90$ GeV	4.4	0.17	5.8	0.91	38	40	2.9
$\Delta\phi < 3.00$	3.9	0.16	5.3	0.9	37	37	2.5
$\Delta\phi > 1.70$	3.3	0.12	3.5	0.85	14	26	1.8
$m_{\tau\tau}$ window	2.6	0.093	1.4	0.33	2.1	8.1	0.57

Table 6.35: Full cut-flows of the signal and background processes for the $m_A = 150$ GeV hypothesis at $\tan\beta = 10$, given in fb. Numbers for the two signal production modes, where the Higgs boson is produced either in association with b-quarks (associated) or by gluon fusion (fusion) are given separately.
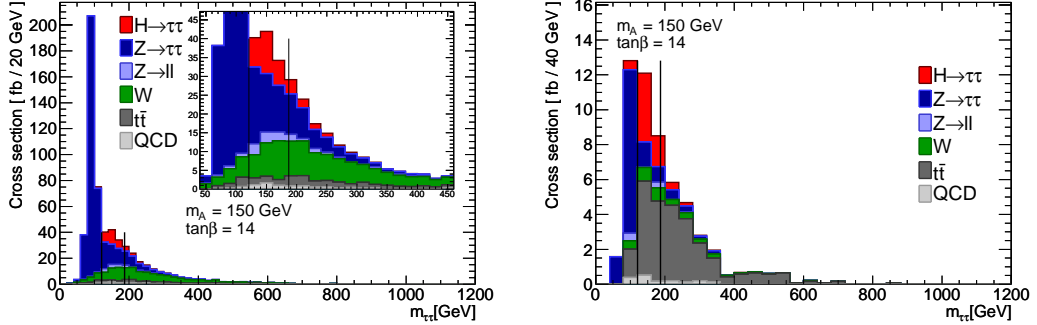

Figure 6.38: Invariant mass of the $\tau\tau$ system for $m_A = 150$ GeV, in the non b-tagged (left) and b-tagged (right) analyses. The mass window is marked by the vertical black lines. The contributions from signal, QCD, W+jets, $Z(\to \ell\ell)$+jets, $Z(\to \tau\tau)$+jets and $t\bar{t}$ are shown by red, light grey, green, violet, blue and dark grey, respectively.

Event Selection for $m_A = 200$ GeV

	Associated	Fusion	W+jets	$Z(\to \ell\ell)$+jets	$Z(\to \tau\tau)$+jets	$t\bar{t}$	QCD
Total	1.8 E3	2.2 E2	2.6 E7	3.2 E6	3.1 E5	4.4 E5	2.2 E8
Z-Veto	1.8 E3	2.2 E2	2.6 E7	1.8 E6	3.1 E5	4.3 E5	2.2 E8
$n_{leptons} > 0$	4.6 E2	86	1.6 E7	1.1 E6	1.1 E5	2.6 E5	3 E7
Lepton Isolation	3.8 E2	72	1.5 E7	9.5 E5	9.8 E4	1.9 E5	4.5 E5
Trigger	3.4 E2	64	1.3 E7	8.5 E5	8.6 E4	1.6 E5	4.2 E5
$E_T^{miss} > 20$ GeV	2.2 E2	44	1.2 E7	2.7 E5	3.2 E4	1.5 E5	7.3 E4
$m_T < 25$ GeV	1.1 E2	28	1.1 E5	1.2 E4	1.4 E4	1.7 E4	4.6 E4
$n_\tau = 1$	59	15	4.9 E4	2.1 E3	2.5 E3	9.6 E2	1.4 E4
Tau-ID	48	12	1.3 E3	1.6 E2	1.9 E3	5.8 E2	1.6 E2
$m_{\tau\tau} > 0$	24	6.9	4.8 E2	65	1.1 E3	2.7 E2	72
OS	24	6.8	2.8 E2	49	1.1 E3	2.3 E2	39
non b-tagged	19	6.7	2.7 E2	48	1 E3	54	35
$E_T(\tau) > 50$ GeV	15	5.1	1.3 E2	12	2.8 E2	27	9.6
$\Delta\phi < 3.00$	7.3	3.5	87	8.5	2.3 E2	23	6.9
$m_{\tau\tau}$ window	5.6	3.1	34	4.5	28	8.5	3.8
b-tagged	5.4	0.14	9.5	1.3	58	1.8 E2	4.5
$n_{jets} < 3$	4.5	0.083	6.5	0.92	39	45	3
$E_T(\tau) > 30$ GeV	4.2	0.082	5.1	0.86	28	39	2.3
$\Delta\phi < 3.00$	3.5	0.077	4.5	0.85	28	35	2
$\Delta\phi > 2.20$	2.9	0.04	2.2	0.78	5.3	20	1.3
$m_{\tau\tau}$ window	2.4	0.036	0.91	0.33	1.5	8.2	0.46

Table 6.36: Full cut-flows of the signal and background processes for the $m_A = 200$ GeV hypothesis at $\tan\beta = 10$, given in fb. Numbers for the two signal production modes, where the Higgs boson is produced either in association with b-quarks (Associated) or by gluon fusion (Fusion) are given separately.
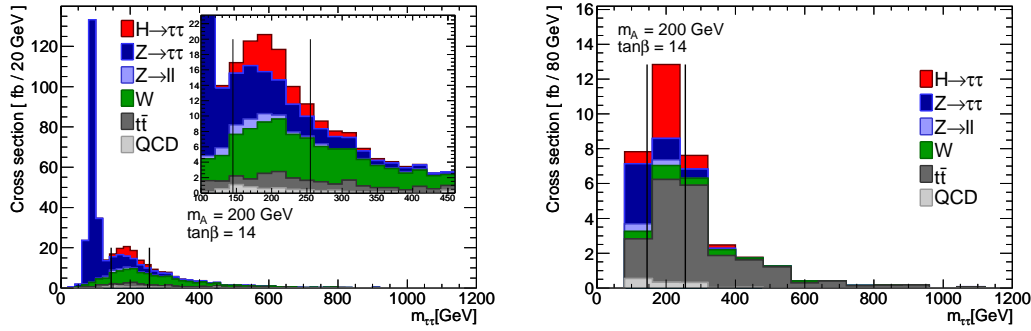

Figure 6.39: Invariant mass of the $\tau\tau$ system for $m_A = 200$ GeV in the non b-tagged (left) and b-tagged (right) analyses. The mass window is marked by the vertical black lines. The contributions from signal, QCD, W+jets, $Z(\to \ell\ell)$+jets, $Z(\to \tau\tau)$+jets and $t\bar{t}$ are shown by red, light grey, green, violet, blue and dark grey, respectively.

Event Selection for $m_A = 300$ GeV

	Associated	Fusion	W+jets	$Z(\to \ell\ell)$+jets	$Z(\to \tau\tau)$+jets	$t\bar{t}$	QCD
Total	8.1 E2	47	2.6 E7	3.2 E6	3.1 E5	4.3 E5	2.2 E8
Z-Veto	8 E2	46	2.6 E7	1.8 E6	3.1 E5	4.2 E5	2.2 E8
$n_{leptons} > 0$	2.7 E2	24	1.6 E7	1.1 E6	1.1 E5	2.5 E5	3 E7
Lepton Isolation	2.2 E2	20	1.5 E7	9.5 E5	9.8 E4	1.8 E5	4.5 E5
Trigger	2 E2	18	1.3 E7	8.5 E5	8.6 E4	1.6 E5	4.2 E5
$E_{\mathrm{T}}^{\mathrm{miss}} > 20$ GeV	1.5 E2	14	1.2 E7	2.7 E5	3.2 E4	1.5 E5	7.3 E4
$m_T < 25$ GeV	80	9.1	1.1 E5	1.2 E4	1.4 E4	1.6 E4	4.6 E4
$n_\tau = 1$	48	5.4	4.9 E4	2.1 E3	2.5 E3	9.5 E2	1.4 E4
Tau-ID	39	4.4	1.3 E3	1.6 E2	1.9 E3	5.7 E2	1.6 E2
$m_{\tau\tau} > 0$	21	2.6	4.8 E2	65	1.1 E3	2.7 E2	72
OS	21	2.5	2.8 E2	49	1.1 E3	2.3 E2	39
non b-tagged	16	2.5	2.7 E2	48	1 E3	53	35
1-prong τ	11	1.7	64	37	6.5 E2	26	10
$E_T(\tau) > 70$ GeV	8.5	1.2	18	2.6	78	6.6	1.3
$\Delta\phi < 3.00$	3.4	0.74	12	2	64	5.4	0.79
$m_{\tau\tau}$ window	2.9	0.66	4.9	0.6	5.2	2.2	0.4
b-tagged	5.2	0.064	9.5	1.3	58	1.8 E2	4.5
$n_{jets} < 3$	4.3	0.037	6.5	0.92	39	44	3
$E_{\mathrm{T}}^{\mathrm{miss}} > 25$ GeV	4.1	0.037	5.3	0.092	33	41	1.7
$E_T(\tau) > 50$ GeV	3.6	0.033	2.3	0.048	8.6	20	0.42
$\Delta\phi < 3.00$	2.7	0.028	2	0.048	8.4	17	0.34
$\Delta\phi > 2.40$	2.2	0.017	1.1	0.028	0.29	9.3	0.24
$m_{\tau\tau}$ window	1.8	0.015	0.53	0.0064	0.17	5.6	0.16

Table 6.37: Full cut-flows of the signal and background processes for the $m_A = 300$ GeV hypothesis at $\tan\beta = 15$, given in fb. Numbers for the two signal production modes, where the Higgs boson is produced either in association with b-quarks (associated) or by gluon fusion (fusion) are given separately.
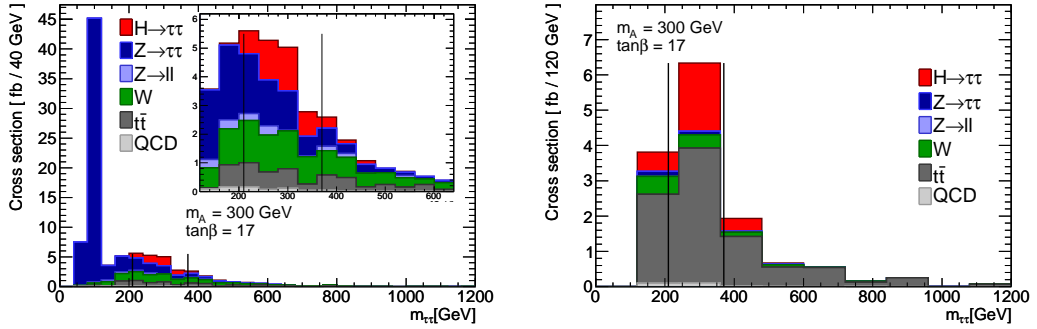

Figure 6.40: Invariant mass of the $\tau\tau$ system for $m_A = 300$ GeV in the non b-tagged (left) and b-tagged (right) analyses. The mass window is marked by the vertical black lines. The contributions from signal, QCD, W+jets, $Z(\to \ell\ell)$+jets, $Z(\to \tau\tau)$+jets and $t\bar{t}$ are shown by red, light grey, green, violet, blue and dark grey, respectively.

Event Selection for $m_A = 450$ GeV

	Associated	Fusion	W+jets	$Z(\to \ell\ell)$+jets	$Z(\to \tau\tau)$+jets	$t\bar{t}$	QCD
Total	2.2 E2	8.5	2.6 E7	3.2 E6	3.1 E5	4.1 E5	2.2 E8
Z-Veto	2.2 E2	8.4	2.6 E7	1.8 E6	3.1 E5	4 E5	2.2 E8
$n_{leptons} > 0$	88	5.2	1.6 E7	1.1 E6	1.1 E5	2.4 E5	3 E7
Lepton Isolation	72	4.3	1.5 E7	9.5 E5	9.8 E4	1.8 E5	4.5 E5
Trigger	64	3.8	1.3 E7	8.5 E5	8.6 E4	1.5 E5	4.2 E5
$E_{\mathrm{T}}^{\mathrm{miss}} > 20$ GeV	56	3.4	1.2 E7	2.7 E5	3.2 E4	1.4 E5	7.3 E4
$m_T < 25$ GeV	29	2.1	1.1 E5	1.2 E4	1.4 E4	1.6 E4	4.6 E4
$n_\tau = 1$	18	1.3	4.9 E4	2.1 E3	2.5 E3	9 E2	1.4 E4
Tau-ID	15	1.1	1.3 E3	1.6 E2	1.9 E3	5.5 E2	1.6 E2
$m_{\tau\tau} > 0$	8.5	0.67	4.8 E2	65	1.1 E3	2.5 E2	72
OS	8.4	0.65	2.8 E2	49	1.1 E3	2.2 E2	39
non b-tagged	6.5	0.64	2.7 E2	48	1 E3	51	35
1-prong τ	4.6	0.45	64	37	6.5 E2	25	10
$E_T(\tau) > 90$ GeV	3.8	0.37	11	1	40	4.3	0.61
$\Delta\phi < 3.00$	1.1	0.19	7.1	0.92	32	3.4	0.35
$m_{\tau\tau}$ window	0.82	0.18	2.4	0.14	1.3	0.94	0.071
b-tagged	1.9	0.016	9.5	1.3	58	1.7 E2	4.5
$n_{jets} < 3$	1.6	0.0086	6.5	0.92	39	42	3
$E_{\mathrm{T}}^{\mathrm{miss}} > 60$ GeV	1.1	0.0079	2.1	0.022	10	15	0.01
$E_T(\tau) > 90$ GeV	0.96	0.0072	0.35	0.0064	0.89	2.8	0.0033
$\Delta\phi < 3.00$	0.59	0.0061	0.24	0.0064	0.85	2.3	0.0031
$\Delta\phi > 2.60$	0.51	0.0024	0.15	0.0064	0.063	1.2	0.0027
$m_{\tau\tau}$ window	0.44	0.0021	0.045	0	0.031	0.46	0.00015

Table 6.38: Full cut-flows of the signal and background processes for the $m_A = 450$ GeV hypothesis at $\tan\beta = 20$, given in fb. Numbers for the two signal production modes, where the Higgs boson is produced either in association with b-quarks (associated) or by gluon fusion (fusion) are given separately.
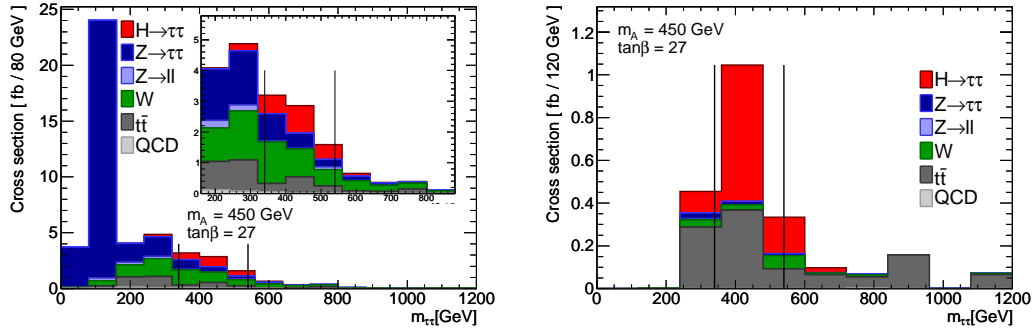

Figure 6.41: Invariant mass of the $\tau\tau$ system for $m_A = 450$ GeV in the non b-tagged (left) and b-tagged (right) analyses. The mass window is marked by the vertical black lines. The contributions from signal, QCD, W+jets, $Z(\to \ell\ell)$+jets, $Z(\to \tau\tau)$+jets and $t\bar{t}$ are shown by red, light grey, green, violet, blue and dark grey, respectively.

Event Selection for $m_A = 600$ GeV

	Associated	W+jets	$Z(\to \ell\ell)$+jets	$Z(\to \tau\tau)$+jets	$t\bar{t}$	QCD
Total	1.6 E2	2.6 E7	3.2 E6	3.1 E5	4.1 E5	2.2 E8
Z-Veto	1.5 E2	2.6 E7	1.8 E6	3.1 E5	4 E5	2.2 E8
$n_{leptons} > 0$	68	1.6 E7	1.1 E6	1.1 E5	2.4 E5	3 E7
Lepton Isolation	55	1.5 E7	9.5 E5	9.8 E4	1.8 E5	4.5 E5
Trigger	49	1.3 E7	8.5 E5	8.6 E4	1.5 E5	4.2 E5
$E_T^{miss} > 20$ GeV	44	1.2 E7	2.7 E5	3.2 E4	1.4 E5	7.3 E4
$m_T < 25$ GeV	23	1.1 E5	1.2 E4	1.4 E4	1.6 E4	4.6 E4
$n_\tau = 1$	15	4.9 E4	2.1 E3	2.5 E3	9 E2	1.4 E4
Tau-ID	12	1.3 E3	1.6 E2	1.9 E3	5.5 E2	1.6 E2
$m_{\tau\tau} > 0$	7.1	4.8 E2	65	1.1 E3	2.5 E2	72
OS	6.9	2.8 E2	49	1.1 E3	2.2 E2	39
non b-tagged	5.1	2.7 E2	48	1 E3	51	35
$E_T^{miss} > 60$ GeV	3.9	69	0.7	2 E2	23	0.15
1-prong τ	2.8	18	0.17	1.4 E2	12	0.049
$E_T(\tau) > 100$ GeV	2.6	4.4	0.034	18	2.2	0.017
$\Delta\phi < 3.05$	1.1	3.1	0.026	15	1.9	0.006
$m_{\tau\tau}$ window	0.95	1.1	0.0045	0.9	0.45	0.0028
b-tagged	1.8	9.5	1.3	58	1.7 E2	4.5
$n_{jets} < 3$	1.4	6.5	0.92	39	42	3
$E_T^{miss} > 60$ GeV	1.1	2.1	0.022	10	15	0.01
$E_T(\tau) > 130$ GeV	0.93	0.13	0.0064	0.53	0.88	0.00067
$\Delta\phi < 3.05$	0.66	0.11	0.0064	0.52	0.81	0.00044
$\Delta\phi > 2.60$	0.62	0.058	0.0064	0.038	0.45	0.0002
$m_{\tau\tau}$ window	0.54	0.026	0	0.02	0.21	3.9 E-5

Table 6.39: Full cut-flows of the signal and background processes for the $m_A = 600$ GeV hypothesis at $\tan\beta = 30$, given in fb. Numbers for the signal where the Higgs boson is produced in association with b-quarks (associated), are given.
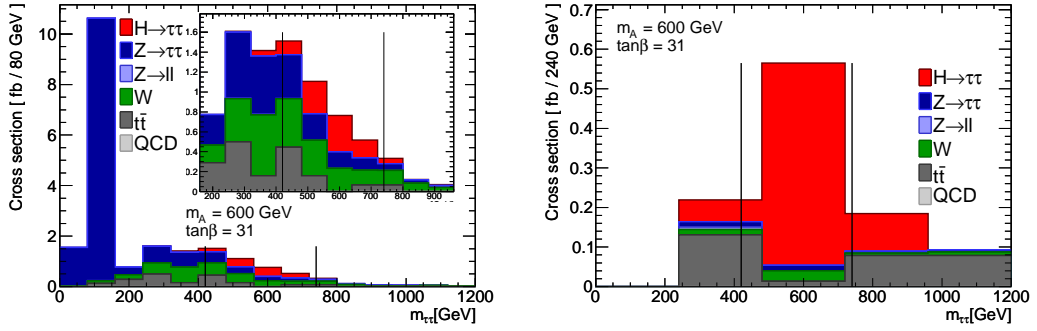

Figure 6.42: Invariant mass of the $\tau\tau$ system for $m_A = 600$ GeV in the non b-tagged (left) and b-tagged (right) analyses. The mass window is marked by the vertical black lines. The contributions from signal, QCD, W+jets, $Z(\to \ell\ell)$+jets, $Z(\to \tau\tau)$+jets and $t\bar{t}$ are shown by red, light grey, green, violet, blue and dark grey, respectively.

Event Selection for $m_A = 800$ GeV

	Associated	W+jets	$Z(\to \ell\ell)$+jets	$Z(\to \tau\tau)$+jets	$t\bar{t}$	QCD
Total	1.1 E2	2.6 E7	3.2 E6	3.1 E5	4.1 E5	2.2 E8
Z-Veto	1.1 E2	2.6 E7	1.8 E6	3.1 E5	4 E5	2.2 E8
$n_{leptons} > 0$	51	1.6 E7	1.1 E6	1.1 E5	2.4 E5	3 E7
Lepton Isolation	40	1.5 E7	9.5 E5	9.8 E4	1.8 E5	4.5 E5
Trigger	36	1.3 E7	8.5 E5	8.6 E4	1.5 E5	4.2 E5
$E_T^{miss} > 20$ GeV	33	1.2 E7	2.7 E5	3.2 E4	1.4 E5	7.3 E4
$m_T < 25$ GeV	17	1.1 E5	1.2 E4	1.4 E4	1.6 E4	4.6 E4
$n_\tau = 1$	11	4.9 E4	2.1 E3	2.5 E3	9 E2	1.4 E4
Tau-ID	9	1.3 E3	1.6 E2	1.9 E3	5.5 E2	1.6 E2
$m_{\tau\tau} > 0$	5.2	4.8 E2	65	1.1 E3	2.5 E2	72
OS	5	2.8 E2	49	1.1 E3	2.2 E2	39
non b-tagged	3.6	2.7 E2	48	1 E3	51	35
$E_T^{miss} > 60$ GeV	2.9	69	0.7	2 E2	23	0.15
1-prong τ	2.3	18	0.17	1.4 E2	12	0.049
$E_T(\tau) > 100$ GeV	2.2	4.4	0.034	18	2.2	0.017
$\Delta\phi < 3.05$	0.83	3.1	0.026	15	1.9	0.006
$m_{\tau\tau}$ window	0.7	0.69	0.004	0.42	0.21	0.0019
b-tagged	1.4	9.5	1.3	58	1.7 E2	4.5
$n_{jets} < 3$	1	6.5	0.92	39	42	3
$E_T^{miss} > 60$ GeV	0.87	2.1	0.022	10	15	0.01
$E_T(\tau) > 130$ GeV	0.78	0.13	0.0064	0.53	0.88	0.00067
$\Delta\phi < 3.05$	0.52	0.11	0.0064	0.52	0.81	0.00044
$\Delta\phi > 2.80$	0.41	0.04	0.0064	0.033	0.45	0.00014
$m_{\tau\tau}$ window	0.35	0.014	0	0.014	0.065	1.6 E-5

Table 6.40: Full cut-flows of the signal and background processes for the $m_A = 800$ GeV hypothesis at $\tan\beta = 45$, given in fb. Numbers for the signal where the Higgs boson is produced in association with b-quarks (Associated) are given.
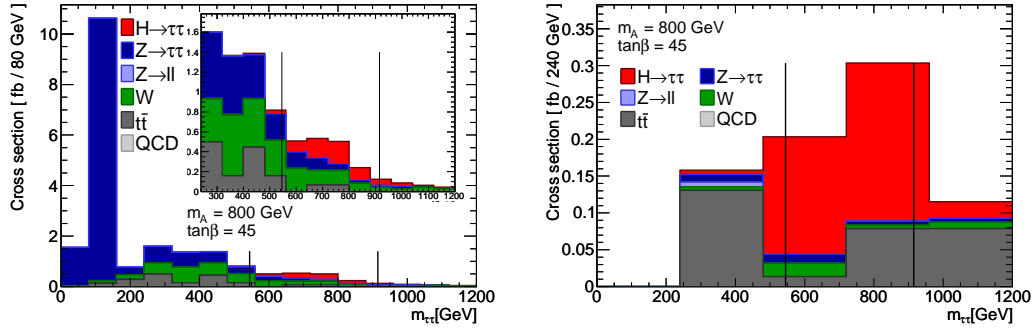

Figure 6.43: Invariant mass of the $\tau\tau$ system for $m_A = 800$ GeV in the non b-tagged (left) and b-tagged (right) analyses. The mass window is marked by the vertical black lines. The contributions from signal, QCD, W+jets, $Z(\to \ell\ell)$+jets, $Z(\to \tau\tau)$+jets and $t\bar{t}$ are shown by red, light grey, green, violet, blue and dark grey, respectively.

6.7.5 Significance and discovery potential

The significance of the analysis was estimated at each of the mass points assuming an integrated luminosity of $30\,\mathrm{fb}^{-1}$. The RooFit framework was used to construct a model of two statistically independent counting experiments, and RooStats [71, 72] was used to calculate their combined significance using a profile likelihood method. The likelihood function for the model can be written as:

$$L(\mu|\vec{\theta}_1, \vec{\theta}_2) = \prod_{i=1}^{2} P(x_i|\lambda_i(\mu, \vec{\theta}_i)) \cdot g(y_i) \qquad (6.19)$$

where $P(x_i|\lambda_i) = \lambda_i^{x_i} e^{-\lambda_i}/x_i!$ are the Poisson distribution functions for the number of observed events in each experiment, with means $\lambda_i(\mu, \vec{\theta}_i) = \mu N_{S,i} + N_{B,i}(1 + \Delta N_{B,i} \cdot \alpha_i)$, where $N_{S,i}$ and $N_{B,i}$ are the fixed number of signal and background events, μ is the total signal strength, $\Delta N_{B,i}$ the fixed systematic uncertainty on the background and α_i the standard normal distributed nuisance parameters $g(y_i) = e^{-y_i^2/2}/\sqrt{2\pi}$, used to model the systematic uncertainty on the background. The significance is then given by the test statistic:

$$S = -2\ln\frac{L_p(\mu_0)}{L_p(\mu_1)}, \qquad (6.20)$$

which is approximately χ^2 distributed with one degree of freedom, where $L_p(\mu) = \max_{\vec{\theta}_1, \vec{\theta}_2} L(\mu|\vec{\theta}_1, \vec{\theta}_2)$, is the profile likelihood (maximised over all nuisance parameters), $\mu_0 = 0$, is the background-only hypothesis (null hypothesis) and μ_1 (μ allowed to vary), is the signal plus background hypothesis. To incorporate the systematic uncertainties on the backgrounds, two extreme cases were considered: firstly the uncertainties from each analysis were assumed to be completely uncorrelated, secondly the uncertainties from each analysis were assumed to be 100% correlated, which was achieved by using only one nuisance parameter $g(y)$. As most of the systematic uncertainties between the analyses are 100% correlated, the second case is quoted as the final discovery potential, however, as this is not true for all uncertainties the result is conservative. Nevertheless, the difference between the two extreme scenarios is small.

Tables 6.41 and 6.42 summarise the results at each mass point for the b-tagged and non b-tagged analyses, respectively. The tables include the estimated cross sections for both the direct gluon fusion (σ_{gg}) and b-quark associated production (σ_{bb}) signal processes, the total estimated background cross section (σ_{bkg}) with the associated

systematic uncertainty ($\Delta\sigma_B^{sys}$), and the significance calculated with and without the inclusion of systematic uncertainty and assuming an integrated luminosity of $30\,\text{fb}^{-1}$. At each mass point, the value of $\tan\beta$ corresponds to the final 5σ discovery limit.

The 5σ discovery potential was calculated as a function of $\tan\beta$ and m_A and is shown in Figure 6.44. At each mass point the value of $\tan\beta$ corresponding to a significance of five was calculated by extrapolating the signal cross sections in $\tan\beta$. Minimum and maximum values for $\tan\beta$ were also calculated by including the theoretical uncertainty on the signal cross sections. The significance calculation incorporated the complete systematic uncertainty on the backgrounds from either the data-driven estimation procedures (where used) or the MC estimate as indicated in Appendix B.5. The 5σ discovery potential was also calculated without the inclusion of systematic uncertainties and is in good agreement with the results from previous studies of the channel [54].

The 95% confidence level exclusion limit was also calculated, in which no signal contribution was assumed. Systematic uncertainties on both the signal and background contributions were included in the calculation and were assumed to be 100% correlated between themselves and across both analyses. Figure 6.45 shows the exclusion limit, including the regions currently excluded by LEP and Tevatron for comparison. The exclusion limit for the ATLAS experiment extends far beyond the currently excluded regions.

Summary of the b-tagged analysis

$m_A\,[\text{GeV}]$	$\tan\beta$	$\sigma_{b\bar{b}}$	σ_{gg}	σ_{bkg}	$\Delta\sigma_B^{sys}$	S (without $\Delta\sigma_B^{sys}$)	S (with $\Delta\sigma_B^{sys}$)
150	14	5.2	0.16	12	1.0	7.8	4.3
200	14	5.0	0.062	11	1.1	7.7	3.9
300	17	2.4	0.019	6.5	0.71	4.8	2.7
450	24	0.75	0.0032	0.53	0.055	4.6	4.2
600	31	0.59	0	0.25	0.035	5.0	4.5
800	45	0.35	0	0.093	0.011	4.4	4.3

Table 6.41: Significance of the b-tagged analysis with and without the systematic uncertainty, $\Delta\sigma_B^{sys}$ on the background, for an integrated luminosity of $30\,\text{fb}^{-1}$. The expected signal and background cross sections in fb, and the absolute systematic uncertainty on the background are also given. The values of $\tan\beta$ at each mass point correspond to the final 5σ discovery limit for the combination of the b-tagged and non b-tagged analyses.

Summary of the non b-tagged analysis

m_A [GeV]	$\tan\beta$	$\sigma_{b\bar{b}}$	σ_{gg}	σ_{bkg}	$\Delta\sigma_{\text{B}}^{sys}$	S (without $\Delta\sigma_{\text{B}}^{sys}$)	S (with $\Delta\sigma_{\text{B}}^{sys}$)
150	14	14	13	99	5.1	14	4.9
200	14	12	5.4	79	2.9	10	5.0
300	17	3.8	0.82	13	0.56	6.5	5.0
450	24	1.4	0.27	4.8	0.23	3.9	3.4
600	31	1.0	0	2.5	0.14	3.3	3.0
800	45	0.7	0	1.3	0.067	3.1	2.9

Table 6.42: Significance of the non b-tagged analysis with and without the systematic uncertainty, $\Delta\sigma_{\text{B}}^{sys}$ on the background, for an integrated luminosity of $30\,\text{fb}^{-1}$. The expected signal and background cross sections in fb, and the absolute systematic uncertainty on the background are also given. The values of $\tan\beta$ at each mass point correspond to the final 5σ discovery limit for the combination of the b-tagged and non b-tagged analyses.

6.7.6 Influence of pile-up

A complete study of the effect of pile-up and cavern background on the discovery potential of the $\ell\tau_h$ channel was not included in the current analysis. Such studies generally take a large amount of time to perform correctly and require additional MC datasets, which were not available and could not be produced with the available resources. Despite this, these effects were considered, especially when selection was applied to quantities considered to be highly effected by pile-up. In particular, the choice of the Lepton Isolation, which is critical to the analysis, was made so that the performance would be robust at high luminosity. Another issue that has raised some concern in general in the ATLAS collaboration is the performance of jet counting in the presence of pile-up. To reduce contamination in the jet counting, the threshold on jet E_{T} was set to 20 GeV, rather than a lower value. In addition to this, selection on the longitudinal impact parameter of charged particles in the jets, similar to what was used in the lepton track isolation could be applied to reject jets from overlapping collisions. As the exact performance of jet counting is not critical to the analysis, this addition would probably be sufficient to retain adequate performance from the selection.

Finally, previous studies of the effect of low luminosity pile-up on the analysis suggest no significant degradation in the discovery potential for instantaneous luminosities up to $10^{33}\,\text{cm}^{-2}\text{s}^{-1}$ [41]. The study indicates that while similar performance from the Tau-ID can be maintained at all luminosities by tightening the selection, above

$10^{33}\,\mathrm{cm^{-2}s^{-1}}$ the b-tagging efficiency is significantly reduced while maintaining the same mistagging rate. Also, above this luminosity the $\not{E}_{\mathrm{T}}$ resolution becomes significantly poorer, which in turn degrades the resolution of the reconstructed Higgs boson mass.

6.7.7   7 TeV projection

In this study the discovery potential of the $\ell\tau_h$ channel was assessed, assuming 14 TeV collision energy with an integrated luminosity of $30\,\mathrm{fb^{-1}}$. At the completion of the project, an effort was made by a few of the members to project the result of the study to the first year of LHC running at 7 TeV [73]. In this period $1\,\mathrm{fb^{-1}}$ of integrated
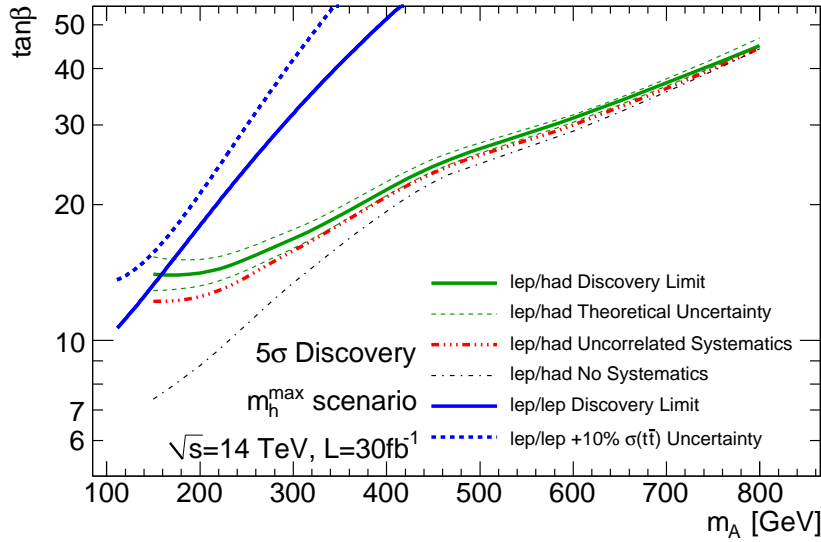
Figure 6.44: The 5σ discovery potential as a function of $\tan\beta$ and m_A. The solid green line is the result for the lepton-hadron analysis, indicating that there is enough sensitivity to discover the A/H bosons in the parameter space above this line. The dashed green lines indicate the effect of the theoretical uncertainty on the signal cross section. The red line gives the results when the systematic uncertainties on the backgrounds are considered completely uncorrelated. The dash-dotted black line shows the discovery potential where no systematic uncertainty is included for comparison with previous results [54]. The results from the lepton-lepton analysis are also superimposed in blue. The solid line indicates the result when only experimental systematic uncertainties were considered and the dashed line indicates the result when a 10% theoretical uncertainty on the $t\bar{t}$ cross section is included.

luminosity is expected to be recorded by the ATLAS experiment. The projection is very crude, due to the lack of time and resources available for the study. In particular, the selection was not re-optimised for the new conditions, which may severely underestimate the potential of the channel. Furthermore, the projection was performed by scaling the production cross sections of the processes, inflating the systematic uncertainties and by comparing the selection efficiency in 10 TeV samples, which were then used to extrapolate to 7 TeV. Thus the result should be taken as a very rough indication of what can be expected for the channel in the first full year of LHC running. Figure 6.46 shows the result of the projection. It is expected that a significant extension to the regions currently excluded by LEP and the Tevatron will be possible.
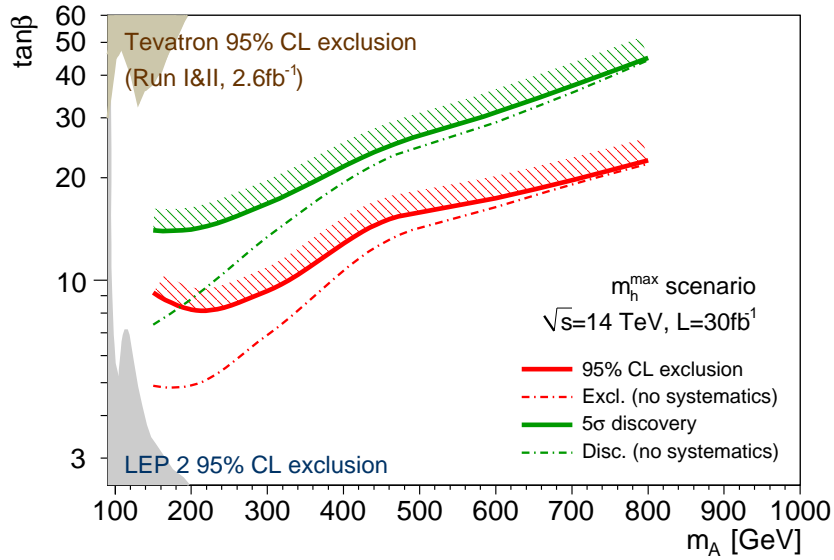
Figure 6.45: The 95% confidence level exclusion limit as a function of $\tan\beta$ and m_A. The parameter space above the solid red line can be excluded at the 95% CL if no events are observed over the SM background. The calculation includes systematic uncertainties on both the signal and background processes, which are assumed to be 100% correlated. The 5σ discovery limit is also included for comparison. The dash-dotted lines indicate the results without the inclusion of systematic uncertainties. The exclusions from LEP [30] and the Tevatron experiments [32, 33, 34] are also included for comparison.
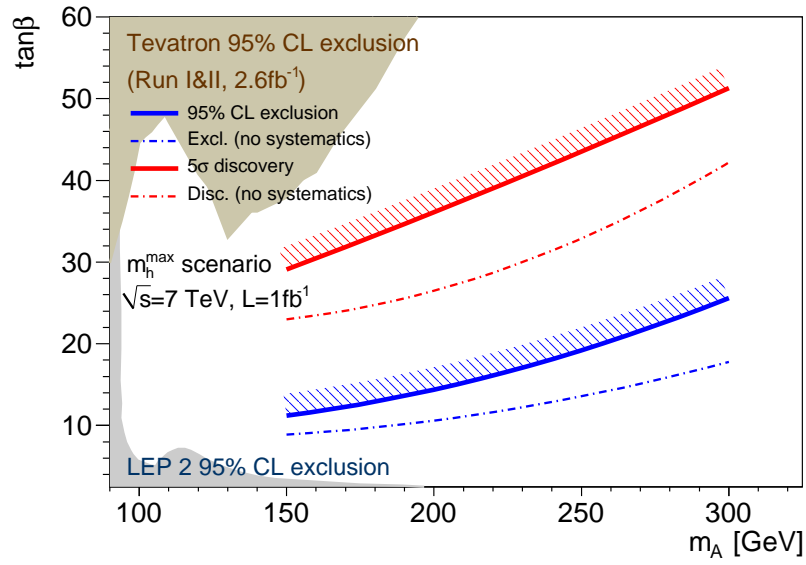
Figure 6.46: Projection of the 14 TeV analysis to 7 TeV and $L = 1\,\text{fb}^{-1}$ [73]. The 5σ discovery potential and the 95% CL exclusion limit are given as functions of $\tan\beta$ and m_A. The parameter space above the lines correspond to the discovery and exclusion regions, respectively. The current exclusions from the Tevatron experiments and LEP are included for comparison. Although the projection is a very rough estimate of the expected performance of the channel in the first full year of LHC running, a significant extension to the regions currently excluded by LEP and the Tevatron should be possible.

6.8   Discussion

The results of this study indicate that discovery or exclusion of the A/H Higgs bosons should be possible over a large region of the parameter space with $30\,\mathrm{fb}^{-1}$ of data recorded by the ATLAS experiment. The region accessible to ATLAS extends far beyond the current exclusion limits from LEP and the Tevatron, and also far beyond the ultimate reach of the Tevatron itself. Although the scenario of $30\,\mathrm{fb}^{-1}$ with 14 TeV collisions may be years off, preliminary studies indicate that large extensions to the current exclusion limits may be possible even in the first year of 7 TeV collisions.

The most dramatic change in the result with respect to previous analyses has come from the inclusion of systematic uncertainties. The impact is largest in the low m_A region where the analysis is dominated by the huge irreducible $Z \to \tau\tau$ background. In fact, in the low mass region the potential of the analysis is almost completely limited by systematic uncertainties. However, this is partially due to the optimisation method, where the significance was calculated without the inclusion of systematic uncertainties. In this case there is a tendency towards looser selection, which reduces the fractional statistical uncertainty, however, may not be optimal with the inclusion of systematic uncertainties. As the selection had to be completely defined before the systematic uncertainties could be evaluated, the inclusion of systematic uncertainties in the optimisation procedure requires an iterative approach. Unfortunately, due to the limited size of the MC event samples the evaluation of the systematic uncertainties was very time consuming and such a method was not plausible in the given time-frame. It would however be useful to re-perform the optimisation to improve the analysis now that the systematic uncertainties have been evaluated. In particular, tightening the upper threshold on $\Delta\phi$(lepton,tau) would significantly improve the mass resolution, providing much stronger suppression against $Z \to \tau\tau$. This would lead to a more even balance between the systematic and statistical uncertainties, which could increase the sensitivity of the analysis.

Finally, the data-driven $Z \to \tau\tau$ estimation procedure that was developed was not included in the analysis. This was because the estimated systematic uncertainty of the method was very large, which was mainly a statistical artefact due to the limited size of the MC samples. If the systematic uncertainty of the method could be evaluated

more accurately, or another method (such as embedding[1]) were developed that could significantly reduce the uncertainty with respect to a direct MC estimate, this could improve the signal sensitivity in the low mass region. In the high mass region the effect of the systematic uncertainty becomes negligible and the statistical uncertainty becomes dominant. In this region the result converges with the previous result for the channel, which did not include systematic uncertainties. Importantly, the current result excluding systematic uncertainties is in good agreement with previous results.

---

[1]In embedding, reconstructed objects from collision data are replaced by MC simulated objects, e.g. $Z \rightarrow \ell\ell$ events can be extracted with high purity from data, and the reconstructed leptons replaced by MC simulated taus to estimate the $Z \rightarrow \tau\tau$ background.

7

Further Work

The three main results from this thesis were the evaluation of the discovery potential for neutral MSSM Higgs bosons with the ATLAS experiment, the parameterisation of the calo-based tau reconstruction for use in ATLFAST-I, and the validation of track-based taus in ATLFAST-II. While each result is complete in itself, there are a number of extensions that could be made to these studies.

The ATLFAST-I parameterisation, while useful for generating large numbers of QCD events, currently requires a separate parameterisation for samples with different jet-type compositions. This has not presented a significant problem in the past as the tau parameterisation in ATLFAST-I has been used primarily to estimate the contribution of the QCD background itself. However, as the LHC moves into its first phase of operation the emphasis on the use of ATLFAST-I has shifted. The use of ATLFAST-I to estimate signal or background contributions in official analyses is now forbidden, due to the extremely simplistic simulation of the detector. On the other hand, its use in the evaluation of systematic variations could be extremely useful. This presents a problem, as the tau parameterisation would have to work on any given sample.

The brute force approach would be to provide a separate parameterisation for each process. Unfortunately, this style of approach would not only require a huge amount of work to setup, but would also have a very large upkeep. The cost of upkeep is critical in ATLAS, due to the rapid evolution of the software. Although this rate should slow as the collaboration is now recording data, tuning of the MC to the data will soon commence, at which point the parameterisations would need to be continually

updated. With the current priorities in the ATLAS collaboration a time intensive ATLFAST-I project would be dismissed. On the other hand, if a parameterisation was made that could easily account for the differences in jet-types, a single parameterisation may be versatile enough for use with any sample. Such a parameterisation could have been exceptionally useful for the estimation of systematic uncertainties in the current analysis of the ℓh channel. Without large sample sizes the estimation was extremely difficult and often resulted in inflated systematic uncertainties. In particular, it may have been possible to evaluate the uncertainties for the data-driven $Z \to \tau\tau$ method with ATLFAST-I samples, which may have resulted in a significant improvement in the performance at low m_A. For the parameterisation to be useful for the estimation of systematic uncertainties in early data, it should include the new *safe* tau identification variables that are intended to be used in the initial stages of data analysis [74].

On the other hand, the validation of ATLFAST-II has been an ongoing process in the ATLAS collaboration and is continually performed with new ATLAS software releases. The process is well developed and the direction of the project well defined. Further information of the direction of the project can be found in [49].

The analysis of the ℓh channel although well advanced requires a considerable amount of work before strong conclusions can be drawn from the data. A proper analysis of the channel should be performed with MC samples generated with a collision energy of 7 TeV. The latest release of the ATLAS software should be used, which in particular employs the anti-k_t jet algorithm by default for hadronic jet reconstruction and as input to the calo-based tau reconstruction algorithm. The analysis should also include MC samples for single top production, and also other possible backgrounds such as WW production. The cross section for WW production including the branching fraction to the irreducible $\ell\tau$ final state is $\sim 4\,\mathrm{pb}$, so may not be negligible. A full investigation of the effect of pile-up on the analysis in the first year of LHC operation at 7 TeV is needed. Also, the background estimation procedures should be tested with early data. The development of a more robust and accurate data-driven QCD estimate would be useful. In some CDF analyses, the QCD contribution has been estimated using the fake-rate for QCD jets, measured from data [75]. In ATLAS, a number of methods have been developed for similar estimations. One method uses the N_{track} distribution of reconstructed tau candidates to estimate the contribution from events with fake-taus [36]. Another method is to relax the Lepton Isolation to define a high purity

QCD control region. All of these methods should be applicable to the current analysis. Finally, An updated evaluation of systematic uncertainty with increased statistical precision, either through production with ATLFAST-I or large official ATLFAST-II production would be useful.

References

[1] The ATLAS Collaboration. "Discovery Potential of $A/H \to \tau\tau \to \ell h$ in ATLAS". *Tech. Rep. ATL-PHYS-PUB-2010-011. ATL-COM-PHYS-2010-194*, CERN, Geneva (2010). v, 90, 94, 95, 122, 154, 177

[2] Thomson, J. J. "XL. Cathode Rays". *Philosophical Magazine Series 5*, **44** 269, pp. 293 – 316 (1897). 3

[3] Rutherford, E. "Collision of alpha Particles with Light Atoms; An Anomalous Effect in Nitrogen". *The Philosophical Magazine*, **37**, pp. 537–87 (1919). 3

[4] Chadwick, J. "Possible Existence of a Neutron". *Nature*, **129**, pp. 312–+ (1932). 3

[5] Abe, F., Akimoto, H., Akopian, A. et al. "Observation of Top Quark Production in $p\bar{p}$ Collisions with the Collider Detector at Fermilab". *Phys. Rev. Lett.*, **74** 14, pp. 2626 – 2631 (1995). 3, 6

[6] Abachi, S., Abbott, B., Abolins, M. et al. "Observation of the Top Quark". *Phys. Rev. Lett.*, **74** 14, pp. 2632 – 2637 (1995). 3, 6

[7] Kodama, K. et al. "Observation of tau-neutrino interactions". *Phys. Lett.*, **B504**, pp. 218–224 (2001). `hep-ex/0012035`. 3, 6

[8] Karagiorgi, G. et al. "Leptonic CP violation studies at MiniBooNE in the $(3+2)$ sterile neutrino oscillation hypothesis". *Phys. Rev. D*, **75** 1, p. 013011 (2007). 6

[9] Glashow, S. L. "Partial-symmetries of weak interactions". *Nucl. Phys.*, **22** 4, pp. 579 – 588 (1961). 6

[10] Salam, A. and Ward, J. C. "Weak and electromagnetic interactions". *Il Nuovo Climento*, **11** 4, pp. 568 – 577 (1959). 6

[11] Weinberg, S. "A Model of Leptons". *Phys. Rev. Lett.*, **19** 21, pp. 1264 – 1266 (1967). 6

[12] Higgs, P. W. "Broken Symmetries and the Masses of Gauge Bosons". *Phys. Rev. Lett.*, **13** 16, pp. 508 – 509 (1964). 6

[13] Lee, B. W., Quigg, C. and Thacker, H. B. "Weak interactions at very high energies: The role of the Higgs-boson mass". *Phys. Rev. D*, **16** 5, pp. 1519 – 1531 (1977). 9, 10

REFERENCES

[14] Hambye, T. and Riesselmann, K. "Matching conditions and Higgs boson mass upper bounds reexamined". *Phys. Rev. D*, **55** 11, pp. 7255 – 7262 (1997). 10

[15] Espinosa, J. R. and Quiros, M. "Improved metastability bounds on the Standard Model Higgs mass". *Phys. Lett. B*, **353**, p. 257 (1995). 10, 11

[16] Casas, J. A., Espinosa, J. R. and Quiros, M. "Standard Model stability bounds for new physics within LHC reach". *Phys. Lett. B*, **382**, p. 374 (1996). 10

[17] Casas, J. A., Espinosa, J. R. and Quiros, M. "Improved Higgs Mass Stability Bound in the Standard Model and Implications for Supersymmetry". *Phys. Lett. B*, **342**, p. 171 (1995). 10

[18] Ellis, J., Espinosa, J. R., Giudice, G. F., Hoecker, A. and Riotto, A. "The Probable Fate of the Standard Model". *Phys. Lett. B*, **679**, p. 369 (2009). 11

[19] Barbieri, R. and Strumia, A. "The 'LEP paradox'". *ArXiv High Energy Physics - Phenomenology e-prints* (2000). `arXiv:hep-ph/0007265`. 12

[20] Martin, S. P. "A Supersymmetry Primer". In G. L. Kane (Editor), "Perspectives on Supersymmetry", pp. 1–+ (1998). `arXiv:hep-ph/9709356`. 13

[21] Arkani-Hamed, N., Dimopoulos, S. and Dvali, G. "The hierarchy problem and new dimensions at a millimeter". *Phys. Lett. B*, **429**, pp. 263 – 272 (1998). `arXiv:hep-ph/9803315`. 13

[22] Schmaltz, M. and Tucker-Smith, D. "Little Higgs Theories". *Annual Review of Nuclear and Particle Science*, **55**, pp. 229 – 270 (2005). `arXiv:hep-ph/0502182`. 13

[23] Weinberg, S. "Implications of dynamical symmetry breaking". *Phys. Rev. D*, **13** 4, pp. 974 – 996 (1976). 13

[24] Susskind, L. "Dynamics of spontaneous symmetry breaking in the Weinberg-Salam theory". *Phys. Rev. D*, **20** 10, pp. 2619 – 2625 (1979). 13

[25] Miransky, V. A., Tanabashi, M. and Yamawaki, K. "Dynamical electroweak symmetry breaking with large anomalous dimension and t quark condensate". *Phys. Lett. B*, **221** 2, pp. 177 – 183 (1989). 13

[26] Agashe, K., Contino, R. and Pomarol, A. "The Minimal Composite Higgs Model". *Nucl. Phys. B*, **719**, p. 165 (2005). 13

[27] M. Carena, S. Heinemeyer, C.E.M. Wagner and G. Weiglein. "Suggestions for benchmark scenarios for MSSM Higgs boson searches at hadron colliders". *Eur. Phys. J. C*, **26** 4, pp. 601 – 607 (2003). 15, 89

[28] Gunion, J. F., Haber, H., Kane, G., Dawson, S. and Haber, H. E. The Higgs Hunter's Guide. Westview Press (2000). ISBN 073820305X. 15

[29] Abbiendi, G. "Search for the Standard Model Higgs Boson at LEP". *Phys. Lett. B*, **565**, p. 61 (2003). 16

[30] Schael, S., Barate, R. et al. "Search for neutral MSSM Higgs bosons at LEP". *Eur. Phys. J. C*, **47**, pp. 547 – 587 (2006). `arXiv:hep-ex/0602042`. 16, 17, 190

[31] The CDF Collaboration, The D0 Collaboration, Tevatron New Physics, t. and Higgs Working Group. "Combined CDF and D0 Upper Limits on Standard Model Higgs-Boson Production with up to 6.7 fb-1 of Data". *ArXiv e-prints* (2010). `1007.4587`. 17, 18

[32] The CDF Collaboration. "Search for Neutral MSSM Higgs Bosons Decaying to Tau Pairs with 1.8 fb^1 of Data". CDF Note 9071 (2008). 17, 19, 190

[33] The CDF Collaboration. "Search for Higgs Bosons Produced in Association with b-Quarks". CDF Note 9284 (2008). 17, 19, 190

[34] The D0 Collaboration. "Combined upper limits on MSSM Higgs-boson production with up to 2.6 fb^{-1} of data at D0". D0 Note 5935-CONF (2009). 17, 19, 190

[35] Flächer, H. et al. "Revisiting the global electroweak fit of the Standard Model and beyond with Gfitter". *Eur. Phys. J. C*, **60**, pp. 543 – 583 (2009). `arXiv:hep-ph/0811.0009`. 18, 19

[36] The ATLAS Collaboration. Expected performance of the ATLAS experiment: detector, trigger and physics. CERN, Geneva (2009). CERN-OPEN-2008-020. 20, 27, 39, 44, 45, 55, 75, 104, 120, 154, 156, 196

[37] The CMS Collaboration. "CMS Physics Technical Design Report, Volume II: Physics Performance". *J. Phys. G*, **34** 6, pp. 995 – 1579 (2007). 20

[38] Evans, L. and Bryant, P. "LHC Machine". *JINST*, **3** 08, p. S08001 (2008). 22, 25

[39] The ATLAS Collaboration. "The ATLAS Experiment at the CERN Large Hadron Collider". *JINST*, **3**, p. S08003 (2008). 22, 28, 31, 32, 34, 36, 39, 43

[40] Campbell, J. M., Huston, J. W. and Stirling, W. J. "Hard interactions of quarks and gluons: a primer for LHC physics". *Reports on Progress in Physics*, **70**, pp. 89 – 193 (2007). `arXiv:hep-ph/0611148`. 24

[41] The ATLAS Collaboration. ATLAS detector and physics performance: Technical Design Report, *Technical Design Report ATLAS*, vol. 1. CERN, Geneva (1999). CERN-LHCC-99-14. 27, 188

[42] The ATLAS Collaboration. ATLAS detector and physics performance: Technical Design Report, *Technical Design Report ATLAS*, vol. 2. CERN, Geneva (1999). CERN-LHCC-99-15. 27

[43] The ATLAS Collaboration. "The ATLAS Inner Detector commissioning and calibration". *ArXiv e-prints* (2010). `arXiv:physics.ins-det/1004.5293`. 37

[44] The ATLAS Collaboration. "Commissioning of the ATLAS Muon Spectrometer with cosmic rays". *European Physical Journal C*, **70**, pp. 875–916 (2010). `1006.4384`. 37

201

REFERENCES

[45] The ATLAS Collaboration. "Readiness of the ATLAS liquid argon calorimeter for LHC collisions". *European Physical Journal C*, **70**, pp. 723–753 (2010). `0912.2642`. 37

[46] The ATLAS Collaboration. "Performance of the ATLAS detector using first collision data". *Journal of High Energy Physics*, **9**, pp. 56–+ (2010). `1005.5254`. 37

[47] Abt, I., Ahmed, T., Aid, S. et al. "The tracking, calorimeter and muon detectors of the H1 experiment at HERA". *Nucl. Inst. & Meth. in Phys. Res. A*, **386** 2-3, pp. 348 – 396 (1997). 43

[48] Speckmayer, P., Hcker, A., Stelzer, J. and Voss, H. "The toolkit for multivariate data analysis, TMVA 4". *Journal of Physics: Conference Series*, **219** 3, p. 032057 (2010). 45

[49] The ATLAS Collaboration. "The ATLAS Simulation Infrastructure". *European Physical Journal C*, **70**, pp. 823–874 (2010). `1005.4568`. 49, 101, 142, 196

[50] Agostinelli, S., Allison, J., Amako, K. et al. "G4–a simulation toolkit". *Nucl. Inst. & Meth. in Phys. Res. A*, **506** 3, pp. 250 – 303 (2003). 51

[51] Heldmann, M. and Cavalli, D. "An improved tau-Identification for the ATLAS experiment". *Tech. Rep. ATL-PHYS-PUB-2006-008. ATL-COM-PHYS-2006-010*, CERN, Geneva (2005). 55, 62

[52] Webber, B. R. "Fragmentation and Hadronization". In J. A. Janos & M. E. Peskin (Editor), "Lepton and Photon Interactions at High Energies", p. 577 (1999). `arXiv:hep-ph/9912292`. 68

[53] Cavalli, D. et al. "Validation of the fast calorimeter simulation FastCaloSim against the Athena release 10 and 13.0.40 full simulation". *Tech. Rep. ATL-PHYS-INT-2009-073. ATL-COM-PHYS-2009-164*, CERN, Geneva (2009). 75

[54] Cavalli, D. and Negri, G. "Extension of the Study of A/H to tau-tau to lepton-hadron in the high mA region". *Tech. Rep. ATL-PHYS-2003-009*, CERN, Geneva (2003). 92, 128, 187, 189

[55] Heinemeyer, S., Hollik, W. and Weiglein, G. "FeynHiggs: A program for the calculation of the masses of the neutral CP-even Higgs bosons in the MSSM". *Comput. Phys. Commun.*, **124**, pp. 76 – 89 (2000). `arXiv:hep-ph/9812320`. 94

[56] Heinemeyer, S., Hollik, W. and Weiglein, G. "The masses of the neutral CP-even Higgs bosons in the MSSM: Accurate analysis at the two-loop level". *Eur. Phys. J. C*, **9**, pp. 343 – 366 (1999). `arXiv:hep-ph/9812472`. 94

[57] Degrassi, G., Heinemeyer, S., Hollik, W., Slavich, P. and Weiglein, G. "Towards high-precision predictions for the MSSM Higgs sector". *Eur. Phys. J. C*, **28**, pp. 133 – 143 (2003). `arXiv:hep-ph/0212020`. 94

[58] Frank, M. et al. "The Higgs boson masses and mixings of the complex MSSM in the Feynman-diagrammatic approach". *JHEP*, **2**, p. 47 (2007). `arXiv:hep-ph/0611326`. 94

[59] Gleisberg, T. et al. "Event generation with SHERPA 1.1". *JHEP*, **2**, p. 7 (2009). `arXiv:hep-ph/0811.4622`. 100

[60] Sjöstrand, T., Mrenna, S. and Skands, P. "PYTHIA 6.4 physics and manual". *JHEP*, **5**, p. 26 (2006). `arXiv:hep-ph/0603175`. 100

[61] Frixione, S. and Webber, B. R. "The MC@NLO Event Generator". *ArXiv High Energy Physics - Phenomenology e-prints* (2002). `arXiv:hep-ph/0207182`. 100

[62] Frixione, S. and Webber, B. R. "Matching NLO QCD computations and parton shower simulations". *JHEP*, **6**, p. 29 (2002). `arXiv:hep-ph/0204244`. 100

[63] Corcella, G. et al. "HERWIG 6: an event generator for hadron emission reactions with interfering gluons (including supersymmetric processes)". *JHEP*, **1**, p. 10 (2001). `arXiv:hep-ph/0011363`. 100

[64] Corcella, G. et al. "HERWIG 6.5 Release Note". *ArXiv High Energy Physics - Phenomenology e-prints* (2002). `arXiv:hep-ph/0210213`. 100

[65] Jadach, S., Kühn, J. H. and Was, Z. "TAUOLA - a library of Monte Carlo programs to simulate decays of polarized τ leptons". *Comput. Phys. Commun.*, **64** 2, pp. 275 – 299 (1991). 100

[66] Barberio, E., van Eijk, B. and Was, Z. "Photos – a universal Monte Carlo for QED radiative corrections in decays". *Comput. Phys. Commun.*, **66** 1, pp. 115 – 128 (1991). 100

[67] Dawson, I. and Prokofiev, K. "Luminosity measurement in the interaction regions of the LHC using proton-proton collision multiplicities". *Nucl. Inst. & Meth. in Phys. Res. A*, **578** 3, pp. 480 – 484 (2007). 110, 111

[68] Cacciari, M., Salam, G. P. and Soyez, G. "The anti-k_T jet clustering algorithm". *Journal of High Energy Physics*, **4**, p. 63 (2008). `arXiv:hep-ph/0802.1189`. 116

[69] Asquith, L., Brelier, B., Butterworth, J. M. et al. "Performance of Jet Algorithms in the ATLAS Detector". *Tech. Rep. ATL-COM-PHYS-2009-630*, CERN, Geneva (2009). 116

[70] Ellis, R. K., Hinchliffe, I., Soldate, M. and Bij, J. J. V. D. "Higgs decay to $\pi^+\pi^-$: A possible signature of intermediate mass Higgs bosons at high energy hadron colliders". *Nucl. Phys. B*, **297** 2, pp. 221 – 243 (1988). 126, 128

[71] Verkerke, W. and Kirkby, D. "The RooFit toolkit for data modeling". *ArXiv Physics e-prints* (2003). `arXiv:physics/0306116`. 186

[72] Brun, R. and Rademakers, F. "ROOT – An object oriented data analysis framework". *Nucl. Inst. & Meth. in Phys. Res. A*, **389**, pp. 81 – 86 (1997). URL `http://root.cern.ch`. 186

[73] Anders, C. et al. "Combined Sensitivity to MSSM $H/A \rightarrow \tau\tau \rightarrow \ell h$ in 7 TeV Collisions at ATLAS". *Tech. Rep. ATL-COM-PHYS-2010-255*, CERN, Geneva (2010). 189, 191

[74] "Cut based identification of hadronic tau decays". *Tech. Rep. ATL-PHYS-PUB-2010-001. ATL-COM-PHYS-2009-583*, CERN, Geneva (2010). 196

[75] The CDF Collaboration. "Search for New Physics Using High-Mass Tau Pairs from 1.96 TeV $p\bar{p}$ Collisions". *Phys. Rev. Lett.*, **95** 13, p. 131801 (2005). `arXiv:hep-ex/0506034`. 196

A

Truth Matching

To evaluate the performance of reconstruction algorithms with Monte Carlo simulated samples, the origin of reconstructed objects must be determined. This is usually performed by consulting the *truth particle record*, which contains information on all the particles created and annihilated in the interactions of the simulation. The most simple way to decide on the origin of an object is to search for a matching truth particle within a given radius, ΔR, in η-ϕ space. Definitions used in the matching procedure are given below.

Stable Particle

A particle that will reach the detector before decaying

Interacting Particle

A particle that will interact with the material in the detector, e.g., electrons, muons and hadrons.

Non Interacting Particle

A particle that will not interact with the material in the detector, e.g., neutrinos and dark-matter candidates (such as the lightest supersymmetric particle).

True Hadronic Tau

A true hadronic tau is a tau from the *truth particle record*, that contains no leptons in its decay chain. Furthermore, the properties of the tau are taken directly before its decay, i.e., after any radiation has occurred.

True Jet

True jets are reconstructed by the standard ATLAS cone jet finding algorithm with $\Delta R < 0.4$, using all stable interacting particles from the *truth particle record* as input.

True QCD Jet

A true QCD jet is a true jet that does not match to a true hadronic tau within a cone of $\Delta R < 0.3$ (unless otherwise specified).

Real Tau Candidate

A real tau candidate is defined as any reconstructed tau candidate that matches to a true hadronic tau within $\Delta R < 0.3$ (unless otherwise specified).

Fake Tau Candidate

A fake tau candidate is defined as any reconstructed tau candidate that does not match to a true hadronic tau within $\Delta R < 0.3$ (unless otherwise specified).

B

MSSM Higgs Appendices

This appendix contains additional figures and information regarding the analysis of the discovery potential for A/H in the ATLAS experiment, presented in Chapter 6. Appendix B.1 shows plots of $t\bar{t}$ discriminating variables. Appendix B.2 shows plots of the optimised selection for the b-tagged and non b-tagged analyses. Further details on the object weighting procedure are given in Appendix B.3. Details regarding the single top estimation are given in Appendix B.4. Finally, the use of data-driven background estimates in the final significance calculation is detailed in Appendix B.5.

B.1 $t\bar{t}$ Rejection
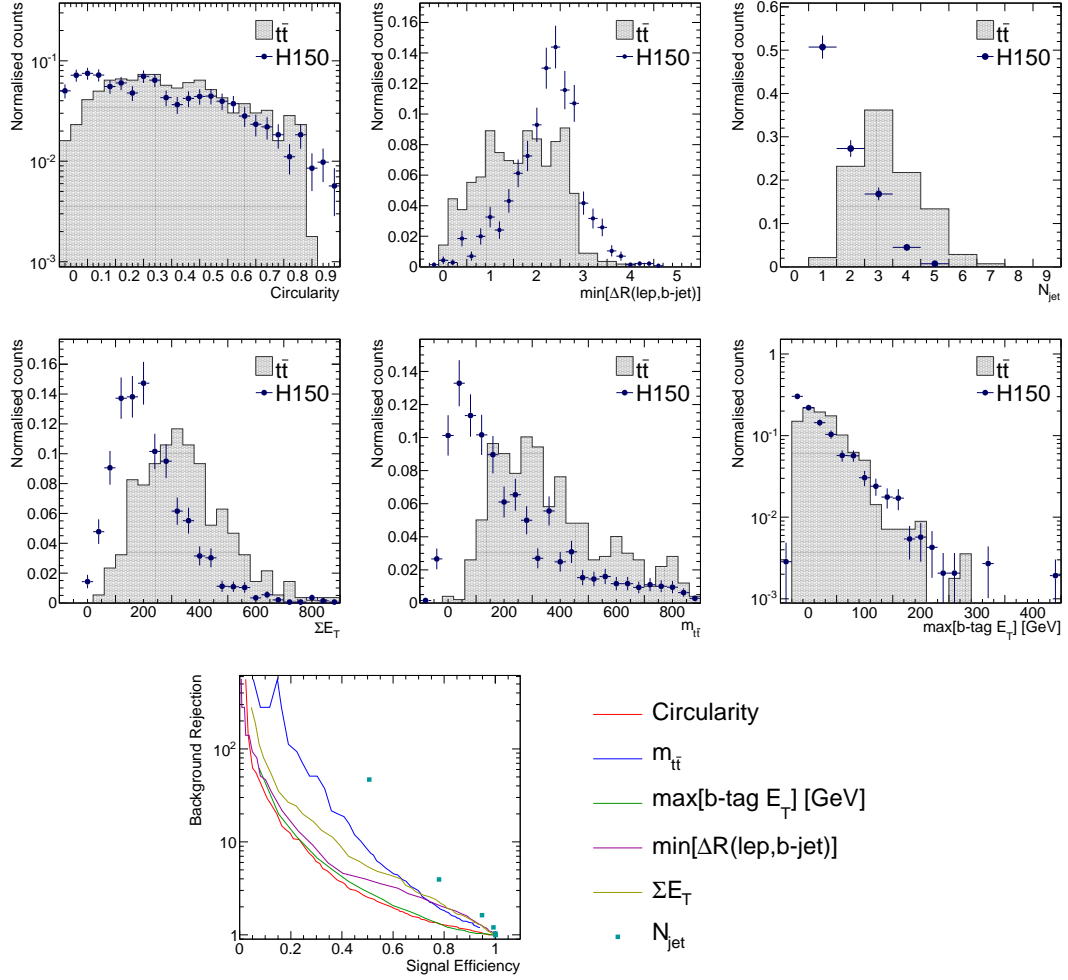
Figure B.1: $t\bar{t}$ discriminating variables, after all selection in the b-tagged analysis at $m_A = 150$ GeV.
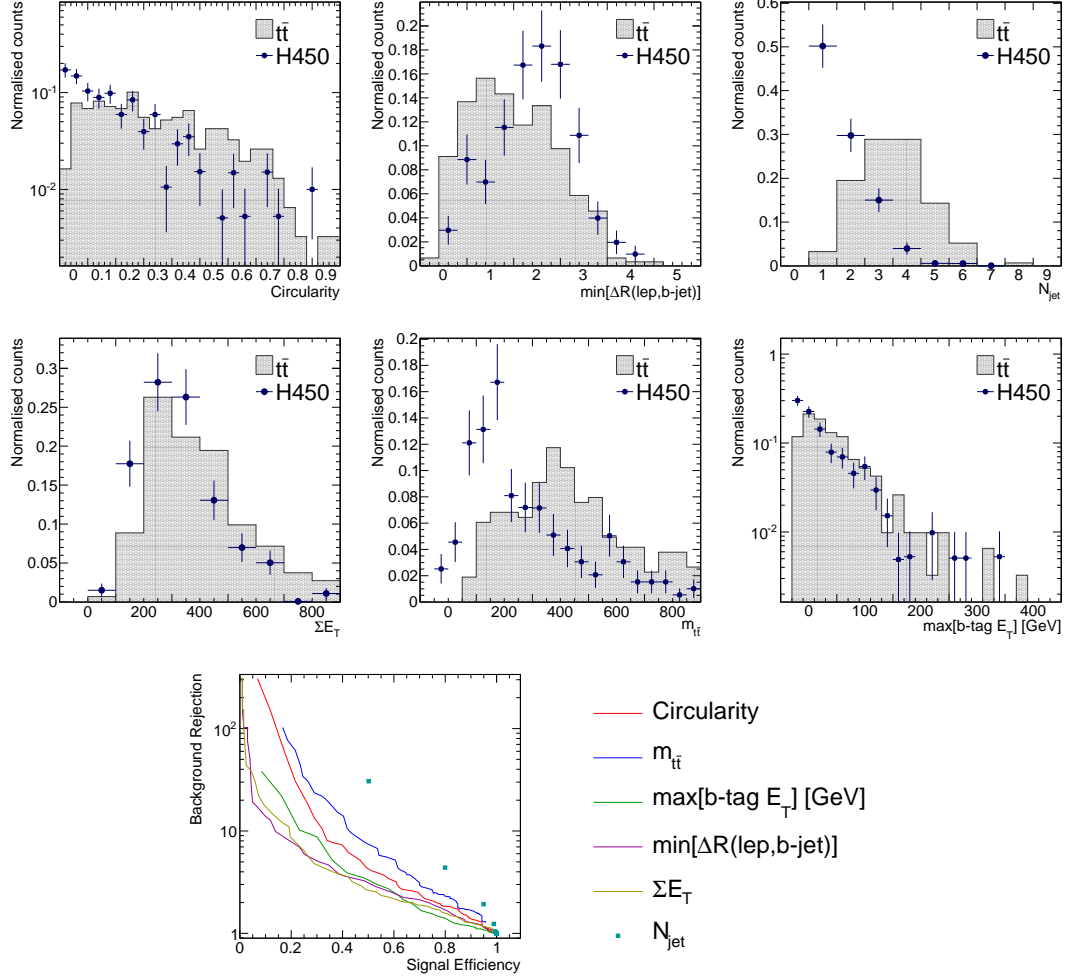
Figure B.2: $t\bar{t}$ discriminating variables, after all selection in the b-tagged analysis at $m_A = 450$ GeV.
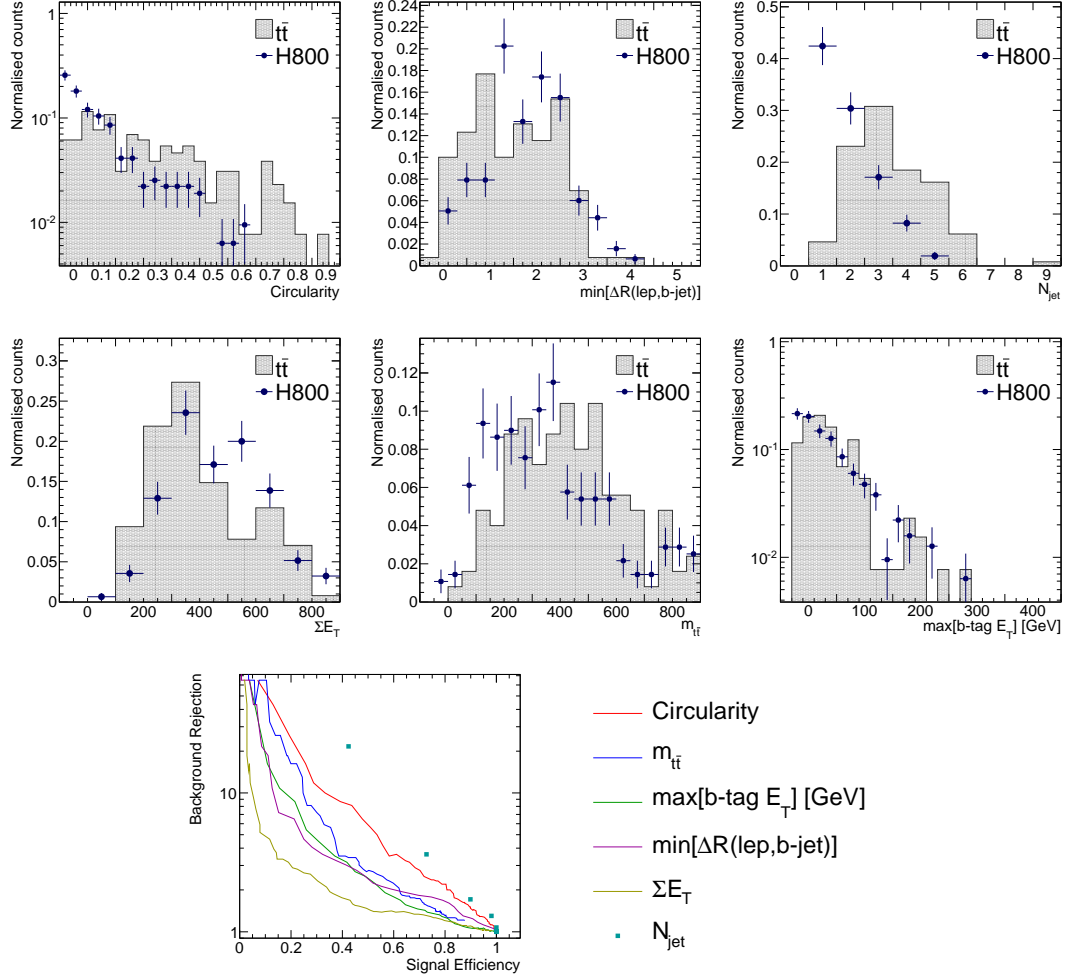
Figure B.3: $t\bar{t}$ discriminating variables, after all selection in the b-tagged analysis at $m_A = 800$ GeV.

B.2 Optimised Selection
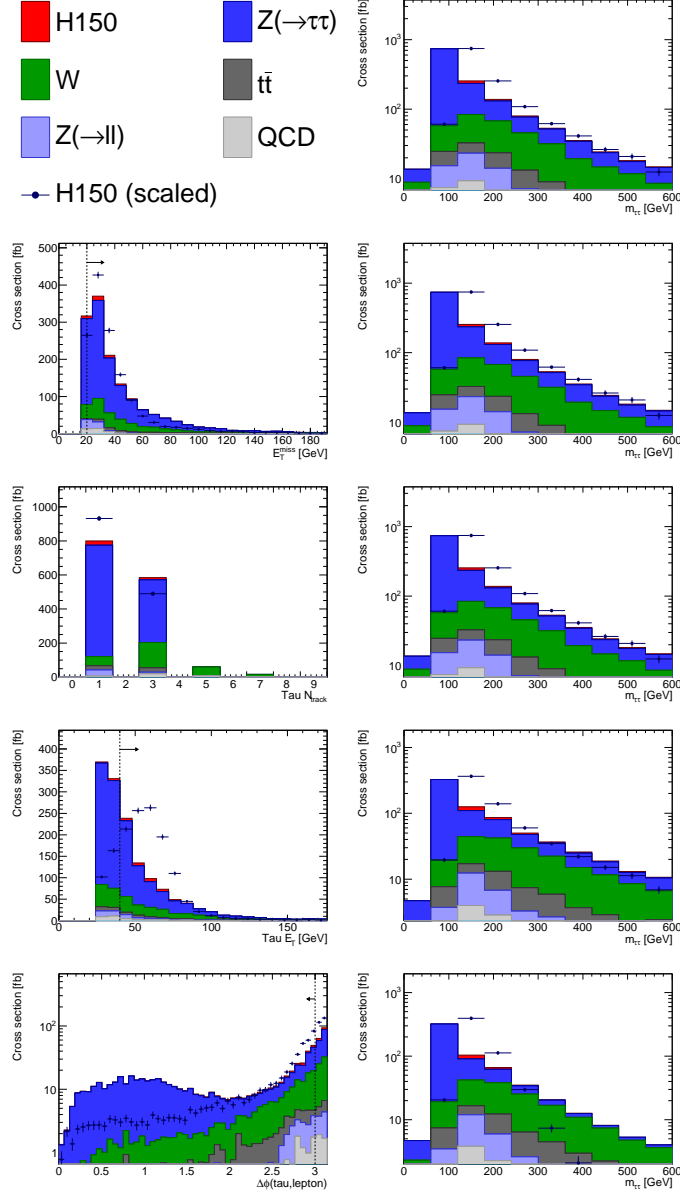
Figure B.4: Optimised selection for the non b-tagged analysis at $m_A = 150$ GeV. The selection variables are shown (left) with the selected regions spanning from the dashed lines in the direction of the arrows. The invariant mass distribution is shown after each cut (right).
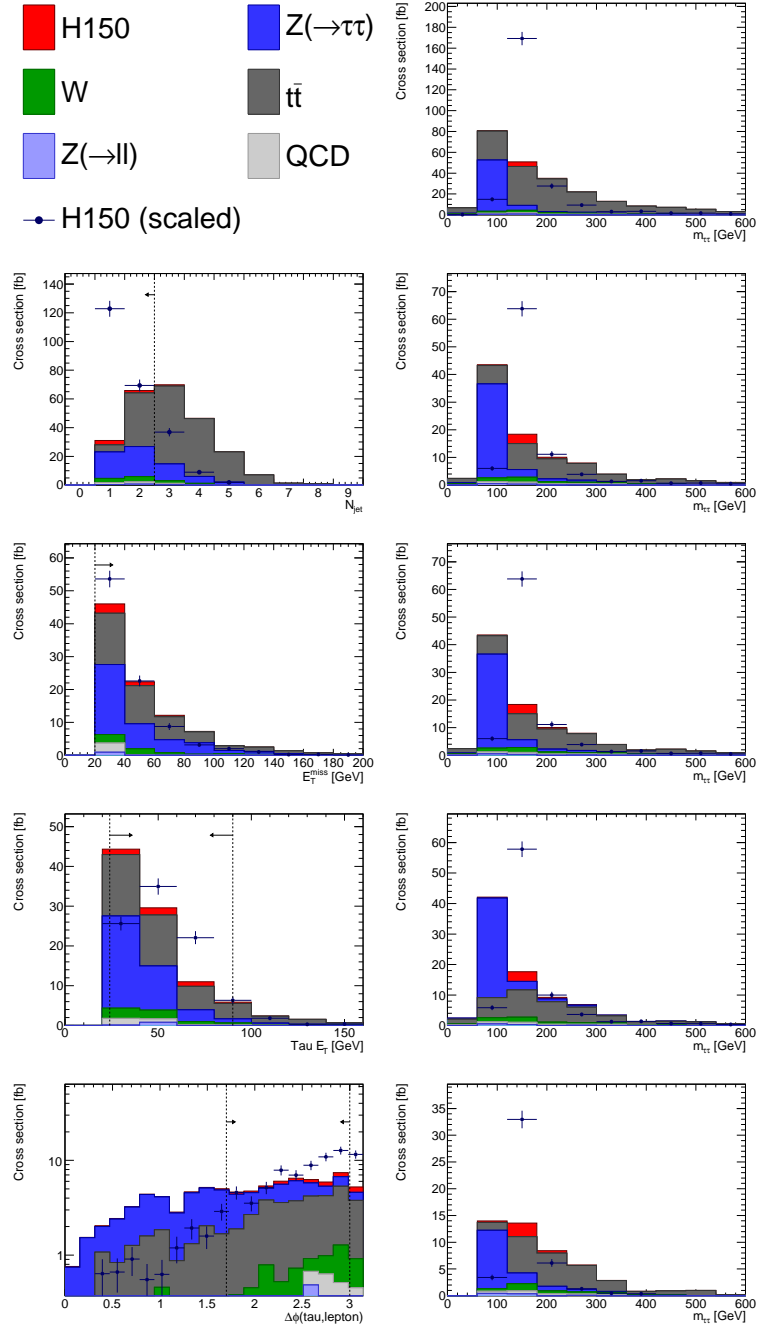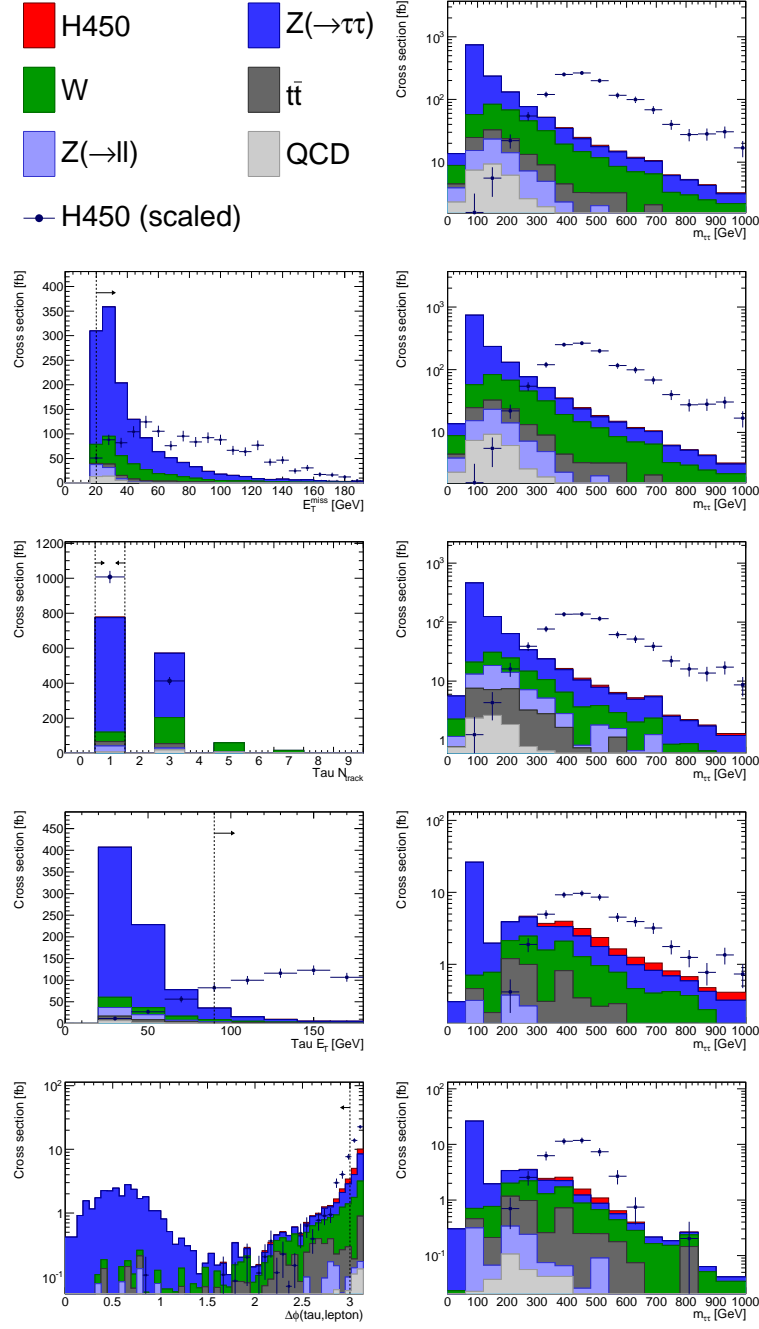
Figure B.5: Optimised selection for the b-tagged analysis at $m_A = 150$ GeV. The selection variables are shown (left) with the selected regions spanning from the dashed lines in the direction of the arrows. The invariant mass distribution is shown after each cut (right).
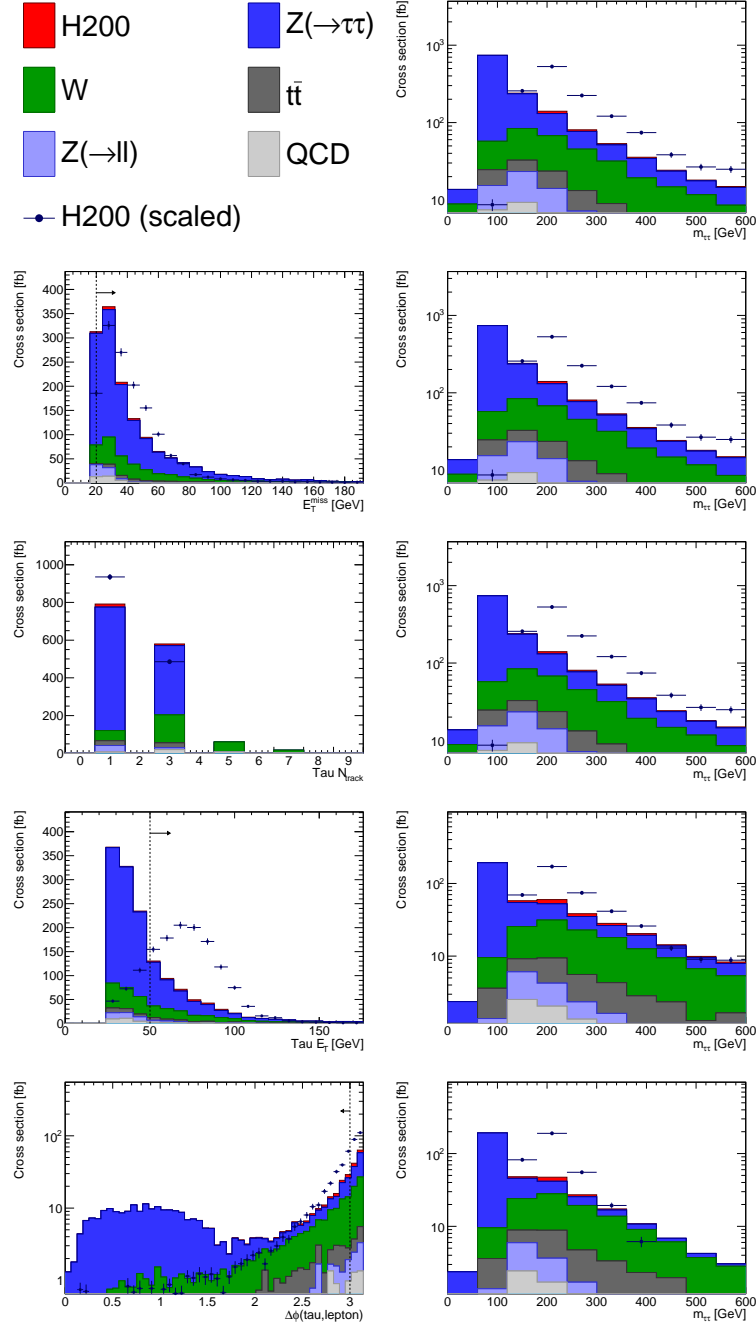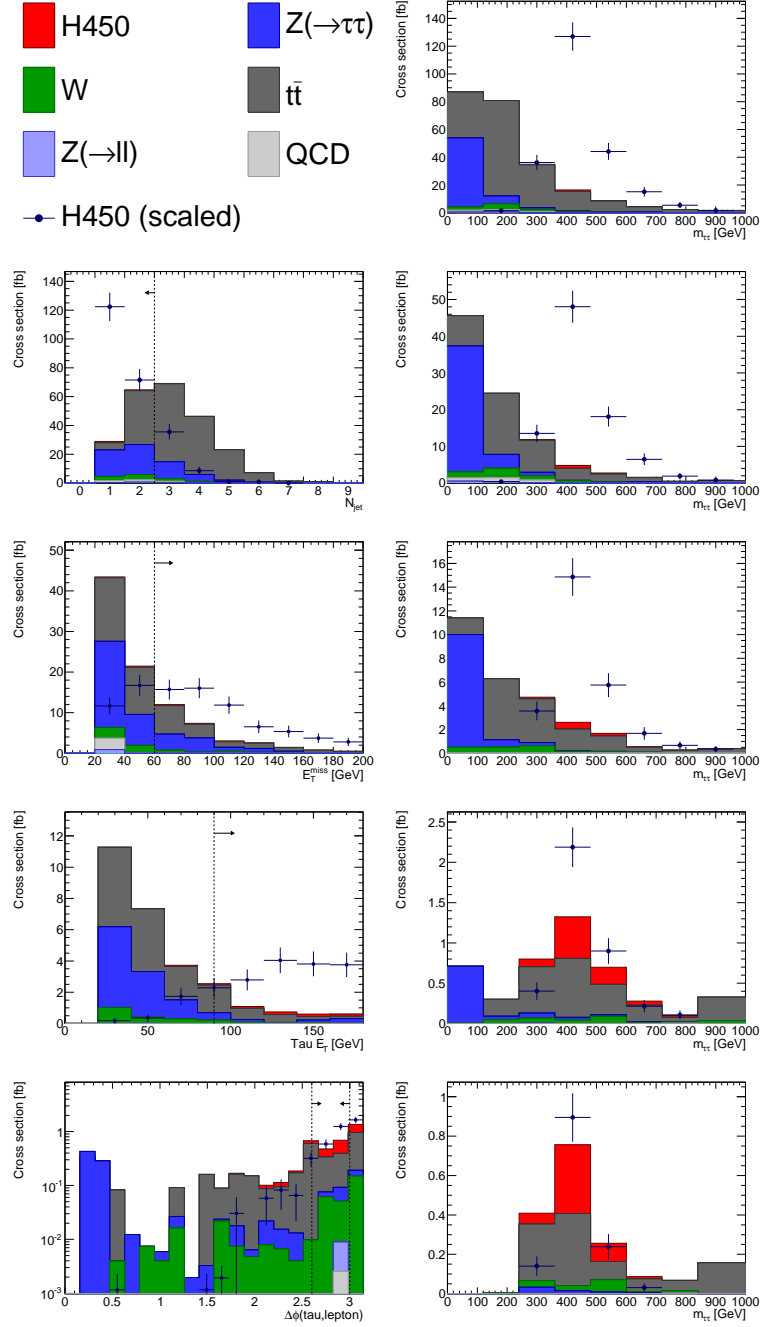
Figure B.6: Optimised selection for the non *b*-tagged analysis at $m_A = 200$ GeV. The selection variables are shown (left) with the selected regions spanning from the dashed lines in the direction of the arrows. The invariant mass distribution is shown after each cut (right).

213
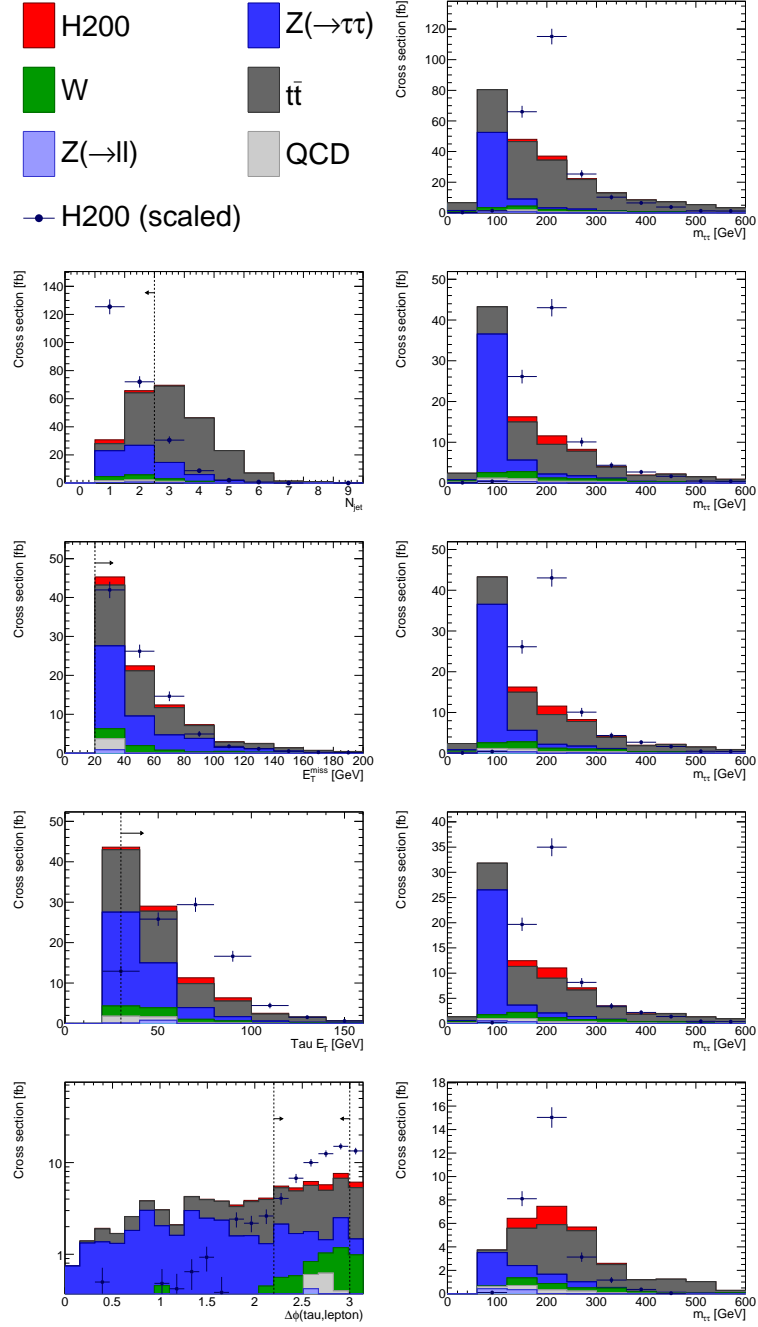
Figure B.7: Optimised selection for the *b*-tagged analysis at $m_A = 200$ GeV. The selection variables are shown (left) with the selected regions spanning from the dashed lines in the direction of the arrows. The invariant mass distribution is shown after each cut (right).
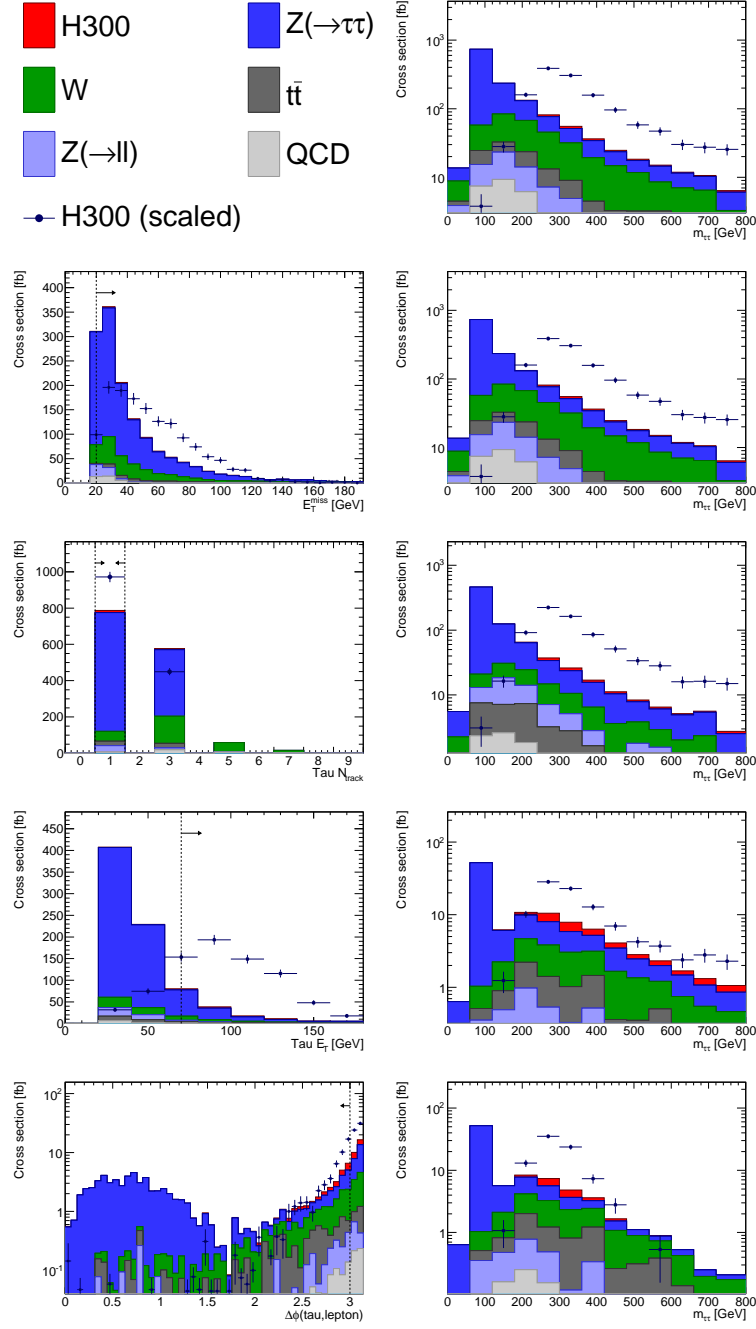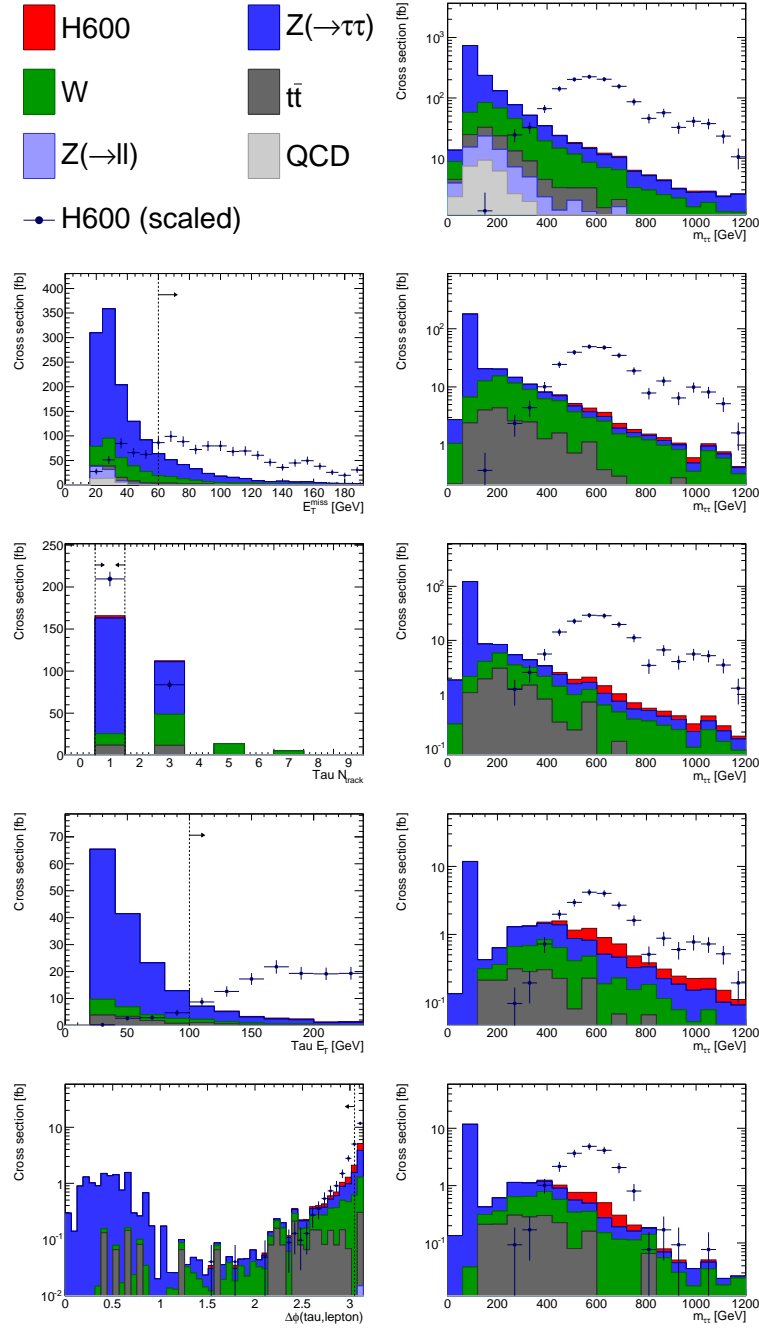
Figure B.8: Optimised selection for the non b-tagged analysis at $m_A = 300$ GeV. The selection variables are shown (left) with the selected regions spanning from the dashed lines in the direction of the arrows. The invariant mass distribution is shown after each cut (right).
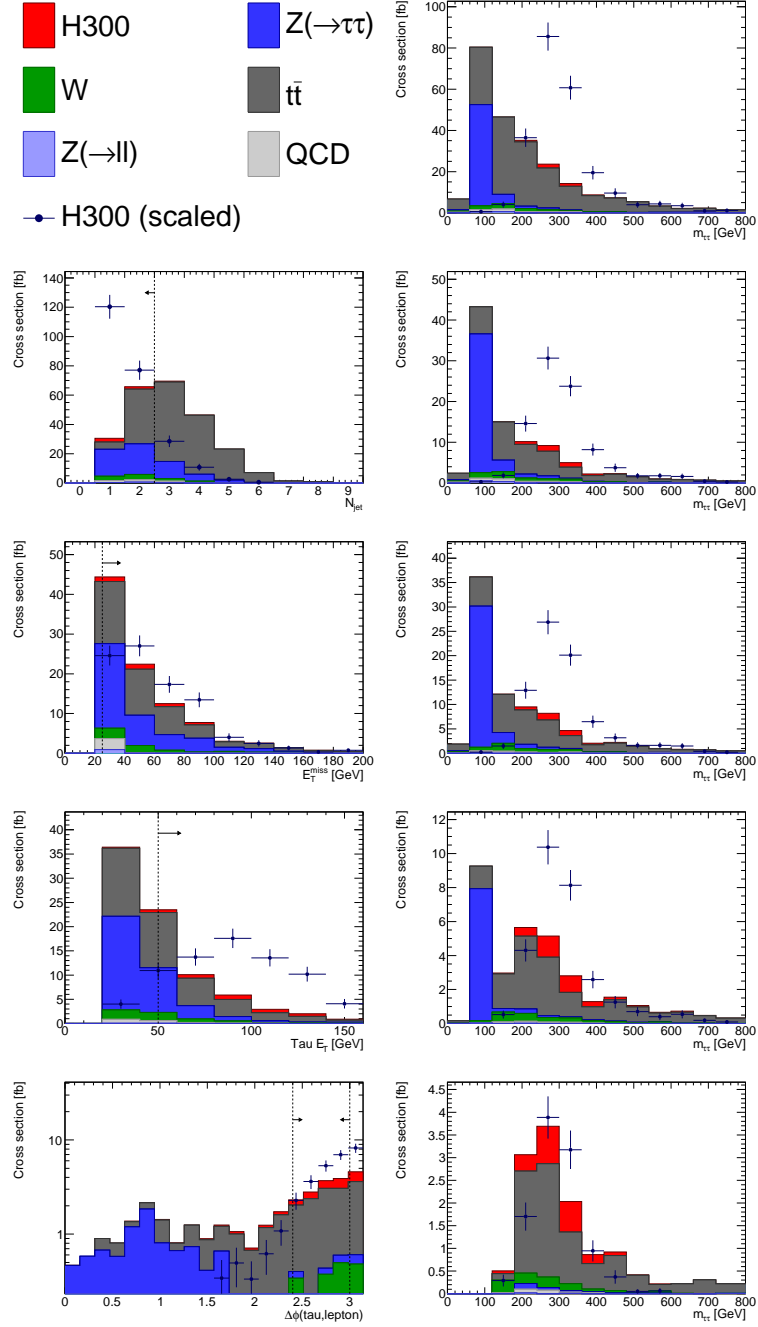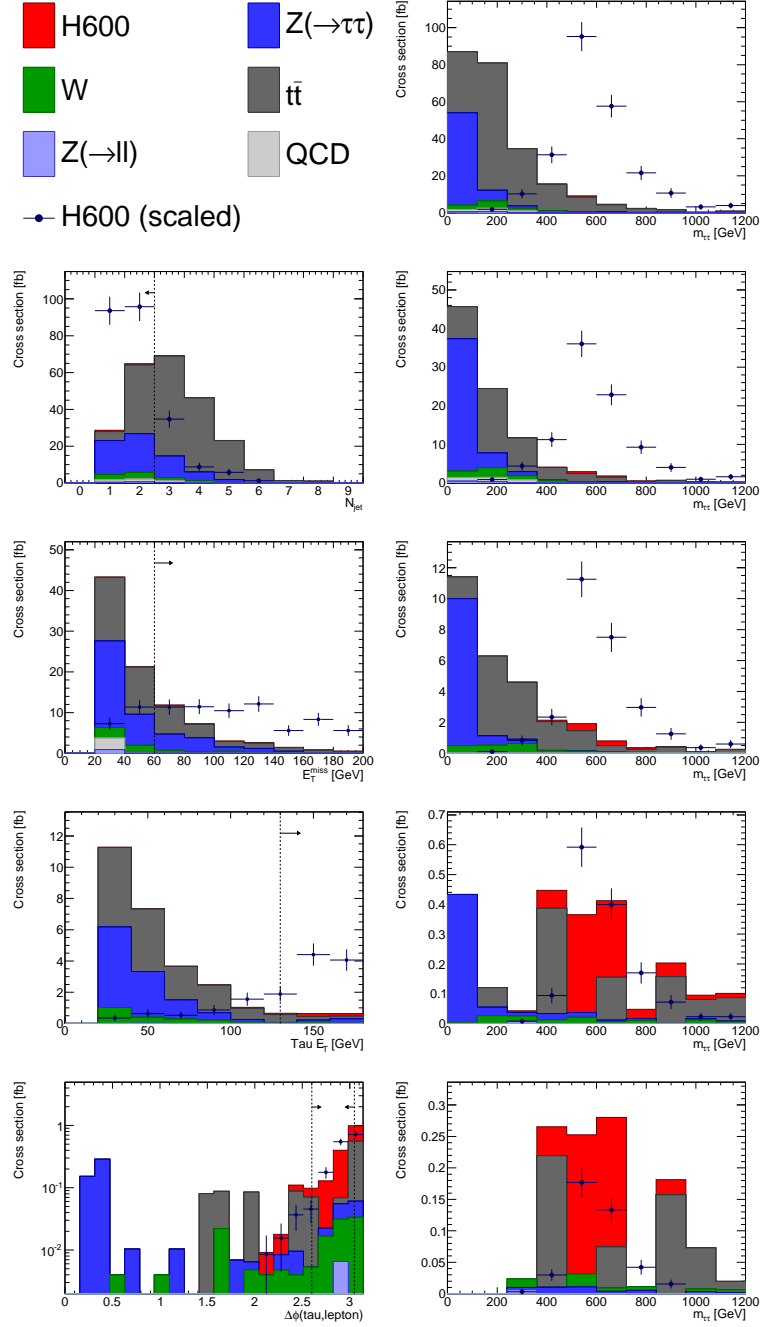
Figure B.9: Optimised selection for the b-tagged analysis at $m_A = 300$ GeV. The selection variables are shown (left) with the selected regions spanning from the dashed lines in the direction of the arrows. The invariant mass distribution is shown after each cut (right).

Figure B.10: Optimised selection for the non *b*-tagged analysis at $m_A = 450$ GeV. The selection variables are shown (left) with the selected regions spanning from the dashed lines in the direction of the arrows. The invariant mass distribution is shown after each cut (right).
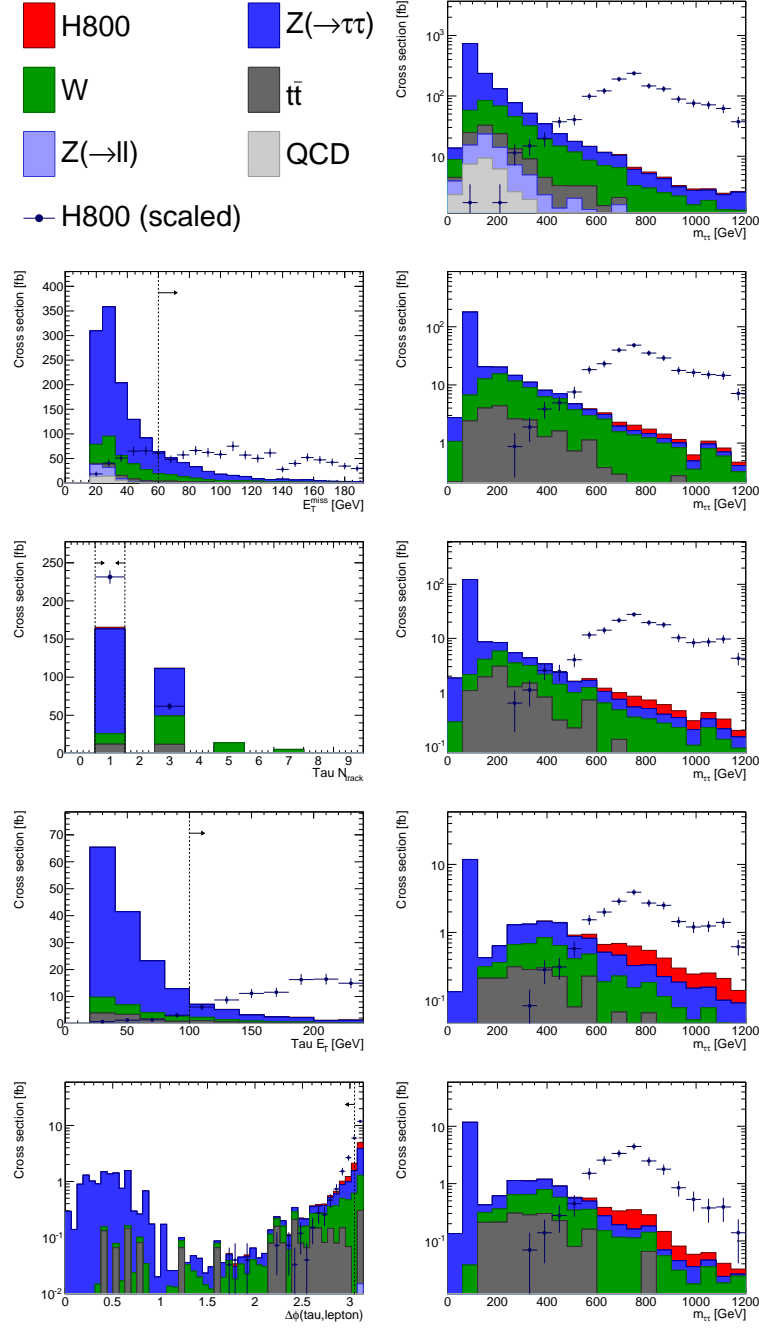
Figure B.11: Optimised selection for the b-tagged analysis at $m_A = 450$ GeV. The selection variables are shown (left) with the selected regions spanning from the dashed lines in the direction of the arrows. The invariant mass distribution is shown after each cut (right).
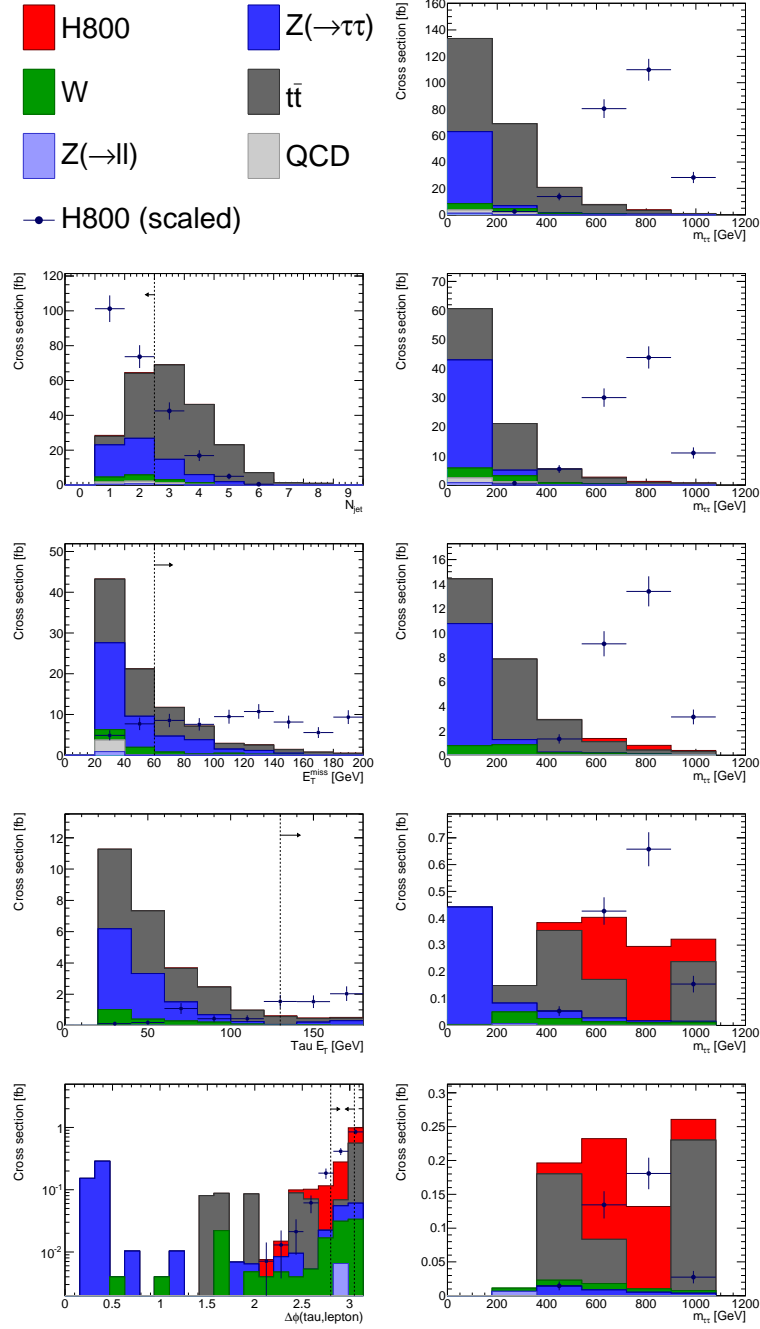
Figure B.12: Optimised selection for the non b-tagged analysis at $m_A = 600$ GeV. The selection variables are shown (left) with the selected regions spanning from the dashed lines in the direction of the arrows. The invariant mass distribution is shown after each cut (right).

Figure B.13: Optimised selection for the *b*-tagged analysis at $m_A = 600$ GeV. The selection variables are shown (left) with the selected regions spanning from the dashed lines in the direction of the arrows. The invariant mass distribution is shown after each cut (right).

Figure B.14: Optimised selection for the non b-tagged analysis at $m_A = 800$ GeV. The selection variables are shown (left) with the selected regions spanning from the dashed lines in the direction of the arrows. The invariant mass distribution is shown after each cut (right).

Figure B.15: Optimised selection for the *b*-tagged analysis at $m_A = 800$ GeV. The selection variables are shown (left) with the selected regions spanning from the dashed lines in the direction of the arrows. The invariant mass distribution is shown after each cut (right).

B.3   Further details on the object weighting procedure

B.3.1   Categorised Tau-ID Weighting

Figures B.16 to B.19 show the composition and fake-rates for the different categories in various samples. Both composition and fake-rate were calculated before the event selection was applied, and also at the point of the Tau-ID. This was done to ensure that the fake-rates calculated independently of the event selection were also valid when weighting the taus in the event selection. One can see that although the overall fake-rate 'All' changes (due to change in the composition of fakes), the fake-rates for the individual categories remain relatively constant. By measuring the fake-rates of the individual categories as opposed to measuring the overall fake-rate of the sample, the Tau-ID Weighting procedure was much less sensitive to changes in the composition of backgrounds due to the event selection.
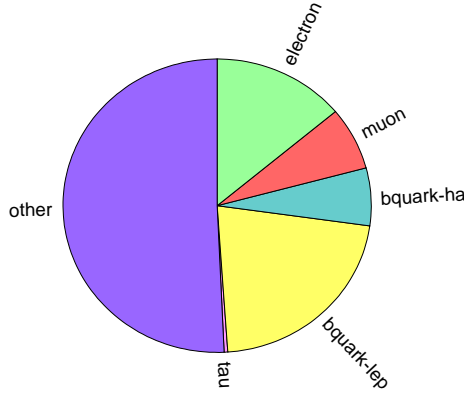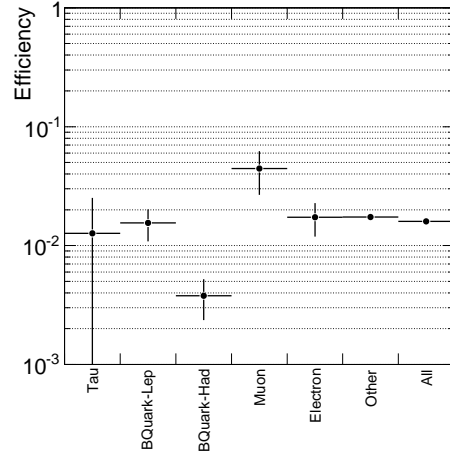
(a) J3 (MLF) Composition (at start)
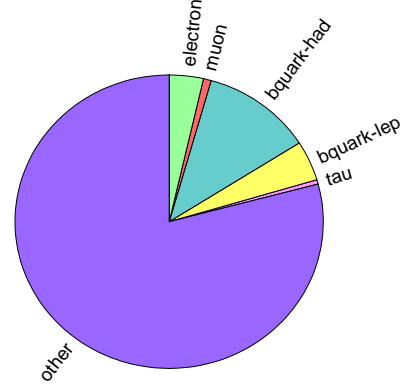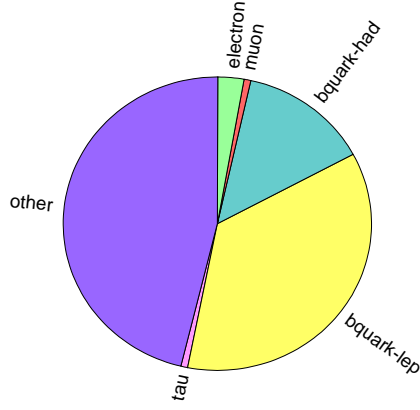

(b) J3 (MLF) Composition (at Tau-ID)
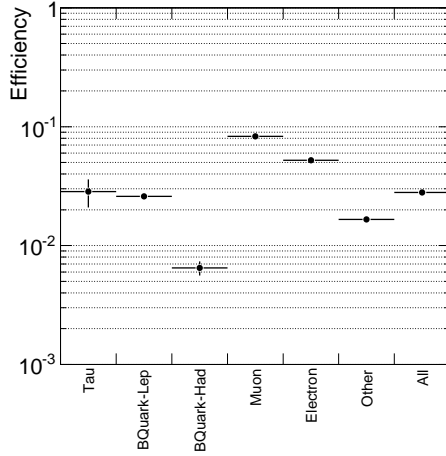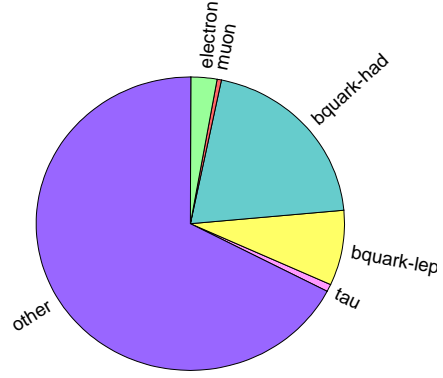

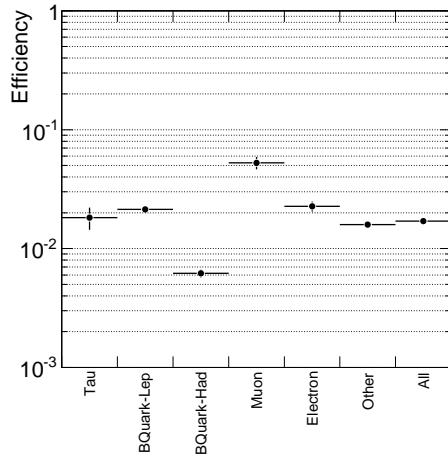(c) J3 (MLF) Fake Rates (at start)

(d) J3 (MLF) Fake Rates (at Tau-ID)

Figure B.16: Tau fake composition for J3 (MLF). 'All' is the fake-rate averaged over all categories. The additional category 'Tau' is included, which indicates tau candidates matched to a true hadronic tau. The contribution from taus is negligible, indicating that the weighting method can be used.
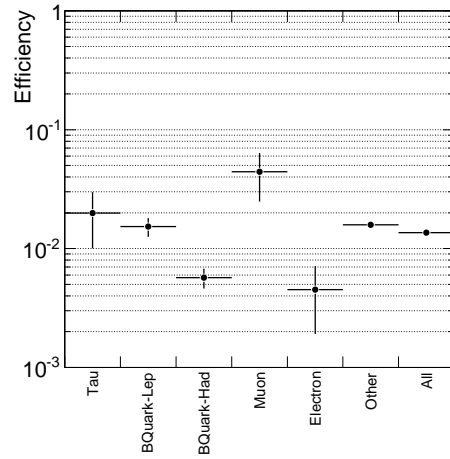
(a) $b\bar{b}$ J3 Composition (at start)

(b) $b\bar{b}$ J3 Composition (at Tau-ID)

(c) $b\bar{b}$ J3 Fake Rates (at start)

(d) $b\bar{b}$ J3 Fake Rates (at Tau-ID)

Figure B.17: Tau fake composition for $b\bar{b}$ J3. 'All' is the fake-rate averaged over all categories. The additional category 'Tau' is included, which indicates tau candidates matched to a true hadronic tau. The contribution from taus is negligible, indicating that the weighting method can be used.

(a) $Z \to ee$ Composition (at start)

(b) $Z \to ee$ Composition (at Tau-ID)

(c) $Z \to ee$ Fake Rates (at start)

(d) $Z \to ee$ Fake Rates (at Tau-ID)

Figure B.18: Tau fake composition for $Z \to ee$. 'All' is the fake-rate averaged over all categories. The additional category 'Tau' is included, which indicates tau candidates matched to a true hadronic tau. The contribution from taus is negligible, indicating that the weighting method can be used.
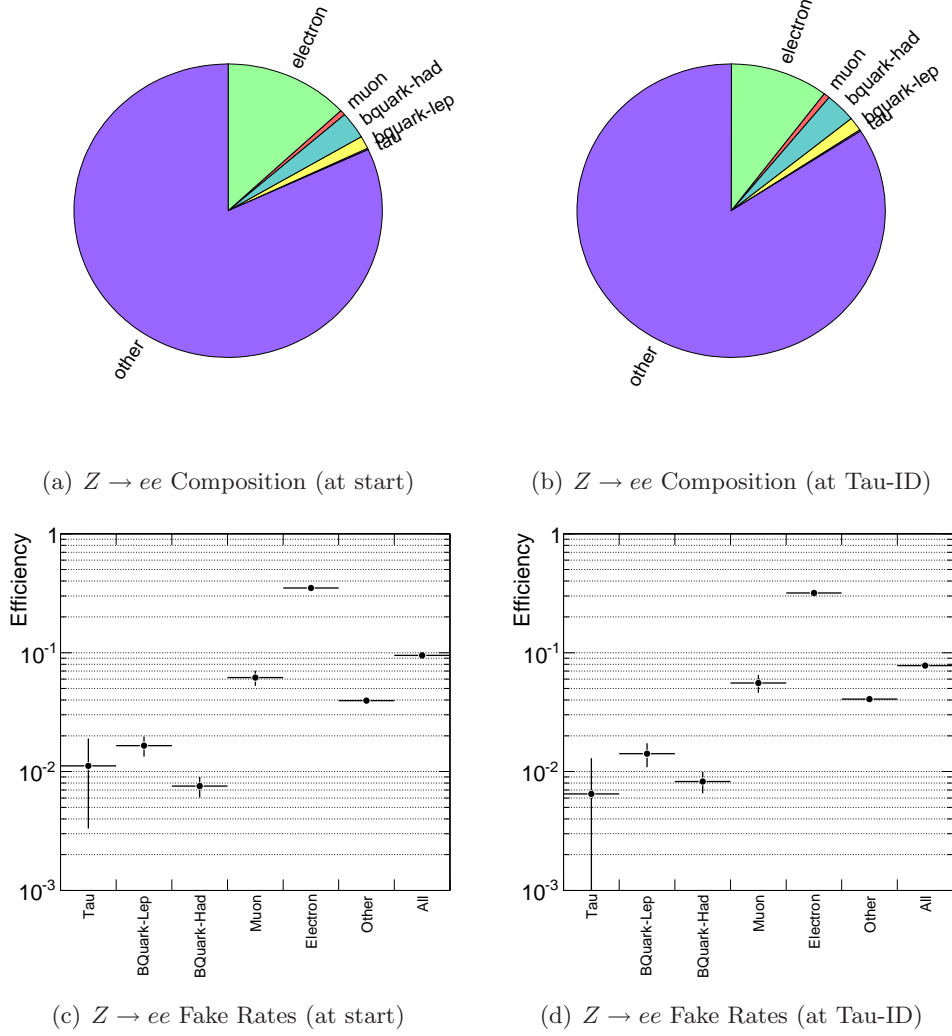
(a) $W \to e\nu$ Composition (at start)

(b) $W \to e\nu$ Composition (at Tau-ID)

(c) $W \to e\nu$ Fake Rates (at start)

(d) $W \to e\nu$ Fake Rates (at Tau-ID)

Figure B.19: Tau fake composition for $W \to e\nu$. 'All' is the fake-rate averaged over all categories. The additional category 'Tau' is included, which indicates tau candidates matched to a true hadronic tau. The contribution from taus is negligible, indicating that the weighting method can be used.
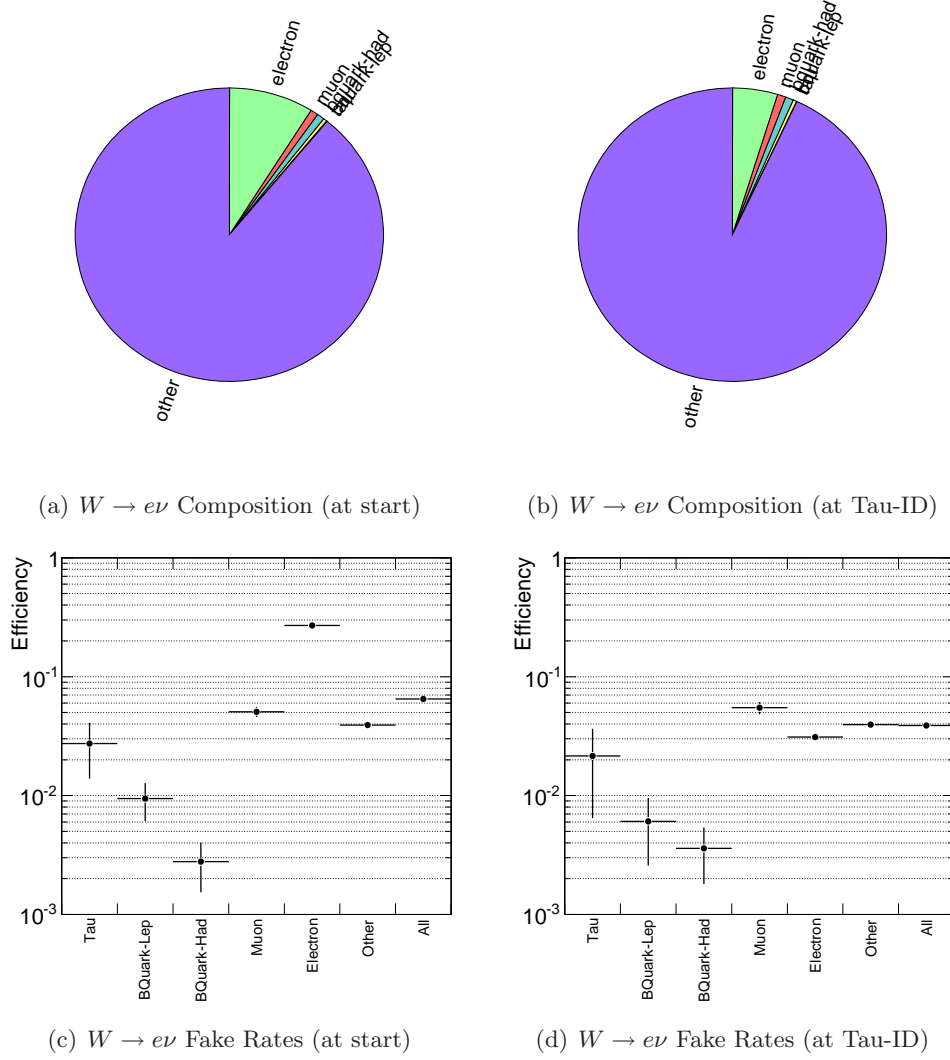
B.3.2 Tau-ID Weighting on $W \to \tau\nu$

The $W \to \tau\nu$ sample has an event weight ~ 10 without any weighting method applied. This is far too large for an accurate estimation of the background. At the same time 65% of the background will contain a real hadronic tau (due to the tau hadronic branching fraction), which should break the assumptions used to justify the use of the Tau-ID Weighting procedure. On the other hand, the channel can only produce an isolated lepton if the tau decays leptonically. The fake-rate for isolated leptons from QCD jets in W events is orders of magnitude lower than the fake-rate for hadronic taus. Therefore, the scenario where a lepton is faked by a QCD jet and the reconstructed tau comes from the real hadronic tau decay from the W, is highly suppressed. To check the contribution, the $W \to \tau\nu$ sample was split into leptonically and hadronically decaying parts using the generator information. In the hadronically decaying sample, no events survived the event selection. Therefore, the leptonically decaying sub-sample was used to estimate the entire $W \to \tau\nu$ background contribution and the Tau-ID Weighting procedure could be used.
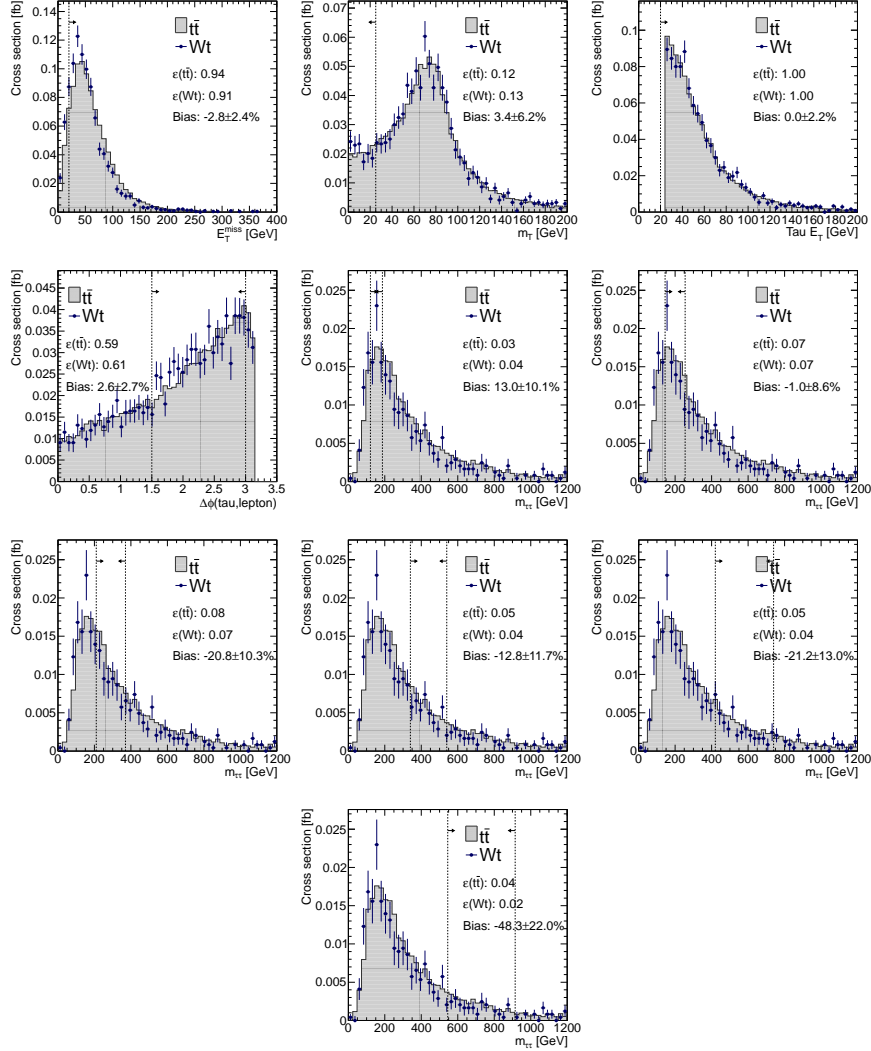
B.4 Single Top Estimation

Figure B.20: Comparison of Wt and $t\bar{t}$ distributions generated at a collision energy of 10 TeV. Events were required to have at least one pre-selected tau and lepton. The selection applied in the b-tagged analysis is indicated by the dashed line. The efficiency of the selection in each sample is also given, as well as the bias $(1 - \epsilon_{t\bar{t}}/\epsilon_{Wt})$. The final six figures show the selection on the invariant mass at each mass hypothesis. No statistically significant difference was found in the kinematic distributions, and differences at a maximum of two standard deviations were found for selection on the invariant mass.

B.5 Data-driven background estimates used for the final result

Use of data-driven estimations in the b-tagged analysis

	m_A [GeV]					
Process	150	200	300	450	600	800
W	MC	MC	MC	MC	MC	MC
$t\bar{t}$	DATA	DATA	DATA	DATA	MC	MC
$Z \to \tau\tau$	MC	MC	MC	MC	MC	MC
$Z \to \ell\ell$	MC	MC	MC	MC	MC	MC
QCD	MC	MC	MC	MC	MC	MC

Table B.1: Background estimations used in the b-tagged analysis for the final significance calculation. 'DATA' indicates when the systematic uncertainty from a data-driven estimation procedure was used and 'MC' indicates when the systematic uncertainty from a direct MC estimate was used.

Use of data-driven estimations in the non b-tagged analysis

	m_A [GeV]					
Process	150	200	300	450	600	800
W	DATA	DATA	DATA	DATA	DATA	DATA
$t\bar{t}$	MC	MC	MC	MC	MC	MC
$Z \to \tau\tau$	MC	MC	MC	MC	MC	MC
$Z \to \ell\ell$	MC	MC	MC	MC	MC	MC
QCD	MC	MC	MC	MC	MC	MC

Table B.2: Background estimations used in the non b-tagged analysis for the final significance calculation. 'DATA' indicates when the systematic uncertainty from a data-driven estimation procedure was used and 'MC' indicates when the systematic uncertainty from a direct MC estimate was used.